Walther Meißner Institut

BAdW BAYERISCHE AKADEMIE DER WISSENSCHAFTEN

Technische Universität München

ONSET OF TRANSMON IONIZATION IN MICROWAVE SINGLE-PHOTON DETECTION

Yuki Nojiri

School of Natural Science
Technische Universität München

Technische Universität München
TUM School of Natural Sciences

Onset of transmon ionization in microwave single-photon detection

Yuki Nojiri

Vollständiger Abdruck der von der TUM School of Natural Sciences der Technischen Universität München zur Erlangung eines

Doktors der Naturwissenschaften (Dr. rer. nat.)

genehmigten Dissertation.

Vorsitz: Prof. Dr. Frank Pollmann

Prüfende der Dissertation:

1. Prof. Dr. Rudolf Gross
2. Prof. Dr. Andreas Reiserer

Die Dissertation wurde am 29.07.2024 bei der Technischen Universität München eingereicht und durch die TUM School of Natural Sciences am 10.09.2024 angenommen.

Contents

Chapter 1

INTRODUCTION

Microwave and Radio Frequency (RF) technology form a cornerstone of current technological advancements, permeating both the commercial and defense sectors. These technologies are pivotal in applications that encompass information processing, sensing, and communications [1, 2]. Commercially, they are integral to the operation of devices and systems ranging from smartphones and 5G, WiFi wireless technologies to radar sensors in various sectors. In defense, microwave technology is essential for passive and active sensing, communication systems, and weapons control. The reliance on and evolution within these domains underscore ongoing challenges in RF and microwave engineering.

As the field of RF and microwave engineering continues to encounter ongoing challenges, quantum physics has begun to play a pivotal role in this expanding domain. In the quantum field, developments over the past two decades have facilitated the creation and control of complex quantum systems. These advancements extend well beyond fundamental research to emerging technologies in computing, communication, and sensing. The superconducting platform, in contrast to other platforms such as electron spins in silicon [3–8], quantum dots [9–12], trapped ions [13–15], ultracold atoms [16–18], nitrogen-vacancies in diamonds [19, 20], and polarized photons [21, 22], offers unique opportunities for parameter manipulation [23, 24]. A significant achievement in this area is the realization of the strong coupling regime, a condition where interaction strengths surpass individual system decay rates [25, 26]. This achievement is facilitated by advances in nanofabrication technology, allowing for the construction of sophisticated superconducting quantum chips. This area of research in physics, where quantum effects are studied in electrical circuits, is called circuit quantum electrodynamics.

In superconducting circuits and cavity quantum electrodynamics systems, Josephson junctions play a pivotal role. Characterized by their strong nonlinearity, and low losses, these junctions are fundamental for various quantum information applications. Their crucial role is evident in the realization of parametrically driven devices, including quantum amplifiers [27–32], frequency converters [33–35], nonclassical light generators [36, 37], stabilizers [38, 39], and microwave single-photon detectors (SPDs) [40, 41]. The operation of these devices is based on three- or four-wave mixing processes enabled by a strong microwave drive, termed a "pump". Among these, SPDs can be applied for many quantum protocols, such as quantum teleportation [42], entanglement distillation [43], entanglement swapping [44], quantum eraser [45], quantum repeater [46], Gaussian boson sampling [47], and quantum error correction [48].

In the optical regime, single-photon detectors are realized in various kinds of implementations such as quantum dots [49–51], superconducting nanowires [52], single-photon avalanche photodiodes [53], and up-conversion detectors [54]. Conversely, development of SPDs in the microwave domain is particularly challenging. This is primarily attributed to the lower energy scales involved [40, 41, 55–58] and the high performance standards demanded by applications in quantum information, quantum sensing, and quantum illumination [59–65]. Despite these obstacles, various microwave SPD designs with quantum efficiencies exceeding 50% have been demonstrated in the recent years [40, 41, 55–58]. The strategic significance of microwave SPDs becomes particularly important in applications such as dark matter axion search [61], spin fluorescence detection [66, 67], and quantum radar [64, 68].

The application of microwave SPDs in the quantum radar systems enables an experimental quantum advantage in a target detection [64]. In the field of spin fluorescence detection, microwave SPDs can surpass the signal-to-noise-ratio performance over the conventional electron spin resonance methods, marking a substantial improvement in detection techniques [66, 67]. Meanwhile, microwave SPD technologies can also further advance the rapidly growing fields of microwave quantum communication and sensing [37, 65, 69, 70].

A common technique for detecting single photons in microwave SPDs involves the use of transmon qubits, a dominant type of superconducting qubits used in quantum computation [40, 41, 57, 58]. The phenomenon of transmon ionization (TI) emerges when the transmon qubit state escapes the confinement of the Josephson potential. Such behavior can be caused by strong microwave pumping, which can set the transmon into a rather complex regime involving many quantum levels [71–74]. This phenomenon is known under various names, such as the quantum-to-classical phase transition [75–77], first-order dissipative phase transition [78–81], chaotic regime [74, 82], and breakdown of photon-blockade [77, 78]. Various tools and representations, such as Rényi entropy, Floquet theory, and Husimi Q functions, are employed to indicate potential phase transitions. Notably, within the framework of the quantum Duffing oscillator, Rényi entropy serves as a quantifier of purity of the quantum system, while the Floquet theory provides insights into the temporal evolution under periodic driving. Concurrently, the Husimi Q function offers a phase space representation, revealing significant quantum fluctuations which arise from tunneling between two metastable states. While this bistability is known to be useful for high-fidelity readout schemes [73, 83], its influence on the SPD behavior remains not very well understood until now. Given the importance of such devices in quantum applications, we investigate its complex dynamical behavior, and quantify the impact of the TI on the SPD performance.

This thesis is organized as follows. In Chap. 2, we review the fundamental theory of superconducting microwave circuits. Beginning with the theory of coplanar waveguide (CPW) transmission lines, we explore the fundamental components including 2D CPW resonators, 3D cavities, and the transmon qubit. We then examine the concepts, sources, and applications of decoherence in quantum systems. The chapter also introduces the four-wave mixing process, pivotal in our SPD study, and delves into quantum-to-classical phase transitions in transmon systems. Subsequently, in Chap. 3, we detail the fabrication techniques developed at the Walther-Meißner-Institute (WMI). We present our findings on the internal quality factors of 2D CPW resonators and the coherence times of 2D transmon qubits, showcasing the advancements made in sample fabrication. In Chap. 4, we present an experimental and numerical study of the TI onset and the SPD performance of a transmon qubit coupled to a multi-mode superconducting 3D cavity. Finally, Chap. 5 discusses the potential application of our SPD system as a multi-photon Fock-state generator. We explore the concept of irreversible coupling and its implications for quantum state generation and manipulation.

Chapter 2

SUPERCONDUCTING MICROWAVE CIRCUITS

Before delving into the details of quantum electromagnetic circuits, it is important to highlight some key points, especially the electromagnetic phenomena, and the linear and nonlinear response.

Quantum electromagnetic circuits can be seen as the quantum mechanical counterpart of microwave circuits, also known as high-frequency circuits. In many situations, electromagnetic phenomena both in vacuum and matter can be described classically based on Maxwell's equation and the concepts of classical optics. In some cases this is no longer possible and the electromagnetic fields, which so far have been treated classically, have to be treated quantum mechanically. This extends classical electrodynamics and optics to quantum electrodynamics and quantum optics.

Whether the considered systems are linear or non-linear is on first sight not relevant for the classical to quantum transition. For example, also in classical optics we can treat systems by a linear approximation only in the simplest case (so-called linear response theory) but have to treat them by a more detailed non-linear description for stronger perturbations, which extends the field to nonlinear optics[1]. In that case for all systems showing a nonlinear response the superposition principle is no longer valid. That is, if one superimposes two electromagnetic waves with two different frequencies, the resulting wave does no longer contain only these two frequency components, but also other frequency components [84, 85]. A phenomenon termed as frequency mixing. The spectrum of these emergent frequencies is modulated by the specific nature of the nonlinearity, potentially leading to three-wave, four-wave, or even higher-order wave mixing. Such nonlinear dynamics underpin parametric processes, a principle already harnessed in commercial devices designed for tasks like parametric amplification and frequency conversion. An illustrative example from our lab is the employment of an I-Q mixer in a room-temperature qubit measurement setup; it adeptly downconverts a GHz-frequency readout signal to the MHz domain, aligning with the operational frequency of an FPGA.

Shifting our focus to superconducting circuits, Josephson junctions emerge as quintessential components characterized by their pronounced nonlinearity, absence of dissipation, and compatibility with high-frequency operations. Parametrically activated devices, such as quantum amplifiers [27–32], frequency converters [33–35], nonclassical-light generator [36, 37], stabilizer [38, 39], and single-photon detectors [40, 41], heavily rely on three- or four-wave mixing processes, making high-frequency operation crucial for their functionality. It is important to note that while these mechanisms are rooted in quantum theory, high pump power prerequisites mean that there are scenarios wherein a classical approach to Josephson circuits suffices. In particular, we can observe a quantum-to-classical phase transition [75–77]. That is, there exists a threshold power beyond which a classical perspective is valid. For example, if we can approximate the Josephson system as a quantum Duffing oscillation, this phenomenon is commonly known as the first-order dissipative phase transition [80, 81, 86]. If quantum devices are coupled to the so-called transmon qubits, which are specific type of superconducting qubits based on Josephson junctions, this crossover is often referred to transmon ionization [73, 74] or other

[1] It is worth to mention that the departure from linearity has nothing to do with the system size but only whether or not the considered systems responds linearly or nonlinearly to a perturbation. But we can describe small systems always as so-called lumped element (zero-dimensional) systems as long as the system size is small compared to the wave length of the electromagnetic fields. This is true for both a classical and quantum description.

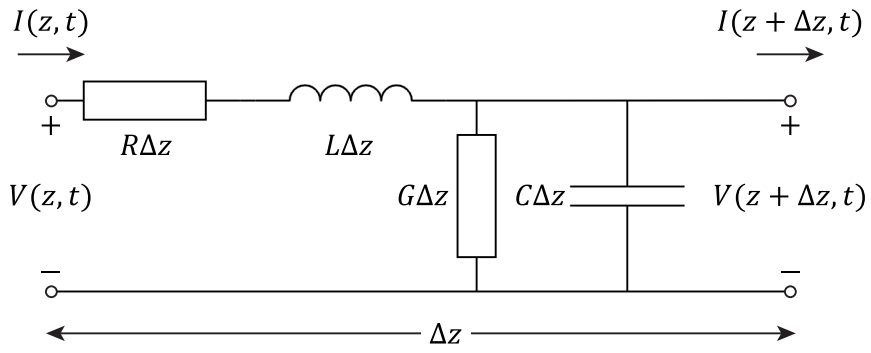

Figure 2.1. Transmission line element represented by a lumped-element circuit.

terms such as break-down of photon blockade [77, 78], or chaotic regime [74, 82].

Hence, the interplay between quantum and classical regimes in superconducting circuits, underscored by the dynamics of frequency mixing and the pivotal role of Josephson junctions, remains a paramount topic of investigation. The phase transitions and the associated operational thresholds emphasize the delicate balance and the non-trivial transition zones in these systems. Therefore, the study of quantum electromagnetic circuits holds significant importance in the analysis of superconducting circuits and the design of novel devices.

2.1 Coplanar waveguide transmission lines

This section is mainly based on the paper [87] and partly based on the books [1, 2, 88]. This section deals with the quantum mechanical description of electromagnetic circuits based on quantum electrodynamics (QED). This field is called circuit quantum elctrodynamics (cQED) and extends the classical treatment of microwave circuits to a full quantum description.

2.1.1 Transmission line theory

The electronic circuits considered in this thesis are composed of discrete components like resistors, capacitors, inductors, and conductors. In classical circuit theory, the predominant parameters used for the description of these circuits are notably voltage and current. In the realm of field analysis, parameters of interest are often characterized in terms of their amplitude and phase. The relationship between these parameters for the input and output fields is systematically captured through the scattering matrix. To reconcile these two distinct paradigms, we resort to transmission line theory, a framework that unifies the terminologies of electronic circuitry with those of (quantum) optics.

Classical transmission line theory

To make the transition between a lumped-element (zero dimensional) theory to a theory capable to describe extended circuits, it is vital to remember that circuit theory fundamentally incorporates four distinct lumped elements: resistance, inductance, conductance, and capacitance. Our aim, if feasible, is to utilize these inherent characteristics as linear elements. To be able to describe extended circuits, we consider an infinitesimal fraction of the transmission line as a lumped-element circuit, such that we can split up the circuit in many lumped-element circuits that are coupled to each other. In this context, R represents the series resistance per unit length, L stands for the series inductance per unit length, G

denotes the shunt conductance per unit length, and C describes the shunt capacitance per unit length (see Fig. 2.1). It is worth mentioning that a transmission line is often schematically represented as a two-wire line since transmission lines always have at least two conductors [1].

If we model our problem as shown in Fig. 2.1 and solve by using the Kirchoff's voltage law and the current law, we obtain the following differential equations by taking the limit as $\Delta z \to 0$,

$$\frac{\partial V(z,t)}{\partial z} = -RI(z,t) - L\frac{\partial I(z,t)}{\partial t}$$

and

$$\frac{\partial I(z,t)}{\partial z} = -GV(z,t) - C\frac{\partial I(z,t)}{\partial t}$$

known as telegrapher equations. In the frequency domain, the solutions of these differential equations are

$$V(z) = V_{\text{in}} e^{-\gamma z} + V_{\text{out}} e^{\gamma z} \tag{2.1}$$

$$I(z) = I_{\text{in}} e^{-\gamma z} + I_{\text{out}} e^{\gamma z}, \tag{2.2}$$

where

$$\gamma = \sqrt{(R - i\omega L)(G - i\omega C)}.$$

The terms with $e^{-\gamma z}$ represents the incoming wave propagation in the $+z$ direction and the term with $e^{\gamma z}$ the outgoing wave propagation in the $-z$ direction with carrier frequency ω. Then, $V_{\text{in,out}}$ is the voltage amplitude of incoming and outgoing wave, respectively, and $I_{\text{in,out}}$ is the current amplitude. Furthermore, we obtain the so-called characteristic impedance Z_0

$$Z_0 = \sqrt{\frac{R - i\omega L}{G - i\omega C}} \overset{R=G=0}{=} \sqrt{\frac{L}{C}}$$

and therefore the Eq. (2.2) can be rewritten as

$$I(z) = \frac{1}{Z_0}(V_{\text{in}} e^{-\gamma z} - V_{\text{out}} e^{\gamma z}). \tag{2.3}$$

Therefore, the entire dynamical process can be captured by V_{in} and V_{out}[2]. To ensure compatibility with industry-standard microwave equipment, we restrict ourselves to a transmission line design with an impedance of $50\,\Omega$. This impedance matching is critical to minimize signal reflections and enhance the performance of our microwave circuits. To realize a $50\,\Omega$ impedance, we adopt specific dimensional parameters for our transmission line designs. Namely, we opt for a center conductor with a width of $12\,\mu$m, along with maintaining a $20\,\mu$m gap between the center conductor and the ground plane. By adhering to these design guidelines, we can effectively achieve the desired impedance, which allows for effortless integration with conventional $50\,\Omega$ microwave systems.

In order to make the transition from a classical to a quantum description, the classical quantities as voltage and current have to be replaced by corresponding field operators, which in turn are associated

[2]Strictly speaking, a distinction must be made between incoming wave and $+z$ propagating wave, as well as outgoing wave and $-z$ propagating wave, especially when we consider Eqs. (2.1) and (2.2). The rationale behind this differentiation stems from the fact that the relationships expressed in Eqs. (2.1) and (2.3) are typically applicable solely for $\pm z$ traveling waves and V_{in} and V_{out} are arbitrary independent functions. However, when two transmission lines are interconnected (like in semi-infinite lines), the incoming and outgoing waves become dependent due to the boundary conditions, leading to an equality between both wave types [1, 89].

with the creation and annihilation operators in quantum mechanics [87, 89]. As a periodic boundary condition, we consider a finite piece of length l of a transmission line, which results in a selection of possible wave numbers k with corresponding mode frequencies ω_k. A reasonable starting point is to begin with the Lagrangian by initially associating the flux variable φ with voltage and current[3] [87, 89].

$$V(z,t) = \partial_t \varphi(z,t), \qquad I(z,t) = -\frac{1}{L}\partial_z \varphi(z,t).$$

Having obtained the flux representation, we can derive the Lagrangian density

$$\mathcal{L}(z,t) \equiv \frac{C}{2}(\partial_t \varphi(z,t))^2 - \frac{1}{2L}(\partial_z \varphi(z,t))^2, \tag{2.4}$$

for which we obtain the momentum conjugate of $\varphi(z,t)$ as the charge per length

$$q(z,t) \equiv \frac{\delta \mathcal{L}(z,t)}{\delta \partial_t \varphi(z,t)} = C\partial_t \varphi(z,t).$$

The Hamiltonian is then given by

$$H(t) \equiv \int \mathrm{d}z \frac{1}{2C}(q(z,t))^2 + \frac{1}{2L}(\partial_z \varphi(z,t))^2.$$

As we can examine a wave equation characterized by the flux, calculating the Euler-Lagrange equation reveals that both the charge per length and the flux are variables undergoing oscillations, resulting in a Hamiltonian that represents a simple harmonic oscillator. Consequently, we are motivated to recast this in terms of field variables in order to observe the quantum analogy of the Hamiltonian expressed in the language of creation and annihilation operators. This can be obtained by defining

$$A_k(t) \equiv \frac{1}{\sqrt{l}} \int \mathrm{d}z e^{-ikz} \left(\frac{1}{\sqrt{2C}} q(z,t) - i\sqrt{\frac{k^2}{2L}} \varphi(z,t) \right),$$

where again the fields as a function of wave vector k have to obey periodic boundary condition on a length l. Then we have

$$H(t) = \frac{1}{2}\sum_k (A_k^* A_k + A_k A_k^*). \tag{2.5}$$

The input voltage V_{in} and output voltage V_{out} can be written as

$$V_{\mathrm{in}}(z,t) = \sqrt{\frac{1}{2lC}} \sum_{k>0} [A_k(0) e^{+i(kz-\omega_k t)} + A_k^*(0) e^{-i(kz-\omega_k t)}] \tag{2.6a}$$

$$V_{\mathrm{out}}(z,t) = \sqrt{\frac{1}{2lC}} \sum_{k<0} [A_k(0) e^{+i(kz-\omega_k t)} + A_k^*(0) e^{-i(kz-\omega_k t)}], \tag{2.6b}$$

where the frequency ω_k is dependent on k.

[3] An alternative pathway is to start with the Maxwell's equations, which would offer a more lucid association between the representations of voltage and current and the field representation, as compared to the Lagrangian methodology. However, this approach makes drawing parallels with quantum optics challenging. For those interested in pursuing this line of reasoning, we direct them to Ref. [1].

With the relationship between the voltage-current and field representation in classical transmission line theory established, we now proceed to its quantization. In the context of the Lagrangian density, we have derived the momentum conjugate of $\varphi(z,t)$, which turned out to be the charge per length. Using the correspondence principle [89], we treat these two physical variables as operators that obey the following commutation relation

$$[\hat{q}(z), \hat{\varphi}(z')] = -i\hbar\delta(z - z').$$

This gives us the basis for the quantization of the field amplitude derived from Eq. (2.6) which obeys

$$[\hat{A}_k, \hat{A}_{k'}] = \hbar\omega_k\delta_{k,k'}.$$

Therefore, we can write down the quantized field operator with creation $\hat{a}_k^\dagger$ and annihilation operators $\hat{a}_k$ by

$$\hat{A}_k = \sqrt{\hbar\omega_k}\hat{a}_k. \tag{2.7}$$

Thus, we see by expressing the quantized Hamiltonian with Eq. (2.7) it is consistent with the classical Hamiltonian form in Eq. (2.5)

$$\hat{\mathcal{H}}_{\text{bath}} = \sum_k \hbar\omega_k \left[\hat{a}_k^\dagger \hat{a}_k + \frac{1}{2}\right]. \tag{2.8}$$

From here on, when we perceive the transmission line as an environment, in a quantum description it can be viewed as a bath of quantum harmonic oscillators. The core concept of the transmission line theory, particularly the correlation between the classical voltage-current representation and the corresponding quantum mechanical field operator description, stems from the Hamiltonian perspective of the infinitesimally small LC circuit. This LC circuit's energy per unit length encapsulates the energy held within the capacitor and the inductor. The quantization of input and output voltage in Eq. (2.6) reads

$$\begin{aligned}
\hat{V}_{\text{in}}(t) &= \sqrt{\frac{1}{2lC}}\sum_{k>0}\sqrt{\hbar\omega_k}\left[\hat{a}_k e^{-i\omega_k t} + \text{h.c.}\right] \\
&= \int_0^\infty \frac{\mathrm{d}\omega}{2\pi}\sqrt{\frac{\hbar\omega Z_0}{2}}\left[\hat{a}_{\text{in}}[\omega]e^{-i\omega t} + \text{h.c.}\right] \qquad (2.9a)\\
\hat{V}_{\text{out}}(t) &= \sqrt{\frac{1}{2lC}}\sum_{k<0}\sqrt{\hbar\omega_k}\left[\hat{a}_k e^{-i\omega_k t} + \text{h.c.}\right] \\
&= \int_0^\infty \frac{\mathrm{d}\omega}{2\pi}\sqrt{\frac{\hbar\omega Z_0}{2}}\left[\hat{a}_{\text{out}}[\omega]e^{-i\omega t} + \text{h.c.}\right], \qquad (2.9b)
\end{aligned}$$

where

$$\hat{a}_{\text{in,out}}[\omega] \equiv 2\pi\sqrt{\frac{1}{l}\frac{1}{LC}}\sum_{k\gtrless 0}\hat{a}_k\delta(\omega - \omega_k) \tag{2.10}$$

is the input/output field annihilation operator obeying the commutation relation

$$\left[\hat{a}_{\text{in,out}}[\omega], (\hat{a}_{\text{in,out}}[\omega'])^\dagger\right] = 2\pi\delta(\omega - \omega').$$

In our analysis, we are often interested in a specific frequency range centered around a characteristic drive or resonance frequency ω_0. Henceforth, it is advantageous to work in the time-domain using a frame rotating at $\omega = \omega_0$. By performing a Fourier transform on Eq. (2.10), we obtain the following expression

$$\hat{a}_{\text{in}}(t) = \sqrt{\frac{1}{l}\frac{1}{LC}} \sum_{k>0} e^{-i(\omega_k - \omega_0)(t-t_0)} \hat{a}_k(t_0) \tag{2.11}$$

$$\hat{a}_{\text{out}}(t) = \sqrt{\frac{1}{l}\frac{1}{LC}} \sum_{k<0} e^{-i(\omega_k - \omega_0)(t-t_1)} \hat{a}_k(t_1). \tag{2.12}$$

Here, $t_0 < t$ is the time in the distant past before any wave packet e.g. launched at the cavity reached it, while $t_1 > t$ is a time in the distant future after the input field has e.g. interacted with the cavity (see also Sec. 2.4). Finally, we obtain for the quantized voltage and current in the frequency domain as

$$\hat{V}[\omega] = \hat{V}_{\text{in}}[\omega] + \hat{V}_{\text{out}}[\omega] = \sqrt{\frac{\hbar\omega Z_0}{2}} (\hat{a}_{\text{in}}[\omega] + \hat{a}_{\text{out}}[\omega]) \tag{2.13a}$$

$$\hat{I}[\omega] = \frac{1}{Z_0} (\hat{V}_{\text{in}}[\omega] - \hat{V}_{\text{out}}[\omega]) = \sqrt{\frac{\hbar\omega}{2Z_0}} (\hat{a}_{\text{in}}[\omega] - \hat{a}_{\text{out}}[\omega]). \tag{2.13b}$$

To summarize this subsection, we have derived the relationship between voltage-current representation and field representation classically and quantum mechanically.

2.1.2 Superconducting transmission line resonators

Superconducting microwave transmission line resonators play a crucial role in cQED for reading out the qubit state [90], studying light-matter interaction [25, 26], serving as quantum buses [91], Purcell filters [92], photon storage devices [93], bosonic cat qubits [94] or waste mode for dissipation engineering [39, 41]. Here, we will provide an overview of resonant transmission line structures and introduce the fundamental concepts involved. In contrast to freely propagating waves on transmission lines in Subsec. 2.1.1, we modify the electromagnetic field to form standing waves with discrete frequencies by imposing specific boundary conditions. The introduction of boundary conditions into a transmission line structure can be achieved through two common methods: shorting the line to ground or creating an open-circuit by cutting the center conductor. Shorting the line to ground forces the voltage at that position to zero, effectively creating a node. On the other hand, an open-circuit structure leads to a vanishing current at the cut point, establishing an antinode in the voltage distribution. These boundary conditions allow us to engineer the electromagnetic field distribution along the transmission line resonator, resulting in the formation of standing waves with integer multiple of fundamental mode frequency. By controlling the boundary conditions and resonator length, we can tailor the resonant frequencies and achieve the desired functionalities for various applications in cQED.

In cQED, there are two types of resonators: quarter-wavelength resonators and half-wavelength resonators. Quarter-wavelength resonators are commonly used in cQED due to their compact size compared to half-wavelength resonators. In a quarter-wavelength resonator, one end is shorted, while the other end is open, as depicted in Fig. 2.5(a). Under these boundary conditions, the electric field distribution constructively interferes for a wavelength given by $\lambda_n = \frac{4l_r}{n}$, where l_r is the resonator length and $n \in \mathbb{N}$ denotes the mode number. This interference results in strong suppression of all other

wavelengths inside the resonator. The wave equation has to satisfy

$$\left(\frac{\partial^2}{\partial x^2} + k_n^2\right)\varphi(x) = 0$$

with the boundary conditions[4]

$$\varphi(0) = 0, \qquad \varphi(l_r) = \varphi_0.$$

The solution is $\varphi(x) = \varphi_0 \sin(kx)$ with $kl_r = \pi n l_r/\lambda_n = \pi n/4$. Hence, the resonator frequency, $\omega_{r,n}$, is formulated as

$$\omega_{r,n} = \frac{1}{\sqrt{L_r C_r}}\frac{n}{4l_r} = \frac{c}{\sqrt{\varepsilon_{\text{eff}}}}\frac{n}{4l_r}. \tag{2.14}$$

Analogously to Eq. (2.5), the Hamiltonian of the transmission line resonator reads as

$$H(t) \equiv \int_0^{l_r} \mathrm{d}z \frac{1}{2C_r}(q(z,t))^2 + \frac{1}{2L_r}(\partial_z \varphi(z,t))^2, \tag{2.15}$$

and its quantized version can be expressed as

$$\hat{\mathcal{H}}_{r,\infty} = \sum_n \hbar\omega_{r,n}\left[\hat{a}_n^\dagger \hat{a}_n + \frac{1}{2}\right].$$

In practice, we are primarily interested in the fundamental mode of the resonator due to the large frequency separation between modes. Thus, the Hamiltonian is simplified to

$$\hat{\mathcal{H}}_r = \hbar\omega_r \hat{a}_r^\dagger \hat{a}_r \tag{2.16}$$

with $\omega_r \equiv \omega_{r,1}$.

In summary, a transmission line resonator can be effectively described as a lumped-element LC circuit with a single resonant frequency of interest. The ability to engineer the resonator's boundary conditions and resonant frequencies offers great flexibility and control in cQED experiments and applications.

2.2 3D cavity

This section is mainly based on the books [85, 95] and partially on [96–98].

A useful realization of a quantum harmonic oscillator in the microwave regime is achieved through a three-dimensional (3D) cavity. The 3D cavity possesses a closed hollow geometry with metallic walls that represent high-reflectivity mirrors for microwave radiation and thereby impose specific boundary conditions on the confined electromagnetic field. Utilizing a 3D cavity offers distinct advantages for quantum systems compared to 1D resonators. A particular advantage of 3D cavities is their weak vacuum field, which leads to high internal quality factors (Q_i) due to weaker coupling of the electromagnetic modes to loss channels such as two-level systems. This characteristic distinguishes them from 1D resonators and enhances their coherence properties. Moreover, the multimode nature of 3D cavities, arising from their three-dimensional spatial structure, leads to a

[4] Again, $\varphi(0) = 0$ physically means the resonator end is open such that no current is flowing, while the other resonator end is shorted for $\varphi(l_r) = \varphi_0$ such that the current is flowing.

spectrum of eigenfrequencies that are not equidistant as in ideal 1D resonators and their separation can be engineered by choosing the specific dimensions of the cavity. That is, unlike 1D resonators where eigenfrequencies are separated by integer multiples of the fundamental mode frequency, the modes in a 3D cavity are located closer to each other. This characteristic allows for multiple modes to interact with a qubit with comparable strengths. The unique capabilities of 3D cavities enable a wide range of applications, including quantum memory, quantum state confinement, and the generation and manipulation of Schrödinger cat states. These functionalities have been explored in various experimental studies [39, 57, 71, 99–108]. Furthermore, the implementation of the Gottesman-Kitaev-Preskill (GKP) encoding, a key approach in fault-tolerant quantum computing, has achieved a breakthrough using a 3D architecture. This significant milestone marks the realization of the first logical qubit beyond the break-even point [109]. The 3D cavity's unique properties make it a promising platform for advancing quantum technologies and exploring new frontiers in quantum information processing.

When comparing 3D cavities with 1D resonators, a crucial figure of merit is the strength of the vacuum field. While 1D resonators usually exhibit smaller mode volumes accompanied by high vacuum field amplitudes, 3D microwave cavities have much larger mode volumes and correspondingly smaller vacuum fields. The average mode volume for a 1D microwave resonator is typically on the order of $V_{m,\mathrm{1D}}/\lambda^3 \approx 10^{-5} \ll 1$ [98, 110], while for a 3D microwave cavity, it is generally $V_{m,\mathrm{3D,mw}}/\lambda^3 \approx 1$ [110]. This is a very large mode volume, if we also compare with a typical 3D optical cavity with $V_{m,\mathrm{3D,opt}}/\lambda^3 \approx 10^{-12} \ll 1$ [111]. The vacuum field amplitudes for the electric and magnetic fields are given by

$$E_0 = \sqrt{\frac{\hbar\omega_r}{2\epsilon_0 V_m}}, \qquad\qquad B_0 = \sqrt{\frac{\mu_0\hbar\omega_r}{2V_m}},$$

respectively. Here, ω_r represents the resonant frequency of the resonator and the cavity. If we insert those values into above equations for $\omega_r/2\pi = 5\,\mathrm{GHz}$ (or equivalently $\lambda = 60\,\mathrm{mm}$), we obtain

	1D resonator	3D Cavity
E_0	4.3 mV/cm	$4.3\,\mu$V/cm
B_0	1.4 nT	1.4 pT

This distinction influences the coupling strength between the cavity and other systems, such as qubits or resonators. While 1D resonators allow for strong coupling and hence faster control and readout, their stronger coupling with the environment can limit coherence times. In contrast, qubits enclosed within a 3D cavity often demonstrate longer coherence times due to reduced coupling to external sources of losses.

To explore the multimode nature of a metallic rectangular cavity, we analyze the TE (transversal electric) mode, which has to satisfy the following wave equation

$$\left(\frac{\partial^2}{\partial x^2} + \frac{\partial^2}{\partial y^2} + \frac{\partial^2}{\partial z^2} + k_c^2\right) E(x,y,z) = 0,$$

where k_c is the so-called cutoff wave number. The differential equation presented above can be resolved using the technique of variable separation, represented as:

$$E(x,y,z) = E_x(x)E_y(y)E_z(z).$$

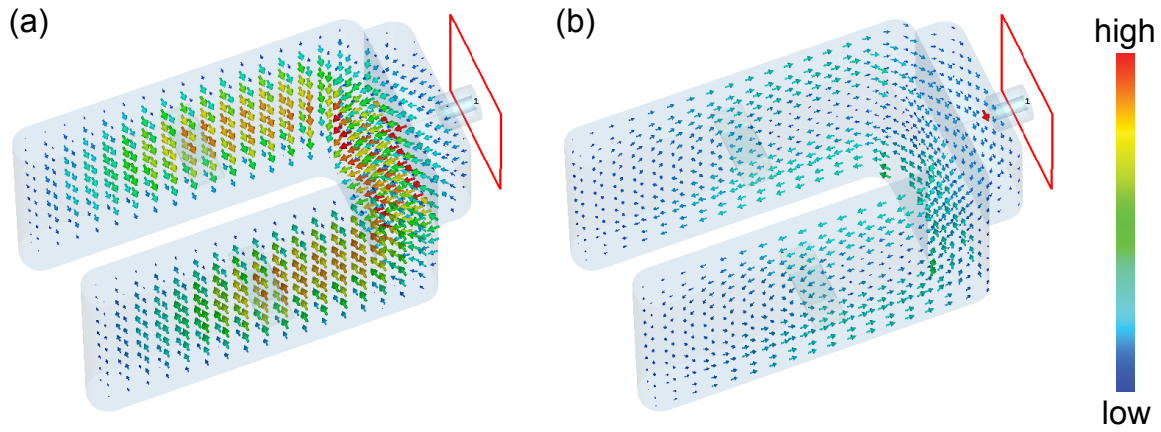

Figure 2.2. (a) Electric and (b) magnetic field distribution of the horseshoe geometry showing the first mode. The red rectangle indicates the input and output port. The color scale represents the field strength in arbitrary logarithmic units, and the arrows indicate the field orientation. On all sides, the boundary conditions for the electric fields are set to $E = 0$.

Furthermore, to consider the boundary conditions for the electric fields at the walls, specifically at $x = 0, a$, $y = 0, b$ and $z = 0, d$, it is essential to note that the walls are metallic and uncharged. Hence, according to Gauss's law, $\nabla \cdot E = \rho/\epsilon_0 = 0$, the field must be zero at every point on the surface. Consequently, the boundary conditions are defined as

$$E_x(0) = E_y(0) = E_z(0) = E_x(a) = E_y(b) = E_z(d) = 0.$$

Henceforth, we obtain

$$E(x, y, z) = E_x E_y E_z \sin\left(\frac{n\pi}{a}x\right) \sin\left(\frac{m\pi}{b}y\right) \sin\left(\frac{l\pi}{d}z\right).$$

We see that the cut-off wave number is given by

$$k_{c,x} = \frac{\pi}{a}, \qquad k_{c,y} = \frac{\pi}{b}, \qquad k_{c,z} = \frac{\pi}{d}$$

which are associated with the fundamental frequencies

$$f_{c,x} = \frac{c}{2a}, \qquad f_{c,y} = \frac{c}{2b}, \qquad f_{c,z} = \frac{c}{2d}.$$

In general, the possible mode frequencies are given by

$$f_{nml} = \frac{c}{2\pi}\sqrt{(nk_{c,x})^2 + (mk_{c,y})^2 + (lk_{c,z})^2}.$$

For more complex cavity structures, simulation software, such as CST Microwave Studio, is often utilized to characterize the modes [112] (see Fig. 2.2).

2.3 Transmon qubit

This section is mainly based on the paper [90] and partially based on the paper [87] and the Ph.D. thesis [113].

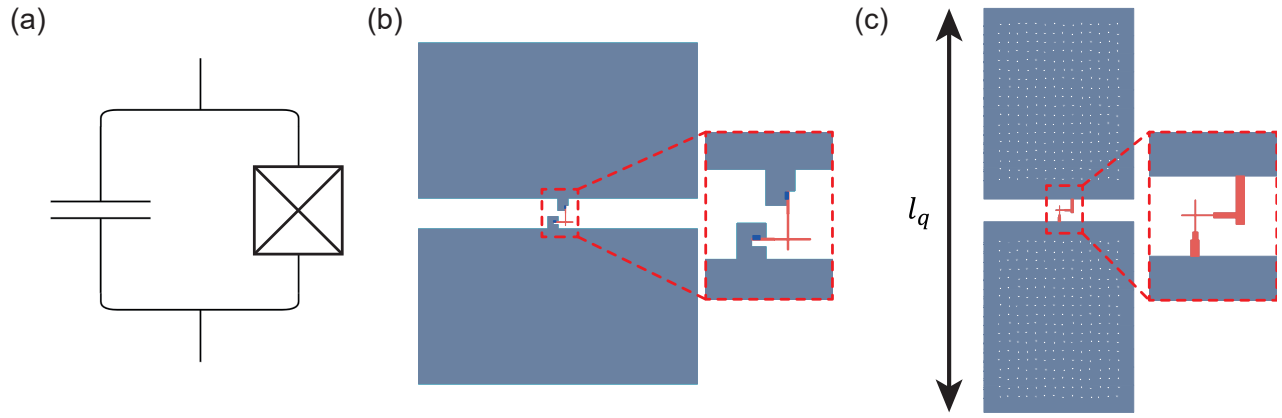

Figure 2.3. (a) Electrical circuit representation of the transmon. Josephson junction is shunted by a capacitor C_q. (b) Design of 2D floating transmon. The red lines represent the Manhattan-type Josephson junction and its lead. The width of Josephson junction is not to scale. (c) Design of 3D transmon. The vertically stretched pads with length l_q is later required for the electric dipole interaction with the electric field of the cavity (see Subsec. 2.5.1). In both cases, 2D and 3D, the large pads (colored in blue) realize the shunted capacitance C_q.

The transmission-line shunted plasma oscillation qubit - briefly called transmon qubit - is one of the most successful superconducting qubit types until today [23, 24, 87, 90, 99, 113]. The advantages of this device are the long coherence time due to the insensitivity against charge noise when compared to the charge qubit [90, 114, 115] and the smaller critical current density of the Josephson junction, which simplifies one step in the whole complex fabrication process since fluctuations in the oxidation process such as in the oxidation time are less critical. Both advantages are based on the required relation between the charge energy and the Josephson energy, namely $E_C \ll E_J$, which will be explained in the following.

The transmon qubit consists of a Josephson junction, which is shunted by a large capacitance C_q as shown in Fig. 2.3. The Hamiltonian of the transmon qubit is described by

$$\hat{\mathcal{H}} = 4E_C \left(\hat{n} - n_g\right)^2 - E_J \cos\hat{\varphi}, \tag{2.17}$$

where the Josephson energy and the charging energy are defined as

$$E_J = \frac{\Phi_0 I_c}{2\pi}, \qquad E_C = \frac{e^2}{2C_q}, \tag{2.18}$$

respectively. The effective offset charge reads

$$n_g = \frac{Q_r}{2e} + \frac{C_g V_g}{2e} \tag{2.19}$$

with the gate voltage V_g, gate capacitance C_g, and the environment-induced offset charge Q_r. Its eigenenergies can be precisely described in terms of Mathieu functions by

$$E_m(n_g) = E_C a_{2[n_g + k(m,n_g)]}\left(-E_J/2E_C\right) \tag{2.20}$$

in the phase basis, where $a_\nu(q)$ denotes the Mathieu characteristic value [90, 114]. If we now

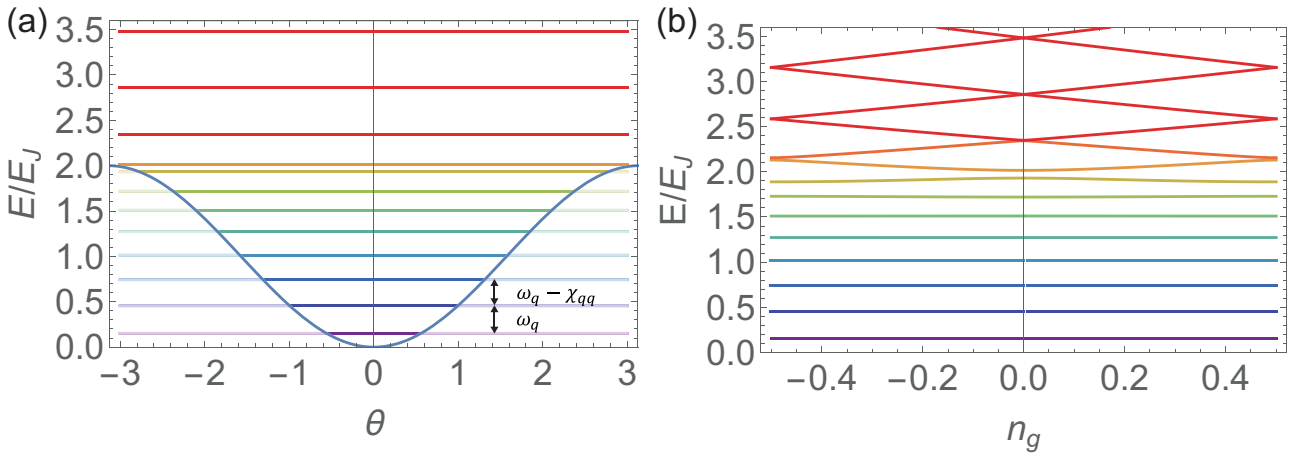

Figure 2.4. (a) Potential energy of a transmon in phase representation with $E_J/E_C \approx 80$. The transition frequency ω_{01} corresponds to the qubit frequency ω_q, while the transition frequency $\omega_{12} = \omega_q - \chi_{qq}$ is different from ω_q. That is, we can make the separation between the first two energy levels different. (b) Energy levels as a function of offset-charge n_g. We observe flat behavior over all n_g for low energy levels leading to insensitivity against charge noise.

approximate these eigenenergies in the limit, $E_C \ll E_J$, they can be formulated as

$$\epsilon_m \cong (-1)^m E_C \frac{2^{4m+5}}{m!}\sqrt{\frac{2}{\pi}}\left(\frac{E_J}{2E_C}\right)^{\frac{m}{2}+\frac{3}{4}} e^{-\sqrt{8E_J/E_C}}. \tag{2.21}$$

Henceforth, the transmon qubits have the properties that its charge dispersion decreases exponentially with E_J/E_C, while its loss in anharmonicity is described by a weak power law[5]. This charge insensitivity can be well observed in Fig. 2.4, where the lower eigenenergies are not dependent on n_g.

The eigenenergy description in Eqs. (2.20) or (2.21) is a precise formulation, but it can be approximated in a more tractable expression. In this regard, we expand the Hamiltonian in Eq. (2.17) up to the fourth order in $\hat{\varphi} = (2E_C/E_J)^{1/4}\left(\hat{a}_q + \hat{a}_q^\dagger\right)$. As derived in Appendix A, we then arrive at

$$\hat{\mathcal{H}}_t = \omega_q \hat{a}_q^\dagger \hat{a}_q + \frac{\chi_{qq}}{2}\hat{a}_q^\dagger \hat{a}_q^\dagger \hat{a}_q \hat{a}_q \tag{2.22}$$

with the qubit frequency $\omega_q = \sqrt{8E_C E_J} - E_C$ and anharmonicity $\chi_{qq} \approx -E_C$. Here, $\hat{a}_q^{(\dagger)}$ is the annihilation (creation) operator. The nonlinearity of the Josephson junction results in unequal energy spacings between quantum states. Specifically, the energy difference between the ground state and the first excited state is different from the energy differences between other states. Consequently, we can designate the ground state as the logical state $|0\rangle$ and the first excited state as the logical state $|1\rangle$. In this regime, where the relevant excitation and dissipation rates are much smaller than the anharmonicity χ_{qq}, we can replace the bosonic annihilation operator $\hat{a}_q$ with the Pauli annihilation operator $\hat{\sigma}$. This substitution leads to the well-known qubit Hamiltonian

$$\hat{\mathcal{H}}_q = \frac{\omega_q}{2}\hat{\sigma}_z. \tag{2.23}$$

The Hamiltonian in Eq. (2.22) is also known as quantum Duffing Hamiltonian and is an active research field with respect to the first order dissipative quantum phase transition, photon blockade and quantum

[5]The typical ratio used in the experiments is $E_J/E_C = 20 - 80$ with $E_C = 200 - 350\,\text{MHz}$ and $E_J = 6 - 20\,\text{GHz}$.

simulations [77, 81, 85, 86, 116–119].

2.4 Decoherence in superconducting circuits

Up to this point, we have focused on discussing closed quantum systems. However, in practical applications, quantum systems invariably interact with their surrounding environment, making them open quantum systems. This interaction with the environment introduces decoherence effects, which ultimately lead to the loss of quantum information encoded in the system. Decoherence manifests as energy relaxation and dephasing processes. Energy relaxation refers to the irreversible leakage of information from the quantum system to the bosonic heat bath of the environment, resulting in the loss of coherence and ultimately the destruction of quantum information. On the other hand, dephasing captures the loss of phase coherence between different quantum states, disrupting the ordered information contained within quantum superpositions. These decoherence processes are significant challenges in quantum technology, as they limit the coherence time and the preservation of fragile quantum states. Understanding and mitigating the effects of decoherence are essential for the development and practical implementation of quantum technologies.

2.4.1 Quantum description of dissipation

In this subsection, we mainly follow the paper [89, 120] and the book [85].

Quantum Langevin equation

Here, we first focus on the equation of motion in the presence of dissipation in the Heisenberg picture and we will see that the result in Sec. 2.1 will play a central role in our discussion. The mathematical description of "opening" the system to the environment means an interaction with the surrounding bath [85, 89], which leads to the following Hamiltonian

$$\hat{\mathcal{H}} = \hat{\mathcal{H}}_{\text{sys}} + \hat{\mathcal{H}}_{\text{bath}} + \hat{\mathcal{H}}_{\text{sb}}, \tag{2.24}$$

where $\hat{\mathcal{H}}_{\text{sys}}$ is the system Hamiltonian and $\hat{\mathcal{H}}_{\text{bath}}$ is the environment Hamiltonian approximated by the bath of harmonic oscillators introduced in Eq. (2.8). For simplicity, we assume a cavity resonator as our system (see Eq. (2.16)). The coupling Hamiltonian within the rotating wave approximation is

$$\hat{\mathcal{H}}_{\text{sb}} = -i\hbar \sum_k \left(f_k \hat{a}_r \hat{a}_k^\dagger - f_k^* \hat{a}_r^\dagger \hat{a}_k \right). \tag{2.25}$$

Here, f_k is the interaction strength of the system mode r with the bath mode k. The resulting Heisenberg equations of motion can be then calculated as

$$\dot{\hat{a}}_k = -i\omega_k \hat{a}_k + f_k^* \hat{a}_r \tag{2.26a}$$

$$\begin{aligned} \dot{\hat{a}}_r &= -i\omega_r \hat{a}_r - \sum_k f_k \hat{a}_k \\ &= -i\omega_r \hat{a}_r - \sum_k f_k e^{-i\omega_k (t-t_0)} \hat{a}_k(t_0) - \sum_k |f_k|^2 \int_{t_0}^{t} \mathrm{d}\tau e^{-i(\omega_k - \omega_r)(t-\tau)} e^{i\omega_r(\tau - t)} \hat{a}_r(\tau). \end{aligned} \tag{2.26b}$$

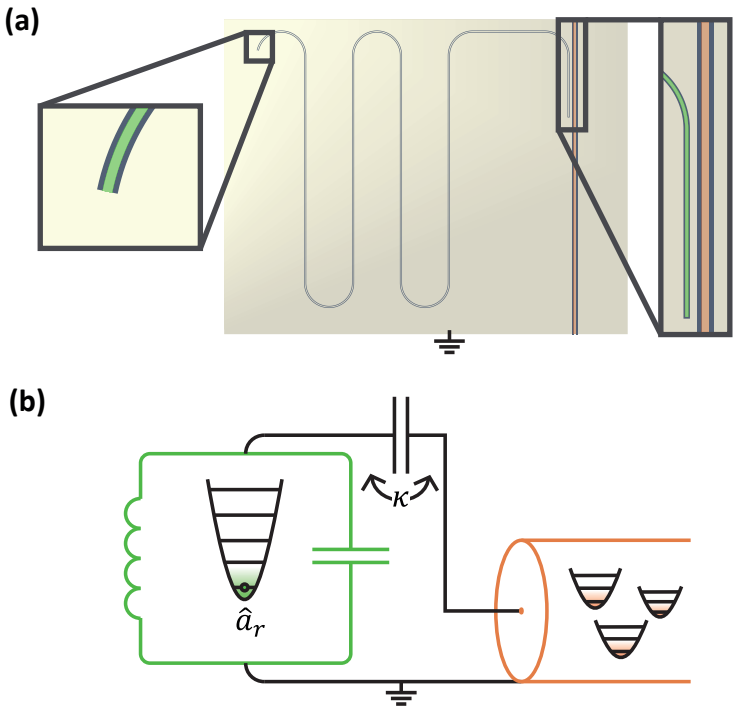

Figure 2.5. (a) Image of a $\lambda/4$ CPW resonator (green) coupled to a coplanar transmission line (orange). The left end is shorted, while the right end is open. (b) Equivalent lumped-element-representation of the CPW resonator, $\hat{a}_r$, (green) capacitively coupled to the transmission line (orange) with the decay rate κ. An infinite number of quantum harmonic oscillators can be used to model the bath represented by the transmission line.

We can further use the Fermi Golden Rule expression such that the decay rate from the $n = 1$ single photon excited state to the $n = 0$ ground state can be expressed as

$$\kappa \equiv 2\pi f^2 g(\omega_r) = 2\pi \sum_k |f_k|^2 \, \delta\left(\omega_r - \omega_k\right), \tag{2.27}$$

where the interaction strength f_k is assumed to be constant within the Markov approximation and the density of states is defined as $g(\omega_r) \equiv \sum_k \delta\left(\omega_r - \omega_k\right)$. Additionally, comparing the second term in Eq. (2.26b) with the result given in Eq. (2.11), we arrive at the quantum Langevin equation for the cavity mode as

$$\dot{\hat{a}}_r = -i\omega_r \hat{a}_r - \frac{\kappa}{2} - \sqrt{\kappa}\hat{a}_{\text{in}} \tag{2.28}$$

with the propagating input field $\hat{a}_{\text{in}}$. Thus, we derived the dynamics of the open cavity system for the energy relaxation process (see Fig. 2.5). For the calculation of the dephasing process, we replace $\hat{a}_r \to \hat{a}_r^\dagger \hat{a}_r$.

The time evolution we considered so far is dependent on the past influence of the input field $\hat{a}_{\text{in}}$, i.e. $t > t_0$. We can, however, also analyze the propagating output field $\hat{a}_{\text{out}}$ after the input mode has interacted with the system, so $t < t_1$. Modifying Eq. (2.26b) as

$$\dot{\hat{a}}_r = -i\omega_r \hat{a}_r - \sum_k f_k e^{-i\omega_k(t-t_1)} \hat{a}_k(t_1) + \sum_k |f_k|^2 \int_t^{t_1} \mathrm{d}\tau e^{-i(\omega_k-\omega_r)(t-\tau)} e^{i\omega_r(\tau-t)} \hat{a}_r(\tau)$$

and again comparing the second term with Eq. (2.12), we obtain for the cavity mode as

$$\dot{\hat{a}}_r = -i\omega_r \hat{a}_r + \frac{\kappa}{2} - \sqrt{\kappa}\hat{a}_{\text{out}}. \tag{2.29}$$

Subtracting Eq. (2.29) from Eq. (2.28) leads to the input-output formalism for the cavity

$$\hat{a}_{\text{out}} = \sqrt{\kappa}\hat{a}_r + \hat{a}_{\text{in}}. \tag{2.30}$$

Henceforth, the output field contains information of the system in form of $\hat{a}_r$, which we will usually measure in our experiment.

Quantum master equation

The counterpart of quantum Langevin equation for the Schrödinger picture is the quantum master equation, which describes the system dynamics using the density operator $\hat{\rho}$. This approach is especially useful for a statistical description of the dynamics of the localized systems since the effects of the propagating fields have been averaged over the trace operation [120]. That is, we compute

$$\hat{\rho}(t) = \text{Tr}_{\text{bath}}\left(\hat{\rho}_{\text{sb}}(t)\right),$$

where $\hat{\rho} \in \mathcal{H}_{\text{sys}}$ is the reduced density matrix of the system and $\hat{\rho}_{\text{sb}} \in \mathcal{H}_{\text{sys}} \otimes \mathcal{H}_{\text{bath}}$ is the density matrix in the entire system-bath Hilbert space. We again start with the Hamiltonian described by Eq. (2.24). The master equation of the system-bath density operator in the interaction picture is given by [121, 122]

$$\dot{\hat{\rho}}_{\text{sb,int}}(t) = \frac{1}{i\hbar}\left[\hat{\mathcal{H}}_{\text{sb}}(t), \hat{\rho}_{\text{sb,int}}(t)\right]$$

with

$$\hat{\mathcal{H}}_{\text{sb}}(t) = e^{i\left(\hat{\mathcal{H}}_{\text{sys}}+\hat{\mathcal{H}}_{\text{bath}}\right)t/\hbar}\hat{\mathcal{H}}_{\text{sb}}e^{-i\left(\hat{\mathcal{H}}_{\text{sys}}+\hat{\mathcal{H}}_{\text{bath}}\right)t/\hbar}.$$

We now assume that the system and the bath are initially independent[6] such that the density operator can be described by a product state $\hat{\rho}_{\text{sb}} = \hat{\rho} \otimes \hat{\rho}_{\text{bath}}$ and $\text{Tr}_{\text{bath}}\left(\hat{\mathcal{H}}_{\text{sb}}(t)\hat{\rho}_{\text{sb,int}}\right) = 0$. This leads to the equation of motion seen solely by the system as

$$\begin{aligned}\dot{\hat{\rho}}(t) &= -\frac{1}{\hbar^2}\int_0^t \mathrm{d}t' \text{Tr}_{\text{bath}}\left(\left[\hat{\mathcal{H}}_{\text{sb}}(t), \left[\hat{\mathcal{H}}_{\text{sb}}(t'), \hat{\rho}_{\text{sb,int}}(t')\right]\right]\right) \\ &\approx -\frac{1}{\hbar^2}\int_0^t \mathrm{d}t' \text{Tr}_{\text{bath}}\left(\left[\hat{\mathcal{H}}_{\text{sb}}(t), \left[\hat{\mathcal{H}}_{\text{sb}}(t'), \hat{\rho}(t) \otimes \hat{\rho}_{\text{bath}}\right]\right]\right),\end{aligned} \tag{2.31}$$

where we have further used the Born-Markov approximation. The Born approximation assumes a weak coupling and a large heat bath, which means that its interaction does not significantly change the reservoir

$$\hat{\rho}_{\text{sb,int}}(t) \approx \hat{\rho}(t) \otimes \hat{\rho}_{\text{bath}}$$

as well as the bath correlation function

$$\text{Tr}_{\text{bath}}\left(\left[\hat{\mathcal{H}}_{\text{sb}}(t), \left[\hat{\mathcal{H}}_{\text{sb}}(t'), \hat{\rho}_{\text{sb,int}}(t')\right]\right]\right) \approx \hat{\rho}(t')\text{Tr}_{\text{bath}}\left(\left[\hat{\mathcal{H}}_{\text{sb}}(t), \left[\hat{\mathcal{H}}_{\text{sb}}(t'), \hat{\rho}_{\text{bath}}\right]\right]\right).$$

[6] That is, the interaction is turned on at $t = 0$.

The Markov approximation states that the future evolution of $\hat{\rho}_{\mathrm{sb,int}}(t)$ is only dependent on the current quantum state $\hat{\rho}_{\mathrm{sb,int}}(t)$, but not on the past history of $\hat{\rho}_{\mathrm{sb,int}}(t')$. This is justified since the reservoir is a large system that remains in thermal equilibrium. That is, we anticipate that any small perturbations caused by its interaction with the system will not persist for an extended period. In other words, the reservoir's correlation time is typically much shorter than the time scale required for significant changes in the system. Thus, the system can be effectively treated as instantaneous and memoryless, allowing for a simplified analysis.

For simplicity, we again assume a cavity-type harmonic oscillator as our system (see Eq. (2.16)). Using Eq. (2.31) we obtain

$$\dot{\hat{\rho}}(t) = \alpha\left(\hat{a}_r\hat{\rho}(t)\hat{a}_r^\dagger - \hat{a}_r^\dagger\hat{a}_r\hat{\rho}(t)\right) + \beta\left(\hat{a}_r\hat{\rho}(t)\hat{a}_r^\dagger + \hat{a}_r^\dagger\hat{\rho}(t)\hat{a}_r - \hat{a}_r^\dagger\hat{a}_r\hat{\rho}(t) - \hat{\rho}(t)\hat{a}_r^\dagger\hat{a}_r\right) + \text{h.c.},$$

where

$$\alpha = \int_0^t \mathrm{d}t' \sum_k |f_k|^2\, e^{-i(\omega_k-\omega_r)(t-t')},$$
$$\beta = \int_0^t \mathrm{d}t' \sum_k \bar{n}_{\mathrm{th}}(\omega_k)\, |f_k|^2\, e^{-i(\omega_k-\omega_r)(t-t')},$$

where $\bar{n}_{\mathrm{th}}(\omega_k)$ is the mean thermal photon number at frequency ω_k. In the similar spirit derived for the quantum Langevin equation and after careful mathematical calculations [85, 120], we arrive at

$$\dot{\hat{\rho}}(t) = -i\omega_r\left[\hat{a}_r^\dagger\hat{a}_r, \hat{\rho}(t)\right] + (\bar{n}_{\mathrm{th}}+1)\,\mathcal{D}[\sqrt{\kappa}\hat{a}_r]\hat{\rho}(t) + \bar{n}_{\mathrm{th}}\mathcal{D}[\sqrt{\kappa}\hat{a}_r^\dagger]\hat{\rho}(t).$$

The second term represents the decay into lower energy states, while the last term corresponds to the excitation into higher states due to thermal excitation. In the cryogenic environment of around 10 mK, the thermal photon number at around 8 GHz is negligibly small, $\bar{n}_{\mathrm{th}} \approx 2\times10^{-17}$. The general formulation of the master equation is written as

$$\dot{\hat{\rho}}(t) = \mathcal{L}(t)\,[\hat{\rho}] = \frac{1}{i\hbar}\left[\hat{\mathcal{H}}, \hat{\rho}(t)\right] + (\bar{n}_{\mathrm{th}}+1)\,\mathcal{D}[\hat{L}]\hat{\rho}(t) + \bar{n}_{\mathrm{th}}\mathcal{D}[\hat{L}^\dagger]\hat{\rho}(t), \tag{2.32}$$

where we have defined the Lindbladian superoperator as $\mathcal{L}(t)\,[\hat{\rho}]$ and the superoperator $\mathcal{D}[\hat{\mathbf{L}}]\hat{\rho}$ as

$$\mathcal{D}[\hat{\mathbf{L}}]\hat{\rho} \equiv \hat{L}\hat{\rho}\hat{L}^\dagger - \frac{1}{2}\left(\hat{L}^\dagger\hat{L}\hat{\rho} + \hat{\rho}\hat{L}^\dagger\hat{L}\right). \tag{2.33}$$

2.4.2 SLH framework

This subsection is mainly based on the paper [120] and focus on specific topics, namely the generalization of input-output relation and quantum Langevin equation, and the SLH composition rules.

As quantum technologies evolve, the complexity extends beyond individual quantum systems to the intricate interconnections established through propagating electromagnetic fields. Such interconnected landscapes, known as quantum input-output networks (QION), can be adeptly modeled using the SLH framework. This framework emphasizes characteristics like modularity and hierarchy, enabling a deeper understanding of these networks. A salient feature of the SLH framework is its compatibility with control-theoretical analysis of quantum coherent systems. This compatibility seamlessly bridges

quantum dynamics with classical control theory principles. Feedback and feedforward, fundamental to control theory, are particularly well-represented in this model. A burgeoning domain, coined as coherent quantum feedback control theory, is under active exploration, manifesting its potential in numerous applications. Active devices boasting specialized functions are emerging [123, 124], alongside advancements in quantum state control [125–127] and innovations in quantum back-action evasion for gravitational wave detection [124, 128]. Notably, research has theoretically underscored the superiority of quantum coherent feedback over quantum measurement feedback in executing specific tasks for linear quantum systems [125, 129]. Additionally, the SLH framework plays a pivotal role in devising unidirectional devices tailored for quantum information routing. Such capabilities are crucial for tasks like heralded quantum state transfers across distant qubits and the orchestration of stabilizer codes, vital for quantum error correction [130]. In the field of quantum filtering, such as Josephson quantum filter, this framework can also offer strategies to circumvent the inherent trade-off between fast control/readout and coherence time of a qubit [131].

In the realm of quantum physics, the SLH formalism, encapsulated by the triple $(S, \hat{L}, \hat{\mathcal{H}})$, serves as a comprehensive framework for delineating the interaction dynamics of distinct quantum entities, including qubits and Josephson parametric amplifiers, with their associated input and output fields. This framework is characterized by three core elements: the scattering matrix S, the loss operator[7] $\hat{L}$, and the Hamiltonian $\hat{\mathcal{H}}$. What sets the SLH triple-based description apart is its versatility and computational efficiency. It paves the way for streamlined software integration, enabling a more automated approach to both the design and analysis of quantum network components, thus alleviating the analytical demands traditionally placed on researchers.

Generalization of input-output relation and quantum Langevin equation

Given the SLH triple $G = (S, \hat{\mathbf{L}}, \hat{\mathcal{H}})$, we arrive at the following input-output relations for the general multiple input/output case and the quantum Langevin equation for an arbitrary system operator $\hat{X}$ [8]

$$\hat{\mathbf{a}}_{\text{out}} = \hat{\mathbf{L}} + S\hat{\mathbf{a}}_{\text{in}} \tag{2.34}$$

$$\frac{\mathrm{d}}{\mathrm{d}t}\hat{X} = \frac{i}{\hbar}\left[\hat{\mathcal{H}}, \hat{X}\right] + \mathcal{D}^{\dagger}[\hat{\mathbf{L}}]\hat{X} + \hat{\mathbf{a}}_{\text{in}}^{\dagger} S^{\dagger}\left[\hat{X}, \hat{\mathbf{L}}\right] + \left[\hat{\mathbf{L}}^{\dagger}, \hat{X}\right] S\hat{\mathbf{a}}_{\text{in}}, \tag{2.35}$$

where we have defined

$$\hat{\mathbf{a}}_{\text{in/out}} \equiv \begin{bmatrix} \hat{a}_{\text{in/out},1} \\ \vdots \\ \hat{a}_{\text{in/out},N} \end{bmatrix}, \qquad \hat{\mathbf{L}} \equiv \begin{bmatrix} \hat{L}_1 \\ \vdots \\ \hat{L}_N \end{bmatrix}, \qquad \left[\hat{X}, \hat{\mathbf{L}}\right] \equiv \begin{bmatrix} \left[\hat{X}, \hat{L}_1\right] \\ \vdots \\ \left[\hat{X}, \hat{L}_N\right] \end{bmatrix},$$

[7] In our cavity example, we have $\hat{X} = \hat{a}_r$ and $\hat{L} = \sqrt{\kappa}\hat{a}_r$ for the energy relaxation process.

[8] Strictly speaking, the quantum Langevin equation is more appropriately expressed within the framework of quantum stochastic differential equations (QSDEs). This preference arises due to the mathematical singularity of the canonical commutation relation, $\left[\hat{a}_{\text{in}}(t), \hat{a}_{\text{in}}^{\dagger}(t')\right] = \delta(t - t')$. To address this issue, we introduce the time-integrated form, $\hat{A}_{\text{in}} = \int_0^t \mathrm{d}\tau \hat{a}_{\text{in}}(\tau)$. This redefined quantity offers a commutation relation given by $\left[\mathrm{d}\hat{A}_{\text{in}}(t), \mathrm{d}\hat{A}_{\text{in}}^{\dagger}(t')\right] = \mathrm{d}t$. However, for the sake of maintaining familiarity and brevity in this thesis, we steer clear of the full QSDE description. Expanding on the broader context, there exists a necessity to incorporate the gauge process, $\Lambda_{\text{in}} = \int_0^t \mathrm{d}\tau \hat{a}_{\text{in}}^{\dagger}(\tau)\hat{a}_{\text{in}}(\tau)$. Yet, as our focus predominantly rests on vacuum noise, this gauge process often vanishes.

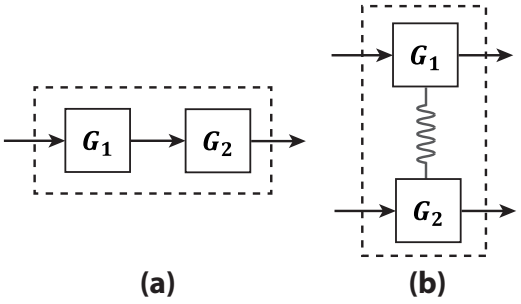

Figure 2.6. Schematic representation of (a) series product and (b) direct coupling, where the wiggle represent the interaction between G_1 and G_2.

$$\left[\hat{\mathbf{L}}^\dagger, \hat{X}\right] \equiv \left[\ \left[\hat{L}_1^\dagger, \hat{X}\right], \ \ldots, \ \left[\hat{L}_N^\dagger, \hat{X}\right]\ \right], \qquad \mathcal{D}^\dagger[\hat{\mathbf{L}}]\hat{X} \equiv \sum_{i=1}^{N} \hat{L}_i^\dagger \hat{X} \hat{L}_i - \frac{1}{2}\left(\hat{L}_i^\dagger \hat{L}_i \hat{X} + \hat{X}\hat{L}_i^\dagger \hat{L}_i\right).$$

SLH composition rules

The SLH composition rules are developed by Gough and James [132, 133] and are algebraic prescriptions for combining the SLH triples of individual components, whose traveling waves are connected in various ways. There are three physical assumptions for these rules: (i) the validity of Markov approximation, (ii) the fields are propagating in a dissipation-less and linear medium and the time for propagation between localized components are negligible, and (iii) the input fields into the network are in the vacuum state. The third assumption, however, can be easily extended for non-vacuum states of the propagating fields. In particular, for the coherent state we describe the triple as $G_{\text{coh}} = (1, \alpha, 0)$ with the classical field amplitude α.

Rule 1 (Series product) We cascade one output from one localized network, $G_1 = (S_1, \hat{L}_1, \hat{\mathcal{H}}_1)$, into the input of another, $G_2 = (S_2, \hat{L}_2, \hat{\mathcal{H}}_2)$, as illustrated in Fig. 2.6 (a). The series product of both networks is given by

$$\begin{aligned} G_T \equiv & G_2 \lhd G_1 = (S_T, \hat{\mathbf{L}}_T, \hat{\mathcal{H}}_T) \\ & = \left(S_2 S_1, \mathbf{L}_2 + S_2 \mathbf{L}_1, \hat{\mathcal{H}}_1 + \hat{\mathcal{H}}_2 + \frac{\hbar}{2i}\left(\mathbf{L}_2^\dagger S_2 \mathbf{L}_1 - \mathbf{L}_1^\dagger S_2^\dagger \mathbf{L}_2\right)\right). \end{aligned} \tag{2.36}$$

Note the directional property of this result which makes $G_2 \lhd G_1 \neq G_1 \lhd G_2$.

Rule 2 (Direct coupling) The direct coupling refers to the situation, when G_1 and G_2 are in parallel and have a direct Hamiltonian interaction between both systems, $\hat{\mathcal{H}}_{\text{int}}$, as shown in Fig. 2.6 (a). In that case, we read

$$\begin{aligned} G_T \equiv & G_1 \boxplus G_2 = (S_T, \hat{\mathbf{L}}_T, \hat{\mathcal{H}}_T) \\ & = \left(\begin{bmatrix} S_1 & 0 \\ 0 & S_2 \end{bmatrix}, \begin{bmatrix} \hat{L}_1 \\ \hat{L}_2 \end{bmatrix}, \hat{\mathcal{H}}_1 + \hat{\mathcal{H}}_2 + \hat{\mathcal{H}}_{\text{int}}\right). \end{aligned} \tag{2.37}$$

Rule 3 (Feedback reduction and network interconnection) The feedback reduction computes the effective SLH triple that results from interconnecting an output of G to an input of G. Suppose the original system G has N input and output ports. We want to connect the output

port x to the input port y. This internal link is eliminated by the feedback reduction rule, which results in a new reduced system $G_{\mathrm{red}} = (S_{\mathrm{red}}, \hat{\mathbf{L}}_{\mathrm{red}}, \hat{\mathcal{H}}_{\mathrm{red}})$ with

$$S_{\mathrm{red}} = S_{\bar{x}\bar{y}} + S_{\bar{x}y} \left(I - S_{xy}\right)^{-1} S_{x\bar{y}} \tag{2.38a}$$

$$\hat{\mathbf{L}}_{\mathrm{red}} = \hat{\mathcal{L}}_{\bar{x}} + S_{\bar{x}y} \left(I - S_{xy}\right)^{-1} \hat{\mathbf{L}}_x \tag{2.38b}$$

$$\hat{\mathcal{H}}_{\mathrm{red}} = \hat{\mathcal{H}} + \frac{\hbar}{2i} \left(\hat{\mathbf{L}}^\dagger S_{:,y} \left(I - S_{xy}\right)^{-1} \hat{\mathbf{L}}_x - \hat{\mathbf{L}}_x^\dagger \left(I - S_{xy}^\dagger\right)^{-1} S_{:,y}^\dagger \hat{\mathbf{L}} \right) \tag{2.38c}$$

and the identity I has the same dimension as the reduced Hilbert space. The subscripts on S and $\hat{\mathbf{L}}$ with overbars denote matrices with certain rows or columns removed. Explicitly,

$$S_{\bar{x}\bar{y}} \equiv \begin{bmatrix} S_{1:x-1;1:y-1} & S_{1:x-1;y+1:n} \\ S_{x+1:n;1:y-1} & S_{x+1:n;y+1:n} \end{bmatrix}, \qquad S_{\bar{x}y} \equiv \begin{bmatrix} S_{1:x-1;y} \\ S_{x+1:n;y} \end{bmatrix},$$

$$S_{x\bar{y}} \equiv \begin{bmatrix} S_{x;1:y-1} & S_{x;y+1:n} \end{bmatrix}, \qquad S_{:,y} \equiv S_{1:n;y}, \qquad \hat{\mathbf{L}}_{\bar{x}} \equiv \begin{bmatrix} \hat{\mathbf{L}}_{1:x-1} \\ \hat{\mathbf{L}}_{x+1:n} \end{bmatrix}.$$

As these rules, especially the feedback reduction rule, are written in an abstract form, we illustrate an explicit example to understand these prescriptions. This example will be also later used for understanding the influence of parasitic modes on the quality factors in Chap. 3. We consider two resonator systems, $G_1 = (S_1, \hat{\mathbf{L}}_1, \hat{\mathcal{H}}_1 + \hat{\mathcal{H}}_{\mathrm{int}})$ and $G_2 = (S_2, \hat{\mathbf{L}}_2, \hat{\mathcal{H}}_2)$ with

$$S_k = \begin{bmatrix} 1 & 0 \\ 0 & 1 \end{bmatrix}, \tag{2.39}$$

$$\hat{\mathbf{L}}_k = \begin{bmatrix} \sqrt{\kappa_{k1}}\hat{a}_k \\ \sqrt{\kappa_{k2}}\hat{a}_k \end{bmatrix}, \tag{2.40}$$

$$\hat{\mathcal{H}}_k/\hbar = \Delta_k \hat{a}_k^\dagger \hat{a}_k, \tag{2.41}$$

$$\hat{\mathcal{H}}_{\mathrm{int}}/\hbar = g_{12} \left(\hat{a}_1^\dagger \hat{a}_2 + \hat{a}_2^\dagger \hat{a}_1 \right). \tag{2.42}$$

Here, the resonators are described by the annihilation operator $\hat{a}_k$ and the detuning Δ_k, which are directly interacting with $\hat{\mathcal{H}}_{\mathrm{int}}$. Additionally, both systems have two input and two output ports, which are coupled with strength κ_{k1} and κ_{k2}. For example, a typical hanger-type resonator in the superconducting circuits, as depicted in Fig. 2.5 (a), has two input and two output ports with the external coupling strengths of $\kappa_{k1} = \kappa_{k2} = \kappa_k/2$. We, furthermore, assume that the propagating wave accumulates some phase ϕ until it reaches the other local network. This is described by the SLH triples $G_3 = G_4 = (e^{i\phi}, 0, 0)$. The whole picture of the network interconnection is shown in Fig. 2.7 (a).

Now, let us apply the SLH composition rules. As we have two systems in parallel directly interacting

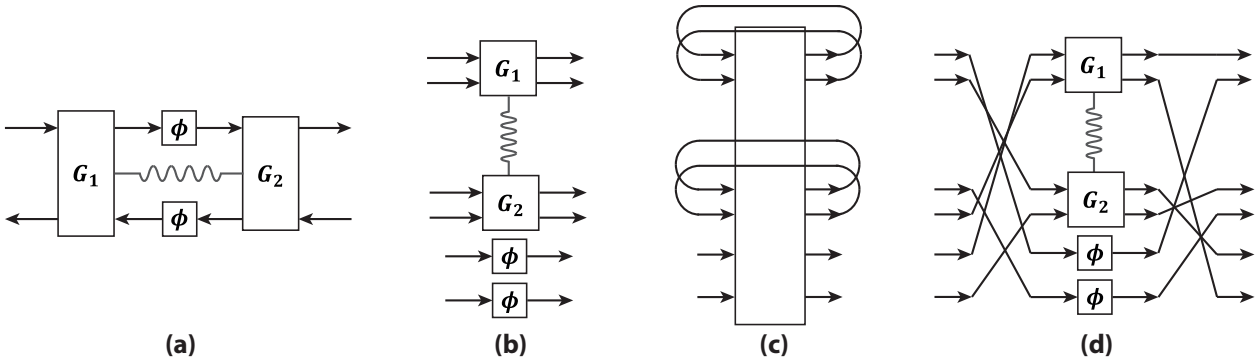

Figure 2.7. Schematic representation of network interconnection via the feedback reduction rule: (a) An illustration of the network under consideration. Note the flexibility in interpreting which ports are designated as 'input' and 'output' in this depiction. (b) The same components, which are concatenated and coupled. All inputs are situated on the left and all outputs on the right. (c) Transformation of the network to ensure eliminated nodes are block-contiguous for the application of Eq. (2.38). For ease of representation, all nodes targeted for elimination are placed at the top of the circuit. (d) The necessary rearrangements of the input and output ports from configuration (c) to set the stage for proper feedback connections. In particular, we require permutations of the input and output ports such that the ports $i \in 1, 2, 3, 4$ are feedback connected. Finally, we obtain (a).

with each other, we apply the "direct coupling" rule resulting to

$$
\begin{aligned}
G_T =& G_1 \boxplus G_2 \boxplus G_3 \boxplus G_4 \qquad (2.43)\\
=& \left(\begin{bmatrix} S_1 & & & \\ & S_2 & & \\ & & e^{i\phi} & \\ & & & e^{i\phi} \end{bmatrix}, \begin{bmatrix} \hat{\mathbf{L}}_1 \\ \hat{\mathbf{L}}_2 \\ 0 \\ 0 \end{bmatrix}, \hat{\mathcal{H}}_1 + \hat{\mathcal{H}}_2 + \hat{\mathcal{H}}_{\text{int}} \right)\\
=& \left(\begin{bmatrix} 1 & & & & & \\ & 1 & & & & \\ & & 1 & & & \\ & & & 1 & & \\ & & & & e^{i\phi} & \\ & & & & & e^{i\phi} \end{bmatrix}, \begin{bmatrix} \sqrt{\kappa_{11}}\hat{a}_1 \\ \sqrt{\kappa_{12}}\hat{a}_1 \\ \sqrt{\kappa_{21}}\hat{a}_2 \\ \sqrt{\kappa_{22}}\hat{a}_2 \\ 0 \\ 0 \end{bmatrix}, \hat{\mathcal{H}}_1 + \hat{\mathcal{H}}_2 + \hat{\mathcal{H}}_{\text{int}} \right). \qquad (2.44)
\end{aligned}
$$

Our next task is to interconnect the composed system to achieve the same result in Fig. 2.7 (a). That is, we want to connect the input and output ports in the following way:

out	in
1	5
4	6
5	3
6	2

We then perform a permutation of input and output ports such that we can use the configuration depicted in Fig. 2.7 (c) and the application of Eq. (2.38) becomes simple. In particular, we use the

scattering matrix for the permutation

$$S_{\text{in}} = \begin{bmatrix} 0 & 0 & 0 & 0 & 1 & 0 \\ 0 & 0 & 0 & 1 & 0 & 0 \\ 0 & 1 & 0 & 0 & 0 & 0 \\ 0 & 0 & 0 & 0 & 0 & 1 \\ 1 & 0 & 0 & 0 & 0 & 0 \\ 0 & 0 & 1 & 0 & 0 & 0 \end{bmatrix} \qquad \text{and} \qquad S_{\text{out}} = \begin{bmatrix} 1 & 0 & 0 & 0 & 0 & 0 \\ 0 & 0 & 0 & 0 & 1 & 0 \\ 0 & 0 & 0 & 1 & 0 & 0 \\ 0 & 0 & 0 & 0 & 0 & 1 \\ 0 & 0 & 1 & 0 & 0 & 0 \\ 0 & 1 & 0 & 0 & 0 & 0 \end{bmatrix},$$

such that we apply the "series product" rule for the rewired system

$$G'_T = (S_{\text{out}}, 0, 0) \lhd G_T \lhd (S_{\text{in}}, 0, 0).$$

This leads to

$$S'_T = \left[\begin{array}{cccc|cc} 0 & 0 & 0 & 0 & 1 & 0 \\ e^{i\phi} & 0 & 0 & 0 & 0 & 0 \\ 0 & 0 & 0 & 0 & 0 & 1 \\ 0 & 0 & e^{i\phi} & 0 & 0 & 0 \\ \hline 0 & 1 & 0 & 0 & 0 & 0 \\ 0 & 0 & 0 & 1 & 0 & 0 \end{array}\right], \qquad \hat{\mathbf{L}}'_T = S_{\text{out}}\hat{\mathbf{L}}_T = \left[\begin{array}{c} \sqrt{\kappa_{11}}\hat{a}_1 \\ 0 \\ \sqrt{\kappa_{22}}\hat{a}_2 \\ 0 \\ \hline \sqrt{\kappa_{21}}\hat{a}_2 \\ \sqrt{\kappa_{12}}\hat{a}_1 \end{array}\right], \qquad \hat{\mathcal{H}}'_T = \hat{\mathcal{H}}_1 + \hat{\mathcal{H}}_2 + \hat{\mathcal{H}}_{\text{int}}.$$

Finally, the "feedback reduction" rule can be utilized to eliminate the interconnections. The reduced form of the scattering matrix and loss operators is read as

$$S_{xy} = \begin{bmatrix} 0 & 0 & 0 & 0 \\ e^{i\phi} & 0 & 0 & 0 \\ 0 & 0 & 0 & 0 \\ 0 & 0 & e^{i\phi} & 0 \end{bmatrix}, \quad S_{\bar{x}\bar{y}} = \begin{bmatrix} 0 & 0 \\ 0 & 0 \end{bmatrix}, \qquad S_{\bar{x}y} = \begin{bmatrix} 0 & 1 & 0 & 0 \\ 0 & 0 & 0 & 1 \end{bmatrix}, \quad S_{x\bar{y}} = \begin{bmatrix} 1 & 0 \\ 0 & 0 \\ 0 & 1 \\ 0 & 0 \end{bmatrix}$$

$$S_{:y} = \left[\begin{array}{cccc} 0 & 0 & 0 & 0 \\ e^{i\phi} & 0 & 0 & 0 \\ 0 & 0 & 0 & 0 \\ 0 & 0 & e^{i\phi} & 0 \\ \hline 0 & 1 & 0 & 0 \\ 0 & 0 & 0 & 1 \end{array}\right], \qquad \hat{\mathbf{L}}_x = \begin{bmatrix} \sqrt{\kappa_{11}}\hat{a}_1 \\ 0 \\ \sqrt{\kappa_{22}}\hat{a}_2 \\ 0 \end{bmatrix}, \qquad \hat{\mathbf{L}}_{\bar{x}} = \begin{bmatrix} \sqrt{\kappa_{21}}\hat{a}_2 \\ \sqrt{\kappa_{12}}\hat{a}_1 \end{bmatrix}.$$

Substituting these expressions in Eq. (2.38), we find

$$S_{\text{red}} = e^{i\phi} \begin{bmatrix} 1 & 0 \\ 0 & 1 \end{bmatrix} \tag{2.45a}$$

$$\hat{\mathbf{L}}_{\text{red}} = \begin{bmatrix} \sqrt{\kappa_{21}}\hat{a}_2 + e^{i\phi}\hat{a}_1 \\ \sqrt{\kappa_{12}}\hat{a}_1 + e^{i\phi}\hat{a}_2 \end{bmatrix} \tag{2.45b}$$

$$\begin{aligned} \hat{\mathcal{H}}_{\text{red}} =& \hat{\mathcal{H}}_1 + \hat{\mathcal{H}}_2 + \hat{\mathcal{H}}_{\text{int}} \\ &+ \frac{\hbar\sqrt{\kappa_{11}\kappa_{21}}}{2i}\left(e^{i\phi}\hat{a}_1\hat{a}_2^\dagger - e^{-i\phi}\hat{a}_1^\dagger\hat{a}_2\right) + \frac{\hbar\sqrt{\kappa_{12}\kappa_{22}}}{2i}\left(e^{i\phi}\hat{a}_1^\dagger\hat{a}_2 - e^{-i\phi}\hat{a}_1\hat{a}_2^\dagger\right). \end{aligned} \tag{2.45c}$$

A more detailed analysis and interpretation of this resulting system can be later found in Chap. 3.

2.4.3 Quality factors

This subsection is mainly based on the paper [134–136] and the book [1, 85].

In many applications, the coherence time of quantum devices is limited by internal loss channels, which can be effectively evaluated using resonators as a chip quality test bed [137, 138]. There are two primary reasons for selecting resonators for this purpose. Firstly, superconducting resonators can be easily fabricated without requiring sub-micrometer size fabrication procedures required for e.g. Josephson junctions. This simplifies the manufacturing process and allows for efficient production. Secondly, when characterizing losses, it is sufficient to use continuous wave microwave spectroscopy techniques using a vector network analyzer (VNA), instead of employing more complex pulsed measurements. This approach enables faster analysis of resonator losses.

The key figure of merit describing the performance of resonator is their quality factor Q. It quantifies the ratio of energy stored in the resonator E_{tot} to the energy dissipated per cycle $E_{\text{diss}} = P_{\text{loss}}/\omega_r$. Mathematically, it can be expressed as the ratio of the resonator's angular frequency ω_r to the total dissipation rate κ_r, which comprises both external loss $\kappa_{r,c}$ and internal loss $\kappa_{r,i}$, giving rise to the following relation

$$Q = \frac{\text{total energy stored}}{\text{energy dissipated per cycle}} = \frac{E_{\text{tot}}}{P_{\text{loss}}/\omega_r} = \frac{\omega_r}{\kappa_r} = \frac{\omega_r}{\kappa_{r,c} + \kappa_{r,i}}. \tag{2.46}$$

The external loss represents the intentionally engineered loss channel due to the finite coupling to the external circuit which is a transmission line in our case. This loss can be accessed and measured in the single-tone spectroscopy, for example, using a VNA. The method of this extraction will be later discussed in the quality factor measurement. On the other hand, the internal loss corresponds to the undesired dissipation due to internal loss channels which may originate from a variety of different mechanisms. To characterize the overall performance, the loaded quality factor Q_l accounts for both external and internal quality factors inversely summed

$$\frac{1}{Q_l} = \frac{1}{Q_c} + \frac{1}{Q_i}, \tag{2.47}$$

where $Q_c = \omega_r/\kappa_{r,c}$ is the external quality factor and $Q_i = \omega_r/\kappa_{r,i}$ is the internal quality factor.

Input-output approach for internal and external losses

In this section, we will derive the output field in terms of internal and external losses, which is directly related to the scattering coefficients. Our focus will be on the reflection measurement, while references [135, 136] provide further information on transmission measurements and different resonator types such as hanger-, necklace-, and bridge-type resonators. To facilitate our analysis, we modify the key equations, Eq. (2.35) and Eq. (2.34), as follows: Considering that the cavity experiences both extrinsic and intrinsic loss channels, we express the loss operators and the propagating input/output fields as

$$\hat{L}_r = \begin{bmatrix} \sqrt{\kappa_{r,c}}\hat{a}_r \\ \sqrt{\kappa_{r,i}}\hat{a}_r \end{bmatrix}, \qquad \hat{a}_{\text{in/out}} = \begin{bmatrix} \hat{a}_{\text{in/out},c} \\ \hat{a}_{\text{in/out},i} \end{bmatrix}. \tag{2.48}$$

Substituting these expressions into the Eq. (2.35) and Eq. (2.34), we obtain

$$\dot{\hat{a}}_r = -i\Delta_{rd}\hat{a}_r - \frac{\kappa_r}{2} - \sqrt{\kappa_{r,c}}\hat{a}_{\mathrm{in},c} - \sqrt{\kappa_{r,i}}\hat{a}_{\mathrm{in},i}, \tag{2.49a}$$

$$\begin{bmatrix} \hat{a}_{\mathrm{out},c} \\ \hat{a}_{\mathrm{out},i} \end{bmatrix} = \begin{bmatrix} \sqrt{\kappa_{r,c}}\hat{a}_r \\ \sqrt{\kappa_{r,i}}\hat{a}_r \end{bmatrix} + \begin{bmatrix} \hat{a}_{\mathrm{in},c} \\ \hat{a}_{\mathrm{in},i} \end{bmatrix}, \tag{2.49b}$$

where we have transformed into the frame rotating with frequency ω_d and defined the detunig as $\Delta_{rd} = \omega_r - \omega_d$. Notably, $\hat{a}_{\mathrm{out},c}$ represents the output field propagating through the transmission line, emerging from the *same port* where the input field $\hat{a}_{\mathrm{in},c}$ is incident. In the steady state, the input-output relation can be rewritten as

$$\hat{a}_{\mathrm{out},c} = \left(1 - \frac{\kappa_{r,c}}{i\Delta_{rd} + \kappa_r/2}\right)\hat{a}_{\mathrm{in},c} - \frac{\sqrt{\kappa_{r,i}\kappa_{r,c}}}{i\Delta_{rd} + \kappa_r/2}\hat{a}_{\mathrm{in},i}. \tag{2.50}$$

If we now assume that the input field responsible for the intrinsic decay is a vacuum field, $\langle \hat{a}_{\mathrm{in},i} \rangle = 0$, we then find for the reflection scattering coefficient

$$S_{11} = \frac{\langle \hat{a}_{\mathrm{out},c} \rangle}{\langle \hat{a}_{\mathrm{in},c} \rangle} = 1 - \frac{\kappa_{r,c}}{i\Delta_{rd} + \kappa_r/2} = 1 - \frac{Q_l/Q_c}{1/2 + iQ_l\left(\omega_d/\omega_r - 1\right))}. \tag{2.51}$$

This result reveals two important features. Firstly, for $\kappa_{r,i} > 0$ and $\Delta_{rd} = 0$, we observe $|S_{11}| < 1$, indicating that a portion of the incoming field's energy is lost to the intrinsic loss channels. Secondly, when $\kappa_{r,i} = 0$ and $\Delta_{rd} = 0$, we have $S_{11} = -1$, implying a complete π-phase shift upon reflection. This result serves as the foundation for practical quality factor extraction.

We note that for the transmission measurement of the notch-type resonator, we read

$$S_{21} = \frac{\langle \hat{a}_{\mathrm{out},c2} \rangle}{\langle \hat{a}_{\mathrm{in},c1} \rangle} = \frac{-\kappa_{r,c}/2}{i\Delta_{rd} + \kappa_r/2} = -\frac{Q_l/Q_c}{1 + 2iQ_l\left(\omega_d/\omega_r - 1\right))}, \tag{2.52}$$

where $\hat{a}_{\mathrm{in},c1}$ is the incoming field from the left, and $\hat{a}_{\mathrm{out},c2}$ the outgoing field to the right, w.o.l.g..

Quality factor measurement

In practice, we need to consider environmental distortions, which include cable delay, cable losses, and impedance mismatches [134–136]. These imperfections are taken into account by an amplitude factor a, phase shift α, cable delay τ_d, and small circuit asymmetry ϕ

$$S_{11} = ae^{i\alpha}e^{-i\omega_d\tau}\left(1 - \frac{Q_l/\left|Q_c\right|e^{i\phi}}{1/2 + iQ_l\left(\omega_d/\omega_r - 1\right))}\right). \tag{2.53}$$

To extract the ideal resonator function (Eq. (2.51)), the circle fit method is employed, which allows us to fit the data points in the phase space [139]. The circle fit is particularly suitable because the ideal resonator function traces out a circle in phase space. In the following, we briefly outline the circle fitting procedure [134, 135], which is visualized in Fig. 2.8.

1. **Correction of frequency-dependent phase shift**
   The first linear fit of the frequency-dependent phase, which changes linearly with $\omega_d\tau$, roughly extracts the cable delay τ. This quantity will be needed as initial parameter guess for the fine phase shift correction. Furthermore, a Lorentzian fit is applied to the frequency-dependent amplitude to obtain the resonance frequency ω_r and to select a reasonable amount of data for

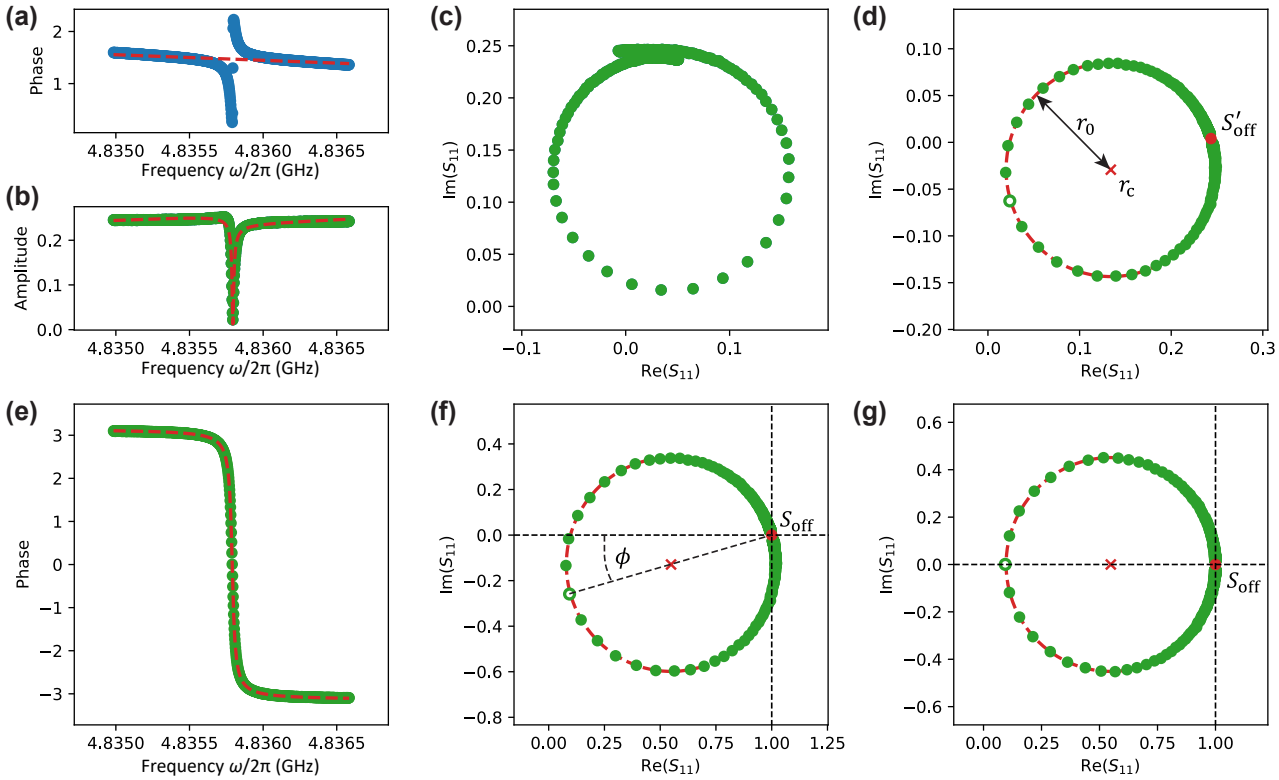

Figure 2.8. Example of circle fitting procedure with acquired data from sample `PRes-061` (blue/green dots). (a) Rough frequency-dependent phase correction by linear fit (red dashed line). (b) Lorentzian fit of the amplitude (red dashed line). (c) Unwrapped data $S_{11,1}$ in the phase space. Due to the residual frequency-dependent phase shift, the data is deformed. (d) Data points $S_{11,2}$ after the removal of the remaining frequency-dependent phase shift. S'_{off} is the off-resonant point altered by the prefactors a and α. (e) Determination of resonance frequency by fitting the frequency-dependent phase shift $\theta(\omega_d)$. (f) Corrected data $S_{11,4}$ after the elimination of the attenuation a and α. The off-resonant point is finally located at $S_{\text{off}} = 1$. Furthermore, phase correction ϕ is determined. (g) Asymmetry corrected data $S_{11,4}$ such that the resonance point is located on the real axis. The circle radius is rescaled by $\cos(\phi)$ to account for a difference $|Q_c|$ and $\text{Re}(Q_c)$.

the following fitting procedure. Now, our aim is to correct the measured data close to a perfect circle as the cable delay introduces a frequency dependent rotation of the phase centered at the origin and, therefore, twists the circle to a loop like curve. Mathematically speaking, we first transform into the rotating frame of ω_r by calculating

$$S_{11,1} = S_{11} e^{i\omega_r \tau},$$

which already looks like a circle as demonstrated in Fig. 2.8 (c). Afterwards, the residual phase shift is corrected by using the circle-fitting technique.

2. **Fine correction of phase shift α and scaling factor a**
   The only imperfection resides in the phase shift α assuming a is independent of the frequency in the close region of the resonance. To determine a and α, we make use of the powerful property of the off-resonant point $S_{\text{off}} = 1$ because it is independent of the resonance frequency, the quality factor and impedance mismatch. Hence, our goal is to determine the position of S'_{off}, which is only altered by the prefactors a and α, and then to place and normalize S'_{off} to $S_{\text{off}} = 1$ in the complex plane. Since it resides in the opposite direction of the circle, we first determine the

precise resonance frequency. Now, the circle fit comes into play, which determines the center of the circle and translates to the origin. Afterwards, we perform a frequency-dependent phase shift fit

$$\theta(\omega_d) = \theta_0 + 2\arctan\left(2Q_l\left(1 - \frac{\omega_d}{\omega_r}\right)\right), \tag{2.54}$$

where θ_0, Q_l and ω_r are the fitting parameters. Finally, the off-resonant point S'_{off} is found via the geometric relations

$$S_{11,2} = x_c + r_0\cos(\theta_0 + \pi) + i\,(y_c + r_0\sin(\theta_0 + \pi))$$

with r_0 being the radius of the circle and $r_c = (x_c, y_c)$ being the circle center. The absolute value of $S_{11,2}$ gives the amplitude scaling factor a and $\arg(S_{11,2})$ the phase offset α. After correcting

$$S_{11,3} = S_{11,2}/S'_{\text{off}}$$

the off-resonant point at $S_{\text{off}} = 1$ is obtained.

3. **Circuit asymmetry correction**
   To correct for circuit asymmetry, we make use of the property that the center of the circle should lie on the real axis in the absence of asymmetry. Therefore, we apply a transformation given by

$$S_{11,4} = \cos(\phi)(S_{11,3} - 1) + 1,$$

where ϕ represents the phase correction. It is important to note that we also rescale the radius of the circle by a factor of $|\cos(\phi)|$ to account for the difference between $|Q_c|$ and $\mathrm{Re}(Q_c)$ [140]. This transformation allows us to effectively correct for any circuit asymmetry and obtain a more accurate representation of the resonator function.

2.4.4 Loss mechanisms

In this subsection, our exposition closely aligns with the discourse presented in the paper [141], supplemented by the insights obtained in [137, 138] for TLSs and [142, 143] for the parasitic modes.

In the field of quantum physics, there are various sources of microwave loss channels that can impact the performance of quantum devices [141]: two-level systems (TLS), quasiparticles, radiative losses, eddy current losses, and parasitic modes. In the single-photon regime, which is commonly encountered in quantum devices, the primary contribution to loss usually arises from TLS. TLS are associated with impurities [144–147], trapped electrons [148, 149], or adsorbates [150] present at the interfaces between different materials such as metal/substrate, metal/air, and substrate/air [137, 138, 151]. Additionally, the generation of quasiparticles in the superconducting material due to stray infrared light or thermal activation can also introduce loss in these resonators. These contributions should not be overlooked, as they can significantly impact the performance of quantum devices. In fact, the presence of these loss mechanisms can lead to an effective qubit temperature that is defined by $T_{\text{eff}} = \hbar\omega_q/k_{\text{B}}\ln(1/\langle n_q\rangle - 1)$ and exceeds the actual temperature of the cryogenic environment, reaching values of up to 150 mK even when the dilution refrigerator temperature is around $10 - 50$ mK [103, 152, 153]. Furthermore, the chip environment plays a crucial role in device performance, particularly with regards to eddy current loss, slotline, chip and box modes [142, 143, 154–156]. Implementing countermeasures to improve coherence times requires careful engineering of the sample box design, including a high density of short grounding

wirebonds, the absence of a normal conducting ground plane under the chip, and a shift of chip and box modes to higher frequencies. These measures help mitigate the detrimental effects of the chip environment, contributing to enhanced coherence times and improved device performance.

TLS losses

TLS are recognized as significant sources of loss in superconducting quantum devices, and they usually can not avoided completely in various dielectric materials [137, 138, 156]. Especially, the TLS are contributing most at positions where the electromagnetic field has a high amplitude. These TLS exhibit two forms of interaction with quantum devices: coherent coupling leading to decoherence [138, 151, 157], and low-frequency environmental noise causing dephasing [150, 158, 159]. As illustrated in Fig. 2.9, the impact of TLS is particularly pronounced at interfaces involving metal/substrate, metal/air, and substrate/air, where the absence of crystalline order characterizes the amorphous state. Disordered oxide layers commonly associated with these interfaces contain a significant density of TLS resulting in an undesired loss channel. For instance, when silicon (Si) is utilized as the substrate, oxidation occurs, resulting in the formation of SiO_2. In the case of Nb/Si or Al/Si layers, silicon oxides can be a prominent source of decoherence at the metal/substrate interface. Similarly, niobium (Nb) as a superconducting material can form surface oxides such as NbO_2 and Nb_2O_5 [160], while aluminum (Al) is subject to oxidation, leading to the formation of Al_2O_x. In crystalline $\alpha-Al_2O_3$, each aluminum atom is bonded to six oxygen atoms. However, in its glassy form, approximately 55% of aluminum atoms are fourfold-coordinated (bonded to four oxygen atoms), and 42% are fivefold-coordinated [161]. Although the precise microscopic origin of these two-level systems remains not fully understood [137], a phenomenological model known as the power and temperature-dependent model provides a suitable description of their behavior in amorphous glasses [162]. This model predicts the TLS loss δ_{TLS} as [162]

$$\delta_{\mathrm{TLS}} = \delta^0_{\mathrm{TLS}} \frac{\tanh\left(\hbar\omega/2k_BT\right)}{\sqrt{1+\left(n_r/n_c\right)^{\beta}}}, \tag{2.55}$$

where δ^0_{TLS} represents the internal unsaturated TLS loss, $n_r = Q_l^2/n\pi Q_c$ denotes the photon number circulating inside the resonator for the nth mode, n_r is the photon number resonantly applied to the input of the resonator, and β is a geometry-dependent design parameter [137, 141, 162–166]. The critical photon number n_c encompasses the average relaxation and dephasing rate of the TLS ensemble [156, 162],

$$n_c = \frac{3\hbar\epsilon}{2\mu^2_{\mathrm{TLS}}\tau_1(T=0)\tau_{\mathrm{ac}}} T^{\alpha} \coth\left(\xi\right), \tag{2.56}$$

with $\xi = \hbar\omega_r/2k_{\mathrm{B}}T$, the effective dipole moment of the TLSs μ_{TLS}, the relaxation time of the TLSs τ_1 and the TLS coupling rate to acoustic phonons τ_{ac}^{-1}.

Quasiparticle losses

Quasiparticles in superconducting materials are generated by breaking up the Cooper pairs. The pair-breaking can occur in various ways: thermal excitation and electromagnetic radiation at frequencies above the gap frequency [141]. The thermally generated quasiparticle density is usually about exponentially dependent on the ratio of the thermal energy and the superconducting energy gap Δ_{sc} at temperatures far below the critical temperature. Henceforth, using superconducting material with larger Δ_{sc} such as Nb is always beneficial.

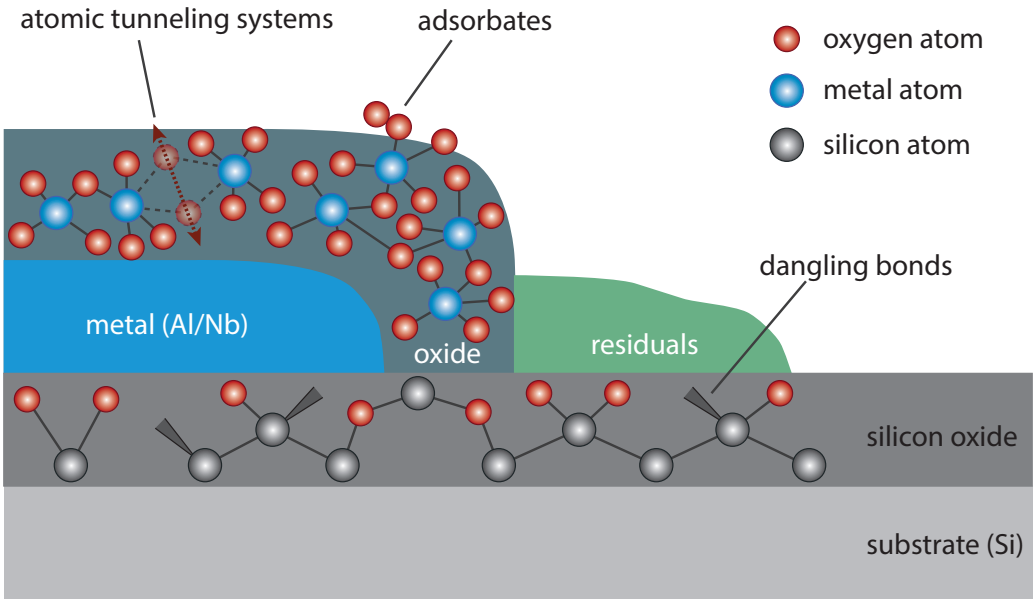

Figure 2.9. Sketch of defects at interfaces metal/substrate, metal/air, and substrate/air, showing a cross-section of a chip with no substrate treatment. At the metal/substrate interface and substrate/air interface, TLS can arise in silicon oxide layers, manifesting as surface defects. In particular, incomplete bonding of silicon atoms leads to the presence of unpaired electrons localized on the defect silicon atom, resulting in the formation of dangling bonds [167]. At the metal/air interface, the metal surface is susceptible to oxidation, which can host TLS in the form of atomic tunneling systems. Additionally, adsorbates like hydrogen and molecular oxygen introduce surface spins. Residual materials from fabrication processes, such as resists, also contribute to the presence of surface defects.

Microwave radiation can induce pair-breaking and power-dependent loss, which is characterized by

$$\delta_{\mathrm{qp}}^{\mathrm{mw}} \propto \left(\frac{P}{P_c}\right)^k \tag{2.57}$$

with an unspecified exponent k. Usually, microwave frequencies of a few GHz are not sufficient for most materials as the gap frequency corresponds to severy 10 (Al) up to several 100 GHz (Nb). However, they can redistribute already generated quasiparticles to higher energies. So, when a sufficiently strong microwave tone excites pre-existing quasiparticles from an energy level $E > \Delta_{\mathrm{sc}}$ to a higher level $E + n\hbar\omega$ ($n \in \mathbb{N}$) with ω being the microwave frequency, the quasiparticles can relax towards energy levels near the superconducting gap by the emission of phonon that are capable to break up additional quasiparticles. This loss mechanism becomes more noticeable at high power levels.

In case of the thermal activated quasiparticles, the quasiparticle density strongly increases with decreasing ratio $\zeta = \Delta_{\mathrm{sc}}/k_{\mathrm{B}}T$, of the gap energy and the thermal energy, i.e. with increasing T or decreasing Δ_{sc}. According to the Mattis-Bardeen theory [168], the loss can be described by

$$\delta_{\mathrm{qp}}^{\mathrm{th}} = \frac{2\mathcal{K}}{\pi} \frac{e^{-\zeta} \sinh(\xi) K_0(\xi)}{1 - e^{-\zeta}\left(\sqrt{2\pi/\zeta} - 2e^{-\xi} J_0(\xi)\right)}, \tag{2.58}$$

where $\mathcal{K}$ is the ratio of kinetic inductance to the total inductance of the material, $\xi = \hbar\omega_r/2k_{\mathrm{B}}T$, and K_0, J_0 are the modified Bessel function of the first and second kind, respectively. In practice, the refrigerator operating temperature ranges between $10 - 50$ mK. At this temperature quasiparticle losses are usually negligible even for materials with small energy gap such as Al.

In contrast, non-equilibrium quasiparticle loss has been identified as a significant factor that can

degrade the performance of quantum devices. This type of loss is attributed to the presence of stray infrared light originating from higher temperature stages [152, 169], which can be effectively mitigated by isolating the devices from the radiative environment using multistage shielding techniques [170]. Additionally, cosmic rays can also generate quasiparticles through particle ionization, which poses a new concern in maintaining device performance [171, 172].

Eddy current loss

Eddy currents are electrical currents that are generated within an electrical conductor by a time-varying electromagnetic field. This phenomenon simply results from by Faraday's law of induction [173]. These flow of currents counterbalance the magnetic fields that created them according to Lenz' rule. In our context, the most proximate conductive material is the normal conducting ground plane underneath the chip, which leads to eddy current loss, also referred to as conductivity loss. This loss depends on the distance $d = d_{\text{chip}} + d_{\text{vac}}$, where d_{chip} denotes the thickness of the substrate and d_{vac} represents the vacuum gap (see Fig. 2.10). Hence, a common strategy to mitigate this is to construct a sample box with a far distant ground plane under the chip or to use a superconducting ground plane. Such a design diminishes conductivity loss and decreases power dissipation by reducing the electric field at the boundary [142, 143, 155, 156]. As shown by [156], the loss can be described by

$$\delta_{\text{eddy}} = \sqrt{\frac{\omega_r \mu}{2\sigma_{\text{box}}}} \left(1 + \frac{d_{\text{chip}} + d_{\text{vac}}}{d_{\text{chip}}/\epsilon_r + d_{\text{vac}}}\right) \frac{Z_0 K(d) l_r}{32(Z_{\text{vac}} w)^2}, \tag{2.59}$$

were $\mu \approx \mu_0$ is the absolute permeability of the conductive material, σ_{box} refers to the electrical conductivity at the resonator frequency ω_r, $Z_0 = 50\,\Omega$, $Z_{\text{vac}} \approx 377\,\Omega$ is the vacuum impedance, and $K(d)^2 = \int_{-\infty}^{\infty} \mathrm{d}y k(y,d)$, where $k(y,d)$ denotes the field distribution at $z = 0$ along the y-direction. l_r stands for the resonator length, w for the resonator gap width, and $\varepsilon_r = 11.9$ is the relative dielectric constant of the Si substrate.

Notably, within a gold-plated copper package with a standard conductivity of $\sigma_{\text{box}} = 4.5 \times 10^9\,\text{S/m}$, eddy current loss approaches a saturation point at $Q_{\text{eddy}} = 4.5 \times 10^6$ when $d_{\text{vac}} \sim 3\,\text{mm}$. This quality factor is reduced by around three orders of magnitude for $d_{\text{vac}} = 0\,\text{mm}$, as indicated by the simulation [142]. Note that Q_{eddy} can be further improved by a proper choice of material, for example Cu coated by superconducting Al with an oxide thickness of 2 nm. In this situation the quality factor is only limited by the dielectric loss of 5×10^{-12} [143].

Parasitic modes

Parasitic modes in quantum devices are primarily caused by the chip environment, including factors such as sample boxes, wire bonding, and air bridges [141]. The main issue arises from the overlap between the parasitic modes and the modes of the quantum device, leading to unwanted cross talk. This cross talk occurs with low-Q_l box modes and slotline modes, resulting in a reduction of the intrinsic quality factor (Q_i) of the device [142, 143, 154, 155]. Several strategies can be employed to mitigate parasitic losses. One approach is to increase the detuning between the resonator mode and other modes present, reducing the field overlap. Additionally, increasing Q_c of all modes can also help to minimize the impact of parasitic losses. The presence of a sample box gives rise to box modes, which correspond to cavity modes within the surrounding free space. These modes exhibit frequencies that are highly dependent on the specific geometry and boundary conditions of the sample box. By

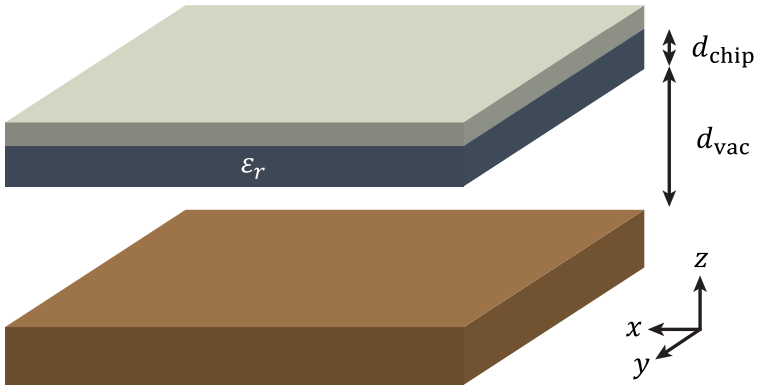

Figure 2.10. Illustration of sample box with chip. The Si substrate with the relative dielectric constant $\varepsilon_r = 11.9$ (dark blue) covered by the superconducting thin film (beige) is separated from the copper floor (brown) by a vacuum gap d_{vac}. For $d_{\text{vac}} = 0$, significant loss contribution from the eddy current loss and cross talk to the chip mode can be expected.

modifying these factors, it is possible to effectively manipulate and control the frequencies of the box modes.

Another important consideration is the influence of the superconducting thin film that covers a significant portion of the chip area. This thin film and the floor of the sample box create an additional cavity inside of the dielectric substrate. The presence of the dielectric medium within this cavity significantly lowers the frequencies of the fundamental modes compared to the vacuum case. For a typical chip size of 6 mm × 10 mm, these fundamental mode frequencies typically range from $8 - 12\,\text{GHz}$ [143, 174]. Consequently, the coupling between the quantum system and these box modes is strengthened, leading to enhanced Purcell decay. To mitigate this effect, it is possible to introduce a vacuum gap between the substrate and the ground plane of the sample box, as illustrated in Fig. 2.10. This helps to minimize the influence of the dielectric medium on the fundamental mode frequencies. Indeed, we can model the relative change in the fundamental mode frequency as

$$\frac{f_0' - f_0}{f_0} = \sqrt{\frac{\varepsilon_r}{\varepsilon_r'}} - 1 = \sqrt{\frac{\varepsilon_r d_{\text{vac}} + d_{\text{chip}}}{d_{\text{vac}} + d_{\text{chip}}}}, \tag{2.60}$$

where ε_r' represents the effective dielectric constant between the thin film and the sample box floor, d_{chip} denotes the thickness of the substrate, and d_{vac} represents the vacuum gap. Here, we have assumed that the cavity dimensions in the z direction are much smaller compared to the (x, y) directions, the fundamental mode f_0 is primarily affected by changes in the dielectric filling. As this equation is a monotonically increasing function, it allows us to place the fundamental mode at higher frequencies by increasing d_{vac}.

Parasitic slotline modes arise when there is a voltage difference across the conductor. This typically occurs when the ground plane is separated from the coplanar waveguides or if there is insufficient electrical connection between the ground plane and the sample box. These slotline modes can couple strongly to CPW resonators due to their significant field overlap, resulting in lower Q_i values due to their extended spatial presence in the dielectric and packaging. To mitigate this effect, techniques such as wire bonding and air bridges can be employed to eliminate or reduce the presence of parasitic slotline modes.

Other losses

Other sources of loss in superconducting quantum devices include loss by vortex motion, vortex loss and radiation loss. Vortex motion induced loss only occurs if there are Abrikosov vortices trapped in the superconducting materials and if they can move under the action of the Lorentz force induced by the microwave currents flowing in the superconducting film. Consequently, to mitigate losses stemming from vortex motion, a technique known as "flux traps" is implemented. These traps are essentially holes strategically incorporated into the superconducting films, designed to reduce the effects of vortex motion. Note that even if type-I superconductors are used for the microwave circuits, the thin superconducting film can exhibit type-II behavior, allowing for the formation of vortices [175, 176].

Radiation loss, on the other hand, stems from the dissipation of energy into free space. The amount of energy dissipated depends on the frequency and geometry of the CPW resonator. To mitigate radiation loss, one approach is to place the chip inside a cavity or inside a sample box. This cavity acts as a filter, reducing the amount of energy radiated into free space and suppressing the radiative loss [154, 177].

2.5 Interacting system

Having introduced the fundamental systems, namely superconducting microwave resonators and transmon qubit, we now turn our attention to the interacting system. We first discuss the qubit-photon interaction following [23, 24] and then address the four-wave mixing process.

2.5.1 Qubit-photon interaction

The qubit-photon interaction, also known as the light-matter interaction, is a central concept. In general, it is described by the quantum Rabi model, which captures the interaction between a qubit described by the Hamiltonian in Eq. (2.23), and the quantized harmonic oscillator, as described by Eq. (2.16) [24, 90, 178, 179]

$$\hat{\mathcal{H}}_{\text{Rabi}} = \hbar\omega_r \hat{a}_r^\dagger \hat{a}_r + \frac{\hbar\omega_q}{2}\hat{\sigma}_z + \hbar g_{qr}\left(\hat{\sigma}^\dagger + \hat{\sigma}\right)\left(\hat{a}_r + \hat{a}_r^\dagger\right), \tag{2.61}$$

where g_{qr} is the vacuum coupling strength. $\hat{\sigma}$ and $\hat{\sigma}^\dagger$ is the de-excitation and excitation Pauli operator of the qubit, respectively, while $\hat{a}_r^{(\dagger)}$ is the annihilation (creation) operator of the resonator mode. This Rabi model is, however, not suited for an analytical study. If the eigenfrequencies of each system, $\omega_{q,r}$ are much larger than the coupling strength g_{qr}, we can apply the rotating wave approximation, which leads to the Jaynes-Cummings Hamiltonian [23, 24, 90, 98, 179]

$$\hat{\mathcal{H}}_{\text{JC}} = \hbar\omega_r \hat{a}_r^\dagger \hat{a}_r + \frac{\hbar\omega_q}{2}\hat{\sigma}_z + \hbar g_{qr}\left(\hat{\sigma}^\dagger \hat{a}_r + \hat{\sigma}\hat{a}_r^\dagger\right). \tag{2.62}$$

We can understand this Hamiltonian as a number preserving process: the qubit can be either excited by annihilating a resonator photon ($\hat{\sigma}^\dagger \hat{a}_r$) or de-excited by creating a photon ($\hat{\sigma}\hat{a}_r^\dagger$). Its eigenfrequencies can be analytically found to be [98]

$$\omega_{n,\pm} = \omega_r n \pm \sqrt{\Delta_{qr}^2 + g_{qr}^2(n+1)}$$

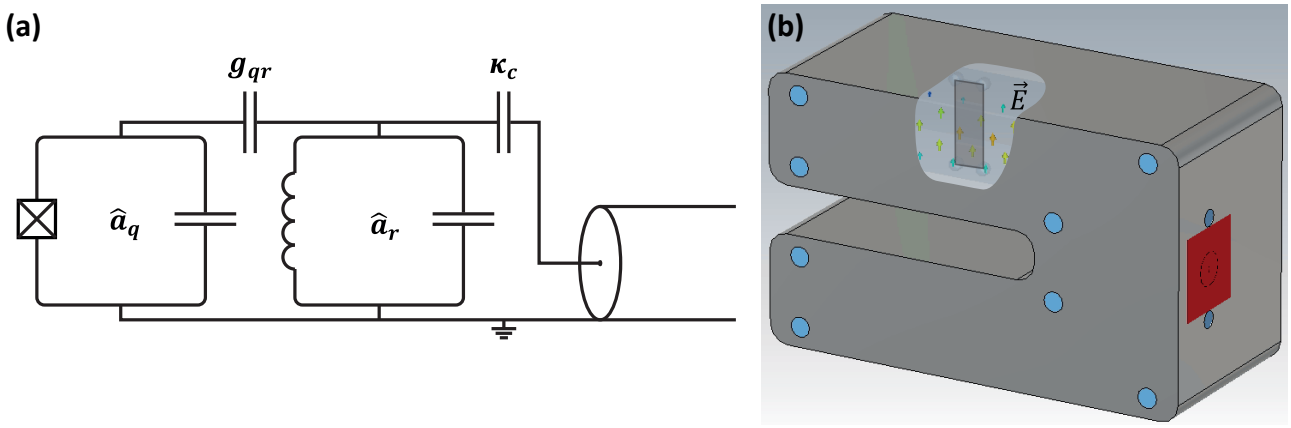

Figure 2.11. (a) Lumped-element-representation of the distributed circuit, where the transmon qubit, $\hat{a}_q$, and resonator, $\hat{a}_r$, are coupled together. (b) Schematic representation of a horseshoe 3D cavity enclosing a transmon qubit chip. A 2D structure placed in a 3D cavity is also called "3D transmon qubit". The colored vertical arrows depict the electric field $\vec{E}(\vec{r})$. The electric field $\vec{E}(\vec{r})$ and the dipole moment $\vec{p}_q$ are aligned in parallel realizing the electric dipole interaction, $g_{qr} = \vec{p}_q \cdot \vec{E}$.

with the detuning $\Delta_{qr} = \omega_q - \omega_r$, and its corresponding eigenstates

$$|n,+\rangle = \cos\Theta_n \,|n+1,0\rangle + \sin\Theta_n \,|n,1\rangle \tag{2.63a}$$

$$|n,-\rangle = \sin\Theta_n \,|n+1,0\rangle - \cos\Theta_n \,|n,1\rangle \tag{2.63b}$$

with the mixing angle

$$\Theta_n = \frac{1}{2}\tan^{-1}\frac{2g_{qr}\sqrt{n+1}}{\Delta_{qr}}.$$

Thus, the eigenstates of the coupled system (also known as dressed states) are superposition of the bare (uncoupled) qubit and resonator states.

As already discussed in Sec. 2.3, the transmon qubit is not a pure two-level system and in many cases the additional levels have to be taken into account. Taking into account only the third level for simplicity, we can rewrite the Hamiltonian in Eq. (2.62) as [24]

$$\hat{\mathcal{H}}_{\mathrm{JC}}/\hbar = \omega_r \hat{a}_r^\dagger \hat{a}_r + \omega_q \hat{a}_q^\dagger \hat{a}_q + \frac{\chi_{qq}}{2}\hat{a}_q^\dagger \hat{a}_q^\dagger \hat{a}_q \hat{a}_q + g_{qr}\left(\hat{a}_q^\dagger \hat{a}_r + \hat{a}_q \hat{a}_r^\dagger\right), \tag{2.64}$$

where we have replaced the Pauli operators to the annihilation (creation) operators $\hat{a}_q^{(\dagger)}$ obeying the commutation relation $\left[\hat{a}_q, \hat{a}_q^\dagger\right] = 1$. For example, if the 2D transmon and the resonator are coupled with capacitance C_c in cQED as shown in Fig. 2.11(a), the coupling strength can be expressed as[9] [90]

$$g_{qr} = \sqrt{\omega_q \omega_r}\frac{C_c}{2\sqrt{(C_q + C_c)(C_r + C_c)}}. \tag{2.65}$$

In case of a cavity QED such as illustrated in Fig. 2.11(b), where the transmon is coupled with the cavity via the electric dipole interaction, we have [24, 104, 106]

$$g_{qr} = \vec{p}_q \cdot \vec{E}(\vec{r}_q) \tag{2.66}$$

with the dipole moment $\vec{p}_q = e\vec{l}_q$ and the cavity electric field $\vec{E}(\vec{r}_q)$ at the position $\vec{r}_q$ of the transmon qubit.

[9] see also Appendix B.1 for the derivation.

Qubit driving

One of the most important methods for manipulating single qubits is through an external microwave drive. Here, we are considering the driving of an interacting qubit-resonator system, but this discussion is also valid for the direct qubit driving.

Eq. (2.62) can be reformulated as a qubit driving Hamiltonian. Assuming a coherent state for the resonator[10], we can transform the Hamiltonian into the displaced frame and obtain[11] [179]

$$\hat{\mathcal{H}}_{q,d} = \frac{\hbar\omega_q}{2}\hat{\sigma}_z + \hbar g_{qr}\left|\alpha_r\right|\left(\hat{\sigma}^\dagger e^{-i\phi}e^{-i\omega_d t} + \hat{\sigma}e^{i\phi}e^{i\omega_d t}\right), \tag{2.67}$$

where the time dependent complex amplitude, $\alpha_r(t)$, due to the coherent drive with frequency ω_d is given by[12]

$$\alpha_r(t) = \left|\alpha_r\right| e^{-i\phi}e^{-i\omega_d t} = -\frac{\sqrt{\kappa_r}\left\langle\hat{a}_{\text{in}}\right\rangle e^{-i\omega_d t}}{i\omega_r - i\omega_d + \kappa_r/2}.$$

Note that the phase ϕ is dependent on the detuning $\omega_r - \omega_d$ as well. Moving furthermore into the rotation frame of the drive, $\hat{\mathcal{H}}_0 = \hbar\omega_d\hat{\sigma}_z/2$, we can get rid of the time dependence. We obtain

$$\hat{\mathcal{H}}'_{q,d} = \frac{\hbar\Delta_{qd}}{2}\hat{\sigma}_z + \frac{2\hbar g_{qr}\left|\alpha_r\right|}{2}\left(\hat{\sigma}^\dagger e^{-i\phi} + \hat{\sigma}e^{i\phi}\right) = \frac{\hbar\Delta_{qr}}{2}\hat{\sigma}_z + \frac{\hbar A}{2}\left(\hat{\sigma}^\dagger e^{-i\phi} + \hat{\sigma}e^{i\phi}\right) \tag{2.68}$$

with the qubit-drive detuning $\Delta_{qd} = \omega_q - \omega_d$. The time evolution of the qubit state for $\left|\psi(0)\right\rangle_{\text{rot}} = \left|0\right\rangle_{\text{rot}}$ can then be read as (see Sec. C.1)

$$\left|\psi(t)\right\rangle_{\text{rot}} = \sin\left(\frac{\theta}{2}\right)e^{-i\phi/2}e^{-i\Omega_{\text{Rabi}}t/2}\left|\Psi_-\right\rangle_{\text{rot}} + i\cos\left(\frac{\theta}{2}\right)e^{i\phi/2}e^{i\Omega_{\text{Rabi}}t/2}\left|\Psi_+\right\rangle_{\text{rot}}$$

with the Rabi frequency $\Omega_{\text{Rabi}} = \sqrt{A^2 + \Delta_{qd}^2}$. The probability of finding the qubit in the excited state is determined by

$$\begin{aligned}
\mathbb{P}(\left|1\right\rangle) =& \left\langle\psi(t)\right| P_e \left|\psi(t)\right\rangle = \left\langle\psi(t)\right| \left|1\right\rangle\left\langle1\right| \left|\psi(t)\right\rangle \\
=& \left|-ie^{i\phi/2 - i\Omega_{\text{Rabi}}t/2}\sin\left(\frac{\theta}{2}\right)\cos\left(\frac{\theta}{2}\right) + ie^{i\phi/2 + i\Omega_{\text{Rabi}}t/2}\sin\left(\frac{\theta}{2}\right)\cos\left(\frac{\theta}{2}\right)\right|^2 \\
=& \frac{\sin^2(\theta)}{4}\left|e^{i\Omega_{\text{Rabi}}t/2} - e^{-i\Omega_{\text{Rabi}}t/2}\right|^2 = \sin^2(\theta)\sin^2\left(\frac{\Omega_{\text{Rabi}}t}{2}\right) \\
=& \frac{A^2}{A^2 + \Delta_{qd}^2}\sin^2\left(\frac{\Omega_{\text{Rabi}}t}{2}\right).
\end{aligned} \tag{2.69}$$

We can determine the qubit frequency by plotting the Rabi frequency Ω_{Rabi} as a function of the detuning Δ_{qr} and identifying its minimum. At this minimum, the driving frequency is equal to the qubit frequency. The Rabi frequency is proportional to the square root of the drive power ε_r due to its dependence on the magnitude of α_r. In this context, the parameter t can be interpreted as the pulse length of the drive.

[10] This assumption is typically valid when using a coherent microwave tone.
[11] Here, we neglect the quantum fluctuation of the resonator, $\hat{a}_r$
[12] Here, we assume that the resonator mode is already in steady state. See Sec. C.3.

Dispersive regime

The conventional readout procedure introduces noise into the system due to the Heisenberg uncertainty relation, making it impossible to obtain the same result repeatedly. However, in certain situations, it is possible to perform a non-destructive readout that does not disturb the system, leading to repeated identical results. This type of measurement is known as a quantum non-demolition measurement (QND measurement) and is essential for measurement-based quantum feedback control.

The readout method for the transmon qubit is based on the reformulation of the Jaynes-Cummings Hamiltonian (Eq. (2.62)) in the dispersive regime, where the condition $|\Delta_{qr}| \gg g_{qr}$ is satisfied. In this regime, the system's Hamiltonian can be accurately described using the Schrieffer-Wolff transformation (refer to Sec. C.2 for more details) [23, 24, 90].

$$\hat{\mathcal{H}}_{q,\mathrm{disp}}/\hbar = \left(\omega_r + \frac{\chi_{qr}}{2}\hat{\sigma}_z\right)\hat{a}_r^\dagger\hat{a}_r + \frac{1}{2}\left(\omega_q + \frac{\chi_{qr}}{2}\right)\hat{\sigma}_z. \tag{2.70}$$

Here, $\chi_{qr} \equiv 2g_{qr}^2/\Delta_{qr}$ is the cross-Kerr strength. The term $\frac{\chi_{qr}}{2}\hat{\sigma}_z\hat{a}_r^\dagger\hat{a}_r$ is known as the ac-Stark shift or dispersive shift related to the finite number $\hat{a}_r^\dagger\hat{a}_r$ of resonator photons, while $\frac{\chi_{qr}}{2}\hat{\sigma}_z$ is called as Lamb shift due to vacuum fluctuations. The Hamiltonian presented can be interpreted in two ways: Firstly, the frequency of the resonator is dependent on the state of the qubit, and secondly, the frequency of the qubit is dependent on the number of photons in the resonator. The former interpretation is utilized for reading out the qubit state, while the latter is employed for photon number calibration and is also the source of increased qubit dephasing.

As discussed in Eqs. (2.51) and (2.54) in Sec. 2.4, the resonator's response within the rotating frame of $\omega_r\hat{a}_r^\dagger\hat{a}_r$ is expressed as

$$S_{11} = 1 - \frac{2\kappa_{r,c}}{\pm i\chi_{qr} + \kappa_{r,c}}, \tag{2.71}$$

where, for the sake of simplicity, we have neglected internal losses. In both instances, the responses are primarily focused around the resonator's resonance frequency. The fundamental principle behind the qubit readout is that, if this frequency alters due to a shift in the qubit state, we can detect changes in either the microwave amplitude in transmission measurements or the phase shift in reflection measurements (in the reflection measurements, we evaluate the phase response as no amplitude change can be discerned.). The optimal ratio for the readout is $\chi_{qr} = \kappa_r$, as suggested in [180]. This optimum can be understood if we consider two extreme scenarios: $\chi_{qr} \ll \kappa_r$ and $\chi_{qr} \gg \kappa_r$. The former scenario makes it challenging to differentiate between states $|0\rangle$ and $|1\rangle$ due to significant overlap of the Gaussian distributions in the I-Q plane, while the latter scenario results in very small signals. Hence, there is an optimum between two extreme regimes.

If we consider the transmon as three level system, we need to account for the anharmonicity. That is, the dispersive shift is reduced to [90]

$$\chi'_{qr} = \chi_{qr}\frac{\chi_{qq}}{\chi_{qq} + \Delta_{qr}},$$

which leads to

$$\hat{\mathcal{H}}_{t,\mathrm{disp}} = \left(\omega_r + \chi'_{qr}\hat{a}_q^\dagger\hat{a}_q\right)\hat{a}_r^\dagger\hat{a}_r + \left(\omega_q + \frac{\chi_{qr}}{2}\right)\hat{a}_q^\dagger\hat{a}_q. \tag{2.72}$$

It is important to note that we need to apply the formula $g_{qr} = \sqrt{\chi'_{qr}\Delta_{qr}}$ for extracting the qubit-resonator coupling strength.

Purcell effect

As discussed in Sec. 2.4, the interaction of a qubit with an open transmission line leads to free-space spontaneous emission, as the qubit is coupled to an infinite number of harmonic modes. However, when the qubit is weakly coupled to a single-mode resonator, a significant enhancement in the qubit decay rate can be observed. This phenomenon is known as the Purcell effect [181, 182]. The key distinction lies in the density of states (number of states per frequency interval), which determines the number of photonic states the qubit can interact with.

The density of states for the transmission line is proportional to ω_q^2, while the density of states for the resonator is described by a Lorentzian function [182]

$$D_r\left(\omega_q\right) = \frac{2}{\pi\kappa_r}\frac{\kappa_r^2}{4\Delta_{qr}^2 + \kappa_r^2}, \tag{2.73}$$

which essentially acts as a band pass filter. If the detuning between qubit and resonator is negligible ($\delta_{qr} \ll \kappa_r$), the density of states is enhanced by the quality factor of the resonator. This high density of states enhances the spontaneous emission rate, surpassing that in free space. However, for a large detuning between the qubit and resonator ($\delta_{qr} \gg \kappa_r$), the reduced density of states suppresses radiative decay. This effect is called Purcell filtering. The Purcell-filtered relaxation rate of the qubit can be expressed as [92]

$$\gamma_{q,\mathrm{P}} = \frac{\kappa_{r,c}}{2} - \frac{\sqrt{2}}{2}\sqrt{-\mathcal{A} + \sqrt{\mathcal{A}^2 + (\kappa_r\Delta_{qr})^2}} \approx \kappa_{r,c}\left(\frac{g_{qr}}{\Delta_{qr}}\right)^2 \tag{2.74}$$

with $\mathcal{A} = \Delta_{qr}^2 + 4g_{qr}^2 - \kappa_{r,c}^2/4$. While the Purcell effect can significantly enhance the coherence time of the qubit, it is important to note that this enhancement is subject to the condition $g_{qr}^2/\Delta_{qr} \ll 1$ and $\kappa_{r,c}/\delta_{qr} \ll 1$ at the same time. However, these requirements may be in conflict with achieving strong qubit-photon coupling and fast qubit readout [100, 106]. In scenarios where a long coherence time of the qubit is desired but the condition (2.74) is not satisfied, we call the system is Purcell-limited. To overcome this limitation,so-called Purcell filters are commonly employed in between the readout resonator and transmission line [183, 184]. These filters can help to control the density of states and improve the qubit's coherence properties further.

2.5.2 Four-wave mixing

In this subsection, we delve into the description understanding of multi-wave mixing in Josephson physics. The Josephson junction, a highly nonlinear element described by a cosine potential in the Hamiltonian, enables the realization of strong multi-wave mixing processes. Particularly, three- or four-wave mixing processes find applications in various parametrically activated devices, including parametric amplifiers [27–32, 185], frequency converters [33–35], nonclassical-light generators [36, 37], stabilizers [38, 39], and single-photon detectors [40, 41]. Our focus here is specifically on the irreversible frequency conversion process demonstrated in the recent work by Lescanne et al. [41].

This idea bears resemblance to the Jaynes-Cummings Hamiltonian discussed in Subsec. 2.5.1. In a similar manner to how the eigenstates in Eq. (2.63) can be described as a superposition of the bare qubit and resonator states due to their coupling, the bare modes can be expressed as a sum of eigenmodes, each multiplied by a kth polynomial order when expanding the Josephson cosine potential. By carefully selecting the appropriate driving frequency, we can engineer specific multi-wave interactions, allowing

for precise control and manipulation of the system.

Hamiltonian

We are considering a system consisting of a 3D cavity containing a qubit that is coupled to two modes of the cavity, the so-called buffer and waste mode (see Fig. 2.12). The transmon qubit is coupled with the buffer and waste mode via electrical dipole interaction. The electrical dipole moment of the transmon, which is realized by the antenna-like long capacitance, interacts with the electrical fields of the buffer and waste, as illustrated in Fig. 2.12 (a). The cavity modes can be excited by external microwave drives via stub antennae by electrical dipole interaction [96, 97]. Hence, the Hamiltonian description of our system is described by

$$\hat{\mathcal{H}} = \hat{\mathcal{H}}_q + \hat{\mathcal{H}}_b + \hat{\mathcal{H}}_w + \hat{\mathcal{H}}_{qb} + \hat{\mathcal{H}}_{qw} + \hat{\mathcal{H}}_{bd} + \hat{\mathcal{H}}_{wd}, \tag{2.75}$$

where

$$\hat{\mathcal{H}}_q = \frac{\left(\hat{Q} - Q_g\right)^2}{2C_\Sigma} - E_J \cos\left(\frac{2\pi}{\Phi_0}\hat{\Phi}\right) \tag{2.76}$$

is the transmon qubit Hamiltonian with the charge $\hat{Q}$, the magnetic flux $\hat{\Phi}$, the gate charge Q_g, the total capacitance C_Σ, the Josephson energy E_J, and the flux quantum Φ_0 [24, 90, 114],

$$\hat{\mathcal{H}}_{b/w} = \frac{1}{2}\int \mathrm{d}^3 r \epsilon_0 \hat{\vec{E}}^2_{b/w} + \mu_0 \hat{\vec{H}}^2_{b/w} \tag{2.77}$$

is the Hamiltonian describing the buffer/waste with the electric field $\hat{\vec{E}}(\vec{r})$ and the magnetic field $\hat{\vec{H}}(\vec{r})$ [85, 95],

$$\hat{\mathcal{H}}_{qb/w} = \hat{\vec{p}}_q \cdot \hat{\vec{E}}_{b/w} \tag{2.78}$$

is the interaction Hamiltonian between the transmon qubit and buffer/waste mode with the electrical dipole moment of the transmon $\hat{\vec{p}}_q = \hat{Q}\vec{l}_q$ with its antenna length l_q [24, 97, 104], and

$$\hat{\mathcal{H}}_{ab/w} = \vec{p}_a(t) \cdot \hat{\vec{E}}_{b/w} \tag{2.79}$$

is the external coupling Hamiltonian between the antenna and buffer/waste mode described by the electrical dipole moment of the antenna $\vec{p}_a(t) = \vec{p}_a \cos(\omega_d t)$ with the driving frequency ω_d [96, 97]. This last term is also called the driving term.

It is convenient for the second quantization, if the unit of all variables is dimensionless. Fortunately, since the Hamiltonian can be generalized to the generalized coordinates and its conjugate momenta [186], we will rewrite them in the dimensionless canonical variables $(\tilde{Q}_x, \tilde{P}_x)$, where the indices $x = q, b, w$ represents the qubit mode, buffer mode and waste mode, respectively. In this case, the above Hamiltonians are reformulated as

$$\begin{aligned}\hat{\mathcal{H}}/\hbar =& \frac{4E_C}{\hbar}\left(\hat{\tilde{P}}_q - n_g\right)^2 - \frac{E_J}{\hbar}\cos\left(\hat{\tilde{Q}}_q\right) + \frac{\omega_b}{4}\left(\hat{\tilde{P}}_b^2 + \hat{\tilde{Q}}_b^2\right) + \frac{\omega_w}{4}\left(\hat{\tilde{P}}_w^2 + \hat{\tilde{Q}}_w^2\right) \\ &+ \tilde{g}_b \hat{\tilde{P}}_q \hat{\tilde{P}}_b + \tilde{g}_w \hat{\tilde{P}}_q \hat{\tilde{P}}_w + 2\varepsilon_b \cos(\omega_d t)\,\hat{\tilde{P}}_b + 2\varepsilon_w \cos(\omega_d t)\,\hat{\tilde{P}}_w,\end{aligned} \tag{2.80}$$

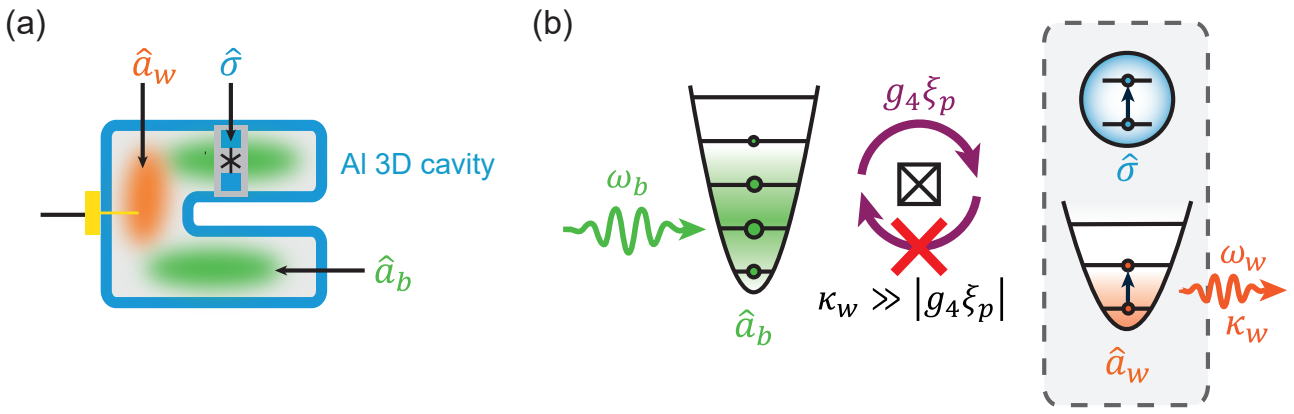

Figure 2.12. (a) A transmon is mounted in a 3D superconducting cavity coupled with the cavity waste/buffer mode (orange/green shaded area representing its electric field distribution in the cavity). (b) Principle of the microwave single-photon detection. A coherent incoming photon (green wave) is absorbed by a buffer mode, $\hat{a}_b$, and is converted to a pair of qubit mode, $\hat{\sigma}$, and waste mode, $\hat{a}_w$, with interaction strength $g_4\xi_p$. Due to the engineered fast dissipiation of the waste mode, $\kappa_w \gg |g_4\xi_p|$, the reverse process ($\hat{a}_b^\dagger\hat{\sigma}\hat{a}_w$) is effectively inhibited.

where we have defined

$$\hat{\tilde{P}}_q \equiv \hat{Q}/(2e), \qquad \hat{\tilde{Q}}_q \equiv \frac{2\pi}{\Phi_0}\hat{\Phi}, \qquad n_g \equiv Q_g/(2e), \qquad \varepsilon_{b/w} = \sqrt{\kappa_{b/w,c}}p_{\text{in}}$$

with the flux quantum Φ_0, gate charge Q_g, external coupling rate $\kappa_{b/w,c}$ of the buffer and waste mode, respectively, and the square root of the pump photon flux p_{in}. Furthermore,

$$E_C \equiv \frac{e^2}{2C_\Sigma}, \qquad \tilde{g}_{b/w} \equiv -\sqrt{\frac{\omega_{b/w}}{2\varepsilon_0 V_{b/w}}}2e\vec{u}_{b/w}\cdot\vec{l}_q,$$

where $\vec{u}_{b/w}$ is the unit vector of $\hat{\vec{E}}_{b/w}$.

Rescaling of the canonical conjugate pair of the transmon qubit

Since what we measure in experiments is the eigenfrequency of the device, it is convenient to transform the Hamiltonian in Eq. (2.80) into the eigenmode basis. Furthermore, the eigenmode description also helps us to understand the four wave mixing process due to the Josephson nonlinearity.

To obtain the eigenmodes, we separate the right hand side of Eq. (2.80) in linear, nonlinear, and driven parts. Additionally, we included $-8E_C n_g\tilde{P}_q$ in the driven Hamiltonian, as it does not have a bilinear form and thus unsuitable for the eigenmode basis calculation. Henceforth, we get

$$\begin{aligned}\hat{\mathcal{H}}_{\text{lin}}/\hbar =& \frac{4E_C}{\hbar}\hat{\tilde{P}}_q^2 + \frac{E_J}{2\hbar}\hat{\tilde{Q}}_q^2 + \frac{\omega_b}{4}\left(\hat{\tilde{P}}_b^2 + \hat{\tilde{Q}}_b^2\right) + \frac{\omega_w}{4}\left(\hat{\tilde{P}}_w^2 + \hat{\tilde{Q}}_w^2\right) \\ &+ \tilde{g}_b\hat{\tilde{P}}_q\hat{\tilde{P}}_b + \tilde{g}_w\hat{\tilde{P}}_q\hat{\tilde{P}}_w, \qquad (2.81)\\ \hat{\mathcal{H}}_{\text{nl}} =& -E_J\left(\cos\left(\hat{\tilde{Q}}_q\right) + \hat{\tilde{Q}}_q^2/2\right), \qquad (2.82)\\ \hat{\mathcal{H}}_{\text{drv}}/\hbar =& -\frac{8E_C}{\hbar}n_g\hat{\tilde{P}}_q + 2\varepsilon_b\cos(\omega_d t)\,\hat{\tilde{P}}_b + 2\varepsilon_w\cos(\omega_d t)\,\hat{\tilde{P}}_w. \qquad (2.83)\end{aligned}$$

It is favorable, if we can write the two qubit terms in Eq. (2.81) in form of $\omega_q(\hat{P}_q^2 + \hat{Q}_q^2)/4$. For that

purpose, we rescale the canonical variables of the transmon qubit as follows[13]

$$\hat{P}_q \equiv 2\left(\frac{E_J}{2E_C}\right)^{-1/4}\hat{\tilde{P}}_q, \qquad \hat{Q}_q \equiv \left(\frac{2E_C}{E_J}\right)^{-1/4}\hat{\tilde{Q}}_q, \tag{2.84}$$

Inserting Eq. (2.84) into the two qubit terms in Eq. (2.81), we obtain

$$\begin{aligned}
4E_C\hat{\tilde{P}}_q^2 + \frac{E_J}{2}\hat{\tilde{Q}}_q^2 =& E_C\left(\frac{E_J}{2E_C}\right)^{1/2}\hat{P}_q^2 + \frac{E_J}{2}\left(\frac{2E_C}{E_J}\right)^{1/2}\hat{Q}_q^2 \\
=& \left(\frac{E_C E_J}{2}\right)^{1/2}\hat{P}_q^2 + \left(\frac{E_C E_J}{2}\right)^{1/2}\hat{Q}_q^2 \\
=& \frac{\hbar\omega_q}{4}\left(\hat{P}_q^2 + \hat{Q}_q^2\right),
\end{aligned}$$

where we have defined the qubit frequency $\omega_q \equiv \sqrt{8E_C E_J}/\hbar$. The coupling parameters can also be redefined as

$$g_{b/w} \equiv \frac{1}{2}\left(\frac{E_J}{2E_C}\right)^{1/4}\tilde{g}_{b/w}.$$

Setting $\hat{P}_{b/w} \equiv \hat{\tilde{P}}_{b/w}$ and $\hat{Q}_{b/w} \equiv \hat{\tilde{Q}}_{b/w}$, we can reformulate Eq. (2.81) in the compact form

$$\hat{\mathcal{H}}_{\text{lin}}/\hbar = \frac{1}{2}\hat{\vec{P}}^T\Omega_{PP}\hat{\vec{P}} + \frac{1}{2}\hat{\vec{Q}}^T\Omega_{QQ}\hat{\vec{Q}} \tag{2.85}$$

with

$$\hat{\vec{P}} \equiv \left[\hat{P}_q, \hat{P}_b, \hat{P}_w\right], \qquad \hat{\vec{Q}} \equiv \left[\hat{Q}_q, \hat{Q}_b, \hat{Q}_w\right],$$

$$\Omega_{PP} \equiv \frac{1}{2}\begin{bmatrix} \omega_q & g_b & g_w \\ g_b & \omega_b & 0 \\ g_w & 0 & \omega_w \end{bmatrix}, \qquad \Omega_{QQ} \equiv \frac{1}{2}\begin{bmatrix} \omega_q & 0 & 0 \\ 0 & \omega_b & 0 \\ 0 & 0 & \omega_w \end{bmatrix}.$$

Diagonalization of the bilinear Hamiltonian

For the diagonalization of the Hamiltonian Eq. (2.85), we transform into the Lagrangian formalism, obtain the eigenmodes, and then transform it back to the Hamiltonian. The key point is that the Lagrange formalism deals with the generalized coordinate $\hat{\vec{Q}}$ and its time derivative $\dot{\hat{\vec{Q}}}$, which are in a direct linear relation. As we will see later, this linear relation is advantageous for the eigenmode calculation [187].

As derived in Appendix C.4, the Lagrangian of Eq. (2.85) reads[14]

$$\mathcal{L}/\hbar = \frac{1}{2}\dot{\vec{Q}}^T\Omega_{PP}^{-1}\dot{\vec{Q}} - \frac{1}{2}\vec{Q}^T\Omega_{QQ}\vec{Q}.$$

Following the approach of [187], we first diagonalize

$$\Omega_{QQ} = O_Q\Lambda_{QQ}\mathbf{1}_\omega O_Q^\dagger = \Lambda_{QQ}\mathbf{1}_\omega,$$

where Λ_{QQ} is a dimensionless diagonal matrix and $\mathbf{1}_\omega$ is the identity matrix with physical dimensions

[13] see [24, 90, 114] and Appendix A for more details.
[14] Within the Lagrangian formalism, we omit the hat denoting the operator for clarity.

of an angular frequency. We transform the principle-axis of Q to

$$\breve{\vec{Q}} \equiv \Lambda_{QQ}^{1/2}\vec{Q},$$

such that

$$\mathcal{L}/\hbar = \frac{1}{2}\dot{\breve{\vec{Q}}}^T\Lambda_{QQ}^{-1/2}\Omega_{PP}^{-1}\Lambda_{QQ}^{-1/2}\dot{\breve{\vec{Q}}} - \frac{1}{2}\breve{\vec{Q}}^T\mathbf{1}_\omega\breve{\vec{Q}}.$$

Further, by diagonalizing the matrix in the first term

$$\Lambda_{QQ}^{-1/2}\Omega_{PP}^{-1}\Lambda_{QQ}^{-1/2} = O_P\Lambda_{PP}^{-1}\mathbf{1}_\omega^{-1}O_P^\dagger,$$

where Λ_{PP} is again a dimensionless diagonal matrix, and defining the eigenmode coordinate as

$$\vec{Q}_m \equiv \Lambda_{PP}^{-1/4}O_P^\dagger\breve{\vec{Q}} = \Lambda_{PP}^{-1/4}O_P^\dagger\Lambda_{QQ}^{1/2}\vec{Q}, \tag{2.86}$$

the linear Lagrangian can be recast as

$$\mathcal{L}/\hbar = \frac{1}{2}\dot{\vec{Q}}_m^T\Lambda_{PP}^{-1/2}\mathbf{1}_\omega^{-1}\dot{\vec{Q}}_m - \frac{1}{2}\vec{Q}_m^T\Lambda_{PP}^{1/2}\mathbf{1}_\omega\vec{Q}_m.$$

The Lagrangian equation of motion yields the harmonic eigenvalue equation

$$0 = \frac{\partial\mathcal{L}}{\partial\vec{Q}_m} - \frac{\mathrm{d}}{\mathrm{d}t}\frac{\partial\mathcal{L}}{\partial\dot{\vec{Q}}_m} = \Lambda_{PP}^{1/2}\mathbf{1}_\omega\vec{Q}_m + \Lambda_{PP}^{-1/2}\mathbf{1}_\omega^{-1}\ddot{\vec{Q}}_m = \Omega\vec{Q}_m + \Omega^{-1}\ddot{\vec{Q}}_m$$

with the diagonal eigenfrequency matrix $\Omega \equiv \frac{1}{2}\mathrm{diag}\left[\omega_{m,q}, \omega_{m,b}, \omega_{m,w}\right]\mathbf{1}_\omega = \Lambda_{PP}^{1/2}\mathbf{1}_\omega$. The indices q, b, w refer to the qubit-, buffer-, and waste-type eigenmode. This is reasonable considering the fact that the ratio $g_{b/w}/\left|\omega_q - \omega_{b/w}\right| \ll 1$ in the undriven case. After having obtained the eigenmodes and their corresponding eigenfrequencies, we can transform back to the Hamiltonian formalism

$$\hat{\mathcal{H}}_{\mathrm{lin}}/\hbar = \frac{1}{2}\hat{\vec{P}}_m^T\Omega\hat{\vec{P}}_m + \frac{1}{2}\hat{\vec{Q}}_m^T\Omega\hat{\vec{Q}}_m \tag{2.87}$$

with $\hat{\vec{P}}_m = \partial\hat{\mathcal{L}}/\partial\dot{\hat{\vec{Q}}}_m = \Omega^{-1}\dot{\hat{\vec{Q}}}_m$.

Here, we want to draw attention to the fact that according to Eq. (2.86) the general coordinate $\vec{Q}$ can be described as a sum of the variables $\hat{Q}_{m,j}$ in the jth eigenmode basis

$$\hat{Q}_i = \sum_j \tilde{\varphi}_{ij}\hat{Q}_{m,j}, \tag{2.88}$$

where $\tilde{\varphi}_{ij}$ can be interpreted as the (dimensionless) zero-point fluctuation of jth eigenmode at ith (original) basis with $[\tilde{\varphi}]_{ij} = \Lambda_{QQ}^{-1/2}O_P\Omega^{1/2}$. Analogously, for the conjugate momenta we can express

$$\hat{P}_i = \sum_j \tilde{n}_{ij}\hat{P}_{m,j} \tag{2.89}$$

with the (dimensionless) zero-point fluctuation $\tilde{n}_{ij}$ of jth eigenmode at ith (original) basis with $[\tilde{n}]_{ij} =$

$\Omega_{PP}^{-1}\Lambda_{QQ}^{-1/2}O_P\Omega^{3/2}$. The full Hamiltonian can then be rewritten as

$$\begin{aligned}\hat{\mathcal{H}}/\hbar =&\frac{1}{2}\hat{\vec{P}}_m^T\Omega\hat{\vec{P}}_m+\frac{1}{2}\hat{\vec{Q}}_m^T\Omega\hat{\vec{Q}}_m-\frac{E_J}{\hbar}\left(\cos\left(\hat{\tilde{Q}}_q\right)+\frac{1}{2}\hat{\tilde{Q}}_q^2\right)\\&-\frac{4E_C}{\hbar}n_g\sum_j n_{qj}\hat{P}_{m,j}\\&+2\varepsilon_b\cos\left(\omega_d t\right)\sum_j n_{bj}\hat{P}_{m,j}+2\varepsilon_w\cos\left(\omega_d t\right)\sum_j n_{wj}\hat{P}_{m,j}\\=&\frac{1}{4}\sum_j\omega_{m,j}\left(\hat{P}_{m,j}^2+\hat{Q}_{m,j}^2\right)-\frac{E_J}{\hbar}\left(\cos\left(\hat{\tilde{Q}}_q\right)+\frac{1}{2}\hat{\tilde{Q}}_q^2\right)\\&-\frac{4E_C}{\hbar}n_g\sum_j n_{qj}\hat{P}_{m,j}\\&+2\varepsilon_b\cos\left(\omega_d t\right)\sum_j n_{bj}\hat{P}_{m,j}+2\varepsilon_w\cos\left(\omega_d t\right)\sum_j n_{wj}\hat{P}_{m,j}\end{aligned}\tag{2.90}$$

with

$$\begin{aligned}\hat{\tilde{Q}}_q=&\sum_j\varphi_{qj}\hat{Q}_{m,j}\equiv\left(\frac{2E_C}{E_J}\right)^{1/4}\sum_j\tilde{\varphi}_{qj}\hat{Q}_{m,j}\\\hat{\tilde{P}}_q=&\sum_j n_{qj}\hat{Q}_{m,j}\equiv\left(\frac{E_J}{2E_C}\right)^{1/4}\sum_j\tilde{n}_{qj}\hat{Q}_{m,j}\end{aligned}$$

according to Eq. (2.84).

Thus, we have successfully expressed the bare modes of the uncoupled system as the sums of the normal modes, which enables the multi-wave mixing process. We further want to note that the driving term in Eq. (2.90) now contains the qubit driving term

$$\begin{aligned}\left(2\varepsilon_b n_{bq}+2\varepsilon_w n_{wq}\right)\hat{P}_{m,q}\cos\left(\omega_d t\right)=&2\left(\sqrt{\kappa_{b,c}}n_{bq}+\sqrt{\kappa_{w,c}}n_{wq}\right)p_{\mathrm{in}}\hat{P}_{m,q}\cos\left(\omega_d t\right)\\\equiv&2\sqrt{\gamma_{q,\mathrm{P}}}p_{\mathrm{in}}\hat{P}_{m,q}\cos\left(\omega_d t\right)\equiv 2\varepsilon_q\hat{P}_{m,q}\cos\left(\omega_d t\right),\end{aligned}\tag{2.91}$$

which is nothing but the Purcell effect with the decay rate, $\gamma_{q,\mathrm{P}}$.

Second Quantization of the Hamiltonian

For the second quantization of the Hamiltonian, we introduce the annihilation $\hat{a}_j$ and creation operators $\hat{a}_j^\dagger$ as

$$\begin{bmatrix}\hat{a}_j\\\hat{a}_j^\dagger\end{bmatrix}\equiv\frac{1}{2}\begin{bmatrix}1&i\\1&-i\end{bmatrix}\begin{bmatrix}\hat{Q}_{m,j}\\\hat{P}_{m,j}\end{bmatrix}\tag{2.92}$$

with the commutation relation $\left[\hat{a}_j,\hat{a}_k^\dagger\right]=\delta_{jk}$. Thus, the Hamiltonian in Eq. (2.90) in the Fock basis is reformulated as

$$\begin{aligned}\hat{\mathcal{H}}/\hbar=&\sum_{j=q,b,w}\omega_{m,j}\hat{a}_j^\dagger\hat{a}_j-\frac{E_J}{\hbar}\left(\cos\left(\hat{\tilde{Q}}_q\right)+\frac{1}{2}\hat{\tilde{Q}}_q^2\right)-\frac{4iE_C}{\hbar}n_g\sum_j n_{qj}\left(\hat{a}_j^\dagger-\hat{a}_j\right)\\&+2i\varepsilon_b\cos\left(\omega_d t\right)\sum_j n_{bj}\left(\hat{a}_j^\dagger-\hat{a}_j\right)+2i\varepsilon_w\cos\left(\omega_d t\right)\sum_j n_{wj}\left(\hat{a}_j^\dagger-\hat{a}_j\right).\end{aligned}\tag{2.93}$$

Four-wave mixing for single-photon detection

Here, we are interested in the four-wave mixing process allowing to use the system shown in Fig. 2.12, where its derivation is mostly adapted from [41]. Our aim is to have a term in the Hamiltonian Eq. (2.93), where the buffer state, which temporary stores the incoming single photon, is converted into a qubit state and waste mode by applying a pump pulse. That is,

$$\hat{\mathcal{H}}_{4\mathrm{wm}}/\hbar = g_4 \xi_p \hat{a}_b \hat{a}_q^\dagger \hat{a}_w^\dagger e^{i(\omega_q' + \omega_w' - \omega_b' - \omega_d)t} + \mathrm{h.c.} \tag{2.94}$$

with the total mean field amplitude $\xi_p \equiv \xi_q + \xi_b + \xi_w$, where the qubit, buffer and waste mode is displaced by $\xi_{q/b/w}$ [41, 72, 188]. Henceforth, we choose the drive frequency $\omega_d = \omega_p = \omega_q' + \omega_w' - \omega_b'$. Here, we use ω_j' indicating that we take into account the ac-Stark shift. g_4 is the interaction strength for the four-wave mixing process, which definition will be shown later.

Thus, to obtain the term given in Eq. (2.94) under the conditions provided above, Eq. (2.93) transforms to

$$\begin{aligned}\hat{\mathcal{H}}' = &\sum_{j=q,b,w} \omega_{m,j} \hat{a}_j^\dagger \hat{a}_j - E_J \left(\cos\left(\hat{\tilde{Q}}_q'\right) + \frac{1}{2}\hat{\tilde{Q}}_q'^2 \right) - 4iE_C n_g n_{qq} \left(\hat{a}_q^\dagger - \hat{a}_q \right) \\ &+ 2i\varepsilon_b \cos(\omega_d t)\, n_{bb} \left(\hat{a}_b^\dagger - \hat{a}_b \right) + 2i\varepsilon_w \cos(\omega_d t)\, n_{ww} \left(\hat{a}_w^\dagger - \hat{a}_w \right) + 2i\varepsilon_q \cos(\omega_d t) \left(\hat{a}_q^\dagger - \hat{a}_q \right)\end{aligned} \tag{2.95}$$

with

$$\hat{\tilde{Q}}_q' = \sum_j \varphi_{qj} \left(\hat{a}_j^\dagger + \hat{a}_j \right) + \varphi_{qj} \left(\xi_j + \xi_j^* \right).$$

Here, we also omitted the terms $4E_C n_{qb}$ and $4E_C n_{qw}$ because we assume $E_C n_{qw}, E_C n_{qw} \ll E_J \varphi_{qq}^3$. As mentioned above, the four wave mixing process occurs due to the high nonlinearity of the Josephson inductance. Henceforth, the fourth order term of $\cos\left(\hat{\tilde{Q}}_q'\right) + \frac{1}{2}\hat{\tilde{Q}}_q'^2 \approx \frac{1}{24}\hat{\tilde{Q}}_q'^4$ is important. As derived in Appendix B.2, after neglecting terms with $\mathcal{O}(\varphi_{qb,qw}^3)$ and performing a rotating wave approximation, we arrive at

$$\begin{aligned}\frac{1}{24}\hat{\tilde{Q}}_q'^4 = &\varphi_{qb}^2 \frac{\varphi_{qq}^2}{2} \hat{a}_b^\dagger \hat{a}_b + \varphi_{qw}^2 \frac{\varphi_{qq}^2}{2} \hat{a}_w^\dagger \hat{a}_w + \frac{\varphi_{qq}^4}{2} \hat{a}_q^\dagger \hat{a}_q \\ &+ \frac{\varphi_{qq}^4}{4} \hat{a}_q^\dagger \hat{a}_q^\dagger \hat{a}_q \hat{a}_q + \varphi_{qb}^2 \varphi_{qq}^2 \hat{a}_q^\dagger \hat{a}_q \hat{a}_b^\dagger \hat{a}_b + \varphi_{qq}^2 \varphi_{qw}^2 \hat{a}_q^\dagger \hat{a}_q \hat{a}_w^\dagger \hat{a}_w \\ &+ \varphi_{qb}\varphi_{qq}\varphi_{qw}\varphi_{qp} \xi_p \left(\hat{a}_q \hat{a}_b^\dagger \hat{a}_w + \hat{a}_q^\dagger \hat{a}_b \hat{a}_w^\dagger \right)\end{aligned}$$

with $\varphi_{qp} \equiv (\varphi_{qq}\xi_q + \varphi_{qb}\xi_b + \varphi_{qw}\xi_w)/\xi_p$. Henceforth, in the rotating frame we arrive at

$$\begin{aligned}\hat{\mathcal{H}}_4'/\hbar \approx &\Delta_q \hat{a}_q^\dagger \hat{a}_q + \Delta_w \hat{a}_w^\dagger \hat{a}_w + \Delta_b \hat{a}_b^\dagger \hat{a}_b \\ &+ \frac{\chi_{qq}}{2} \hat{a}_q^\dagger \hat{a}_q^\dagger \hat{a}_q \hat{a}_q + \chi_{qw} \hat{a}_q^\dagger \hat{a}_q \hat{a}_w^\dagger \hat{a}_w + \chi_{qb} \hat{a}_q^\dagger \hat{a}_q \hat{a}_b^\dagger \hat{a}_b + g_4 \xi_p \left(\hat{a}_q^\dagger \hat{a}_w^\dagger \hat{a}_b + \hat{a}_q \hat{a}_w \hat{a}_b^\dagger \right) \\ &+ i\varepsilon_q(t) \left(\hat{a}_q^\dagger - \hat{a}_q \right) + i\varepsilon_w'(t) \left(\hat{a}_w^\dagger - \hat{a}_w \right) + i\varepsilon_b'(t) \left(\hat{a}_b^\dagger - \hat{a}_b \right),\end{aligned} \tag{2.96}$$

we have defined

$$\begin{aligned}&\Delta_j \equiv \omega_{m,j} - \omega_j', && g_4 \equiv -\frac{E_J}{\hbar} \varphi_{qb}\varphi_{qq}\varphi_{qw}\varphi_{qp}, \\ &\chi_{qq} \equiv -\frac{E_J}{\hbar}\frac{\varphi_{qq}^4}{2}, && \chi_{qw} \equiv -\frac{E_J}{\hbar} \varphi_{qq}^2 \varphi_{qw}^2, && \chi_{qb} \equiv -\frac{E_J}{\hbar} \varphi_{qq}^2 \varphi_{qb}^2,\end{aligned}$$

and for driving strength

$$\varepsilon'_w = \varepsilon_w n_{ww}, \qquad \varepsilon'_b = \varepsilon_b n_{bb}$$

For simplicity, we neglected terms with χ_{ww}, χ_{bb}.

2.5.3 Dissipation engineering for irreversible qubit-photon coupling

In this subsection, we follow [41], which derives the nonlinear decay by tracing out the waste modes with adiabatic elimination. After canceling out the ac-Stark terms and restrict the Hilbert space of the qubit mode to a two level system ($\hat{a}_q \to \hat{\sigma}$), we arrive at

$$\begin{aligned}
\hat{\mathcal{H}}''_4 =& \hat{\mathcal{H}}_w + \hat{\mathcal{H}}_{qb} \\
\hat{\mathcal{H}}_w/\hbar =& g_4 \xi_p \hat{a}_b \hat{a}_w^\dagger \hat{\sigma}^\dagger + g_4 \xi_p^* \hat{a}_b^\dagger \hat{a}_w \hat{\sigma} + \left(\Delta_w - \chi_{qw} \hat{\sigma}^\dagger \hat{\sigma}\right) \hat{a}_w^\dagger \hat{a}_w \\
\hat{\mathcal{H}}_{qb}/\hbar =& \chi_{qb} \hat{\sigma}^\dagger \hat{\sigma} \hat{a}_b^\dagger \hat{a}_b,
\end{aligned}$$

which dynamics is described by the Lindblad master equation

$$\begin{aligned}
\frac{\mathrm{d}}{\mathrm{d}t}\hat{\rho} =& -i\left[\hat{\mathcal{H}}''_4, \hat{\rho}\right] + \kappa_w \mathcal{D}[\hat{a}_w]\hat{\rho} + \kappa_b \mathcal{D}[\hat{a}_b]\hat{\rho} + \gamma_q \mathcal{D}[\hat{\sigma}]\hat{\rho} + \gamma_{q,\phi}\mathcal{D}[\hat{\sigma}^\dagger\hat{\sigma}]\hat{\rho} \\
=& -i\left[\hat{\mathcal{H}}_w, \hat{\rho}\right] + \kappa_w \mathcal{D}[\hat{a}_w]\hat{\rho} + \mathcal{L}_{qb}\left[\hat{\rho}\right]
\end{aligned} \tag{2.97}$$

where

$$\mathcal{L}_{qb}\left[\hat{\rho}\right] = -i\left[\hat{\mathcal{H}}_{qb}, \hat{\rho}\right] + \kappa_b \mathcal{D}[\hat{a}_b]\hat{\rho} + \gamma_q \mathcal{D}[\hat{\sigma}]\hat{\rho} + \gamma_{q,\phi}\mathcal{D}[\hat{\sigma}^\dagger\hat{\sigma}]\hat{\rho}.$$

Adiabatic elimination

For the adiabatic elimination of the waste mode, we assume that

$$\left|\frac{g_4\xi_p}{\kappa_w}\right|, \left|\frac{\chi_{jj'}}{\kappa_w}\right| \sim \delta \ll 1,$$

such that the waste mode is dominantly in the vacuum state due to the fast decay rate κ_w. Hence, we can reduce the Hilbert space of the waste mode to $\mathcal{H}_w = \mathrm{span}\left(|0_w\rangle, |1_w\rangle\right)$. In particular, for the density matrix $\hat{\rho} \in \mathcal{H}_q \otimes \mathcal{H}_b \otimes \mathcal{H}_w$, the reduced density matrices acting on the qubit and buffer Hilbert space we have the following relations

$$\langle 0_w|\,\hat{\rho}\,|0_w\rangle = \hat{\rho}_{00}, \qquad \langle 0_w|\,\hat{\rho}\,|1_w\rangle = \delta\hat{\rho}_{01}, \qquad \langle 1_w|\,\hat{\rho}\,|1_w\rangle = \delta^2\hat{\rho}_{11}, \qquad \langle 0_w|\,\hat{\rho}\,|2_w\rangle = \delta^2\hat{\rho}_{02}$$

with $|j_w\rangle, |j'_w\rangle$ being the Fock basis of the waste mode. Note that $\hat{\rho}_{00} \in \mathcal{H}_q \otimes \mathcal{H}_b$. By projecting Eq. (2.97) with $\langle 0_w| \dots |0_w\rangle, \langle 0_w| \dots |1_w\rangle, \langle 1_w| \dots |1_w\rangle$, respectively, we obtain

$$\begin{aligned}
\frac{\mathrm{d}}{\mathrm{d}t}\hat{\rho}_{00} =& - i \langle 0_w| \left[g_4 \xi_p \hat{a}_b \hat{a}_w^\dagger \hat{\sigma}^\dagger + g_4 \xi_p^* \hat{a}_b^\dagger \hat{a}_w \sigma + \left(\Delta_w - \chi_{qw} \sigma^\dagger \sigma \right) \hat{a}_w^\dagger \hat{a}_w, \hat{\rho} \right] |0_w\rangle \\
&+ \langle 0_w| \kappa_w \mathcal{D}[\hat{a}_w] \hat{\rho} |0_w\rangle + \mathcal{L}_{qb}\left[\hat{\rho}_{00}\right] \\
=& - i\delta \left[g_4 \xi_p^* \hat{a}_b^\dagger \hat{\sigma} \hat{\rho}_{10} - g_4 \xi_p \hat{\rho}_{01} \hat{a}_b \hat{\sigma}^\dagger \right] + \delta^2 \kappa_w \hat{\rho}_{11} + \mathcal{L}_{qb}\left[\hat{\rho}_{00}\right] + \mathcal{O}\left(\delta^3\right) \qquad (2.98) \\
\delta \frac{\mathrm{d}}{\mathrm{d}t}\hat{\rho}_{01} =& - i\delta^2 \left[g_4 \xi_p^* \hat{a}_b^\dagger \hat{\sigma} \hat{\rho}_{11} - g_4 \xi_p \hat{\rho}_{02} \hat{a}_b \hat{\sigma}^\dagger \right] + i \hat{\rho}_{00} \left[g_4 \xi_p^* \hat{a}_b^\dagger \hat{\sigma} \right] + i\delta \hat{\rho}_{01} \left[\Delta_w - \chi_{qw} \hat{\sigma}^\dagger \hat{\sigma} \right] \\
&- \delta \frac{\kappa_w}{2} \hat{\rho}_{01} + \delta \mathcal{L}_{qb}\left[\hat{\rho}_{01}\right] + \mathcal{O}\left(\delta^3\right) \\
\overset{\delta \sim g_4 \xi_p / \kappa_w}{=}& i \hat{\rho}_{00} \left[g_4 \xi_p^* \hat{a}_b^\dagger \hat{\sigma} \right] + i\delta \hat{\rho}_{01} \left[\Delta_w - \chi_{qw} \hat{\sigma}^\dagger \hat{\sigma} \right] - \delta \frac{\kappa_w}{2} \hat{\rho}_{01} + \delta \mathcal{L}_{qb}\left[\hat{\rho}_{01}\right] + \mathcal{O}\left(\delta^3\right) \qquad (2.99) \\
\delta^2 \frac{\mathrm{d}}{\mathrm{d}t}\hat{\rho}_{11} =& - i\delta^3 \left[g_4 \xi_p^* \hat{a}_b^\dagger \hat{\sigma} \hat{\rho}_{21} - g_4 \xi_p \hat{\rho}_{12} \hat{a}_b \hat{\sigma}^\dagger \right] - i\delta \left[g_4 \xi_p \hat{a}_b \hat{\sigma}^\dagger \hat{\rho}_{01} - g_4 \xi_p^* \hat{\rho}_{10} \hat{a}_b^\dagger \hat{\sigma} \right] \\
&+ i\delta^2 \left[\Delta_w - \chi_{qw} \hat{\sigma}^\dagger \hat{\sigma}, \hat{\rho}_{11} \right] \\
&+ \delta^2 \kappa_w \left(\underbrace{\hat{\rho}_{02}}_{|2\rangle \notin \mathcal{H}_w} - \hat{\rho}_{11} \right) + \delta^2 \mathcal{L}_{qb}\left[\hat{\rho}_{11}\right] + \mathcal{O}\left(\delta^3\right) \\
=& - i\delta \left[g_4 \xi_p \hat{a}_b \hat{\sigma}^\dagger \hat{\rho}_{01} - g_4 \xi_p^* \hat{\rho}_{10} \hat{a}_b^\dagger \hat{\sigma} \right] + i\delta^2 \left[\Delta_{bwq} - \chi_{qw} \hat{\sigma}^\dagger \hat{\sigma}, \hat{\rho}_{11} \right] \\
&- \delta^2 \kappa_w \hat{\rho}_{11} + \delta^2 \mathcal{L}_{qb}\left[\hat{\rho}_{11}\right] + \mathcal{O}\left(\delta^3\right) \qquad (2.100)
\end{aligned}$$

Focusing the relevant dynamics, we find that Eqs. (2.99) and (2.100) include a damping term of order δ^0, while all terms in Eq. (2.98) are of order δ^2. Hence, this allows us to treat $\hat{\rho}_{01}$ and $\hat{\rho}_{11}$ as a steady state (adiabatic approximation), which results to

$$\begin{aligned}
\hat{\rho}_{01} =& i \hat{\rho}_{00} \left[g_4 \xi_p^* \hat{a}_b^\dagger \hat{\sigma} \right] \left[\delta \left(\frac{\kappa_w}{2} - i \left(\Delta_w - \chi_{qw} \hat{\sigma}^\dagger \hat{\sigma} \right) \right) \right]^{-1} \\
\approx& \hat{\rho}_{00} \frac{i g_4 \xi_p^* / \delta}{\frac{\kappa_w}{2} - i \left(\Delta_w - \chi_{qw} \right)} \hat{a}_b^\dagger \hat{\sigma}, \qquad (2.101)
\end{aligned}$$

where we used $\hat{a}_b^\dagger \hat{\sigma} \hat{\sigma}^\dagger \hat{\sigma} = \hat{a}_b^\dagger \sigma$. As for the steady state solution for $\hat{\rho}_{11}$, we get

$$\hat{\rho}_{11} = \frac{1}{\left(\frac{\kappa_w}{2}\right)^2 + \left(\Delta_w - \chi_{qw} \right)^2} \frac{\left| g_4 \xi_p \right|^2}{\delta^2} \hat{a}_b \hat{\sigma}^\dagger \hat{\rho}_{00} \hat{a}_b^\dagger \hat{\sigma}. \qquad (2.102)$$

Inserting the steady state solutions into Eq. (2.98), we obtain

$$\begin{aligned}
\frac{\mathrm{d}}{\mathrm{d}t}\hat{\rho}_{00} =& - i \left[\frac{-i \left| g_4 \xi_p \right|^2}{\frac{\kappa_w}{2} + i \left(\Delta_w - \chi_{qw} \right)} \hat{a}_b^\dagger \hat{a}_b \hat{\sigma} \hat{\sigma}^\dagger \hat{\rho}_{00} - \frac{i \left| g_4 \xi_p \right|^2}{\frac{\kappa_w}{2} - i \left(\Delta_w - \chi_{qw} \right)} \hat{\rho}_{00} \hat{a}_b^\dagger \hat{a}_b \hat{\sigma} \hat{\sigma}^\dagger \right] \\
&+ \frac{\left| g_4 \xi_p \right|^2}{\left(\frac{\kappa_w}{2}\right)^2 + \left(\Delta_w - \chi_{qw} \right)^2} \hat{a}_b \hat{\sigma}^\dagger \hat{\rho}_{00} \hat{a}_b^\dagger \hat{\sigma} \\
&+ \mathcal{L}_{qb}\left[\hat{\rho}_{00}\right] \\
=& i \left[\frac{\left| g_4 \xi_p \right|^2}{\left(\frac{\kappa_w}{2}\right)^2 + \left(\Delta_w - \chi_{qw} \right)^2} \left(\Delta_w - \chi_{qw} \right) \hat{a}_b^\dagger \hat{a}_b \hat{\sigma} \hat{\sigma}^\dagger, \hat{\rho}_{00} \right] \\
&+ \kappa_{\mathrm{nl}} \mathcal{D}\left[\hat{a}_b \hat{\sigma}^\dagger \right] \hat{\rho}_{00} + \mathcal{L}_{qb}\left[\hat{\rho}_{00}\right] \qquad (2.103)
\end{aligned}$$

with the nonlinear decay rates $\hat{L}_{\mathrm{nl}} = \sqrt{\kappa_{\mathrm{nl}}}\hat{a}_b\hat{\sigma}^\dagger$

$$\kappa_{\mathrm{nl}} \equiv \frac{|g_4\xi_p|^2}{\left(\frac{\kappa_w}{2}\right)^2 + (\Delta_w - \chi_{qw})^2}\kappa_w \overset{\Delta_w=\chi_{qw}}{=} \frac{4\,|g_4\xi_p|^2}{\kappa_w}. \tag{2.104}$$

Qubit evolution

The dynamics describing the transfer of quantum information to the buffer mode is derived. We add the driving term $i\sqrt{\kappa_b}b_{\mathrm{in}}\left(\hat{a}_b - \hat{a}_b^\dagger\right)$ into the master equation (Eq. (2.103)), where b_{in} is the amplitude of the coherent drive. For simplicity, we set $\Delta_w = \chi_{qw}$ in Eq. (2.103) and assume $\hat{\mathcal{H}}_{qb}/\hbar, \gamma_q, \gamma_{q,\phi} \ll \kappa_w$ in the zeroth order approximation. This gives us

$$\frac{\mathrm{d}}{\mathrm{d}t}\hat{\rho}_{00} = \kappa_{\mathrm{nl}}\mathcal{D}\left[\hat{a}_b\hat{\sigma}^\dagger\right]\hat{\rho}_{00} + \kappa_b\mathcal{D}\left[\hat{a}_b\right]\hat{\rho}_{00} + \varepsilon_b'\left[\hat{a}_b - \hat{a}_b^\dagger, \hat{\rho}_{00}\right] \tag{2.105}$$

with $\varepsilon_b' = \sqrt{\kappa_b}b_{\mathrm{in}}$. Since the time evolution of the buffer mode is dependent on the qubit state, we first consider $\hat{\rho}_g \equiv \langle g|\,\hat{\rho}_{00}\,|g\rangle$ and $\hat{\rho}_e \equiv \langle e|\,\hat{\rho}_{00}\,|e\rangle$, such that

$$\frac{\mathrm{d}}{\mathrm{d}t}\hat{\rho}_g = -\frac{1}{2}\kappa_{\mathrm{nl}}\left(\hat{\rho}_g\hat{a}_b\hat{a}_b^\dagger + \hat{a}_b\hat{a}_b^\dagger\hat{\rho}_g\right) + \kappa_b\mathcal{D}\left[\hat{a}_b\right]\hat{\rho}_g + \varepsilon_b'\left[\hat{a}_b - \hat{a}_b^\dagger, \hat{\rho}_g\right], \tag{2.106a}$$

$$\frac{\mathrm{d}}{\mathrm{d}t}\hat{\rho}_e = \kappa_{\mathrm{nl}}\hat{a}_b\hat{\rho}_g\hat{a}_b^\dagger + \kappa_b\mathcal{D}\left[\hat{a}_b\right]\hat{\rho}_e + \varepsilon_b'\left[\hat{a}_b - \hat{a}_b^\dagger, \hat{\rho}_e\right]. \tag{2.106b}$$

In our case, since the applied buffer tone is a coherent tone, we can safely assume that the buffer is in a coherent state $|\beta\rangle$ with the dimensionless amplitude[15] $\beta = -2\varepsilon_b'/(\kappa_{\mathrm{nl}} + \kappa_b)$. That is, $\hat{\rho}_{g/e} \propto |\beta\rangle\langle\beta|$. We can now calculate the qubit ground and excited state probability by tracing them, $p_{g/e} = \mathrm{Tr}(\hat{\rho}_{g/e})$. This leads us to formulate

$$\frac{\mathrm{d}}{\mathrm{d}t}p_g = -\kappa_{\mathrm{nl}}\,|\beta|^2\,p_g, \tag{2.107a}$$

$$\frac{\mathrm{d}}{\mathrm{d}t}p_e = \kappa_{\mathrm{nl}}\,|\beta|^2\,p_g. \tag{2.107b}$$

Assuming the qubit is in the ground state for $t = 0$, we obtain

$$p_e(t) = 1 - \exp\left(-\frac{4\varepsilon_b'^2\kappa_{\mathrm{nl}}}{(\kappa_{\mathrm{nl}} + \kappa_b)^2}t\right) = 1 - \exp\left(-\eta_c\,|b_{\mathrm{in}}|^2\,t\right) \tag{2.108}$$

with the conversion efficiency

$$\eta_c := \frac{4\kappa_b\kappa_{\mathrm{nl}}}{(\kappa_{\mathrm{nl}} + \kappa_b)^2}. \tag{2.109}$$

2.5.4 Limitation

Influence of qubit decoherence rate

In our previous discussions, the effects of qubit decoherence on its temporal evolution have not been taken into account. To address this issue, we delve into the impact of qubit decoherence on its dynamics. Notably, it becomes evident that the qubit population never reaches unity. This is a direct implication of the fact that qubit decoherence inherently reduces the detection efficiency in single-photon detection scenarios.

[15] The amplitude can be calculated for steady state using $\hat{L}_{\mathrm{nl}}$ and $\hat{L}_{b,c/i} = \sqrt{\kappa_{b,c/i}}\hat{a}_b$ as the loss operators.

The qubit decoherence term is added to the master equation in Eq. (2.105), such that we obtain

$$\frac{\mathrm{d}}{\mathrm{d}t}\hat{\rho}_{00} = \kappa_{\mathrm{nl}}\mathcal{D}\left[\hat{a}_b\hat{\sigma}^\dagger\right]\hat{\rho}_{00} + \kappa_b\mathcal{D}\left[\hat{a}_b\right]\hat{\rho}_{00} + \varepsilon_b'\left[\hat{a}_b - \hat{a}_b^\dagger, \hat{\rho}_{00}\right] + \gamma_q\mathcal{D}\left[\hat{\sigma}\right]\hat{\rho}_{00}. \tag{2.110}$$

After following the same procedure as in the previous subsection, the differential equation is formulated as

$$\frac{\mathrm{d}}{\mathrm{d}t}\begin{bmatrix} p_g \\ p_e \end{bmatrix} = \begin{bmatrix} -\eta_c\left|b_{\mathrm{in}}\right|^2 & \gamma_q \\ \eta_c\left|b_{\mathrm{in}}\right|^2 & -\gamma_q \end{bmatrix}\begin{bmatrix} p_g \\ p_e \end{bmatrix}, \tag{2.111}$$

which solution gives

$$\begin{bmatrix} p_g(t) \\ p_e(t) \end{bmatrix} = \begin{bmatrix} \frac{\eta_c|b_{\mathrm{in}}|^2}{\eta_c|b_{\mathrm{in}}|^2+\gamma_q}e^{-\eta_c|b_{\mathrm{in}}|^2t-\gamma_q t} + \frac{\gamma_q}{\eta_c|b_{\mathrm{in}}|^2+\gamma_q} & \frac{\gamma_q}{\eta_c|b_{\mathrm{in}}|^2+\gamma_q}\left(1-e^{-\eta_c|b_{\mathrm{in}}|^2t-\gamma_q t}\right) \\ \frac{\eta_c|b_{\mathrm{in}}|^2}{\eta_c|b_{\mathrm{in}}|^2+\gamma_q}\left(1-e^{-\eta_c|b_{\mathrm{in}}|^2t-\gamma_q t}\right) & \frac{\eta_c|b_{\mathrm{in}}|^2}{\eta_c|b_{\mathrm{in}}|^2+\gamma_q} + \frac{\gamma_q}{\eta_c|b_{\mathrm{in}}|^2+\gamma_q}e^{-\eta_c|b_{\mathrm{in}}|^2t-\gamma_q t} \end{bmatrix}\begin{bmatrix} p_g(0) \\ p_e(0) \end{bmatrix}. \tag{2.112}$$

We find the excitation probability of the transmon qubit for sufficiently long time t as

$$p_e(t\to\infty) = \frac{\eta_c\left|b_{\mathrm{in}}\right|^2}{\eta_c\left|b_{\mathrm{in}}\right|^2+\gamma_q} < 1. \tag{2.113}$$

It is noteworthy that the saturation level of the qubit population establishes a relative dependency on the qubit energy relaxation rate γ_q, and the "effective buffer photon conversion rate" $\eta_c\left|b_{\mathrm{in}}\right|^2$. Particularly, the impact of the energy relaxation rate becomes significant when the value of $\eta_c\left|b_{\mathrm{in}}\right|^2$ is comparably small. This observation underscores an interplay or a steady-state dynamics between the information gain from the incoming buffer photon flux and information loss into the environment. In other words, while the qubit becomes excited due to photon conversion, it concurrently relaxes back into its surrounding bath.

Influence of residual waste photon number

In our prior discussions, we assumed that our quantum system experienced only vacuum noise, excluding the influence of the coherent drive (refer to Sec. 2.4). This is a standard assumption, primarily justified by the extremely low temperatures of dilution refrigerators, typically in the range of $10-50\,\mathrm{mK}$. Nevertheless, heating due to strong system pumping and microwave noise from the input lines can increase the waste photon number [103, 152, 153]. This is particularly relevant in our case: the presence of a residual waste photon number can influence the detection efficiency. This is attributed to the fact that the reversal process ($\hat{a}_b^\dagger\hat{a}_w\hat{\sigma}$) has a finite probability. Given this potential complication, it is imperative to thoroughly examine how the residual waste photon number impacts the qubit's temporal evolution.

We model the residual waste photon number as arising from a thermal bath. According to Eq. (2.32),

the Eqs. (2.98), (2.99) and (2.100) are modified to

$$\begin{aligned}\frac{\mathrm{d}}{\mathrm{d}t}\hat{\rho}_{00} =& - i \langle 0_w| \left[g_4 \xi_p \hat{a}_b \hat{a}_w^\dagger \hat{\sigma}^\dagger + g_4 \xi_p^* \hat{a}_b^\dagger \hat{a}_w \sigma, \hat{\rho} \right] |0_w\rangle \\ &+ \langle 0_w| \left(\kappa_w \left(1 + n_{\mathrm{th},w}\right) \mathcal{D}[\hat{a}_w]\hat{\rho} + \kappa_w n_{\mathrm{th},w} \mathcal{D}[\hat{a}_w^\dagger]\hat{\rho} \right) |0_w\rangle + \mathcal{L}_{qb}\left[\hat{\rho}_{00}\right] \\ =& - i\delta \left[g_4 \xi_p^* \hat{a}_b^\dagger \hat{\sigma} \hat{\rho}_{10} - g_4 \xi_p \hat{\rho}_{01} \hat{a}_b \hat{\sigma}^\dagger \right] + \delta^2 \kappa_w \left(1 + n_{\mathrm{th},w}\right) \hat{\rho}_{11} - \kappa_w n_{\mathrm{th},w} \hat{\rho}_{00} + \mathcal{L}_{qb}\left[\hat{\rho}_{00}\right] + \mathcal{O}\left(\delta^3\right)\end{aligned} \tag{2.114}$$

$$\begin{aligned}\delta \frac{\mathrm{d}}{\mathrm{d}t}\hat{\rho}_{01} =& - i\delta^2 \left[g_4 \xi_p^* \hat{a}_b^\dagger \hat{\sigma} \hat{\rho}_{11} - g_4 \xi_p \hat{\rho}_{02} \hat{a}_b \hat{\sigma}^\dagger \right] + i\hat{\rho}_{00} \left[g_4 \xi_p^* \hat{a}_b^\dagger \hat{\sigma} \right] \\ &+ \langle 0_w| \left(\kappa_w \left(1 + n_{\mathrm{th},w}\right) \mathcal{D}[\hat{a}_w]\hat{\rho} + \kappa_w n_{\mathrm{th},w} \mathcal{D}[\hat{a}_w^\dagger]\hat{\rho} \right) |1_w\rangle + \delta \mathcal{L}_{qb}\left[\hat{\rho}_{01}\right] + \mathcal{O}\left(\delta^3\right) \\ =& i\hat{\rho}_{00} \left[g_4 \xi_p^* \hat{a}_b^\dagger \hat{\sigma} \right] - \delta \frac{\kappa_w \left(1 + 4n_{\mathrm{th},w}\right)}{2} \hat{\rho}_{01} + \delta \mathcal{L}_{qb}\left[\hat{\rho}_{01}\right] + \mathcal{O}\left(\delta^3\right)\end{aligned} \tag{2.115}$$

$$\begin{aligned}\delta^2 \frac{\mathrm{d}}{\mathrm{d}t}\hat{\rho}_{11} =& - i\delta^3 \left[g_4 \xi_p^* \hat{a}_b^\dagger \hat{\sigma} \hat{\rho}_{21} - g_4 \xi_p \hat{\rho}_{12} \hat{a}_b \hat{\sigma}^\dagger \right] - i\delta \left[g_4 \xi_p \hat{a}_b \hat{\sigma}^\dagger \hat{\rho}_{01} - g_4 \xi_p^* \hat{\rho}_{10} \hat{a}_b^\dagger \hat{\sigma} \right] \\ &+ \langle 1_w| \left(\kappa_w \left(1 + n_{\mathrm{th},w}\right) \mathcal{D}[\hat{a}_w]\hat{\rho} + \kappa_w n_{\mathrm{th},w} \mathcal{D}[\hat{a}_w^\dagger]\hat{\rho} \right) |1_w\rangle + \delta^2 \mathcal{L}_{qb}\left[\hat{\rho}_{11}\right] + \mathcal{O}\left(\delta^3\right) \\ =& - i\delta \left[g_4 \xi_p \hat{a}_b \hat{\sigma}^\dagger \hat{\rho}_{01} - g_4 \xi_p^* \hat{\rho}_{10} \hat{a}_b^\dagger \hat{\sigma} \right] \\ &- \delta^2 \kappa_w \left(1 + 3n_{\mathrm{th},w}\right) \hat{\rho}_{11} + n_{\mathrm{th},w} \hat{\rho}_{00} + \delta^2 \mathcal{L}_{qb}\left[\hat{\rho}_{11}\right] + \mathcal{O}\left(\delta^3\right)\end{aligned} \tag{2.116}$$

Here, we set $\Delta_w = \chi_{qw}$ for simplicity. With the same argument as in Subsec. 2.5.3, we can find the steady state solutions for $\hat{\rho}_{01}$ and $\hat{\rho}_{11}$

$$\begin{aligned}\hat{\rho}_{01} \approx& \hat{\rho}_{00} \frac{2ig_4 \xi_p^*}{\delta \kappa_w (1 + 4n_{\mathrm{th},w})} \hat{a}_b^\dagger \hat{\sigma} \\ \hat{\rho}_{11} \approx& \frac{1}{\delta^2 \kappa_w \left(1 + 3n_{\mathrm{th},w}\right)} \left[\frac{4\left|g_4 \xi_p\right|^2}{\kappa_w (1 + 4n_{\mathrm{th},w})} \hat{a}_b \hat{\sigma}^\dagger \hat{\rho}_{00} \hat{a}_b^\dagger \hat{\sigma} + \kappa_w n_{\mathrm{th},w} \hat{\rho}_{00} \right]\end{aligned}$$

and insert them into

$$\begin{aligned}\frac{\mathrm{d}}{\mathrm{d}t}\hat{\rho}_{00} =& - \frac{2\left|g_4 \xi_p\right|^2}{\kappa_w (1 + 4n_{\mathrm{th},w})} \left[\hat{a}_b^\dagger \hat{a}_b \hat{\sigma} \hat{\sigma}^\dagger \hat{\rho}_{00} + \hat{\rho}_{00} \hat{a}_b^\dagger \hat{a}_b \hat{\sigma} \hat{\sigma}^\dagger \right] \\ &+ \frac{1 + n_{\mathrm{th},w}}{1 + 3n_{\mathrm{th},w}} \left[\frac{4\left|g_4 \xi_p\right|^2}{\kappa_w (1 + 4n_{\mathrm{th},w})} \hat{a}_b \hat{\sigma}^\dagger \hat{\rho}_{00} \hat{a}_b^\dagger \hat{\sigma} + \kappa_w n_{\mathrm{th},w} \hat{\rho}_{00} \right] - \kappa_w n_{\mathrm{th},w} \hat{\rho}_{00} + \mathcal{L}_{qb}\left[\hat{\rho}_{00}\right] + \mathcal{O}\left(\delta^3\right) \\ \approx& \kappa_{\mathrm{nl}} \left(1 - 4n_{\mathrm{th},w}\right) \mathcal{D}[\hat{a}_b \hat{\sigma}^\dagger]\hat{\rho}_{00} - 2\kappa_{\mathrm{nl}} n_{\mathrm{th},w} \hat{a}_b \hat{\sigma}^\dagger \hat{\rho}_{00} \hat{a}_b^\dagger \hat{\sigma} + \mathcal{L}_{qb}\left[\hat{\rho}_{00}\right] + \mathcal{O}\left(\delta^3, n_{\mathrm{th},w}^2\right).\end{aligned} \tag{2.117}$$

Eq. (2.105) can therefore be rewritten as

$$\frac{\mathrm{d}}{\mathrm{d}t}\hat{\rho}_{00} = \kappa_{\mathrm{nl}} \left(1 - 4n_{\mathrm{th},w}\right) \mathcal{D}\left[\hat{a}_b \hat{\sigma}^\dagger\right] \hat{\rho}_{00} - 2\kappa_{\mathrm{nl}} n_{\mathrm{th},w} \hat{a}_b \hat{\sigma}^\dagger \hat{\rho}_{00} \hat{a}_b^\dagger \hat{\sigma} + \kappa_b \mathcal{D}\left[\hat{a}_b\right] \hat{\rho}_{00} + \varepsilon_b' \left[\hat{a}_b - \hat{a}_b^\dagger, \hat{\rho}_{00} \right], \tag{2.118}$$

which results to

$$\frac{\mathrm{d}}{\mathrm{d}t} p_g = - \kappa_{\mathrm{nl}} \left(1 - 4n_{\mathrm{th},w}\right) \left|\beta'\right|^2 p_g, \tag{2.119a}$$

$$\frac{\mathrm{d}}{\mathrm{d}t} p_e = \kappa_{\mathrm{nl}} \left(1 - 6n_{\mathrm{th},w}\right) \left|\beta'\right|^2 p_g \tag{2.119b}$$

with

$$\beta' = - \frac{2\varepsilon_b'}{\kappa_{\mathrm{nl}} \left(1 - 4n_{\mathrm{th},w}\right) + \kappa_b}.$$

Finally, we obtain the qubit evolution

$$p_e(t) = \frac{1 - 6n_{\mathrm{th},w}}{1 - 4n_{\mathrm{th},w}} \left(1 - \exp\left(-\eta_c' \left|b_{\mathrm{in}}\right|^2 t\right)\right) \tag{2.120}$$

with the modified conversion efficiency

$$\eta_c' := \frac{4\kappa_b \kappa_{\mathrm{nl}} \left(1 - 4n_{\mathrm{th},w}\right)}{\left(\kappa_{\mathrm{nl}} \left(1 - 4n_{\mathrm{th},w}\right) + \kappa_b\right)^2}. \tag{2.121}$$

We clearly see that the qubit population is limited by the waste photon number $n_{\mathrm{th},w}$ and can never reach unity. For example, if we have $n_{\mathrm{th},w} = 0.05$ corresponding to an effective temperature of 120 mK, we obtain $p_e(t \to \infty) = n_q^* = 0.875$.

2.6 Quantum-to-classical phase transition of a transmon system

In the previous sections, we have discussed an open and interacting quantum system. In both scenarios, the system is treated quantum mechanically or semi-classically, where for example the resonator is treated in classical means (see e.g. the qubit driving in Sec. 2.5). In other words, the full classical treatment fails to correctly describe its underlying physics. However, in some extreme scenarios, such as extremely strong driving of the quantum system, the behavior of such system can be well described classically.

A good example is the Josephson circuit. As the Josephson potential is a cosine potential, its classical analogue is often represented by a pendulum, where the deviation angle from the equilibrium position corresponds to the phase difference across the Josephson junction [90, 189]. For a weak drive, the pendulum acquires some kinetic energy and starts to oscillate around the equilibrium. This oscillation is described differently in a the quantum and classical treatment: In the quantum mechanical treatment, the energy is quantized and the system can only acquire discrete energies. In the first-order approximation such system is known as the simple quantum harmonic oscillator (see App. A). In the classical description, any energy is allowed, thus it fails to "reproduce" the discretization of the energy levels. In contrast, for a strong drive, it acquires sufficient energy to escape from its trapping potential well and rotates indefinitely. That is, the phase particle behaves as a free particle and the energy quantization is not existent. In other words, the classical treatment is possible.

One may then think, where is the threshold between quantum and classical? Is it a smooth transition or not? In the transmon case, we actually can observe a quantum-to-classical phase transition [75–77]. That is, there exists a threshold power, where the behavior of the system suddenly changes. This phenomenon is also known under various names such as transmon ionization [73, 74], first-order dissipative phase transition [78–81, 190, 191], chaotic regime [74, 82], and breakdown of photon-blockade [77, 78].

In this section, we briefly introduce various tools and representation, such as Rényi entropy, second-order correlation function, Floquet theory, and Husimi Q functions, which are employed to indicate potential phase transitions. Lastly, we first discuss the quantum Duffing oscillator, which is an approximation of a transmon qubit up to its anharmonicity, with focus on the first-order dissipative (quantum-to-classical) phase transition and expand it to the discussion for the transmon.

2.6.1 Rényi entropy, correlation function, Husimi Q distribution, Floquet theory

Rényi entropy

Here, we briefly discuss the Rényi entropy based on the papers [192, 193]. As we will see later, the focus of the discussion lies on the measure of the purity of the quantum system and quantum phase transition.

The Rényi entropy is a term coming from the information theory and is a generalization of various entropy notions such as Shannon entropy[16] (von Neumann entropy in the quantum context[17]) and collision entropy. It finds many applications in the context of phase transition in quantum information theory and quantum computing [194], quantum communication [195], condensed matter physics [196] and also holography in quantum gravity [193, 197]. This quantity is defined as

$$S_\alpha = \frac{1}{1-\alpha} \log \mathrm{Tr} \hat{\rho}^\alpha, \tag{2.122}$$

where α is an order parameter. We emphasize that for $\alpha = 1$ we obtain the von Neumann entropy, $S_\mathrm{N} = -\mathrm{Tr}\hat{\rho} \log \hat{\rho}$. The advantage of the Rényi entropy compared to the von Neumann entropy is the simple calculation as the computation of $\log \hat{\rho}$ is a hard task [193]. For the special case of $\alpha = 2$,

$$S_2 = -\log \mathrm{Tr}\hat{\rho}^2 = -\log P, \tag{2.123}$$

we observe that S_2 measures the purity of a quantum system, $P = \mathrm{Tr}\hat{\rho}^2$, in a logarithmic scale. For a completely mixed state, the Rényi entropy approaches the limit $-\log(1/d_q)$, where d_q represents the dimensionality of the associated Hilbert space. The proof that the completely mixed state is an equiprobable probability distribution of the state can be shown by using the Cauchy-Schwarz inequality

$$\frac{1}{d_q^2} = \left(\frac{1}{d_q} \sum_k p_k \right)^2 \leq \frac{1}{d_q} \sum_k p_k^2$$

for the density matrix $\hat{\rho} = \sum_k p_k |k\rangle \langle k|$ with $\sum_k p_k = 1$. The equality holds only for $p_k = 1/d_q$. Hence, the minimum of the purity is $\min P = \min \sum_k p_k^2 = 1/d_q$. Therefore, the entropy is always upper-bounded by $S_2 \leq -\log(1/d_q)$. In the context of quantum-to-classical phase transition, this method is especially suited to clarify the phase transition to the classical state: According to [73], the transmon ionization is associated with a sharp drop in the purity. That is, a sudden transition to a (mostly) completely mixed state.

Second-order correlation function

Here, the second-order correlation function is briefly introduced based on the books [85, 182].

The second-order correlation function is an important concept used to understand and describe the statistical properties of the quantum state. It is defined as

$$g^{(2)}(0) = \frac{\langle \hat{a}_q^\dagger \hat{a}_q^\dagger \hat{a}_q \hat{a}_q \rangle}{\langle \hat{a}_q^\dagger \hat{a}_q \rangle^2} \tag{2.124}$$

[16] The Shannon entropy has been introduced as a classical quantity in the context of information theory.

[17] The von Neumann entropy is an extension of the concept of Gibbs entropy from classical statistical mechanics to quantum statistical mechanics.

for $t = 0$. In the context of quantum optics, it is a measure of detecting two photons at the same time. This function helps us to understand the nature of light. For example, for a perfectly coherent state, we obtain $g^{(2)}(0) = 1$, and for any other type of classical light we always have a greater value than unity. In contrast, if we measure $g^{(2)}(0) < 1$, it is a signature of non-classical nature of light such as photon anti-bunching and quantum entanglement.

Husimi Q distribution

Here, the Husimi Q distribution is briefly introduced based on the book [85].

The Husimi Q function is a quasi-probability distribution over a phase-space, usually applied to represent the density matrix $\hat{\rho}$ of the electromagnetic fields[18]. It is used to describe the states in quantum mechanics, where the usual concept of probability distribution is not applicable due to the Heisenberg uncertainty principle. The Husmi Q distribution is defined on the coherent state basis $|\alpha\rangle$, where $\alpha = \mathrm{Re}(\alpha) + i\mathrm{Im}(\alpha)$ corresponds to a point in the phase space

$$Q(\alpha) = \frac{\langle\alpha|\hat{\rho}|\alpha\rangle}{\pi} \geq 0. \tag{2.125}$$

The advantage of this representation is the non-negativity without any singularity as opposed to the Glauber-Sudarshan P representation, while its relatively large uncertainty makes it hard to distinguish e.g. between a vacuum state from a thermal state as opposed to a Wigner representation. Nevertheless, in the case of the quantum Duffing oscillator and related study, the Husimi Q distribution is a widely used method to visualize its quantum state [74, 78, 79, 82, 190, 198, 199]. As this topic will be covered later in more detail, the existence of two metastable states of the Duffing oscillator in its bistable regime can be well observed in the phase space [78, 79, 81, 86, 191].

Floquet theory

Here, we briefly delve into the Floquet theory, drawing predominantly from [200–203]. Floquet theory offers a comprehensive framework for understanding periodic systems.

Floquet theory plays a crucial role in analyzing quantum systems characterized by periodic dynamics. This periodicity in the Hamiltonian often arises due to various factors, such as crystal potentials, a concept well-articulated in condensed matter physics through Bloch's theorem, or due to externally applied time-periodic potentials.

The essence of Floquet theory lies in its ability to render time-dependent problems in a rotating frame tractable, leveraging the inherent periodicity of the Hamiltonian. Specifically, the theory aids in decomposing the dynamics into two distinct categories: the fast dynamics within a single period T of the Hamiltonian and the slower dynamics that evolve from one period to the next. This separation is crucial for understanding and predicting the system's behavior over time. An especially valuable application of Floquet theory is in examining the effects of rapid rotational terms in the Hamiltonian. While these terms are often neglected in the rotating wave approximation, especially in weakly driven systems, they become critically significant in scenarios involving strong driving forces. This significance is exemplified in the phenomenon known as the Bloch-Siegert shift, where the strong drive alters the resonance conditions of the system. The Bloch-Siegert shift is typically analyzed using a frequency expansion method, which provides insights into the impact of these otherwise disregarded terms.

[18]The Husimi Q representation is one of several phase space distributions. Others include Glauber-Sudarshan P representation and Wigner representation.

Here, we focus on the time-periodic problem. Beginning with the time-dependent Schrödinger equation, our wave function is described as

$$i\hbar\frac{\mathrm{d}}{\mathrm{d}t}\left|\psi(t)\right\rangle = \hat{\mathcal{H}}(t)\left|\psi(t)\right\rangle$$

with $\hat{\mathcal{H}}(t) = \hat{\mathcal{H}}(t+T)$. Its dynamics is captured by the unitary time-evolution operator $\hat{U}\left(t, t_0\right)$

$$\left|\psi(t)\right\rangle = \hat{U}\left(t, t_0\right)\left|\psi(t_0)\right\rangle,$$

which is in general a complicated time-ordered exponential. As we are considering a time-periodic Hamiltonian, the important feature of the Floquet theory can be well found in the one-period evolution Floquet operator

$$\hat{F}_0 \equiv \hat{U}\left(t_0+T, t_0\right) = e^{-i\hat{\mathcal{H}}_F T/\hbar}, \tag{2.126}$$

where $\hat{\mathcal{H}}_F$ is the Hermitian operator. That is, the eigensystem of $\hat{F}_0$ gives our desired Floquet modes $\left|u_n(t_0)\right\rangle$ and its quasi-energies ϵ_n determined by

$$\hat{F}_0\left|u_n(t_0)\right\rangle = e^{-i\epsilon_n T/\hbar}\left|u_n(t_0)\right\rangle. \tag{2.127}$$

The prefix "quasi-" underscores the fact that this quantity is strictly defined within the confines of the Brillouin zone and hence ϵ_n is only determined by modulo $\hbar\Omega$ with $\Omega = 2\pi/T$. This is analogous to the quasi-momentum in the Bloch theorem [189]. A complete set of solution of the time-dependent Schrödinger equation has the form

$$\left|\psi_n(t)\right\rangle = e^{-i\epsilon_n(t-t_0)}\left|u_n(t)\right\rangle$$

with $\left|u_n(t+T)\right\rangle = \left|u_n(t)\right\rangle$. For completeness, any state $\left|\psi(t)\right\rangle$ can therefore be expressed in the basis of the Floquet modes

$$\begin{aligned}\left|\psi(t)\right\rangle =& \hat{U}\left(t, t_0\right)\left|\psi(t_0)\right\rangle \\ =& \sum_n a_n e^{-i\epsilon_n(t-t_0)}\left|u_n(t)\right\rangle\end{aligned} \tag{2.128}$$

with the coefficients $a_n = \langle u_n(t_0)|\psi(t_0)\rangle$.

In the context of phase transitions, the analysis of Floquet modes gains particular significance when exploring the chaotic regime of a quantum system [74, 82, 198, 199, 204]. Floquet modes, fundamentally, are the eigenstates of the system's propagator over a single drive period, as described in Eqs. (2.126) and (2.127). These modes can be conceptualized as the quantum analog of the stroboscopic Poincaré map, a tool quintessential in classical dynamics for visualizing and understanding the intricate behavior of chaotic systems in phase space [205]. The Poincaré map, in classical mechanics, serves as a powerful method to detect and characterize chaos by graphically representing the trajectory of a system in phase space. This representation makes it possible to identify patterns and structures that are characteristic of chaotic dynamics, such as fractals and strange attractors. In a quantum context, the Husimi Q representation of the Floquet modes serves a similar purpose. This representation provides a phase-space distribution of the quantum states, analogous to the classical phase-space trajectories depicted in the Poincaré map. Employing the Husimi Q representation to analyze Floquet modes enables a deeper understanding of the underlying chaotic behavior in quantum systems. This approach effectively

bridges the gap between quantum and classical chaos theories. By correlating the quantum Floquet modes with their classical counterparts through the Poincaré map, we can gain insights into the nature of the quantum phase transitions, particularly in how they correlate with chaotic dynamics. Such an analysis is instrumental in unraveling the complex interplay between quantum mechanics and classical chaos, further enriching our comprehension in chaotic regimes.

2.6.2 From quantum Duffing oscillator to transmon

We first start with the discussion of the quantum Duffing oscillator, which is an approximated form of the transmon qubit up to its anharmonicity. The quantum Duffing Hamiltonian has already been introduced in Eq.(2.22). Its quantum Langevin equation given in Eq.(2.35) obeys the following expression

$$\frac{\mathrm{d}}{\mathrm{d}t}\hat{a}_q = -i\Delta_{qd}\hat{a}_q - i\chi_{qq}\hat{a}_q^\dagger\hat{a}_q^2 - \frac{\gamma_q}{2}\hat{a}_q - \sqrt{\gamma_q}\hat{a}_{\mathrm{in}}, \tag{2.129}$$

where $\Delta_{qd} = \omega_q - \omega_d$ is the frequency detuning between the transmon qubit and the driving field, γ_q is the energy dissipation rate of the transmon qubit and $\hat{a}_{\mathrm{in}}$ is the input field. For relatively strong driving field, we can treat it classically such that $\varepsilon_q = \sqrt{\gamma_q}\langle\hat{a}_{\mathrm{in}}\rangle$. Henceforth, we can express the effective Duffing Hamiltonian as

$$\hat{\mathcal{H}}_{\mathrm{D}}/\hbar = \Delta_{qd}\hat{a}_q^\dagger\hat{a}_q + \frac{\chi_{qq}}{2}\hat{a}_q^\dagger\hat{a}_q^\dagger\hat{a}_q\hat{a}_q + i\varepsilon_q\left(\hat{a}_q - \hat{a}_q^\dagger\right). \tag{2.130}$$

According to [85, 86], we can obtain the correlation function of the signal moments by solving the Fokker-Planck equation in the steady state and the correlation function is written as

$$\left\langle\left(\hat{a}_q^\dagger\right)^j\hat{a}_q^k\right\rangle = d^{*j}d^k\frac{\Gamma(c)\Gamma(c^*)\,{}_0\mathcal{F}_2\left(k+c, j+c^*, 4\left|d\right|^2\right)}{\Gamma(k+c)\Gamma(j+c^*)\,{}_0\mathcal{F}_2\left(c, c^*, 4\left|d\right|^2\right)} \tag{2.131}$$

with the unitless detuning c, the unitless driving strength d, the generalized hypergeometric function ${}_0\mathcal{F}_2$, and the gamma special function Γ defined as

$$c = \frac{2\Delta_{qd} - i\gamma_q}{\chi_{qq}}, \qquad d = \frac{2i\varepsilon_q}{\chi_{qq}}, \qquad {}_0\mathcal{F}_2\left(x, y, z\right) = \sum_{n=0}^{\infty}\frac{\Gamma(x)\Gamma(y)z^n}{\Gamma(x+n)\Gamma(y+n)n!}.$$

The importance of this result is that all orders of signal moments are always single valued.

This conclusion is completely different from the classical treatment, which states that there is a bistability or hysteresis [86]. Indeed, if we treat Eq. (2.129) fully classically, i.e. $\alpha_q = \langle\hat{a}_q\rangle$, we obtain the classical equation of motion

$$\frac{\mathrm{d}}{\mathrm{d}t}\alpha_q = -i\Delta_{qd}\alpha_q - i\chi_{qq}\alpha_q^*\alpha_q^2 - \frac{\gamma_q}{2}\alpha_q - \varepsilon_q, \tag{2.132}$$

which is equivalent to the Duffing equation under a rotating wave approximation. Its steady state equation gives

$$\chi_{qq}^2\left|\alpha\right|^6 + 2\Delta_{qd}\chi_{qq}\left|\alpha\right|^4 + \left[\Delta_{qd}^2 + \left(\frac{\gamma_q}{2}\right)^2\right]\left|\alpha\right|^2 - \varepsilon_q^2 = 0. \tag{2.133}$$

It is evident that the solution of this third-order polynomial equation of $|\alpha|^2$ has three roots. In other words, a unique solution is not guaranteed [79, 86, 116]. The turning point of the stability region [86]

is given by

$$|\alpha_{\pm}|^2 = \frac{-2\Delta_{qd} \pm \sqrt{\Delta_{qd}^2 - 3\left(\gamma_q/2\right)^2}}{3\chi_{qq}}. \tag{2.134}$$

We can then verify that the bistability occurs for $\Delta_{qd}^2 \geq 3\left(\gamma_q/2\right)^2$ and $\Delta_{qd}\chi_{qq} < 0$ as $|\alpha|^2$ is real and positive.

In the study of the quantum Duffing oscillator, it is intriguing to note that despite the existence of only a singular steady-state solution, analogies to the bistability observed in its classical counterpart can be drawn. In the classical regime, bistability is manifested through two distinct solutions which, in the quantum context, correspond to two metastable states with exceptionally long lifetimes relative to other system timescales. These metastable states persist before the system eventually relaxes into the unique steady state as $t \to \infty$. This persistence of metastable states can be described by the concept of the Liouvillian gap. This gap is defined as the difference between the lowest two eigenvalues of the Liouvillian superoperator[19], obtained through the following relation

$$\hat{\rho}(t) = \exp\left(t\mathcal{L}_{\mathrm{D}}(t)\right)\left[\hat{\rho}(0)\right] = \sum_n \exp\left(t\lambda_n\right)\left(\sum_m c_{n,m} r_{n,m}\right). \tag{2.135}$$

The Lindbladian superoperator $\mathcal{L}_{\mathrm{D}}(t)$ for the quantum Duffing oscillator is described as

$$\mathcal{L}_{\mathrm{D}}(t)\left[\hat{\rho}(t)\right] = -\frac{i}{\hbar}\left[\hat{\mathcal{H}}_{\mathrm{D}}, \hat{\rho}(t)\right] + \gamma_q \mathcal{D}\left[\hat{a}_q\right]\hat{\rho}(t). \tag{2.136}$$

Here, $c_{n,m} = \mathrm{Tr}(l_{n,m}\hat{\rho})$ represents the trace of the product of the left eigenmatrix $l_{n,m}$ and the density operator $\hat{\rho}$. The left $l_{n,m}$ and corresponding right $r_{n,m}$ eigenmatrices of the Liouvillian superoperator $\mathcal{L}_{\mathrm{D}}$ correspond to the nth eigenvalue with a geometric multiplicity of m, i.e., λ_n for $n = 0, 1, \cdots$. We order these eigenvalues such that $\delta_n = \mathrm{Re}(\lambda_n)$ with $\delta_n < \delta_{n+1}$, creating a discrete spectrum known as the Liouvillian spectrum. When the second smallest eigenvalue δ_1 is significantly smaller and well-separated from the subsequent values in the Liouvillian spectrum, $\delta_1 \ll \delta_2$, a two-stage relaxation process ensues: Initially, the system undergoes a rapid relaxation into the metastable states, followed by a slower convergence to the stable steady state [81, 206].

In the context of phase transitions within quantum systems, a critical parameter often delineates the boundary between quantum and classical behaviors. For the quantum Duffing oscillator, this transition to what can be described as the thermodynamic limit occurs as $\varepsilon_q \to \infty$ while keeping the product $\chi_{qq}\varepsilon_q$ constant. This limit intuitively aligns with the concept that, under the regime of strong drive, the mean-field approximation becomes increasingly valid, thereby permitting a classical treatment of the system. This theoretical transition is underpinned by the Langevin equation, as formulated in Eq. (2.132). Here, we rescale the operator $\hat{a}_q = \sqrt{N}\hat{a}_c$, such that

$$\begin{aligned} \frac{\mathrm{d}}{\mathrm{d}t}\hat{a}_q &= -i\left[\Delta_{qd}\hat{a}_q - \frac{U}{N}\hat{a}_q^\dagger\hat{a}_q^2\right] - \frac{\gamma_q}{2}\hat{a}_q - \sqrt{N}\varepsilon_0, \\ \longrightarrow \frac{\mathrm{d}}{\mathrm{d}t}\hat{a}_c &= -i\left[\Delta_{qd}\hat{a}_c - U\hat{a}_c^\dagger\hat{a}_c^2\right] - \frac{\gamma_q}{2}\hat{a}_c - \varepsilon_0, \end{aligned} \tag{2.137}$$

where $\chi_{qq} = U/N$ and $\varepsilon_q = \sqrt{N}\varepsilon_0$ with constants U and ε_0 and a scaling factor N. In this framework, the bosonic commutation relation diminishes as $\left[\hat{a}_c, \hat{a}_c^\dagger\right] = 1/N$, becoming negligible for large N and thus validating the classical treatment. As an additional note, another perspective on

[19] see also Eq. (2.32) for more details

the thermodynamic limit involves transforming the system into Fourier space, resulting in a Bose-Hubbard lattice with N sites. For an in-depth exploration of this topic, the reader is directed to the comprehensive discussion provided in the literatures [207–211]. Furthermore, to develop an intuitive understanding of the first-order dissipative phase transition, we consider the concept of photon-blockade breakdown [77, 78]. In this scenario, the driving force is off-resonant with the eigenfrequencies of the oscillator. Below a critical threshold, energy conservation is not satisfied for excitation to higher energy states, a consequence of the anharmonicity of the system, which is characterized by unequally spaced energy levels. This suppression maintains the system predominantly in its ground state, illustrating the essence of photon-blockade. However, in the driven, dissipative regime, the bandwidth of the eigenenergies is broadened due to the influence of drive photons, as briefly discussed in Subsec. 2.5.1. Once the bistability threshold is surpassed, this bandwidth expansion can be sufficient to allow off-resonant drive photons to induce excitations in the quantum Duffing oscillator. Consequently, the discrete nature of the energy levels becomes less pronounced, leading to a transition where the behavior of the system increasingly resembles classical dynamics.

Now, we examine the response of the quantum Duffing oscillator to varying pump power levels, applying parameters that correlate closely with those of a "transmon qubit" ω_q. Additionally, the driving frequency is significantly detuned from the transmon qubit's resonant frequency. These parameters will subsequently form the foundational basis for the analyses in Chap. 4. Our initial focus is on the steady-state population of the quantum Duffing oscillator, $n_q = \langle \hat{a}_q^\dagger \hat{a}_q \rangle$. According to Eq. (2.133), a pronounced increase in the steady-state population is anticipated in proximity to the classical bistability region. This expectation is confirmed by the data presented in Fig. 2.13 (a), where a sharp rise in population is observed at approximately $-73\,\mathrm{dBm}$. Below the critical pump power, the steady-state population remains near zero, but after the threshold, it converges to the classical steady-state population. The Rényi entropy S_2 supports this observation. It yields a value of zero at instances where the system is in a pure state, characterized by a purity $P = 1$. At the critical point, the entropy shows a peak, which indicates the maximum mixture of the coherent and the squeezed state. The Husimi Q function visualizes the equiprobable mixture of both phase in Fig. 2.14 (a). At $-98\,\mathrm{dBm}$ and at $-70\,\mathrm{dBm}$, we recognize the coherent and the squeezed state, respectively, while at the critical pump power of $-73.1\,\mathrm{dBm}$ we find both phases in the phase space. After the threshold, the entropy drops down monotonically as the state becomes "purely coherent". We further study its behavior in the context of the Floquet modes. The bottom panel of Fig. 2.13 (a) shows the probability of finding Floquet modes in the steady-state density matrix of the quantum Duffing oscillator. Interestingly, we have an equiprobable mixture of the Floquet modes $|0\rangle_F, |1\rangle_F, |2\rangle_F$ associated with a partial mixture of the Floquet mode $|3\rangle_F$ at $-73.1\,\mathrm{dBm}$. The Husimi Q distribution of these Floquet modes demonstrates that they capture the main feature of the quantum Duffing oscillator: The coherent vacuum state is one of the eigenstate of the driven system, which is the Floquet state $|0\rangle_F$, while the squeezed state can be found for the Floquet state $|3\rangle_F$ (and $|1\rangle_F$ at around $-50\,\mathrm{dBm}$). The progressive transition of the squeezed state can be confirmed by the second-order correlation function. After the threshold, it starts with a slightly smaller value than unity because of the squeezed state, which eventually reaches the unity (see Fig. 2.13 (a)).

Extending our analysis, we now apply the theoretical framework developed for the quantum Duffing oscillator to the transmon qubit system. Numerical simulations, depicted in Fig. 2.13 (b), exhibit behaviors in the transmon system that are qualitatively similar to those observed in the quantum Duffing oscillator, particularly in the lower power regime. A notable parallel is the emergence of a peak

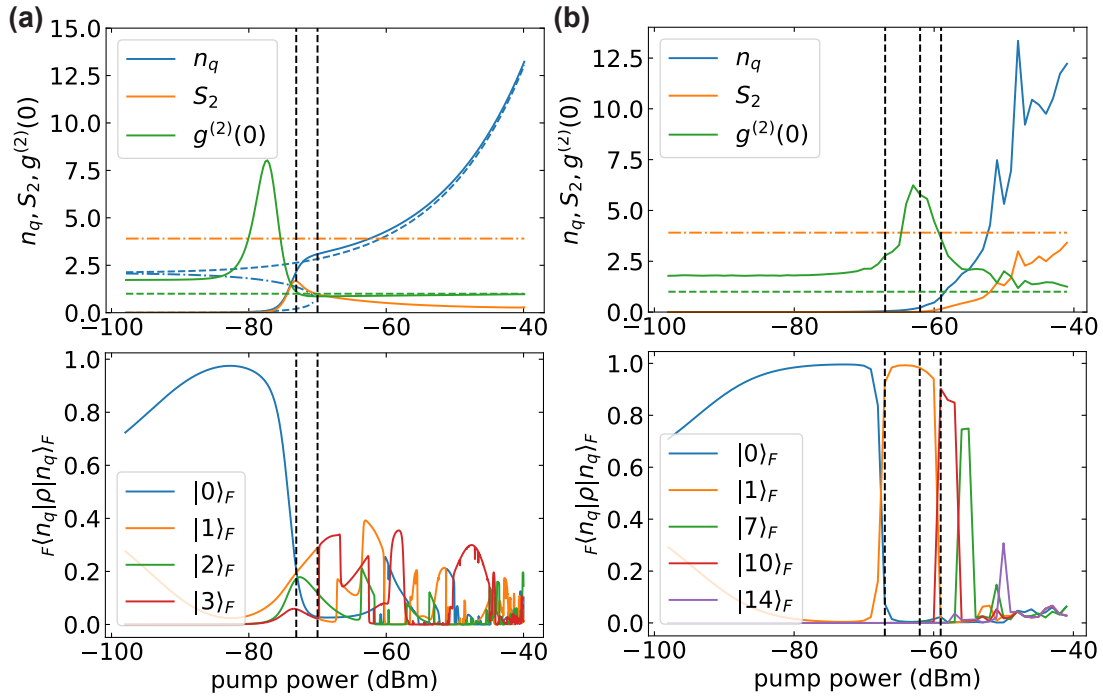

Figure 2.13. Numerical simulations allowing to compare the behavior of (a) quantum Duffing oscillator and (b) transmon qubit. (a) Steady-state population n_q calculated by the quantum (blue solid line) and classical theories (blue dashed line). The unstable classical steady-state solution is represented by the blue dash-dotted line. Rényi entropy S_2 (orange solid line) with its maximum entropy (orange dashed-dotted line), correlation function $g^{(2)}(0)$ (green solid line) with the unity value (green dashed line). The probability of finding Floquet modes $|0\rangle_F, |1\rangle_F, |2\rangle_F, |3\rangle_F$ (blue, orange, green, red solid line) in the simulated density matrix ${}_F\langle n_q|\hat{\rho}|n_q\rangle_F$. The critical point of equiprobable mixture of the coherent and squeezed state is indicated by the vertical black dashed line at $-73.1\,\mathrm{dBm}$, while the vertical black dashed line at $-70\,\mathrm{dBm}$ is the starting point of the squeezed state. Rényi entropy S_2 (b) Steady-state transmon population n_q (blue solid line), Rényi entropy S_2 (orange solid line) with its maximum entropy (orange dashed-dotted line), correlation function $g^{(2)}(0)$ (green solid line) with the unity value (green dashed line). The probability of finding Floquet modes $|0\rangle_F, |1\rangle_F, |7\rangle_F, |10\rangle_F, |14\rangle_F$ (blue, orange, green, red, purple solid line) in the simulated density matrix ${}_F\langle n_q|\hat{\rho}|n_q\rangle_F$. The black vertical dashed lines are positioned at $-67, -62, -59\,\mathrm{dBm}$. The parameters used for both simulations are $\omega_q/2\pi = 5.664\,\mathrm{GHz}$, $\chi_{qq}/2\pi = -242\,\mathrm{MHz}$, $\omega_d/2\pi = 5.156\,\mathrm{GHz}$, and $\gamma_q = 1/80\ \mu\mathrm{s}$ with the Hilbert space dimension of $d_q = 25$. In the case of the transmon qubit, $E_C/\hbar$ and $E_J/\hbar$ are chosen such that ω_q and χ_{qq} coincide with the Duffing parameters.

in the second-order correlation function, $g^{(2)}(0)$, corresponding to an increase in both the transmon population and the Rényi entropy. The value of this correlation function at the lower power limit ($g^{(2)}(0) \approx 1.8$) closely mirrors that observed in the quantum Duffing oscillator, thereby supporting the approximation of the transmon qubit as a Duffing system within this specific power regime. However, the similarity between these systems becomes less pronounced as we move beyond this threshold. In this higher power regime, the transmon qubit exhibits distinct behavior compared to the quantum Duffing oscillator, particularly in terms of the Rényi entropy. While the Duffing system demonstrates a monotonic decrease in entropy, the entropy in the transmon qubit system asymptotically approaches $S_2 = -\log(1/d_q)$, indicative of a transition towards a completely mixed state. This observation is in agreement with both numerical and experimental studies [71–73], further validating our findings.

The examination of the Husimi Q function within the phase space offers significant insights into the evolving dynamics of the transmon qubit system, as depicted in Fig. 2.15 (a). Initially, at a pump power

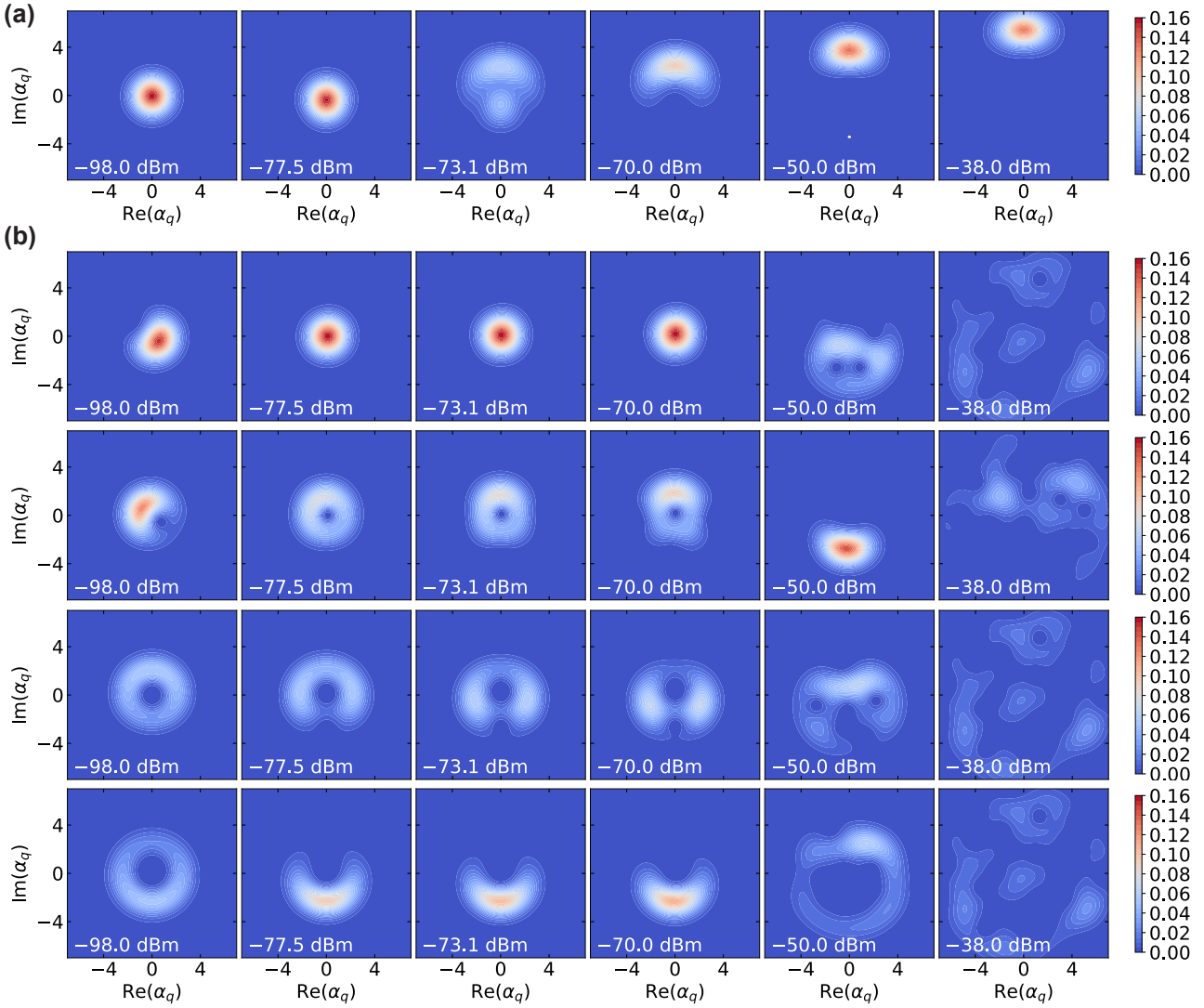

Figure 2.14. Simulated Husimi Q function of the quantum Duffing oscillator for various drive powers. (a) The Husimi Q function of the steady-state density matrix. (b) The Husimi Q function of the Floquet modes $|0\rangle_F, |1\rangle_F, |2\rangle_F, |3\rangle_F$ (from top to bottom).

of −62 dBm, the Husimi Q function exhibits a slight deformation from its Gaussian-like distribution, indicative of the onset of non-trivial quantum effects. As the pump power increases to −53 dBm, this distribution transitions into a squeezed-like form, characterized by its distinct elongation in the phase space. For higher pump powers, we observe an irregular delocalization over the phase space, as shown at −47 dBm in Fig. 2.15 (a). This delocalization within the phase space can be attributed to changes in the Husimi Q distribution, along with the statistical distribution of the Floquet modes. Up to approximately −59 dBm, the density matrix of the transmon primarily comprises one, occasionally two at very low powers, Floquet modes. This is evidenced in the bottom panel of Fig. 2.13 (b). However, with an increase in pump power, there is a marked reduction in the probability of the leading Floquet mode's presence within the density matrix, resulting to an almost equiprobable distribution of these modes. Concurrently, the Husimi Q functions associated with these Floquet modes begin to show widespread delocalization across the phase space, as shown in Fig. 2.15 (b). This phenomenon is being studied in relation to the regular and chaotic states [74, 200, 212]. Regular states in quantum systems are characterized by predictability and order, typically manifested as well-defined, smooth, and closed orbits or tori in phase space. In contrast, chaotic states are defined by their sensitivity to initial

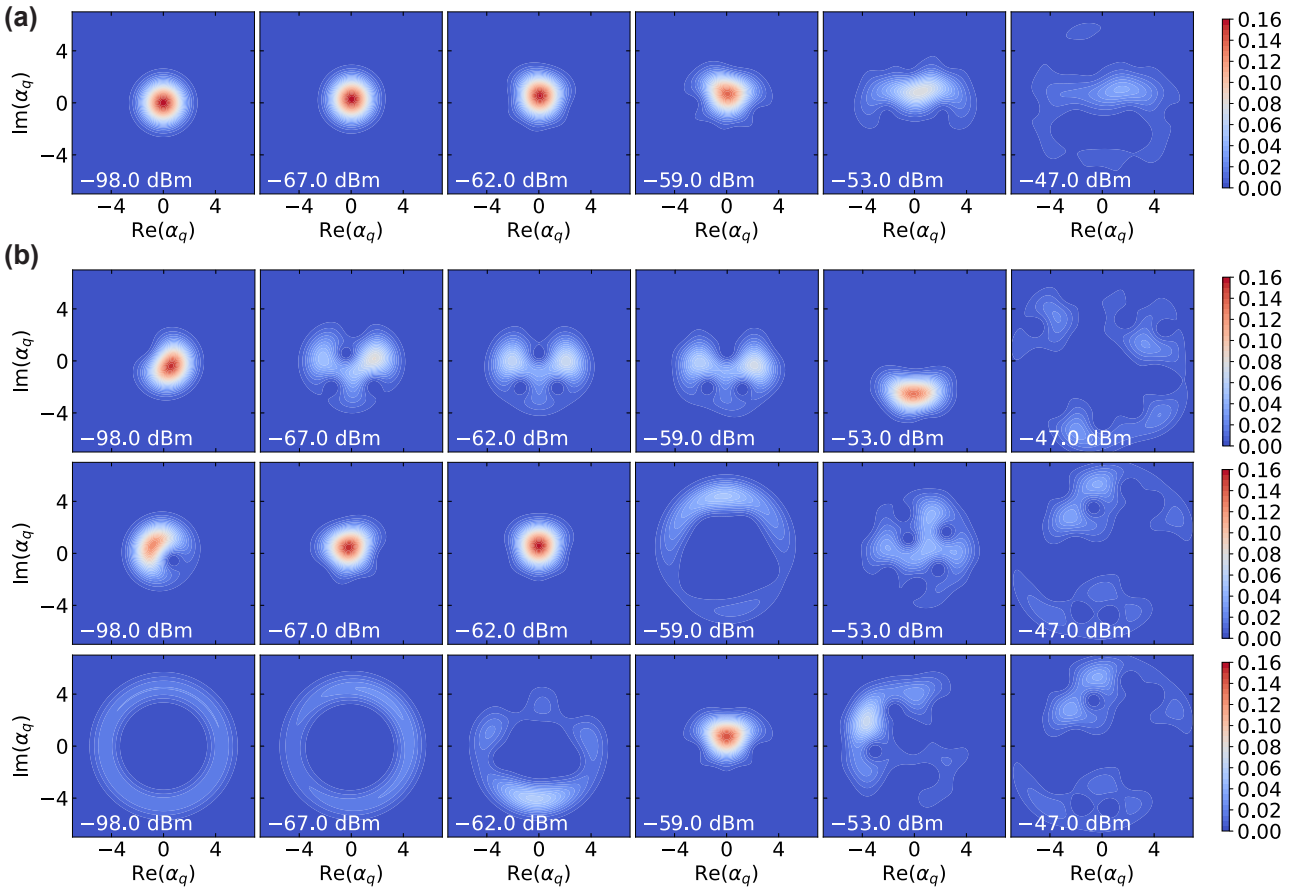

Figure 2.15. Simulated Husimi Q function of the transmon qubit for various drive powers. (a) The Husimi Q function of the steady-state density matrix. (b) The Husimi Q function of the Floquet modes $|0\rangle_F, |1\rangle_F, |10\rangle_F$ (from top to bottom).

conditions and aperiodic long-term behavior, often resulting in fractal structures in phase space. In the context of the transmon qubit, chaotic behavior is observed at the boundary of confined and unconfined states in the Josephson potential, a region known as the separatrix [74]. To quantitatively analyze this transition, we consider the mean energy per cycle for a given Floquet mode $|\psi_k(t)\rangle_F$

$$\langle\langle H\rangle\rangle_k = \frac{1}{T}\int_0^T \mathrm{d}t \, {}_F\langle\psi_k(t)|\,\hat{\mathcal{H}}(t)\,|\psi_k(t)\rangle_F,$$

where $\langle\langle H\rangle\rangle_k \approx 2E_J$ marks the onset of irregular and chaotic behavior in the Floquet modes. Observations indicate that as the pump power increases, the mean energy per cycle of all Floquet modes, initially below $2E_J$, steadily approaches this critical value, signifying a transition to irregular and chaotic dynamics [74]. Hence, the widespread delocalilzation of the Floquet modes in the Husimi Q representation across the phase space is associated with the transition to irregular and chaotic dynamics. In summary, our investigation into the transmon qubit system reveals that at high pump powers, there is a complete mixture of chaotic Floquet modes, underscoring the complex quantum-to-classical transition in this regime.

Chapter 3

SAMPLE FABRICATION AND CHARACTERIZATION

Sample fabrication plays a critical role in realizing high-performance quantum chips with a continuously increasing number of circuits components. It involves meticulous material selection, precise chemical treatment of surfaces and interfaces, and sub-micrometer control in electron/laser beam writing. Major advancements in fabrication techniques have led to the development of highly coherent quantum systems with precise frequency control. Notably, IBM recently achieved a transmon coherence time exceeding 1 ms [213], underscoring the significance of nanofabrication technology in the field of circuit quantum electrodynamics.

In this chapter, we present the fabrication steps and parameters relevant to the production of our samples based on the superconductors niobium (Nb) and aluminum (Al). A significant breakthrough in sample fabrication is the use of buffered-oxide etching (BOE), which effectively eliminates surfaces oxides and contaminants leading to so-called Two-Level-Fluctuators (TLSs), which represent the dominant sources of loss in superconducting circuits (see Chap. 2). By implementing this technique, we can minimize the impact of TLS-induced losses and enhance the overall performance of our quantum devices by increasing their coherence time. We characterize the quality of our fabrication processes through the extraction of the internal quality factors of the resonators and the measurement of the coherence time of the transmon qubits.

3.1 Fabrication techniques

In this section, we outline the multi-step process for fabricating high-quality superconducting resonators and transmon qubits. The fabrication workflow comprises essential stages such as cleaning, material deposition, lithography, and post-processing. The effective reduction of losses is predominantly achieved through two key steps: the cleaning step and the post-processing step. These steps involve processes such as Piranha etching, buffered oxide etching (BOE), argon (Ar) ion milling, and bandaging. We will delve into each fabrication step in the respective subsections to provide a comprehensive understanding of their roles in minimizing losses. Moreover, due to the distinct characteristic dimensions of Josephson junctions and coplanar waveguides, we present separate discussions on the fabrication techniques for these components. An overview of the whole fabrication procedure is shown in Figs. 3.1 and 3.2. All fabrication steps are based on the investigations presented in Refs. [214–219].

3.1.1 Fabrication of coplanar waveguides

Substrate treatment

The initial step of our fabrication process involves thorough cleaning of the silicon substrates to establish a pristine crystal surface. This cleaning procedure is crucial to ensure the success of subsequent fabrication steps. To remove the protective resist layer from the substrate, we employ hot acetone and subsequently 2-isopropanol (IPA) in an ultrasonic bath. The application of heat and mechanical agitation provided by the ultrasonic bath supports the effective dissolution and removal of the resist layer, leaving behind a clean substrate.

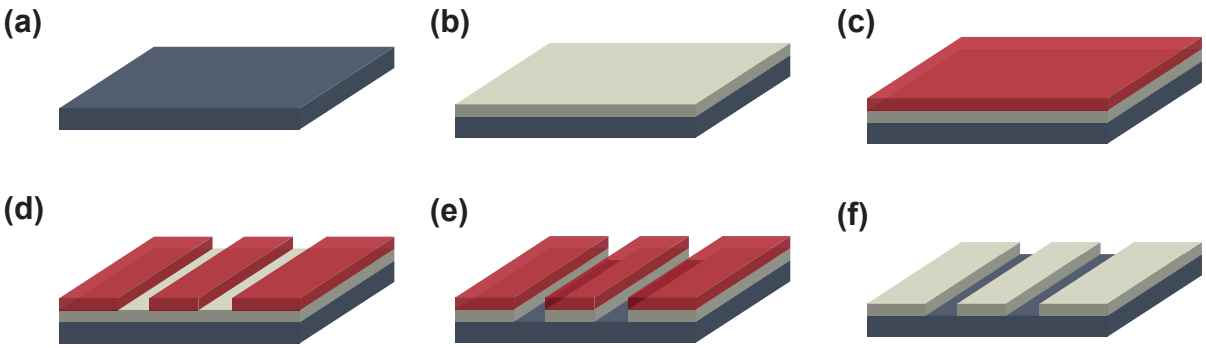

Figure 3.1. Overview of coplanar waveguide fabrication steps. Here, we take Nb as a concrete example. **(a)** Substrate treatment. The protective resist layer is removed by hot acetone and IPA. Afterwards, the substrate is chemically etched by Piranha mixture and BOE. **(b)** Sputtering of Nb. After the cleaning process, Nb is sputtered onto the substrate in the PLASSYS system. **(c)** Resist coating. Photoresist is spin-coated onto the Nb layer. **(d)** Optical lithography and development. The laser writer transfers the desired circuit design into the resist. The unexposed areas will then be removed by the developer. **(e)** RIE etching. Removal of uncovered Nb by RIE. **(f)** Post-processing. After the removal of the remaining resist in the remover solution, HF dip is employed to remove a niobium oxide layer.

However, to achieve an even higher level of cleanliness and eliminate any residual organic contaminants, we implement **Piranha etching** as a secondary cleaning step. Piranha etching involves the use of a powerful etchant composed of concentrated sulfuric acid (H_2SO_4 (100 wt%)) and aqueous hydrogen peroxide (H_2O_2 (35 wt%)) in a 3:1 ratio. This mixture undergoes a chemical reaction, resulting in the production of atomic oxygen [220]

$$H_2SO_4 + H_2O_2 \longleftrightarrow H_3O^+ + HSO_4^- + O. \tag{3.1}$$

The atomic oxygen generated during Piranha cleaning exhibits strong reactivity towards organic materials. It disrupts the hybridized C-C bonds present in carbon-based residues, effectively removing any remaining resist residues or other organic contaminants from the substrate surface. We place the sample for 10 min in a beaker with piranha solution at 80°C, and afterwards rinse it in DI water.

During the etching process, a thick silicon oxide layer is formed on the surface [167, 221, 222], which needs to be removed for further fabrication steps. To address this, we utilize **BOE**, an aqueous solution composed of hydrofluoric acid (HF, 6.5 wt%) and ammonia fluoride (NH_4F, 34.8 wt%). HF plays a key role in removing the silicon oxide layer through the following reaction [223]:

$$Si - O - X + H^+ \longrightarrow Si - O(H)^+ - X, \quad (X = Si \text{ or } H) \tag{3.2}$$

$$Si - O(H)^+ - X + HF_2^- \longrightarrow Si - F + HO - X + HF \tag{3.3}$$

This reaction results in the formation of Si˘F, which effectively slows down the oxidation process when the substrate is exposed to air. This helps to preserve the quality of the etched surface and prevents rapid re-oxidation, allowing for a smooth transition to subsequent fabrication steps. In addition to its role in oxide removal, NH_4F plays a crucial role in maintaining a constant etch rate. It continuously provides F^- ions, ensuring a consistent etching process throughout the duration. This constant etch rate is essential for a smooth substrate surface [160]. To perform the BOE, our samples are immersed in the BOE solution for a duration of 30 s. Subsequently, they are rinsed with DI water to remove any

residual etchant. After rinsing, the samples are carefully blow-dried using nitrogen gas to avoid any contamination or watermarks. Finally, the samples are transferred to the load lock of the PLASSYS deposition system for further processing.

Sputtering deposition

Sputtering is a widely used physical vapor deposition (PVD) technique in which a target material, such as Nb in our case, is bombarded with ions, typically Ar ions. The sputtering process takes place in a UHV chamber filled with the sputtering gas, which is ionized by applying a high voltage between the target (cathode) and an anode. This ionization creates a plasma of ionized gas, specifically ionized argon. The ionized argon ions are accelerated towards the Nb target and upon collision, they transfer kinetic energy to the Nb atoms. If the transferred kinetic energy exceeds the binding energy of the Nb atoms, they are dislodged from the target material and travels along a straight trajectory, ultimately depositing onto the substrate surface. This process allows for the controlled deposition of a thin film of Nb onto the substrate. In order to achieve high-purity Nb layers, a high-purity target material (99.95%), a UHV deposition chamber with a base pressure below 10^{-9} mbar, and a high-purity sputtering gas (Ar, 99.9999%) are used.

In our work, we utilize a sputtering system provided by PLASSYS. The PLASSYS system features a confocal sputtering layout, where the target is tilted and offset from the substrate holder. To enhance the uniformity of the deposited film, the substrate holder rotates during sputtering.

Resist spin coating

Spin coating is employed in this step using an optical negative resist, where the unexposed areas will be removed in the development process. To achieve a uniform resist thickness, a spin coater is used, which applies centrifugal force to distribute the resist evenly. Subsequently, the resist is baked to evaporate the solvent, to improve the adhesion to the substrate and to prevent it from further dispersion.

In our case, the photoresist AZ MiR 701 14cP is spin-coated at 4000 rpm for 1 min and soft-baked for 75 s at 90°C. This results in a resist thickness of 900 nm.

Optical lithography

To modify the polymer chain structure of the spin-coated sample, we employ a laser writer in our fabrication process. The laser writer is utilized to irradiate the sample with a focused laser beam. This irradiation induces changes in the polymer chain structure, allowing us to create the desired circuit design. The laser writer is well-suited for writing structures with larger spatial dimensions, such as transmission lines and coplanar waveguide (CPW) resonators, due to its beam spot size between 300 nm and 5 μm. This feature enables precise and efficient fabrication of these components.

For the laser writing process, we use a 405 nm laser in the Picomaster 200 system to draw the desired circuit design onto the resist. The laser exposes specific areas of the resist, creating patterns and structures as defined in the design layout. After the laser exposure, a post-exposure bake step is performed at a temperature of 110°C for a duration of 90 s. This bake step helps mitigate potential standing wave effects [214].

Resist development

In the development stage, an appropriate resist developer is used to remove the unexposed areas, leaving behind the desired resist pattern.

Here, we utilize a developer called AZ 726 MIF for 60 s, which contains 2.38% tetra methyl ammonium hydroxide ($N(CH_3)_4^+OH^-$) (TMAH).

Reactive ion etching and wet etching process

we employ **reactive ion etching (RIE)** to etch our Nb layers. RIE is a versatile etching technique that can remove material both physically and chemically, depending on the ionized gas and the kinetic energy of the plasma ions. In our case, we utilize SF_6 to produce the ionized gas F^- and the Nb film as the target material. Similar to the sputtering mechanism, RIE involves bombarding the target material with ionized gases. This is achieved by applying a potential difference between the plasma and the target material underneath. The ions from the plasma are accelerated towards the target, resulting in the physical removal of the uncovered Nb material. This physical process leads to an anisotropic etching, primarily occurring in the direction of particle incident. In addition to this physical process, RIE also involves a chemical process. Radicals formed in the plasma chemically react with the target material, in this case, Nb. After the chemical reaction, the byproducts desorb from the surface and are pumped out of the etching chamber. This chemical process, driven by the reaction of radicals, contributes to the etching process by removing material evenly in all directions. This is known as isotropic etching, and it can result in undercutting of the Nb material once the etch reaches the Si substrate. To enhance the anisotropic etching process and mitigate undercutting, we utilize Ar gas. This ion-assisted etching allows for a more controlled etch process. Our RIE processes are carried out using a Plasmalab 80 Plus system from Oxford Instruments. It is an inductively coupled plasma RIE systems, which allows to change the plasma density and the kinetic energy of the ions separately. By carefully controlling the etching parameters such as gas composition, pressure, power, and etch time, we can precisely control the etching process and achieve the desired etch profile and depth in the Nb material.

In contrast to using RIE for etching Nb, when it comes to etching Al, we employ a **wet etching process**. This is due to the unavailability of a suitable etching gas in our RIE system for etching Al. In our wet etching process, we utilize the same solution as for the development, AZ 726 MIF. Here, the development AND the etching is carried out at room temperature for a duration of 180 s, simultaneously. After the etching step, the sample is rinsed twice with DI water. Unlike RIE, wet etching does not attack Si and is a completely isotropic process, which means that it removes aluminum uniformly in all directions. This includes the sidewalls of the etched structure, resulting in lateral etching of approximately 0.5 μm. It is important to take this lateral etching into account when designing the device, as it can impact the overall dimensions and geometry of the structures.

To remove any remaining resist, the chip is immersed in a suitable remover solution as part of the cleaning process.

Post-processing

In the course of the fabrication process, Nb is susceptible to oxidation when exposed to ambient atmospheric conditions. To address this, when the ground layer is composed of Nb, we begin by removing the niobium oxide layer through a 30-minute immersion in BOE. As elaborated in the

subsequent subsection, following this de-oxidation, the Nb metal layer undergoes spin-coating, a pivotal step in the Josephson junctions' fabrication. This procedure shields the Nb from re-oxidation such that it ensures an oxide-free substrate.

3.1.2 Fabrication of Josephson junction

In the fabrication of the Al Josephson junction, we utilize a lift-off process. Central to this procedure is the so-called shadow evaporation technique, a key method that facilitates the formation of the junction through aluminum deposition [224]. This technique, established over decades, ensures precise control and deposition of aluminum, enabling the creation of reliable and consistent junctions.

Following the etching of larger structures as described in Subsec. 3.1.1, we initiate the lift-off procedure. Successfully merging these processes necessitates precise alignment of the structures. As an illustrative example, it is important that the Josephson junctions are meticulously positioned between the pads, as depicted in Fig. 2.3 (b). To facilitate this precision, the etched thin film incorporates the so-called markers. These markers serve as guides for the electron-beam lithography process, which subsequently writes the design for the Josephson junction. A more detailed explanation on electron-beam lithography will be presented later in this subsection. However, for the fabrication of 3D transmon qubits introduced in Sec. 2.5, we can directly start with an all-aluminum lift-off process. The all-aluminum process offers several advantages, including a reduced number of process steps, simplifying the overall fabrication procedure. Additionally, the design of the 3D transmon qubit, resembling a floating transmon, ensures that the electric field is mainly concentrated around the Josephson junctions. Consequently, the dominant decoherence source arises from the TLSs distributed in the junction region. Even in the presence of potential residual resist contamination stemming from the lift-off process, we can still expect a high coherence time for our qubit.

The typical junction size for transmon qubits is in a sub-micrometer regime[1] requiring a precise patterning of the double-layer resist system by resist electron-beam lithography.

Substrate cleaning (for lift-off process)

We use the cleaning step introduced in the fabrication of coplanar waveguide.

Resist spin coating

In Josephson junction fabrication, we use a double-layer resist system that plays a crucial role in the successful fabrication of our devices in a shadow evaporation process. This resist system consists of two distinct layers: a bottom layer with enhanced sensitivity to electron radiation and a top layer that acts as a "roof" for high-precision resolution at the nanometer scale.

The bottom layer is instrumental in creating an undercut, which prevents the deposition of aluminum to the resist walls during subsequent deposition steps. This is particularly important for maintaining the integrity of thin Josephson junctions, which are highly susceptible to variations in the fabrication process. The top layer of the resist system is designed to have considerable overhangs over the bottom layer, creating a clear boundary. The overhanging resist structure allows one to avoid any connection between the Al film deposited on top of the restist and that on the substrate. This prevents unintended removal of the aluminum during the subsequent lift-off process.

[1] For a transmon frequency between $4 - 8\,\mathrm{GHz}$, we require a junction width of around $200\,\mathrm{nm}$ to $300\,\mathrm{nm}$.

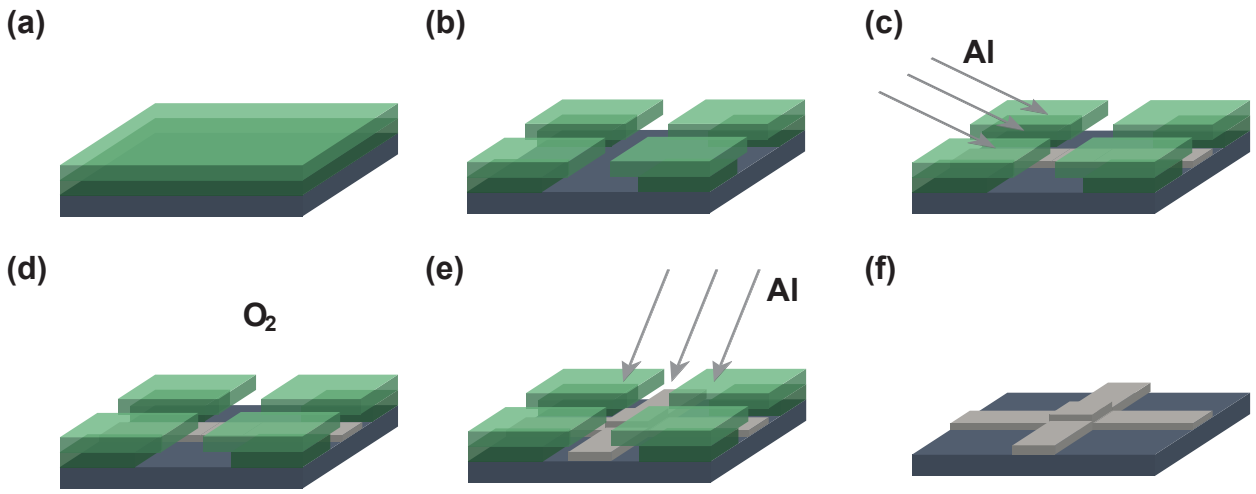

Figure 3.2. Overview of the Josephson-junction fabrication steps. **(a)** Resist spin coating. Bottom layer with enhanced sensitivity to electron beam irradiation and top layer for high precision resolution forming a double-layer system. **(b)** Electron-beam lithography and development. The electron-beam draws the desired Josephson-junction circuit design into the resist. Here, we design the junctions in such a way such that a so-called Manhattan-type Al evaporation technique can be applied. The exposed area will then be removed by the developer. **(c)** First Al evaporation. In the Josephson junction evaporation technique, Al is deposited onto the sample surface at a shallow angle (Al film deposited on top of the resists is not shown for clarity), ensuring that only the microstrip parallel to the direction of evaporation is coated with Al, while the orthogonal microstrips remain unaffected. Using a shallow evaporation angle allows for selective deposition, ensuring the desired pattern and configuration of the Al layer on the sample. **(d)** Oxidation. In-situ oxidation of Al to form an insulating AlO_x layer. **(e)** Second Al evaporation. The sample is rotated and tilted to evaporate the second strip. The $Al/AlO_x/Al$ Josephson junction is now formed. **(f)** Lift-off. All remaining resist is removed after the lift-off process.

For this process, we utilize a positive electron-sensitive resist that can be selectively removed after the development process. To ensure a uniform thickness of the resist layer (bottom resist: 700 nm, top resist: 300 nm), we employ a spin coater that applies centrifugal force to evenly distribute the resist across the substrate surface. Following the coating step, the resist system is subjected to a baking procedure to harden the resist layer, enhancing its stability and durability. This step is then repeated for the top layer to complete the double-layer resist structure.

During this work, we changed our resist layer stack[2] in a chronological order (bottom resist, top resist): (AR-P 617.08, AR-P 679.02), (AR-P 617.08, AR CSAR 6200.09), and (AR CSAR 6200.13, AR-P 672.045). The reason behind these transitions will be elucidated subsequently.

Electron-beam lithography

In the realm of nanoscale structures, the resolution of optical lithography is limited by the wavelength of the laser, making it challenging to achieve fine features. In contrast, electron beam lithography (EBL) offers a much higher resolution, reaching down to a few nanometers. The resolution of EBL is primarily limited by electron scattering in the resist and substrate [225]. To ensure reproducibility of structures at the nanometer scale, it is crucial to optimize the writing dose of the electron beam. Monte Carlo simulations of the electron-solid interaction are employed to simulate a point spread function, which

[2] All resist products are supplied from Allresist GmbH.

allows for the correction of proximity effects. This correction is achieved using the BEAMER software from GenISys, which takes into account the characteristics of the double-layer resist system and silicon. The resist used in our process contains long polymer chains that are susceptible to damage from electron bombardment at a critical dose. These damaged polymer chains are subsequently removed during the development step. For electron beam lithography, we utilize the NanoBeam nB5 system from NanoBeam Limited, which is located at WMI. The typical parameter values of the beam current and beam voltage are 6 nA and 80 kV, respectively. This system provides the necessary capabilities for precise electron beam patterning.

Resist development

As mentioned before, we remove the exposed resist areas by a developer, which dissolves away all broken-up polymer chains. We employ different development processes for each resist layer stack.

- (AR-P 617.08, AR-P 679.02): We develop the structures with AR 600-56 for 30 s followed by a 5 min bath in 4°C cold IPA. Owing to the instability of the cold temperature environment, attributed to factors like a small cold bath and fluctuating room temperature, we encountered poor reproducibility. [215, 216, 218].

- (AR-P 617.08, AR CSAR 6200.09): We develop the structures with AR 600-546 for 60 s, and subsequently with AR 600-56 for 90 s for undercut and finally rinse it with IPA. Due to strong adhesion of AR-P 617.08 to the silicon substrate, complete resist removal is not ensured [217].

- (AR CSAR 6200.13, AR-P 672.045): We develop the structures with AR 600-56 for 180 s, rinse it with IPA for 30 s, subsequently with AR 600-546 for 90 s for undercut and finally rinse it with IPA for 30 s.

Aluminum evaporation and oxidation

In our Al evaporation technique, we employ an ultra-high vacuum deposition system operating under ultra-high vacuum conditions to ensure the purity of the Al films and prevent any contamination. The process involves the deposition of Al with a purity of 99.999% in two steps, with an initial evaporation onto a shutter to eliminate any potential crucible contamination and to stabilize the evaporation rate, followed by deposition onto the substrate.

During the electron beam evaporation process, high-energy electrons, generated by a filament, are accelerated and deflected using a magnetic field. The resulting electron beam heats the Al crucible, causing the aluminum material to evaporate. The evaporated aluminum atoms then fly to the substrate, where they condense and form a thin film.

In the context of our Al evaporation process, we initially employed a home-built evaporation system as documented in [226]. However, as the research advanced, we transitioned to using an evaporation system sourced from PLASSYS. Notably, the base pressure for our home-built system is at below 10^{-8} mbar, while the PLASSYS system is an even lower pressure of 10^{-9} mbar.

A significant differentiation between the two setups is the location of oxidation chamber. In our original system, oxidation occurred directly within the evaporation chamber. In contrast, the PLASSYS system separates the evaporation chamber from the oxidation chamber, with a gate valve after film deposition. Such an arrangement is crucial as it avoids any oxidation of the Al in the crucible. Nonetheless, both systems facilitate in-situ oxidation processes, thereby enhancing the precision and

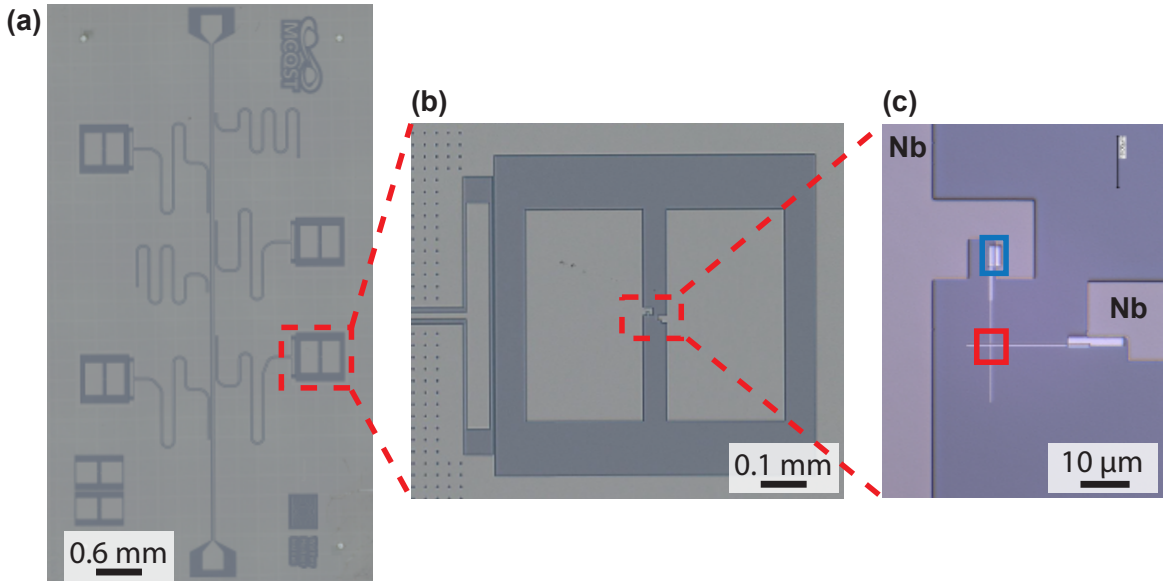

Figure 3.3. Optical micrograph of the qubit chip `Qubit-KH079`. (a) Overview of the whole qubit chip with four transmon qubits and two reference CPW resonators. (b) Zoomed-in 2D floating transmon qubit, which is capacitively coupled with the readout CPW resonator. (c) Josephson junction (red box) with its bandage (blue box). The bandage clearly covers the pad (Nb layer) and the lead of the Josephson junction (Al layer), ensuring the galvanic contact between both metals. See also Fig. 2.3 (b) for reference.

reproducibility of our experiments. Furthermore, the substrate holder in our system is designed to rotate around two axes, enabling a Manhattan-type shadow evaporation technique [227].

Lift-off process

After the shadow evaporation step, it is necessary to remove any remaining resist and unwanted metal on the resist from the sample. To achieve this, we employ a cleaning process involving several steps. First, the sample is immersed in acetone and heated to 80°C for a duration of 10 min. This helps to dissolve and remove most of the resist layers together with the Al on the resist. Next, the sample is placed in IPA at room temperature. Careful stirring with a plastic pipette is performed for 2 min to ensure thorough cleaning of the sample surface. Following the IPA treatment, the sample is transferred to a supersonic bath set at te lowest level for a duration of 2 s. Finally, the sample is dried using a stream of nitrogen gas. The gentle flow of nitrogen helps to remove any remaining traces of solvent, leaving the sample in a clean and dry state. This cleaning procedure ensures the removal of unwanted residues.

3.1.3 Ar ion milling and bandaging

In our fabrication process, we have chosen Nb ground planes due to their lower losses. However, there is an inherent limitation as it is difficult to make Nb Josephson junctions fulfilling our parameter requirements. As a result, we have optimized the fabrication process for Al Josephson junctions. This brings about a deliberate design choice where we physically separate the Nb metal layer, used for the coplanar waveguide, from the Al metal layers designated for the Josephson junction. This separation ensures there is no direct galvanic contact between the two metals, mitigating potential effects from the lossy oxide layer inherent in the coplanar waveguide material. If aluminum were to be directly deposited

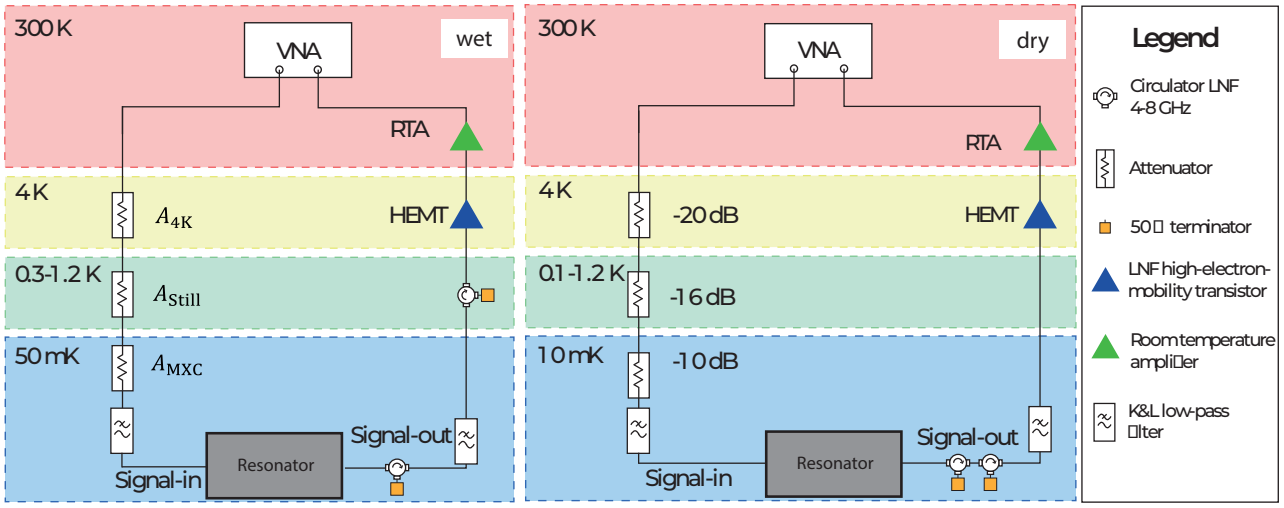

Figure 3.4. Schematic drawing of wet (left) and dry dilution refrigerator (right) embedding resonator chip. In the wet dilution refrigerator, $A_{4K,Still,MXC}$ are attenuators, where the values can vary for each resonator experiment due to the limited availability of input lines.

onto the prefabricated structures, the oxide layer on those structures might introduce additional loss channels detrimental to our quantum system.

To address this issue, we employ a technique known as argon ion milling. This process involves using a beam of argon ions to remove the oxide layer from the coplanar waveguide material. Once the oxide layer is removed, we proceed to deposit another layer of aluminum that covers both the Nb base layer and the Josephson junction lead. This method is commonly referred to as the bandaging technique, as it involves "bandaging" or covering the structures with a new layer of aluminum.

By utilizing the bandaging technique, we are able to overcome the challenges posed by the oxide layer and ensure a high-quality fabrication of our quantum system. The bandaging technique has been widely adopted in the field and has been shown to be effective in reducing unwanted losses and improving the performance of the fabricated devices [228].

A typical transmon qubit chip incorporating all fabrication procedures is depicted in Fig. 3.3. Here, the transmission lines, CPW resonators, and the large qubit pads are fabricated with the Nb etching process, while the Josephson junctions and the bandages are realized with the Al lift-off process.

3.2 Resonator characterization

3.2.1 Cryogenic setup

As discussed in Chap. 2, the observation of various quantum phenomena necessitates cryogenic temperatures. To achieve this, we utilize both our in-house built wet dilution refrigerator and a dry dilution refrigerator from Bluefors.

The dilution refrigerator is a cryogenic system extensively employed in quantum physics experiments to achieve extremely low temperatures. It consists of multiple thermal stages, including 50 K, 4 K, and 800 mK, leading to a final sample stage temperature ranging from 7 mK to 50 mK. The refrigeration process is based on the mixing of two helium isotopes, helium-3 (^{3}He) and helium-4 (^{4}He), and takes advantage of their unique properties.

When the ^{3}He/^{4}He mixture is cooled down to approximately 870 mK, it undergoes a phase

separation, resulting in the formation of two coexisting phases with different concentrations of ^{3}He. At low themperature (10 mK) the two phases are a pure ^{3}He phase and a ^{4}He rich phase with a ^{3}He content of 6.5%. The pure ^{3}He phase floats in the ^{4}He-rich phase, as the ^{3}He phase has a larger volume due to increased zero-energy fluctuations and therfore it is lighter than the ^{4}He-rich phase. By removing ^{3}He from the diluted phase, the minimum possible content of 6.5% of ^{3}He has to be restored by the diffusion of ^{3}He across the phase boundary. Since the entropy in the diluted phase is larger, this process is associated with a removal of heat $\Delta Q = T\Delta S = T\left(S_{\mathrm{dil}}(T) - S_{\mathrm{con}}(T)\right)$, which in turn provides the cooling power for the refrigerator[3]. The cooling power is proportional to the amount of ^{3}He atoms per time and can in principle made large by increasing the pumping speed. However, at millikelvin temperatures, the vapor pressure of ^{3}He becomes extremely low, making it challenging to extract ^{3}He using conventional pumps. To address this, a distillation chamber (still) is employed, where the pump acts on the liquid surface at a higher temperature. This arrangement allows for the efficient removal of ^{3}He from the diluted phase and facilitates the cooling process.

In our setup, we have two distinct dilution refrigerators: the **wet dilution refrigerator** and the **dry dilution refrigerator**. The wet dilution refrigerator undergoes precooling using liquid nitrogen and liquid helium, while the dry dilution refrigerator employs a pulse tube cryocooler for precooling. Detailed information regarding the working principle of our wet dilution refrigerator can be found in Ref. [214].

Wet dilution refrigerator

The cryogenic setup used for measuring the internal quality factor of our resonators in the CIRQUS lab is depicted in Fig. 3.4. The resonator chip is carefully mounted on the mixing chamber (MXC) stage, which operates at a base temperature of approximately 50 mK. To minimize thermal photon effects on the chip, the input lines are equipped with attenuators ($A_{4\mathrm{K}} + A_{\mathrm{Still}} + A_{\mathrm{MXC}}$), typically providing an attenuation between -40 to $-56\,\mathrm{dB}$. The cable loss is $15\,\mathrm{dB}$. Additionally, a K&L low-pass filter is incorporated to further reduce the influence of thermal photons.

To detect the small output signals, amplification is necessary. The output is amplified using a cryogenic HEMT amplifier ($+42\,\mathrm{dB}$), and subsequently, an RF amplifier at room temperature ($+22\,\mathrm{dB}$) is employed. This amplification setup enables the measurement of weak output signals. To prevent the amplified reflected signals from the amplifiers from passing through the chip, $50\,\Omega$ terminated circulators are utilized.

Dry dilution refrigerator

During this work, a dry dilution refrigerator has arrived in the institute, an LD400 from Bluefors, and we have been strongly engaged in setting it up. The cryogenic setup used for measuring the internal quality factor of our resonators in the MCQST lab is depicted in Fig. 3.4.

The basic configuration is the same as that of the CIRQUS lab.

3.2.2 Single-tone spectroscopy

Microwave spectroscopy is a powerful technique used in the frequency domain to determine the eigenfrequencies of a quantum device under investigation. These eigenfrequencies serve as a basis

[3]Note that the ^{3}He liquids are Fermi liquids and in the diluted phase the Fermi energy is much lower due to the lower density of ^{3}He. As the temperature of both liquids are the same (10 mK) the relative smearing of the Fermi distribution T/T_{F} is larger in the diluted phase due to the smaller T_{F} leading to a larger entropy.

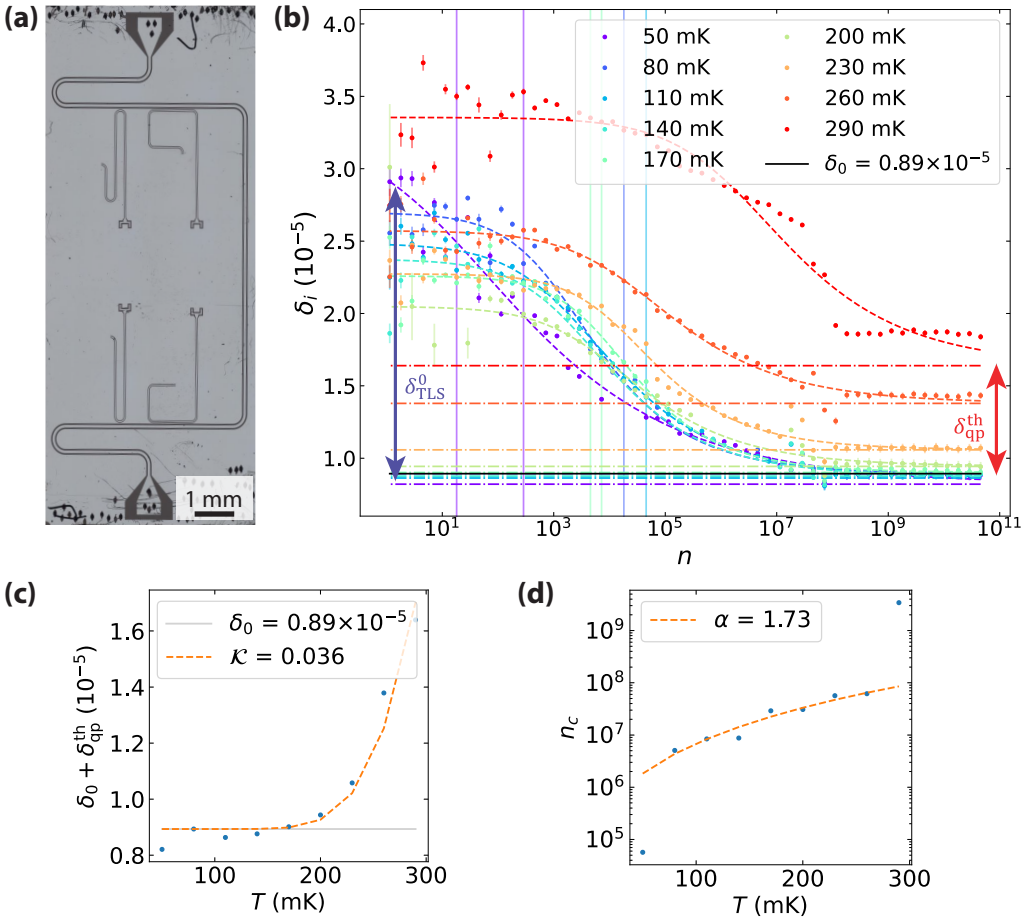

Figure 3.5. (a) Optical micrograph of the chip `Res-005`. The U-shape end of the resonators was initially designed with the intent to capacitively couple with an Xmon qubit in later stages. (b) Internal losses $\delta_i = 1/Q_i$ of the chip `Res-005` as a function of photon number n for different temperatures at $f_r = 5.82\,\text{GHz}$. The measurement data is represented by symbols, while the dashed lines correspond to the fit using Eq. (2.55). The dash-dotted lines indicate the base lines of power-independent losses, and the black solid line represents the base line of power- and temperature-independent losses. (c) Temperature dependence of power-independent losses $\delta_0 + \delta^{\rm th}_{\rm qp}$. The power- and temperature independent loss is found to be $\delta_0 = 0.89 \times 10^{-5}$. (d) Temperature dependence of the critical photon number n_c. The extracted exponent is $\alpha = 1.73$.

for further research and investigations and are often essential in understanding the device's behavior.

In single-tone spectroscopy, a continuous wave with a single carrier frequency, denoted as ω_d, is applied to the device. The amplitude and phase response of the device are then measured as a function of the driving frequency to identify its eigenfrequencies. This measurement is typically performed using a vector network analyzer (VNA), which measures the complex scattering coefficients $S_{ij}(\omega_d)$. The VNA provides information about the steady-state response of the system. Fig. 3.4 illustrates the setup of a VNA measurement. One common application of single-tone spectroscopy is the characterization of resonators or cavities, where resonant frequencies and quality factors (both external and internal) are determined using the methods described in Chap. 2.

3.2.3 Experimental results

Baseline resonators

In order to assess the quality factor of devices fabricated with the process developed at the WMI, we studied resonators fabricated with the Al lift-off technique. The chip design of the fabricated resonators is depicted in Fig. 3.5 (a). These resonators serve as a reference for subsequent optimization processes. The measurement of the quality factor is performed in a wet dilution refrigerator.

To distinguish between various sources of losses, such as TLS and quasiparticles, we investigate the dependence of the quality factor on probe power and temperature, as discussed in Chap. 2. The contribution of TLSs can be determined by studying the power dependence, while the influence of thermal quasiparticles can be quantified by measuring the temperature dependence. Fig. 3.5 (b) shows the internal losses $\delta_i = 1/Q_i$ as a function of the resonator photon number at different temperatures, with the mean resonator photon number calculated using

$$n_r = \left\langle \hat{a}_r^\dagger \hat{a}_r \right\rangle_{\mathrm{ss}} = \frac{4\kappa_{r,c}}{\kappa_r^2} \left| \langle \hat{a}_{\mathrm{in}} \rangle \right|^2 . \tag{3.4}$$

Here, κ_r is the total dissipation rate of the resonator, $\kappa_{r,c}$ is the external coupling strength of the resonator, and $|\langle \hat{a}_{\mathrm{in}} \rangle|^2$ is the input photon flux, which is proportional to the microwave power[4]. As anticipated, we observe that the TLS contribution increases as the photon number decreases. In the low photon number regime, there is significant absorption of resonator photons by the unsaturated TLS. Conversely, in the high power regime, the TLSs are getting increasingly saturated by already having absorbed photons, making it unable to absorb additional photons. Consequently, the amount of photons absorbed by the TLS becomes negligible compared to the number of photons present in the resonator. As the quality factor is defined as the ratio of stored energy and power loss per cycle, i.e. as the relative loss, it increases, although the absolute amount of loss stays the same. That is, δ_i decreases but not the loss per cyle. For our reference sample, the TLS loss is measured to be on the order of $\sim 10^{-5}$.

Additionally, we conduct a fitting analysis of the power-independent losses using Eq. (2.58), as depicted in Fig. 3.5 (c). Here, we utilize only the ratio of kinetic inductance to the total inductance of the material $\mathcal{K}$ as the free fitting parameter (see Eq. (2.58)). In Fig. 3.5 (d), we also observe that the critical photon number n_c increases with temperature, as higher temperatures lead to increased relaxation rates of the TLSs and broader energy level distributions due to their interactions, as described by Eq. (2.56). The extracted exponent, α, was found to be $\alpha = 1.73$, which is close to the typical literature values ranging from 2 to 3 [156, 162, 163]. This value deviates from the expected $\alpha = 1$ of the spin-boson model, which can be attributed to the fact that $\hbar\omega_r/k_{\mathrm{B}}T \approx 3 - 6$ for $T = 50 - 100\,\mathrm{mK}$, indicating that we are not operating in a sufficiently low-temperature limit $\hbar\omega_r/k_{\mathrm{B}}T \gg 1$ [164]. Notably, we discovered that thermal quasiparticle losses become negligible below 170 mK. Specifically, at the base temperature of CIRQUS of 50 mK, the losses due to thermal quasiparticles are expected to be below 10^{-20}. We note, however, the non-thermal quasiparticles, which can be generated for example by an insufficient protection of samples against infrared radiation, have to be avoided to keep quasiparticle losses small[5].

In contrast to thermal losses, we observe that other types of losses, represented by δ_0, are of a similar magnitude to the TLS losses, around 10^{-5}. This finding is consistent with the values reported

[4] See also Eq. (2.49) in Subsec. 2.4.3

[5] See also Subsec. 2.4.4 for more details.

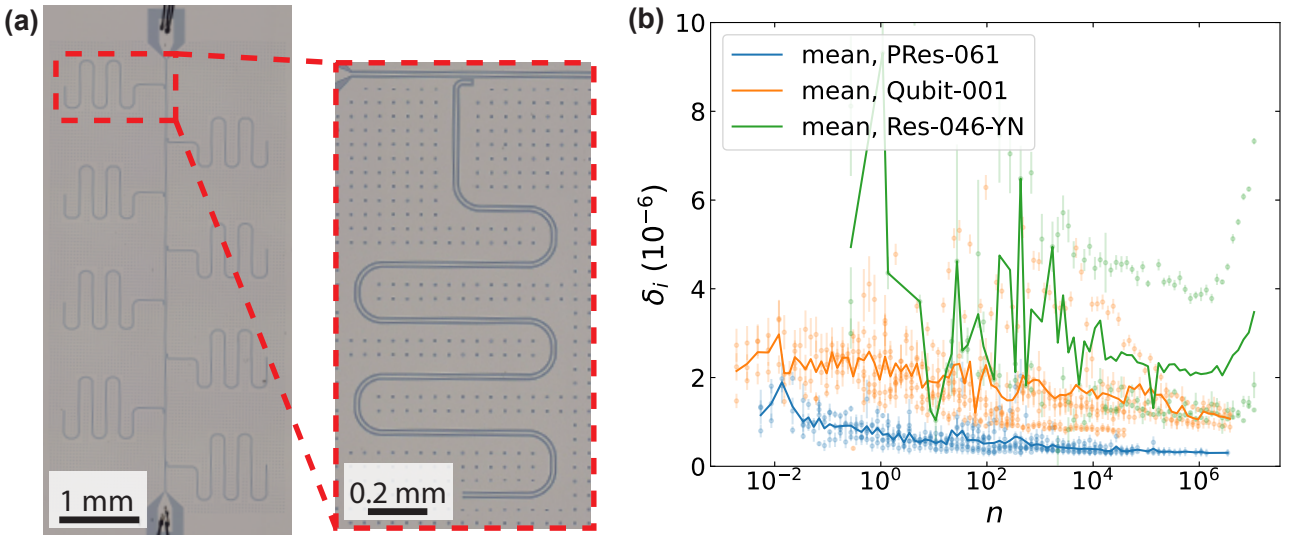

Figure 3.6. (a) Optical micrograph of the chip `PRes-061` with a zoomed picture of one resonator. The same design has been used for the chip `Qubit-001`. (b) Comparison of internal losses δ_i versus mean resonator photon number n across different fabrication processes and materials. Individual measured internal losses are indicated by dots for different resonances, with their mean values illustrated by solid lines. All chips underwent surface treatment: `Res-046-YN` is an Al sample with HF-dipped lift-off process, `Qubit-001` is an Al sample with Piranha and BOE using etching process, and `PRes-061` is a Nb sample with Piranha and BOE using etching process.

in [156], where the sample was fabricated using the same recipe at WMI [214]. However, we notice that δ_0 increases by one order of magnitude for the resonator at 6.21 GHz. This can be attributed to the parasitic mode of our sample box, which will be discussed in more detail later. A summary of our reference sample for different resonators is provided in Tab. 3.1.

f_r (GHz)	δ_i (10^{-5})	δ^0_{TLS} (10^{-5})	δ_0 (10^{-5})	α	β
5.82	3.38	2.49	0.89	1.73	0.70
6.21	17.5	1.79	15.8	2.19	0.57

Table 3.1. Summary of the reference sample `Res-005` for different resonators. The parameters f_r, δ_i, δ^0_{TLS}, δ_0, α and β are obtained by fitting Eqs. (2.54), (2.55), (2.56) and (2.58) to the measured power and temperature sweeps. The high loss δ_0 at $f_r = 6.21$ GHz is due to a parasitic mode, as it will be explained later. The sample `Res-005` is taken at $T = 50$ mK in the wet dilution refrigerator.

Resonators with surface treatment

Given that the dominant source of loss arises from SiO_2 layer covering the substrate surface, which hosts a significant number of TLS, we have performed a surface treatment to mitigate SiO_2 related losses. In this analysis, we consider three different samples: an Al sample fabricated using the HF-dipped lift-off process[6], an Al sample treated with Piranha and BOE using the wet etching, and an Nb sample treated with Piranha and BOE using the dry etching process.

In Fig. 3.6, we present a plot depicting the relationship between internal losses and the mean photon number for the various samples. Notably, we observe a significant enhancement of the internal quality factors compared to the previously reported values of the reference sample. These findings strongly suggest that the prominent contribution to losses arises from the presence of the silicon

[6]Here, we deeply appreciate Mora Linda and Prof. Dr. Ralf Meyer from Walther-Schottky Institute for making the HF-dip possible.

oxide layer. Upon closer examination of the internal losses among the different samples, a consistent trend emerges: $\delta_i^{\mathrm{LO,Al}} > \delta_i^{\mathrm{Etch,Al}} > \delta_i^{\mathrm{Etch,Nb}}$. The increased losses observed for the lift-off sample, in comparison to the etched samples, can likely be attributed to the residual resist that remains after the development process. This residual resist may contribute to additional TLS losses at the metal/substrate interface. This explains the comparatively large δ_{TLS}^0, while similar power-independent loss values $\delta_0^{\mathrm{LO,Al}} \approx \delta_0^{\mathrm{Etch,Al}}$ are measured when compared to the Al etched sample. It is worth noting that the resistivity of the Si substrate has increased from $2\,\mathrm{k\Omega \cdot cm}$ to $10\,\mathrm{k\Omega \cdot cm}$, resulting in improved internal quality factors [229]. However, it is important to consider that these values may change completely different at low temperatures and the impact of resistivity is relatively limited, as achieving internal quality factors on the order of $Q_i \sim 10^7$ is still possible even with a resistivity of $3\,\mathrm{k\Omega \cdot cm}$ [230]. Furthermore, it is crucial to investigate the influence of parasitic modes, as the lift-off sample appears to be primarily limited by such modes. Detailed discussions regarding this issue will be provided in more detail later in this thesis.

sample	material	surface treat.	process	f_r (GHz)	δ_i (10^{-6})	δ_{TLS}^0 (10^{-6})	δ_0 (10^{-6})
`Res-046-YN`	Al	HF, 3 min	lift-off	5.08	2.47	1.76	0.71
				5.72	5.81	4.60	1.21
				5.99	11.59	9.89	1.70
`Qubit-001`	Al	Piranha	etch	5.16	2.09	1.27	0.82
		+BOE, 30 s		5.38	2.01	1.21	0.80
				5.65	1.86	1.05	0.81
				5.90	2.53	0.49	2.04
				6.14	1.6	0.98	0.62
				6.39	3.65	2.52	1.13
				6.63	2.44	1.02	1.42
`PRes-061`	Nb	Piranha	etch	4.84	2.46	2.27	0.19
		+BOE, 30 s		5.21	1.11	0.95	0.16
				5.41	1.11	0.91	0.20
				5.46	0.72	0.54	0.18
				5.69	0.66	0.45	0.21
				5.92	1.07	0.76	0.31
				6.14	1.38	1.24	0.14
				6.37	1.24	0.98	0.26

Table 3.2. Summary of the samples with surface treatment for different resonators: `Res-046-YN`, `Qubit-001`, and `PRes-061`. The parameters f_r, δ_i, δ_{TLS}^0, and δ_0 are obtained by fitting Eqs. (2.54) and (2.55) to power sweeps. The sample `Res-046-YN` is taken at $T = 50\,\mathrm{mK}$ in the wet dilution refrigerator, while the samples `Qubit-001`, and `PRes-061` are measured at $T < 7\,\mathrm{mK}$ in the dry dilution refrigerator.

Additionally, when comparing the Al and Nb samples, we observe a further improvement in the internal quality factors for Nb resonator. Specifically, the power independent losses δ_0 are reduced by one order of magnitude. This can be attributed to the larger superconducting gap of Nb, with a critical temperature of 9.3 K compared to Al with 1.2 K. As a result, fewer non-thermal quasiparticles are generated in Nb, leading to improved quality factors. A summary of our samples is provided in Tab. 3.2.

Furthermore, we can enhance the internal quality factors of Nb by employing a post-BOE process to reduce the niobium oxides on the metal surface, potentially reaching values up to 5×10^6. This enhancement has been investigated in more detail by another research group at WMI [217, 219].

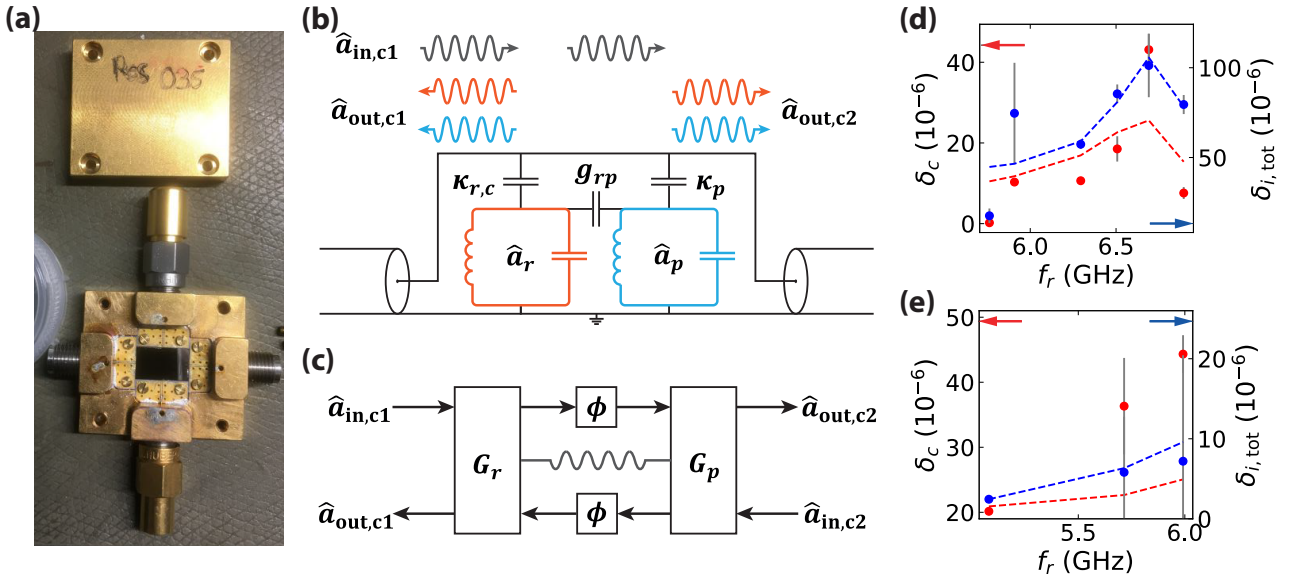

Figure 3.7. (a) Picture of four-port sample box with a resonator chip. (b) Lumped-element representation of the theoretical model. The progression of an incoming propagating wave, $\hat{a}_{\text{in,c1}}$, is illustrated (grey wave). This wave encounters and engages with two distinct modes: the resonator mode, $\hat{a}_r$, and the parasitic mode, $\hat{a}_p$. After absorption, each mode reemits as distinct outgoing traveling waves, $\hat{a}_{\text{out,c1}}$ and $\hat{a}_{\text{out,c2}}$. As a consequence, an interference effect appears between the waves originating from the resonator mode (orange wave) and parasitic mode (blue wave). (c) Schematic representation of the same theoretical model with $G_r = (S_r, \hat{L}_r, \hat{\mathcal{H}}_r)$ and $G_p = (S_p, \hat{L}_p, \hat{\mathcal{H}}_p)$. The wiggle represents the interaction between the resonator and parasitic mode. (d) External (red) and internal (blue) losses of the sample `Res-086-YN` as a function of resonator frequencies. The dots are measurement data, and the dashed lines are the fit using the Eqs. (3.10) and (3.11). (e) External (red) and internal (blue) losses of the sample `Res-046-YN` as a function of resonator frequencies. The dots are measurement data, and the dashed lines are the fit using the Eqs. (3.10) and (3.11). Here, due to insufficient data points, we assumed that the parasitic mode frequency ω_p and its bandwidth κ_p are the same.

.

Influence of chip and box modes

Previously, we observed the increase of losses for certain resonance frequencies both in baseline resonators and resonators with surface treatment. There, we pointed out the presence of chip and box modes which can introduce additional loss channels in quantum devices. These modes correspond to chip modes forming inside the substrate and cavity modes within the sample box, where the electric fields can overlap with the electric field generated by the quantum system, allowing for interaction. Our investigations reveal that these parasitic modes - a term we adopt due to our inability to distinguish between chip and box modes in this study - may have significant impact on both internal and external quality factors. To differentiate them, similar to designing cavity eigenmodes, the eigenfrequencies of the box and chip modes can be engineered by carefully designing the sample boxes. In particular, the size and the effective dielectric constant determine these eigenfrequencies. Indeed, we show that the internal quality factors change dependent on the sample boxes we use.

Our analysis begins by exploring the influence of parasitic modes in the four-port sample box on the system's internal and external quality factors. The corresponding loss measurements are presented in Fig. 3.7 (d). An initial observation reveals that it displays increased losses around 6.7 GHz coinciding with the eigenfrequency of the parasitic mode. The interesting point is that the `Res-086-YK` design experiences an increase in internal *and* external losses. To explain the underlying physics, we delve

into the scenario illustrated in Fig. 3.7 (b, c): the resonator and parasitic mode are directly interacting with each other and are both linked to the transmission line.

The outgoing traveling wave of the resonator serves as the incoming wave for the parasitic mode after accumulating a phase shift ϕ, and vice versa. Representing this interplay via a block diagram in Fig. 3.7 (c), a coherent feedback mechanism becomes evident. As anticipated in Chap. 2, such feedback pathways can be integrated within the SLH framework, leading to the determination of an effective SLH $G_{rp} = (S_{rp}, \hat{\mathbf{L}}_{rp}, \hat{\mathcal{H}}_{rp})$. After a slight modification of Eq. (2.45), we find

$$S_{rp} = e^{i\phi} \begin{bmatrix} 1 & 0 \\ 0 & 1 \end{bmatrix} \tag{3.5a}$$

$$\hat{\mathbf{L}}_{rp} = \begin{bmatrix} \sqrt{\kappa_p/2}\hat{a}_p + e^{i\phi}\sqrt{\kappa_{r,c}/2}\hat{a}_r \\ \sqrt{\kappa_{r,c}/2}\hat{a}_r + e^{i\phi}\sqrt{\kappa_p/2}\hat{a}_p \\ \sqrt{\kappa_{r,i}}\hat{a}_r \end{bmatrix} \tag{3.5b}$$

$$\hat{\mathcal{H}}_{rp}/\hbar = \Delta_r \hat{a}_r^\dagger \hat{a}_r + \Delta_p \hat{a}_p^\dagger \hat{a}_p + g_{rp}\left(\hat{a}_r^\dagger \hat{a}_p + \hat{a}_r \hat{a}_p^\dagger\right) + \sqrt{\frac{\kappa_{r,c}\kappa_p}{4}} \sin\phi \left(\hat{a}_r^\dagger \hat{a}_p + \hat{a}_r \hat{a}_p^\dagger\right), \tag{3.5c}$$

with the phase $\phi = 2\pi\omega_d\sqrt{\epsilon_r}\bar{d}/c$ acquired by a photon along the propagation path. Here, $\bar{d}$ is the physical distance between the resonator and parasitic mode. The external dissipation rate of the resonator and the parasitic mode is given by $\kappa_{r,c}$ and κ_p, respectively, while the internal one of the resonator is defined as $\kappa_{r,i}$. $\Delta_{r/p} = \omega_{r/p} - \omega_d$ is the detuning, $\hat{a}_{r/p}^{(\dagger)}$ are annihilation (creation) operators of the resonator and parasitic mode, respectively, and g_{rp} is the effective coupling strength between the resonator and parasitic mode. Interestingly, our Hamiltonian, as expressed in Eq. (3.5c), reveals an effective coupling between the two modes. This phenomenon can be rooted in the established principle of the input-output relation, which dictates that an outgoing traveling wave invariably carries information of the originating quantum system. For clarity, we consider, without loss of generality, the scenario where we are examining the outgoing traveling wave emanating from the parasitic mode, $\hat{a}_p$. Given its trajectory, this wave eventually engages with the resonator mode, $\hat{a}_r$, due to their shared connection to the same transmission line. Consequently, the outgoing wave from the parasitic mode is perceived as the incoming wave for the resonator mode. As this wave retains information from the parasitic mode, it effectively mediates an interaction between the resonator and the parasitic mode.

Given $G_{rp} = (S_{rp}, \hat{\mathbf{L}}_{rp}, \hat{\mathcal{H}}_{rp})$ in Eq. (3.5), the quantum Langevin equation yields

$$\begin{aligned} \frac{\mathrm{d}}{\mathrm{d}t}\begin{bmatrix} \hat{a}_r \\ \hat{a}_p \end{bmatrix} = &\begin{bmatrix} -i\Delta_r - \frac{\kappa_{r,c}+\kappa_{r,i}}{2} & -ig_{rp} + \sqrt{\frac{\kappa_r\kappa_p}{2}}e^{i\phi} \\ -ig_{rp} + \sqrt{\frac{\kappa_r\kappa_p}{4}}e^{i\phi} & -i\Delta_p - \frac{\kappa_p}{4} \end{bmatrix}\begin{bmatrix} \hat{a}_r \\ \hat{a}_p \end{bmatrix} \\ &- \begin{bmatrix} \sqrt{\frac{\kappa_{r,c}}{2}} & \sqrt{\frac{\kappa_{r,c}}{2}}e^{i\phi} & \sqrt{\kappa_{r,i}} \\ \sqrt{\frac{\kappa_p}{2}}e^{i\phi} & \sqrt{\frac{\kappa_p}{2}} & 0 \end{bmatrix}\begin{bmatrix} \hat{a}_{\mathrm{in,c1}} \\ \hat{a}_{\mathrm{in,c2}} \\ \hat{a}_{\mathrm{in,i1}} \end{bmatrix}, \end{aligned}$$

and the corresponding input-output relation

$$\begin{bmatrix} \hat{a}_{\mathrm{out,c1}} \\ \hat{a}_{\mathrm{out,c2}} \\ \hat{a}_{\mathrm{out,i1}} \end{bmatrix} = \begin{bmatrix} \sqrt{\frac{\kappa_{r,c}}{2}}e^{i\phi} & \sqrt{\frac{\kappa_{r,c}}{2}} \\ \sqrt{\frac{\kappa_p}{2}} & e^{i\phi}\sqrt{\frac{\kappa_p}{2}} \\ \sqrt{\kappa_{r,i}} & 0 \end{bmatrix}\begin{bmatrix} \hat{a}_r \\ \hat{a}_p \end{bmatrix} + \begin{bmatrix} \hat{a}_{\mathrm{in,c1}} \\ \hat{a}_{\mathrm{in,c2}} \\ \hat{a}_{\mathrm{in,i1}} \end{bmatrix}. \tag{3.6}$$

The scattering coefficient for the transmission measurement can be then written in the steady state as

$$S_{21} = \frac{\langle \hat{a}_{\text{out,c2}} \rangle}{\langle \hat{a}_{\text{in,c1}} \rangle} = \frac{-z_{r,c}^{(\text{eff})}}{i\Delta_r + z_{r,i}^{(\text{eff})}/2 + z_{r,c}^{(\text{eff})}/2} \tag{3.7}$$

with the effective external and internal complex "dissipation rate"

$$z_{r,c}^{(\text{eff})} = \frac{\kappa_{r,c}}{2} - \frac{ig_{rp}\sqrt{\kappa_{r,c}\kappa_p}e^{i\phi} + \kappa_{r,c}\kappa_p e^{2i\phi}/4 + i\Delta\kappa_p e^{2i\phi}/2}{i\Delta_p + \kappa_p/2} \tag{3.8}$$

$$z_{r,i}^{(\text{eff})} = \kappa_{r,i} + \frac{2g_{rp}^2}{i\Delta_B + \kappa_p/2} - \frac{ig_{rp}\sqrt{\kappa_{r,c}\kappa_p}e^{i\phi} + \kappa_{r,c}\kappa_p e^{2i\phi}/4 + i\Delta_r\kappa_p e^{2i\phi}/2}{i\Delta_p + \kappa_p/2}. \tag{3.9}$$

For a consistency check, we can observe that we recover Eq. (2.52) for $|\Delta_p| \to \infty$. The real-valued external and internal dissipation rate is given by

$$\begin{aligned}
\kappa_{r,c}^{(\text{eff})} &= \text{Re}\left[z_{r,c}^{(\text{eff})}\right] \\
&= \frac{\kappa_{r,c}}{2} + \frac{g_{rp}\sqrt{\kappa_{r,c}\kappa_p}\left(\frac{\kappa_p}{2}\sin(\phi) - \Delta_p\cos(\phi)\right) - \frac{\kappa_{r,c}\kappa_p}{4}\left(\Delta_p\sin(2\phi) + \frac{\kappa_p}{2}\cos(2\phi)\right)}{\Delta_p^2 + (\kappa_p/2)^2}
\end{aligned} \tag{3.10}$$

$$\begin{aligned}
\kappa_{r,i}^{(\text{eff})} &= \text{Re}\left[z_{r,i}^{(\text{eff})}\right] \\
&= \kappa_{r,i} + \frac{g_{rp}^2\kappa_p}{\Delta_p^2 + (\kappa_p/2)^2} \\
&\quad + \frac{g_{rp}\sqrt{\kappa_{r,c}\kappa_p}\left(\frac{\kappa_p}{2}\sin(\phi) - \Delta_p\cos(\phi)\right) - \frac{\kappa_{r,c}\kappa_p}{4}\left(\Delta_p\sin(2\phi) + \frac{\kappa_p}{2}\cos(2\phi)\right)}{\Delta_p^2 + (\kappa_p/2)^2}.
\end{aligned} \tag{3.11}$$

Here, we have set $\Delta_r = 0$ because the measurements are conducted at around resonator frequencies, which are equivalent to the driving frequencies.

First, our observations highlight a Lorentzian distribution in both internal and external couplings. Notably, changes in the external dissipation rate can arise from interactions mediated by the transmission line, as highlighted in Eq. (3.10). Naturally, one might wonder about the underlying mechanism allowing for these variations in the external coupling rate. The answer lies in the interference of the traveling waves. In a scenario where the phase shift is $\pi/2$ and $\Delta_p = g_{rp} = 0$, we see a pronounced scattering value, $S_{21} = 1$, as opposed to the more typical $S_{21} = 1/2$ observed in transmission measurements. In conventional scenarios, half the information is typically lost due to reflection, making this maximal value look like as the signal has undergone "amplification", even in passive systems. However, it is pivotal to recognize that our unique configuration introduces a secondary traveling wave, as illustrated in Fig. 3.7 (b). This wave is originating from the second mode, which has absorbed the propagating wave coming from the first mode and then reemitted. Given its path length, this wave accumulates a phase shift of 2ϕ. Specifically, at $\phi = \pi/2$, the primary and secondary waves undergo destructive interference, ensuring no information loss. In tandem, the wave we measure undergoes constructive interference, effectively doubling the observed signal.

In terms of the internal losses, this outcome underscores the existence of an alternate decay pathway for the resonator photon, facilitated by the parasitic mode. Once the resonator photon is converted into the parasitic photon, it rapidly dissipates into the surrounding environment, characterized by the rate κ_p. The pronounced Lorentzian trend can be attributed to the detuning between the resonator and the parasitic mode. When these frequencies are perfectly aligned, photon interaction peaks, optimizing

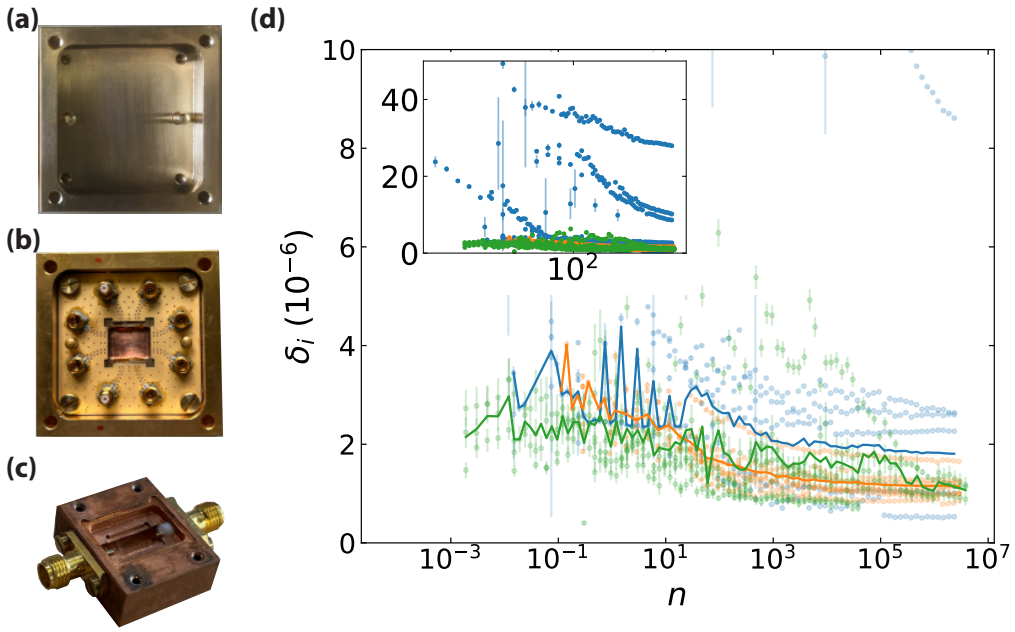

Figure 3.8. (a) Picture of an eight-port sample box without valley. (b) Picture of eight-port sample box with valley. The size of the rectangular hole in the center is 12 mm × 9 mm × 2 mm. (c) Picture of two-port sample box with valley. This sample box is simulated and fabricated by [174]. (d) Comparison of internal losses δ_i versus photon number n between different sample boxes: eight-port sample box without valley (blue), eight-port sample box with valley (orange), and two-port sample box with valley (green). Individual measured internal losses are indicated by dots for different resonances, with their mean values illustrated by solid lines. The losses of parasitic modes shown in "eight-port sample box without valley" are not included in the mean value calculation.

conversion. Conversely, as the detuning widens, the conversion efficiency is suppressed considerably.

Using the Eqs. (3.10) and (3.11), we can extract all parasitic mode and resonator parameters. In particular, we obtain $\omega_p/2\pi = 6.73\,\text{GHz}$ with $\kappa_p/2\pi = 0.50\,\text{GHz}$ for parasitic modes, while $\kappa_{r,i}/2\pi = 0.23\,\text{MHz}$ for the resonator modes. The coupling strength between both modes is determined to be $g_{rp}/2\pi = 6.79\,\text{MHz}$. We can already find the large influence of the parasitic mode. For example, if we take the resonator mode at 6.69 GHz, we can extract that the internal loss due to the direct interaction is $\delta_{i,\text{int}} \approx 54 \times 10^{-6}$, which is even larger than the intrinsic loss of resonator with $\delta_{i,r} \approx 34 \times 10^{-6}$. The loss originating from the mediated interaction is also comparable to other losses with $\delta_{i,\text{med}} \approx 12 \times 10^{-6}$. Furthermore, if we want to suppress the influence of parasitic modes less than 10^{-6}, we need to locate our resonator frequencies in the range below 4.5 GHz.

Indeed, regarding the limitations of the lift-off sample discussed earlier, we can observe this problem in Fig. 3.7 (e). `Res-046-YN` was measured using the same four-port sample box, which was not optimized for mitigating parasitic modes. We find that the external and internal losses are increasing with higher resonator frequencies, which already suggest the influence of the parasitic mode. Assuming that the extracted parasitic mode parameters are applicable to the lift-off sample as well, we obtain the intrinsic loss of the resonator as $\delta_{i,r} \approx 2 \times 10^{-6}$, which is consistent with the values obtained for `Qubit-001` and other aluminum resonator chips [218]. The coupling strength is extracted to be $g_{rp}/2\pi = 1.31\,\text{MHz}$, which is comparable to the value obtained for `Res-086-YN`.

Despite adopting certain assumptions that may not fully align with actual conditions - such as the same parasitic mode parameters, constant dissipation rates given by $\kappa_{r,i}$ and $\kappa_{r,c}$, and consistent coupling strength g_{rp} across all resonators - the data was still fitting reasonably well. This further

sample box	f_r (GHz)	δ_i (10^{-6})	δ^0_{TLS} (10^{-6})	δ_0 (10^{-6})
eight-port	5.16	3.75	1.51	2.24
w/o valley	5.53	20.15	10.91	9.24
	5.65	4.13	3.67	0.46
	5.895	4.68	2.42	1.66
	6.14	2.26	1.21	1.05
	6.39	3.81	1.22	2.59
	6.63	4.12	1.39	2.73
eight-port	5.16	2.60	1.40	1.20
w/ valley	5.38	2.17	1.29	0.88
	5.65	3.85	2.82	1.03
	5.90	2.02	1.01	1.01
	6.14	3.10	1.91	1.19
	6.39	3.00	1.33	1.67
	6.63	2.76	1.47	1.29
two-port	5.16	2.09	1.27	0.82
w/ valley	5.38	2.01	1.21	0.80
	5.65	1.86	1.05	0.81
	5.90	2.53	0.49	2.04
	6.14	1.6	0.98	0.62
	6.39	3.65	2.52	1.13
	6.63	2.44	1.02	1.42

Table 3.3. Summary of the sample `Qubit-001` characterized in different sample boxes: eight-port without valley, eight-port with valley, and two-port with valley. The parameters f_r, δ_i, δ^0_{TLS}, and δ_0 are obtained by fitting Eqs. (2.54) and (2.55) to power sweeps.

highlights the importance of careful sample box engineering to reduce the influence of parasitic modes.

We now study how to mitigate the loss induced by the chip mode. Here, we study three different sample boxes: eight-port sample box without valley, eight-port sample box with valley, which has a hole size of 12 mm × 9 mm × 2 mm, and two-port sample box with valley, which has a semi-cylindrical shape with a radius of 2 mm and a length of 14 mm.

The impact of box modes is shown in Fig. 3.8 (d). As discussed in Chap. 2, mitigation of chip modes can be achieved through two approaches: minimizing the overlap of the electric fields and shifting the eigenfrequencies to higher values. The former can be accomplished by drilling a hole into the eight-port box, while the two-port sample box achieves both objectives. Specifically, reducing the dimensions of the sample box results in a higher eigenfrequency.

We observe significant improvement of the quality factors of in the Piranha and BOE treated Al sample when changing the sample box from an eight-port box without a hole to an eight-port box with a hole, and finally to the two-port box. The internal quality factor was found to improve by 70% from $\delta^{\mathrm{Etch,Al}}_{i,\mathrm{eight-port\ w/o\ hole}} = 2.3 \times 10^{-6}$ to $\delta^{\mathrm{Etch,Al}}_{i,\mathrm{two-port}} = 1.6 \times 10^{-6}$. The summary of the relevant parameters of this sample can be found in Tab. 3.3.

3.3 Qubit characterization

As our goal of this chapter is to benchmark the coherence time of the superconducting qubit, we finally perform an investigation of a fixed-frequency transmon qubit chip, using the insights gained in Sec. 3.2. The fabrication of this chip integrates the Nb etching process for constructing the larger structures,

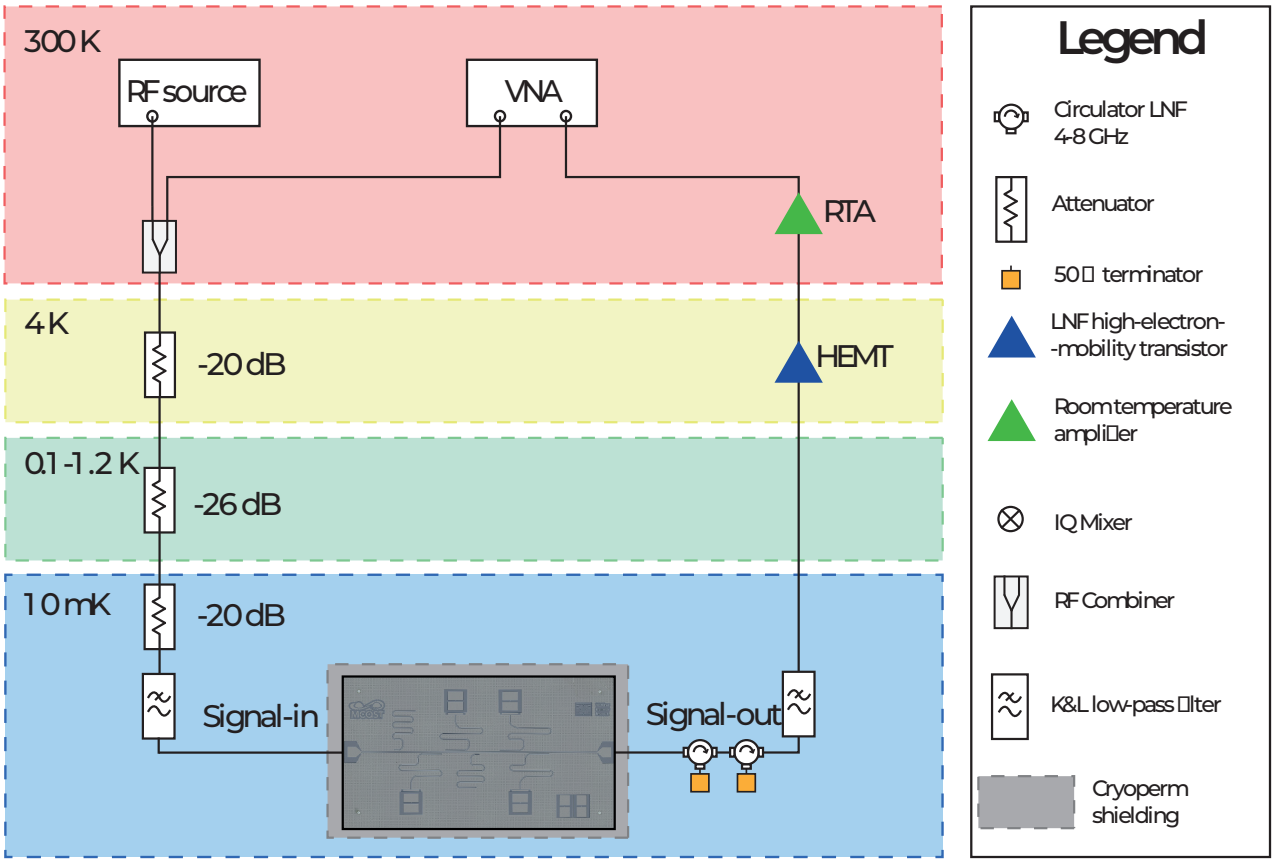

Figure 3.9. Schematic drawing of dry dilution refrigerator embedding qubit chip for the spectroscopy measurement.

followed by the lift-off procedure for creating the $Al/AlO_x/Al$ Josephson junctions, as discussed in detail in Sec. 3.1. Our fabrication process commences with a silicon $\langle 100 \rangle$ substrate, which possesses a resistivity of $\rho = 10\ k\Omega \cdot cm$. We begin by subjecting the substrate to a Piranha etch followed by a 30 s HF dip. Subsequently, we deposit a 150 nm-thick layer of Nb on the substrate using a PLASSYS system. Once the Nb layer is in place, we employ optical lithography in combination with reactive ion etching to pattern the desired structures into the Nb film. The chip is then coated with a double-layer electron beam resist to provide the mask needed for the formation of $Al/AlO_x/Al$ Josephson junctions. As the final step in the fabrication process, we lay 300 nm-thick Al bandages between the Al stripes and the Nb ground plane. This arrangement ensures a galvanic contact between the two materials. Fig. 3.3 shows the optical micrograph of our transmon qubit chip.

3.3.1 Qubit spectroscopy measurement

Qubit spectroscopy is a fundamental technique used to probe and characterize qubits. By studying the response of qubits to specific input signals, we gain valuable insights into their properties and behavior. Two commonly used spectroscopy methods in qubit measurement are single-tone spectroscopy and two-tone spectroscopy. They allow us to probe the behavior of qubits and extract important information about their characteristic frequencies, as well as their presence and coupling dynamics. In the following sections, we will delve deeper into the principles and applications of single-tone and two-tone spectroscopy techniques. In Fig. 3.9, the schematic drawing of our spectroscopy measurement is shown. All power levels depicted in Fig. 3.10 are at the sample stage. Calibration was performed using two-tone spectroscopy in conjunction with the dispersion relation provided by Eqs. (2.72) and (3.4).

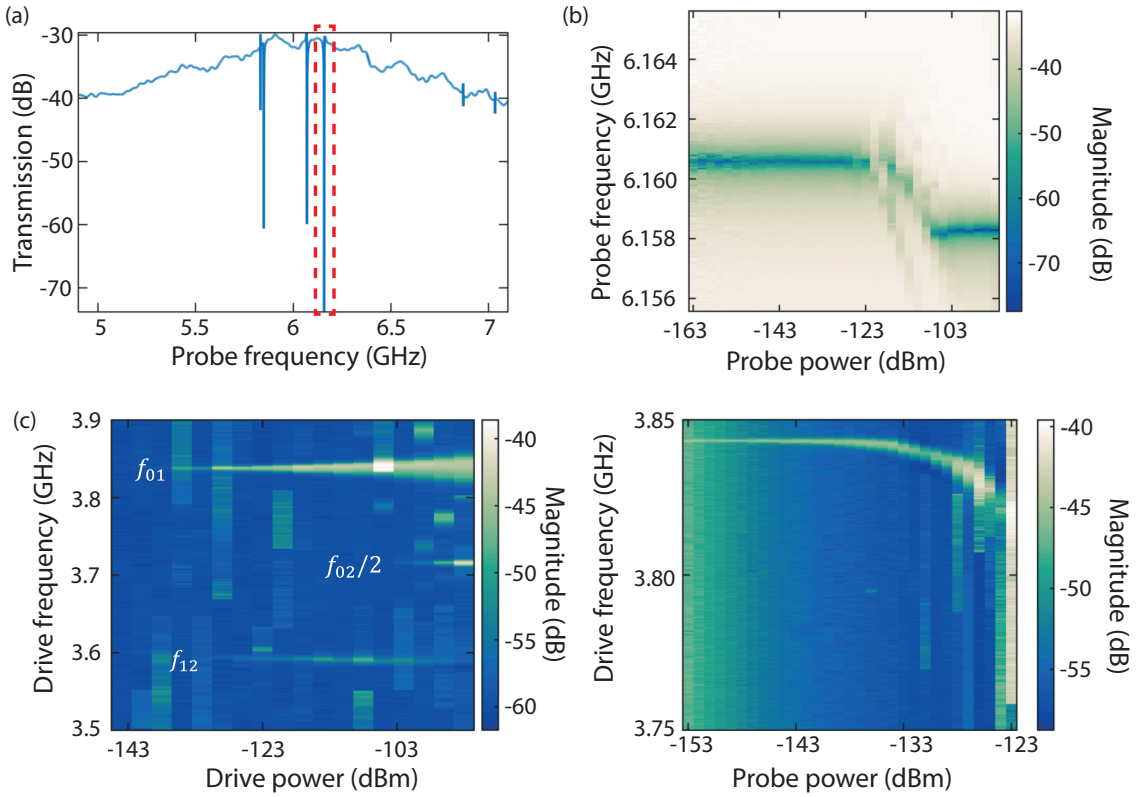

Figure 3.10. Spectroscopy measurement of the qubit chip `Qubit-KH079`. (a) Microwave transmission amplitude plotted over a broad frequency range. The dashed red box highlights the transmission dip due to the readout resonator at around 6.158 GHz, which is coupled to the qubit and is here used as an example. (b) Single-tone spectroscopy measurement as a function of probe power around the specific readout frequency of 6.158 GHz. The "punch out" effect can be observed above −113 dBm. In addition, we notice that the readout frequency in the dressed state is greater than that in the bare state. This demonstrates that the qubit frequency is lower than the readout frequency, as implied by the relationship $\omega_r + \chi_{qr}\hat{\sigma}_z$. (c) Two-tone spectroscopy measurement as a function of drive prower. The qubit frequency at $f_{01} = 3.843$ GHz and the two-photon process at $f_{02}/2 = 3.721$ GHz can be seen. Due to a finite qubit temperature, we can observe a transition between the first and second excited state $f_{12} = 3.599$ GHz. (d) Two-tone spectroscopy as a function of probe power. The qubit frequency shifts as a function of readout photon due to ac-Stark shift.

Single-tone spectroscopy

Single-tone spectroscopy serves three main purposes in qubit measurement. Firstly, it enables us to determine the readout frequency of the resonator similarly to Sec. 3.2. Secondly, it confirms the presence of the qubit within the qubit-coupled resonator system. Lastly, it allows us to determine whether the qubit frequency is above or below the readout frequency. These objectives are achieved simultaneously through a probe power sweep.

In the low power regime, where the resonator is weakly driven, the eigenfrequency of the resonator corresponds to the dressed eigenstate of the resonator mode. However, in the high power regime, a phenomenon known as "punch out" occurs [83] as demonstrated in Fig. 3.10(b). This refers to the observation of the eigenfrequency of the bare resonator mode as the transmon qubit is strongly off-resonantly driven. In this regime, the transmon qubit occupies highly excited states above the Josephson potential, behaving like a free phase particle [71, 72]. Consequently, the charge state becomes highly localized, resulting in a vanishing electric dipole moment and effective decoupling

of the transmon from the resonator. This phenomenon is often referred to as transmon ionization [73] or other terms such as first order dissipative phase transition [80, 81, 86], break-down of photon blockade [77], or chaotic regime [74].

Furthermore, in the dispersive regime, the sign of the cross-Kerr interaction strength (or ac-Stark shift) is determined by the detuning between the qubit and readout frequencies Δ_{qr}, as shown in Eq. (2.70). By comparing the eigenfrequencies in the dressed state and the bare state, we can determine whether the qubit frequency is above or below the readout frequency.

Two-tone spectroscopy

In two-tone spectroscopy, an advanced technique for characterizing quantum devices, two carrier frequencies are employed to measure both the amplitude and phase response of the device under test. This method utilizes a VNA to measure the scattering coefficients and requires a microwave source, such as an SGS source, to generate the second carrier frequency.

In the case of qubit measurements, the VNA serves as the readout instrument providing the probe tone, while the microwave source is responsible for driving the qubit. For instance, to determine the qubit frequency or transmon multi-photon transitions, the driving frequency of the microwave source is swept across the expected frequency range. Meanwhile, the readout power is set to a few readout photon level at a fixed readout frequency. By varying the drive power, we obtain a spectroscopy measurement that reveals characteristic features, as depicted in Fig. 3.10 (c). Another application of two-tone spectroscopy is photon number calibration, which makes use of the dispersive regime and the associated equations. Once the qubit frequency has been determined, we can perform sweeps around this eigenfrequency while adjusting the readout photons. As the photon number increases linearly, it induces changes in the qubit frequency and the bandwidth of the Lorentzian shape[7] (see Fig. 3.10 (d)).

3.3.2 Time-domain measurement setup

Pulse generation setup

By establishing precise synchronization and utilizing arbitrary waveform generators (AWG) and microwave sources, we can generate tailored microwave pulses for qubit control and readout, enabling accurate manipulation and measurement of the qubit state.

The pulse generation setup is a crucial component for controlling and reading out the qubit state in our experiments. We employ microwave pulses, which are shaped using an AWG. Specifically, we use the HDAWG from Zurich Instruments as our AWG, along with the R&S SMF100A and R&S SMB100A microwave sources[8]. To combine the pulsed qubit drive and readout drive, we utilize a power combiner. The combined signal is then sent to the cryostat, where the qubit control and measurement take place. A schematic of the pulse generation setup can be found in Fig. 3.11.

[7] This holds true as long as we can ensure homogeneous broadening. Nevertheless, at a certain threshold of photon number, a transition to inhomogeneous broadening occurs, a broadening that grows with $\sqrt{n_r}$ due to a Gaussian distribution. The emergence of this Gaussian line can be traced back to strong measurements where the measurement rate surpasses the external coupling rate of the readout resonator. Consequently, the qubit transition frequency becomes contingent upon the instantaneous value of the photon number in the readout resonator. For large photon numbers, this distribution tends towards Gaussian [231]. In certain instances, this critical photon number could be so low that calibration of the photon number based on a linear relation becomes challenging. Hence, an alternative and dependable method for photon number calibration is the use of Ramsey measurements, which will be later performed for single-photon detection measurements.

[8] Note: The phase stability of these devices was found to be insufficient for certain measurements, such as T_2 measurements and phase readout. Consequently, we replaced these microwave sources with the R&S SGS100A for single-photon detection measurements.

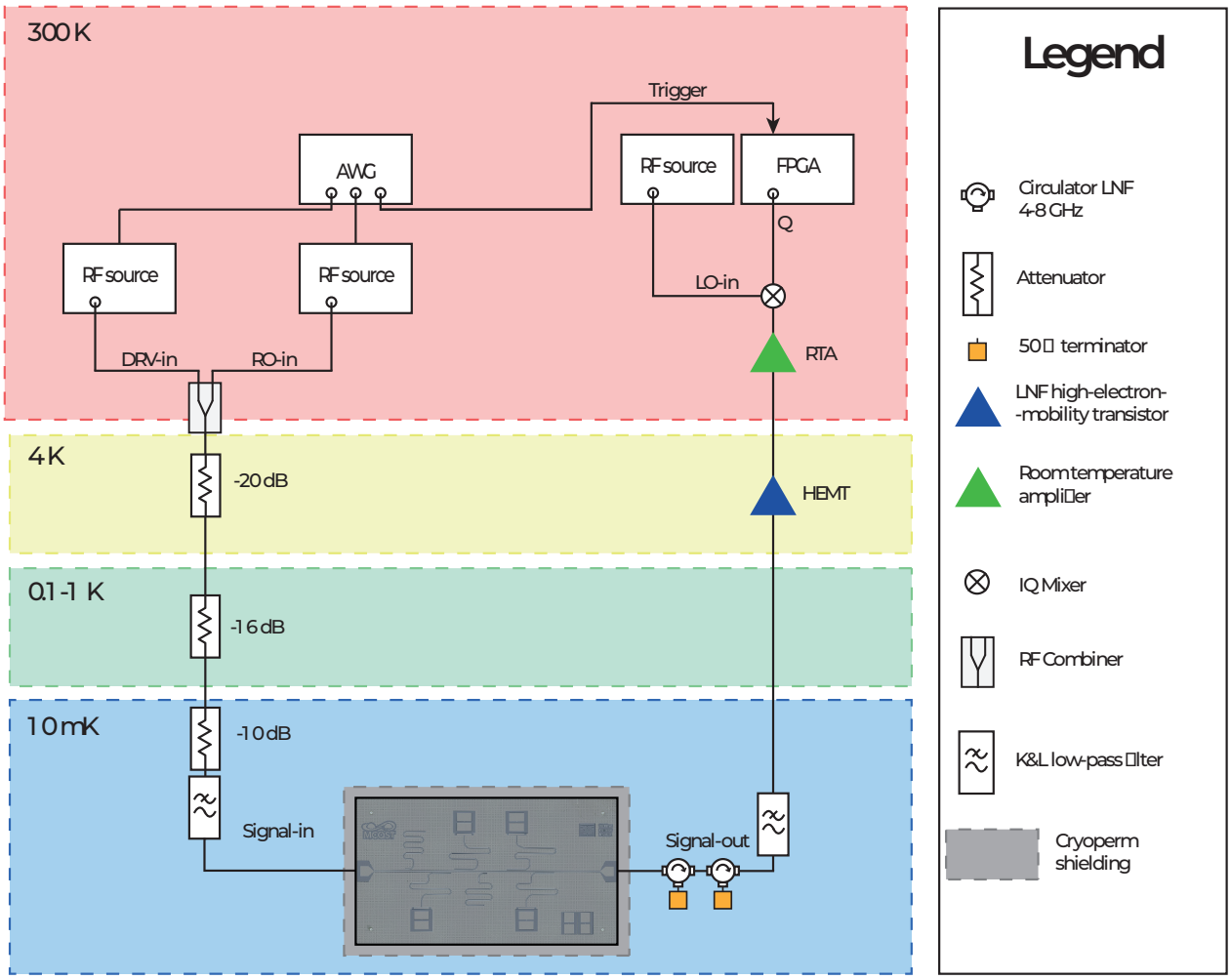

Figure 3.11. Schematic drawing of dry dilution refrigerator embedding qubit chip for the time-domain measurement.

To generate the waveforms that drive the qubit and readout pulses, we digitally synthesize them and load them into the HDAWG using our measurement software, which is programmed in LabView. Our measurement software dynamically adapts the number of waveform points to match the desired cycle length, ensuring a temporal precision of approximately 3.3 ns. Typically, a waveform consists of 2400 points for a cycle time of 1 μs[9].

Precise synchronization among all devices is crucial for performing accurate time-resolved measurements. In our setup, synchronization serves two main purposes. First, it ensures that all devices share the same frequency standard, which is essential for coherent control and measurement of the qubit. Second, it ensures that the readout pulse arrives precisely at the start of data acquisition by the digitizer card. To achieve this, the TTL synchronization output of the readout marker channel triggers the FPGA for data acquisition. This trigger is sent to the FPGA immediately after the readout pulse. To account for the propagation time of the pulse through the setup, we introduce a delay in the generated pulse using the synthesized waveform from that channel. Typically, the time delay for the trigger pulse in our system is approximately 250 ns.

To maintain a common frequency standard, we rely on an atomic clock based on rubidium-87 atoms.

[9]Note: The HDAWG has a sampling rate of 2.4 GSa, with a sequencer clock rate of 0.3 GHz, which is required for the instructions from the 16 bit sequencer. As a result, waveform lengths must be multiples of 16 sample-clock cycles to comply with the waveform granularity specification.

This clock provides a precise 10 MHz frequency reference, which is connected to the synchronization input of all pulse generating devices and microwave sources.

By establishing precise synchronization and utilizing the AWG and microwave sources, we can generate tailored microwave pulses for qubit control and readout, enabling accurate manipulation and measurement of the qubit state.

Down-conversion setup

The measurement of the classical readout signal in our experiment is performed in the I-Q plane, where we measure both the in-phase (I) and quadrature (Q) components of the voltage [23]. This allows us to distinguish between the ground state and excited state of the qubit. Mathematically, the readout signal can be described by

$$s(t) = \mathrm{Re}\left\{A_{\mathrm{RO}} e^{i\theta_{\mathrm{RO}}} e^{i\omega_{\mathrm{RO}} t}\right\}, \tag{3.12}$$

where A_{RO} and θ_{RO} contain information about the qubit state. To visualize this signal, we project it onto the I-Q plane. To measure the readout signal, we utilize an FPGA. However, since the FPGA operates in a different frequency regime compared to the readout signal, we need to downconvert the readout frequency to an intermediate frequency (IF), ω_{IF}. This is where the I-Q mixer comes into play.

The I-Q mixer performs multiplication with the frequency of the local oscillator (LO), ω_{LO}, resulting in a mixed signal. This mixed signal contains both sum and difference frequencies $\omega_{\mathrm{LO}} \pm \omega_{\mathrm{RO}}$. In our case, we are interested in the difference frequency. To extract this difference frequency, a low-pass filter is employed to filter out the sum frequency, allowing only the difference frequency to pass through. The choice of the LO frequency determines the type of demodulation used in the measurement. In **homodyne demodulation**, the LO frequency is set equal to the readout frequency, $\omega_{\mathrm{LO}} = \omega_{\mathrm{RO}}$. On the other hand, in **heterodyne demodulation**, the LO frequency is offset by an intermediate frequency on top of the readout frequency, such that $\omega_{\mathrm{IF}} = |\omega_{\mathrm{LO}} - \omega_{\mathrm{RO}}|$. In our measurement, we use the heterodyne measurement with $\omega_{\mathrm{IF}}/2\pi = 60\,\mathrm{MHz}$ to avoid electronic $1/f$ noise due to the ac-coupled analog-to-digital conversion.

Our I-Q mixing setup is electromagnetically shielded by a homemade copper box, in which all IF components are installed such as I-Q mixer, IF amplifier, low-, band-, and high-pass filters. This shielding ensures a significant reduction of the noise contribution at 10 MHz below the noise floor of the amplifiers[10].

Averaging and Digital homodyning

Here, we elaborate on the digital component of our experimental setup, which is made up of two key operations: averaging and digital homodyning.

The purpose of the initial step, averaging, is to mitigate the noise integrated from the carrier signal. In our experimental context, the most significant source of noise is the linear phase-insensitive amplifier. This device amplifies both quadratures equally, contributing a minimum of $1/2$ noise photons, a result derived from the Caves formula for an ideal case at $T = 0\,\mathrm{K}$ [232]. However, under real conditions, the amplifier introduces additional thermal noise photons instead of vacuum noise, with their amount corresponding to the noise temperature of the device. The effect of the thermal noise on the signal quality can be interpreted via the Friis equation, which states that the first amplifier in the amplification chain predominantly determines the signal-to-noise ratio [233]. Within the context of our experimental

[10] for more details the readers are referred to [214].

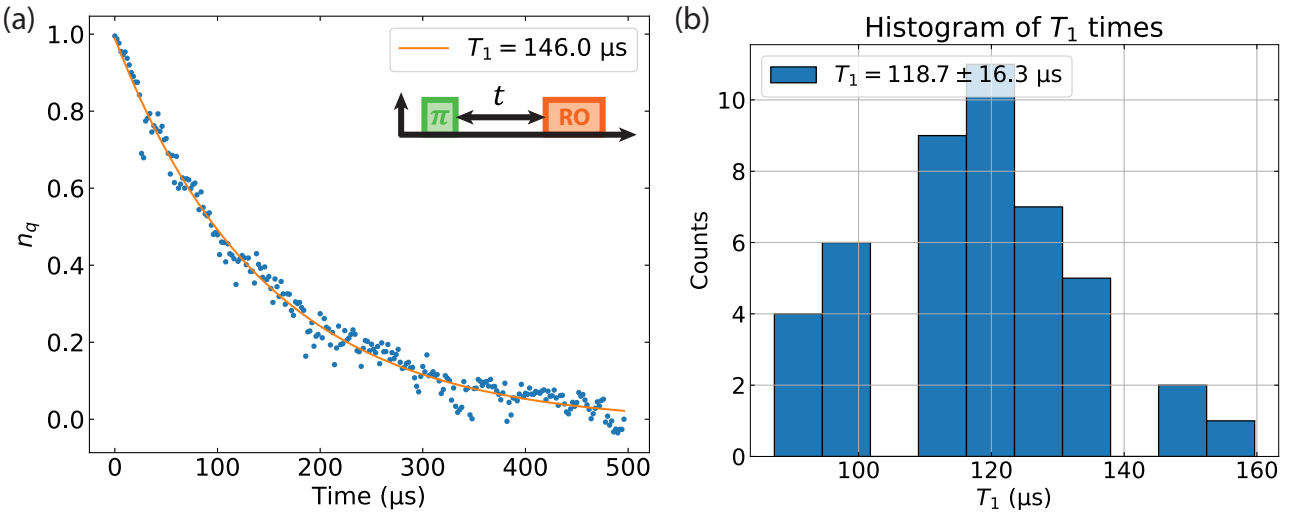

Figure 3.12. T_1 time measurement of the qubit. (a) An example of a T_1 measurement. The measured data (blue dots) are fitted by $n_q(t) = n_q(0)\exp(-t/T_1)$ (orange line) which yields $T_1 = 146\,\mu$s. The inset shows the pulse sequence used in the experiment. (b) Histogram of T_1 times obtained in subsequent measurements. The fluctuation of the T_1 times is attributed to the thermal activation of low-energy TLS, which manifest themselves over time intervals that range from milliseconds to several hours, even days [149, 234–237].

apparatus, the cold HEMT amplifier serves as this initial amplifier which typically contributes $5-10$ noise photons at 5 GHz. As the carrier signal contains only few photons, a single readout trace is completely covered by noise. The averaging is conducted by the snap-tool software. When the maximum number of iterations N is reached, we calculate the mean value of each point in time by dividing the accumulated value by N and the second order moment.

The ultimate objective of our data analysis is to determine the values of A_{RO} and θ_{RO}. To this end, we utilize the digitized and averaged IF signals given by

$$s_{\mathrm{IF}}(t) = \mathrm{Re}\left\{A_{\mathrm{RO}} e^{i\theta_{\mathrm{RO}}} e^{i\omega_{\mathrm{IF}} t}\right\} = A_{\mathrm{RO}}\cos\left(\omega_{\mathrm{IF}} t + \theta_{\mathrm{RO}}\right) \tag{3.13}$$

These signals are then subjected to a homodyning procedure, which we implemented in LabView, to eliminate the IF carrier frequency. The ideal operations we wish to accomplish are

$$I = \frac{\omega_{\mathrm{IF}}}{2\pi}\sum_{n}^{N} s_{\mathrm{IF}}(t_n)\cos\left(\omega_{\mathrm{IF}} t_n\right) \overset{N\to\infty}{\longrightarrow} \frac{A}{2}\cos\left(\theta_{\mathrm{RO}}\right), \tag{3.14a}$$

$$Q = \frac{\omega_{\mathrm{IF}}}{2\pi}\sum_{n}^{N} s_{\mathrm{IF}}(t_n)\sin\left(\omega_{\mathrm{IF}} t_n\right) \overset{N\to\infty}{\longrightarrow} \frac{A}{2}\sin\left(\theta_{\mathrm{RO}}\right). \tag{3.14b}$$

In reality, our LabView setup must deal with with DC offsets and a non-zero spectral component at $2\omega_{\mathrm{IF}}$. Consequently, it implements an optimization process to account for these modulations before applying Eq. (3.14) [11].

[11] For a more thorough discussion on this, readers may refer to [214]. An important point to note, based on the assertions in [214], is that even though they claim no need for calibration measurements, we do require a calibration measurement for our qubit phase readout to establish a reliable phase reference point.

3.3.3 Measurement results

The qubit performance is evaluated by measuring the T_1 and T_2 times. For determining the T_1 lifetime, we initially prepare the qubit in an excited state using a π pulse and measure its relaxation. Each measurement point is averaged over 10.000 times with a repetition time of $500\,\mu s$ between successive projective measurements. This interval allows the qubit to return to its ground state. Given the phase instabilities inherent to our apparatus, combined with the constraint of time, we were unable to carry out T_2 measurements in this particular investigation.

Here, we characterize a fixed-frequency transmon qubit with its transition frequency at $\omega_q = 3.843\,\text{GHz}$. In Fig. 3.12 the corresponding data sets for the qubit measurement are shown.

The extracted qubit lifetime is $T_1 = 118.7 \pm 16.3\,\mu\text{s}$. After the photon number calibration and power-dependent Rabi oscillations, we can extract the Purcell decay rate of $\gamma_{q,\text{P}}/2\pi = 0.33\,\text{kHz}$ and intrinsic qubit lifetime of $T_{1,i} = 157\,\mu\text{s}$ using Eqs. (2.68), (2.72) and (2.74). The corresponding internal quality factor is $Q_i = \omega_q T_{1,i}/2\pi = 603\,351$, which is in a good agreement with the resonator measurements in Sec. 3.2. The coherence time is predominantly limited by the losses in the junction area due to strong electric fields coupled to the TLSs and thus to the non-optimized resists stack. Improving the undercut potentially leads to an improved coherence time. All extracted parameters can be found in Tab. 3.4.

$\omega_r/2\pi$ (GHz)	$\omega_q/2\pi$ (GHz)	$\omega_{02}/2/2\pi$ (GHz)	$\chi_{qq}/2\pi$ (MHz)	$\chi_{qr}/2\pi$ (MHz)	$g_{qr}/2\pi$ (MHz)
6.158	3.843	3.721	−244	−2.25	21.4

Table 3.4. Measured readout resonator and qubit parameters of the sample `KH-079`.

Chapter 4

ONSET OF TRANSMON IONIZATION IN MICROWAVE SINGLE-PHOTON DETECTION

By strongly driving a transmon-resonator system, the transmon qubit may eventually escape from its cosine-shaped potential. This process is called transmon ionization (TI) and known to be detrimental to the qubit coherence and operation. In this work, we investigate the onset of TI in an irreversible, parametrically-driven, frequency conversion process in a system consisting of a superconducting 3D-cavity coupled to a fixed-frequency transmon qubit. Above a critical pump power we find a sudden increase in the transmon population. Using Rényi entropy, Floquet modes, and Husimi Q functions, we infer that this abrupt change can be attributed to a quantum-to-classical phase transition. Furthermore, in the context of the single-photon detection, we measure a TI-uncorrected detection efficiency of up to 86% and estimate a TI-corrected value of up to 78% by exploiting the irreversible frequency conversion. Our numerical simulations suggest that increasing the detuning between the pump and qubit frequencies and increasing the qubit anharmonicity can suppress the TI impact. Our findings highlight the general importance of the TI process when operating coupled qubit-cavity systems. Key results presented in this chapter have been published in [238].

In this chapter, we focus on the onset of TI in the irreversible frequency conversion process, which is applied for the realization of the single-photon detection in the microwave regime. We start with the experimental techniques in Sec. 4.1, where we explain the microwave single-photon detector device and the cryogenic setup used in our experiments. In Sec. 4.2, we describe the preparatory measurements required for the characterization of the different components of the single-photon detection scheme. Specifically, we characterize our aluminum 3D horseshoe cavity and transmon qubit, and calibrate our steady-state photon number of the buffer resonator. The model and the detection principle of our device is explained in Sec. 4.3. In Sec. 4.4, we study conversion of the incoming photons to the transmon excitations and waste photons as a function of the pump power. Once the pump power eventually approaches the critical threshold, it triggers the sudden increase in the transmon population in response to the incoming buffer photons. We study the process by using the Rényi entropy, the Floquet theory, and the Husimi Q function. Our results indicate that the abrupt change of the transmon response can be attributed to a quantum-to-classical phase transition. Subsequently in Sec. 4.5, we provide a comprehensive analysis of the irreversible frequency conversion in our system, observing the maximum detection efficiency of 86%. Then, we consider the influence of TI into account and estimate the TI-corrected detection efficiency to be notably lower, around 78%. Concluding our study, we systematically evaluate strategies to enhance the SPD detection efficiency by adjusting specific system parameters. Specifically, we find that increasing the detuning between the pump and qubit frequencies and increasing the qubit anharmonicity are the most beneficial steps for the detection efficiency. Furthermore, the arrangement of the buffer and waste frequencies should be done based on the sign of the qubit anharmonicity, in order to ensure that the pump drive and multi-photon qubit transitions do not coincide in the frequency space.

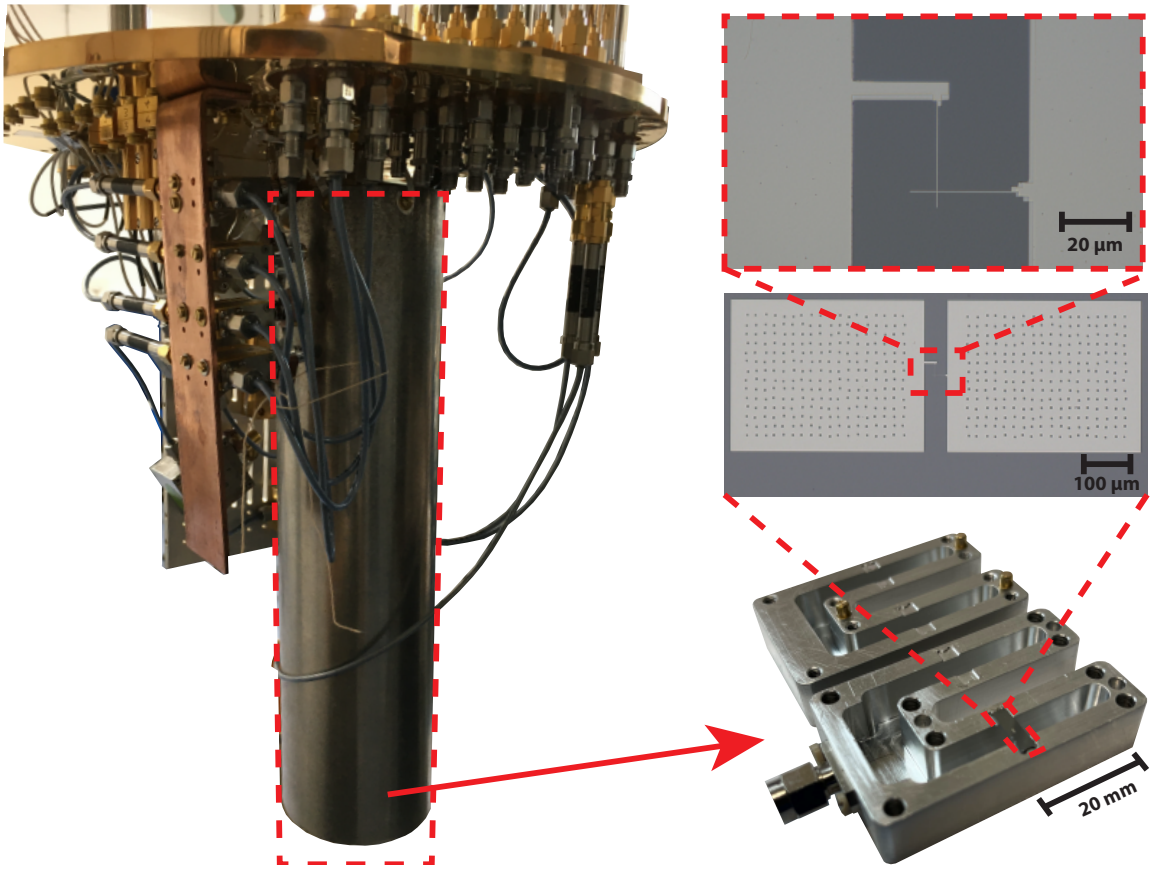

Figure 4.1. Picture of dry dilution refrigerator embedding Al horseshoe cavity with the transmon qubit chip inside.

4.1 Experimental techniques

4.1.1 Microwave single-photon detector sample

As outlined in Sec. 2.5, our single-photon detection scheme is comprised of two main components: a horseshoe cavity and a transmon qubit chip. The cavity, consisting of aluminum (Al) with a high purity level of 99.99%, has been fabricated by the workshop at the WMI. To address the relatively low thermal conductance of superconducting aluminum, we mount a gold-plated copper plate, 1.5 mm in thickness, onto the cavity. This plate significantly enhances the thermal conductance of the system, ensuring more efficient heat dissipation. For a comprehensive understanding of the horseshoe cavity's design, its simulation, and experimental studies, we refer readers to the master thesis of Julia Lamprich [239], where these aspects have been intensively explored.

The transmon qubit, central to our detection mechanism, is fabricated on a silicon chip with spatial dimension of 3.5 mm by 10 mm. The fabrication process of the transmon qubit, particularly the lift-off technique employed, is detailed in Chap. 3. The antenna of the qubit has an area of 890 μm by 330 μm, ensuring a sufficient dipole interaction strength with the cavity. Additionally, the Josephson junctions are designed with a width of 240 nm.

A visual representation of the assembly, showcasing the integration of the horseshoe cavity with the embedded transmon qubit chip, can be found in Fig. 4.1.

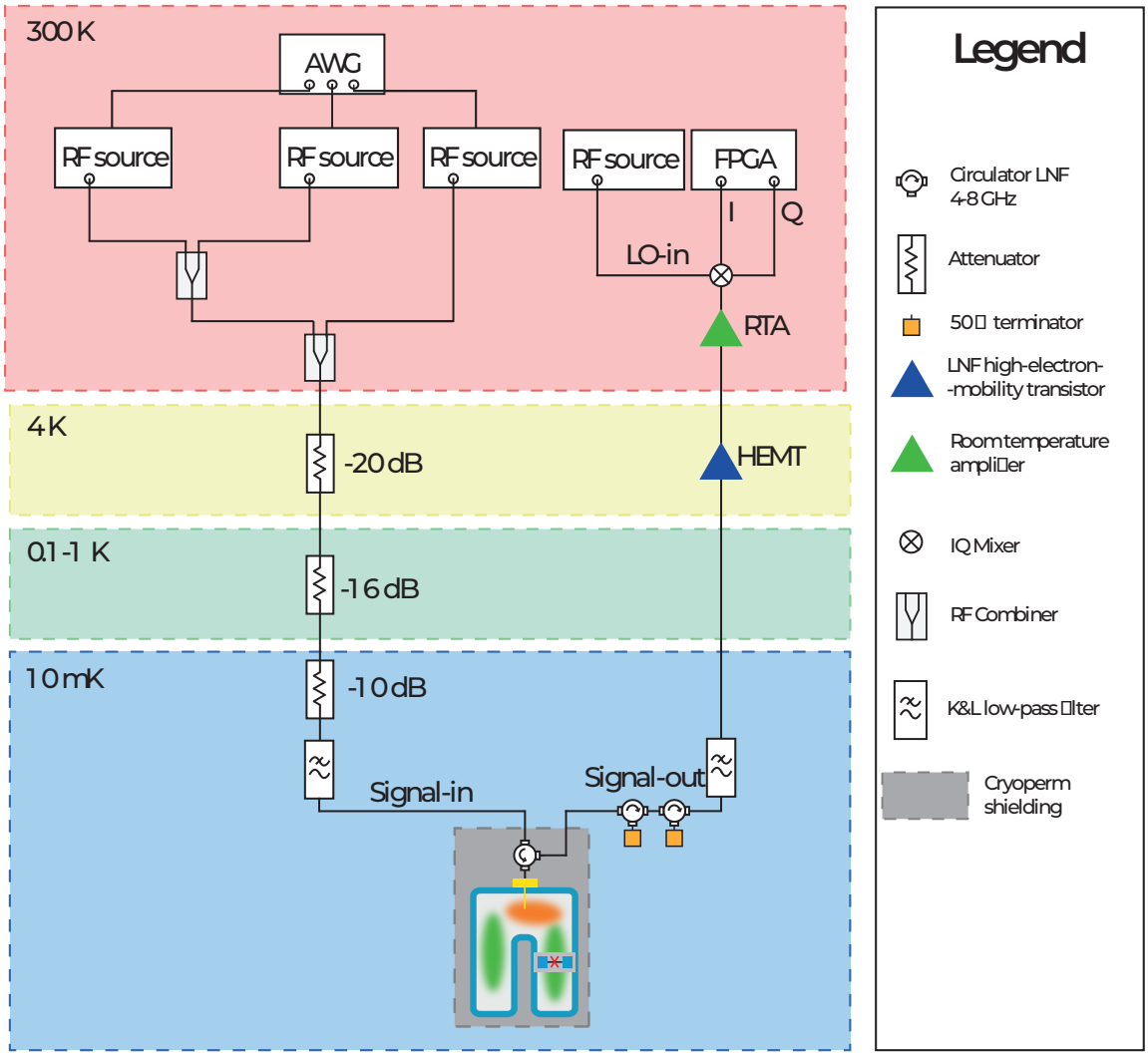

Figure 4.2. Schematic drawing of dry dilution refrigerator embedding Al horseshoe cavity with the transmon qubit chip inside.

4.1.2 Cryogenic setup

The cryogenic arrangement of the experimental setup used in our measurements is illustrated in Fig. 4.2. This setup shares several core components with the qubit measurement configuration already introduced in Sec. 3.3. Consequently, our discussion here will focus on the modifications and additions unique to the present setup.

For the generation of arbitrary waveforms, we employ the HDAWG from Zurich Instruments. Additionally, the setup incorporates three microwave sources (R&S SGS100A). These sources are critical for generating the pump, buffer, and readout signals necessary for our experiments. To integrate these three pulsed drives, we utilize two power combiners. Initially, the pump and buffer pulses are merged, followed by their subsequent combination with the readout pulse. This combined signal is then fed into the cryostat, facilitating both the frequency conversion process and the qubit readout.

It is noteworthy that a similar configuration is employed for spectroscopy measurements. In this context, the microwave generator designated for readout, along with the measurement components situated on the output line after the room-temperature amplifier, is substituted by a VNA.

The combined signals pass a series of attenuators mounted at various cooling stages within the cryostat, followed by a low-pass filter to suppress high-frequency noise. Upon reaching the mixing

chamber stage, the signal is delivered to the cavity-qubit system. The Al horseshoe cavity, housing the transmon qubit chip, is shielded from external magnetic fields by a cryoperm shield. The single-port design of the cavity is coupled with a circulator to separate the output signal from the incoming signal. This configuration is pivotal in attenuating input signals originating from room-temperature stages while at the same time amplifying the outgoing output signals.

The output path includes a low-pass filter, followed by passage through two isolators. Amplification is achieved via a HEMT amplifier located at the 4 K stage, and subsequently, through a room-temperature amplifier.

4.2 Preparatory measurements

In the following section, we present the results of preparatory measurements of our quantum device, designed to facilitate the implementation of irreversible frequency conversion. The device comprises a 3D cavity made from aluminum, along with a transmon chip. As part of our cavity characterization, we determine the first couple of eigenmodes and extract their associated quality factors. Subsequently, we perform a thorough analysis of our transmon qubit, delving into aspects such as its level structure, coherence properties, and an assessment of the effective qubit temperature. To conclude, we calibrate the photon number present in the steady-state waste and buffer.

4.2.1 Characterization of 3D cavity

For the cavity characterization, we apply the single-tone spectroscopy measurement introduced in Chap. 3 to extract the resonant frequencies and the external and internal quality factors.

As depicted in Fig. 4.3 (c), a broad-band microwave sprectroscopy allows to determine the two lowest two eigenmodes positioned at around 7.61 GHz and 7.95 GHz. This result agrees well with the prediction of the CST simulation, yielding an eigenfrequency of 7.45 GHz for the first and of 7.915 GHz for the second one. Beyond this, we aim to determine the coupling rates between both cavity eigenmodes and the transmon qubit. To achieve this, we conduct spectroscopy measurements around the first and second eigenfrequencies, varying the power of the probe tone. By doing so, we are able to observe the distinct "punch-out" effect, a characteristic of the coupled cavity-qubit system, as shown in Fig. 4.3 (a,b). Here, we extract the parameters of the *bare* cavity modes. These are obtained from the high probe power regime at which the cavity decouples from the qubit due to the transmon ionization effect [71–73]. We extract $\omega_w/2\pi = 7.607$ GHz with the coupled and intrinsic quality factors of $Q_{c,w} = 515$ and $Q_{i,w} = 122\ 000$, respectively, as well as $\omega_b/2\pi = 7.954$ GHz with $Q_{c,b} = 2\ 525$ and $Q_{i,b} = 175\ 000$, respectively. As the dissipation rate of the first cavity mode is much larger than that of the second mode, we therefore attribute the first eigenmode to the waste mode and the second one to the buffer mode. As an additional but crucial observation, it is important to mention the significance of the "punch-out" effect in both the waste and buffer modes, particularly at elevated probe power levels. This effect is not just a completeness of our spectroscopy measurement but has practical implications, especially considering our reliance on single-photon detection mechanisms that hinge on the four-wave mixing process. The successful implementation of single-photon detection in our system is deeply intertwined with the four-wave mixing dynamics, where the pump, the qubit, the waste, and buffer modes are key participants. Without a robust coupling between the qubit and both cavity modes, the four-wave mixing process - essential for our experiments - is hindered. This coupling ensures that the intricate interplay between these components leads to the desired outcomes. Hence, the verification of

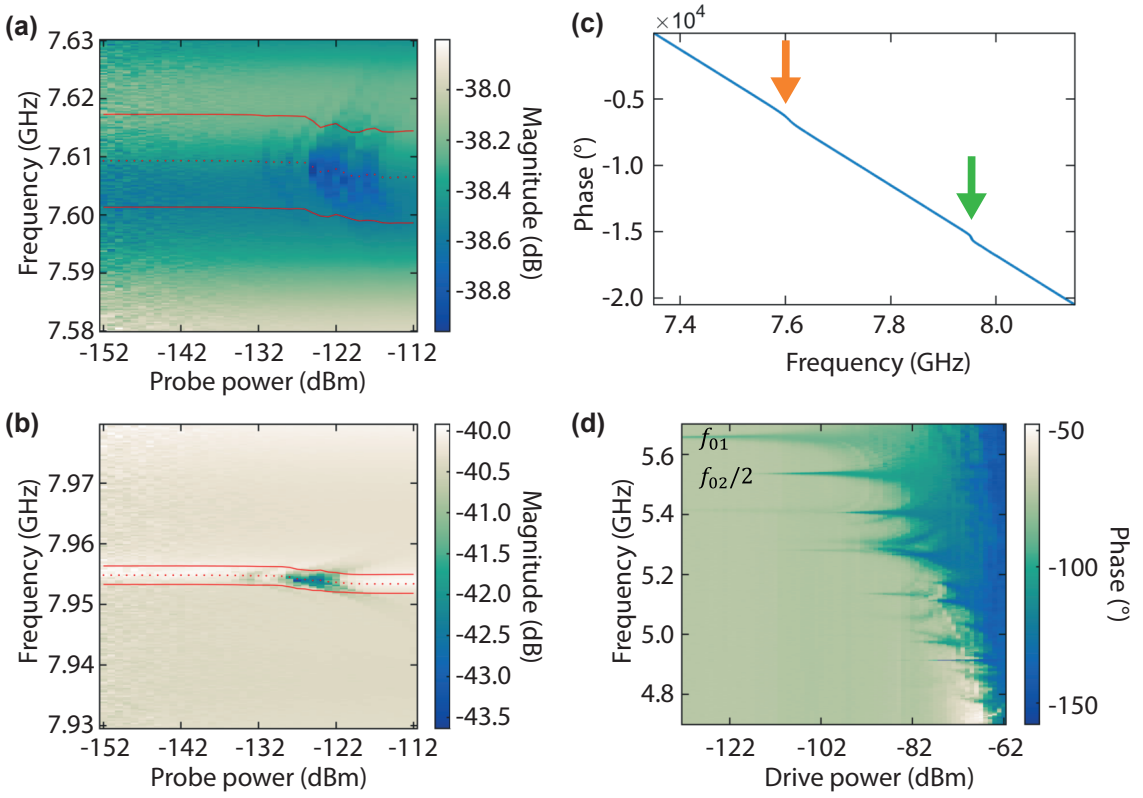

Figure 4.3. Spectroscopy measurement of the device `Qubit-036B` (a) Single-tone spectroscopy measurement as a function of the probe power around the waste mode frequency of 7.6 GHz. The "punch-out" effect can be found at around −122 dBm. The red dots are the resonance frequency, the red solid lines are the FWHM of the waste mode, i.e. $(\omega_w \pm \kappa_w/2)/2\pi$. The label "Magnitude (dB)" here refers to the magnitude of the readout signal, where we set the reference at the input at the room temperature stage. (b) Single-tone spectroscopy measurement as a function of the probe power around the buffer mode frequency of 7.95 GHz. The "punch-out" effect can be found at around −125 dBm. The red dots are the resonance frequency, the red solid lines mark the FWHM of the buffer mode, i.e. $(\omega_b \pm \kappa_b/2)/2\pi$. The label "Magnitude (dB)" here refers to the magnitude of the buffer signal, where we set the reference at the input at the room temperature stage. (c) Microwave phase response plotted between 7.35 GHz and 8.15 GHz. The orange (green) arrow indicates the resonance frequency of the waste (buffer) mode. Here, the phase refers to the phase of the probe signal. (d) Two-tone spectroscopy as a function of drive power. The qubit frequency at $f_{01} = 5.660$ GHz and the two-photon process at $f_{02}/2 = 5.536$ GHz can be seen. Here, the phase refers to the phase of the readout signal.

this coupling is not just a procedural step, but a fundamental prerequisite for advancing to practical applications in our research.

4.2.2 Characterization of the transmon qubit

Adopting the experimental procedures outlined in Chap. 3, we initially deduce the rough level scheme of the transmon by employing two-tone spectroscopy, as depicted in Fig. 4.3 (d). However, the transition frequencies between the qubit level ascertained through this method is subject to ac-Stark shift induced by the readout tone, given the simultaneous application of two CW tones. In order to pinpoint the frequency with greater precision, we turn to Rabi measurements and vary the driving frequency ω_d. This approach leads to the generation of a characteristic Chevron pattern, as demonstrated in Fig. 4.4 (a). As per Eq. (2.69), the driving frequency that corresponds to the minimal Rabi frequency serves as the precise qubit frequency, as shown in Fig. 4.4 (b).

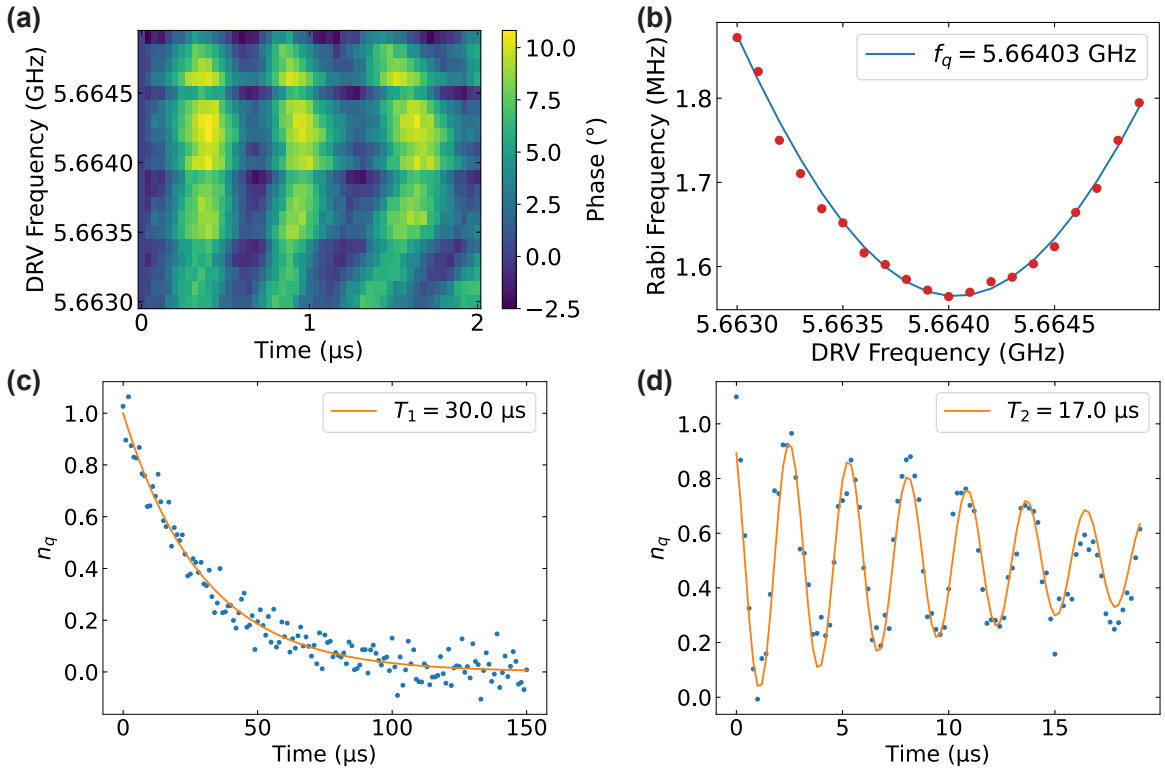

Figure 4.4. Time-domain measurement of the qubit. (a) Chevron pattern of the qubit obtained by varying the drive frequency ω_d. (b) Rabi frequency as a function of the drive frequency. The red dots are the extracted values from (a), and are fitted by $\Omega_{\text{Rabi}} = \sqrt{A^2 + \Delta_{qd}^2}$ (blue solid line). The error bars are hidden behind the data points. (c) An example of a T_1 measurement. The measured data (blue dots) are fitted by $n_q(t) = n_q(0)\exp(-t/T_1)$ (orange line) which yields $T_1 = 30\,\mu$s (d) An example of T_2 measurement with a slightly detuned frequency of 0.4 MHz, such that Ramsey fringes appear. The measured data (blue dots) are fitted by $n_q(t) = n_q(0)\cos(\Delta_{qd}t + \phi)\exp(-t/T_2)/2 + B$ (orange line) which yields $T_2 = 17\,\mu$s.

The method to obtain the T_1 times was explained in Chap. 3. In case of T_2 time extraction, we first prepare the qubit in $|\psi\rangle = (|0\rangle + |1\rangle)/\sqrt{2}$ via a $\pi/2$ pulse, wait for a certain amount of time, and finally send another $\pi/2$ pulse before reading out the qubit state. Each measurement point consists of 5.000 averages with a repetition time of 150 μs between subsequent projective measurements to let the qubit relax to its ground state. We extract $T_1 = 28 \pm 5$ and $T_2 = 16 \pm 3$.

4.2.3 Photon-number calibration

In our experimental setup, the calibration of the steady-state photon number within the cavity mode is achieved through Ramsey measurements. Specifically, we conduct measurements of the Ramsey fringe frequency and the dephasing rate of the qubit as a function of the cavity drive amplitude [240]. These measurements yield precise values for both the dispersive shift and the power associated with a single photon in the cavity.

The key advantage of utilizing a Ramsey measurement for this calibration lies in its high sensitivity to the steady-state photon number within the cavity. This sensitivity is particularly pronounced when compared to the two-tone spectroscopy method, as discussed in Sec. 3.3. In the context of two-tone spectroscopy, the extraction of the dispersive shift may be compromised by inhomogeneous broadening, especially when a certain threshold in photon number is exceeded [231]. This broadening

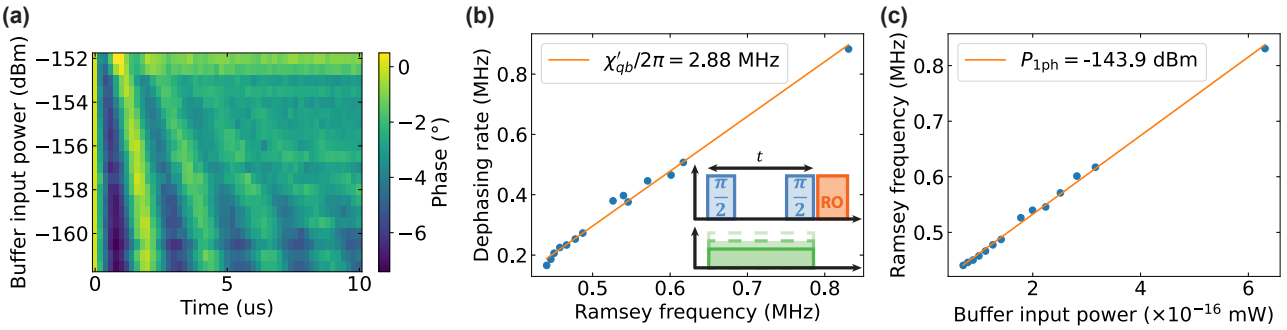

Figure 4.5. Photon number calibration measurement for the buffer mode. The values of the buffer input power shown in the plots are all at the cavity. (a) Ramsey measurements at different buffer input power levels. (b) Dephasing rate as a function of the Ramsey frequency. The blue dots are the data points extracted from the Ramsey measurements in (a) with the model function, $n_q(t) = n_q(0)\cos(\Delta_{qd}t + \phi)\exp(-t/T_2)/2 + B$. Some of the Ramsey measurements could not be fitted with the model function, and thus omitted for the linear fit. The extracted qubit-buffer dispersive shift is $\chi'_{qb}/2\pi = 2.88 \pm 0.07$ MHz. The inset shows the pulse sequence used in the experiment. Qubit $\pi/2$ pulse is represented by blue, readout pulse by orange, and buffer pulse by green. (c) Ramsey frequency as a function of the buffer input power. All error bars are smaller than the symbol size.

effect obscures the linear relationship between frequency shift and bandwidth broadening, posing a challenge for accurate photon number calibration. Typically, two-tone spectroscopy demands a steady-state photon number in the order of 0.1 to 1 for reasonable resolution of frequency shifts and bandwidth alterations. However, these photon numbers might exceed the photon number threshold, which can lead to the aforementioned inhomogeneous broadening issues. Conversely, the method based on Ramsey measurements operates effectively within a lower photon number regime, typically between 0.01 and 0.1 photons. This lower range not only circumvents the complications associated with inhomogeneous broadening but also provides a more reliable and precise means for calibrating the photon number in the cavity. The Hamiltonian introduced in Eq. (2.72) can be rewritten in the rotating frame $\hat{\mathcal{H}}_0/\hbar = \omega_d \hat{a}_r^\dagger \hat{a}_r + \omega_d \hat{a}_q^\dagger \hat{a}_q$ such that

$$\hat{\mathcal{H}}'_{q,\mathrm{disp}}/\hbar = \Delta_{rd}\hat{a}_r^\dagger \hat{a}_r + \left(\Delta_{qd} + \chi'_{qr}\hat{a}_r^\dagger \hat{a}_r\right)\hat{a}_q^\dagger \hat{a}_q \tag{4.1}$$

with $\Delta_{rd} = \omega_r - \omega_d$ and $\Delta_{qd} = \omega_q + \chi'_{qr}/2 - \omega_d$. We remind ourselves that we observe a pure exponential decay with the time constant T_2, if the qubit term is zero, otherwise we observe oscillations denoted as Ramsey fringes [23]. This oscillation can be again confirmed in Fig. 4.4 (d). Based on this knowledge, we can deduce that the Ramsey fringes increase with $\chi'_{qr}n_r$ with $n_r = \langle \hat{a}_r^\dagger \hat{a}_r \rangle$ being the average steady-state resonator photon number. Moreover, the oscillations decay faster with the increase of the photon number with the relation $\Gamma_2(n_r) = 2\chi'^2_{qr}n_r/\kappa_r + \Gamma_{2,0}$ [240]. Fig. 4.5 (a) shows both phenomena. Consequently, we obtain the relation between the dephasing rate and Ramsey frequency

$$\Gamma_2(\omega_\mathrm{R}) = \frac{\chi'^2_{qr}n_r}{\kappa_r} + \Gamma_{2,0} = \frac{\chi'_{qr}(\omega_\mathrm{R} - \Delta_{qd})}{\kappa_r} + \Gamma_{2,0} = \frac{\chi'_{qr}}{\kappa_r}\omega_\mathrm{R} - \frac{\chi'_{qr}\Delta_{qd}}{\kappa_r} + \Gamma_{2,0}, \tag{4.2}$$

where the Ramsey frequency is expressed as $\omega_\mathrm{R} = \Delta_{qd} + \chi'_{qr}n_r$. Therefore, we can extract the dispersive shift from the slope of the linear fit, as demonstrated in Fig. 4.5 (b) for the buffer mode.

Furthermore, the single-photon power $P_{1\mathrm{ph}}$ can be extracted by relating

$$\chi'_{qr}n_r = aP_\mathrm{RT}$$

with P_{RT} being the power of the room-temperature device. Hence, the single-photon power is obtained by $P_{1\mathrm{ph}} = \chi'/a$ for $n_r = 1$, as shown in Fig. 4.5 (c) for the buffer mode. We can also extract the total attenuation in the input line at this frequency. We can apply the Eq. (3.4) and relate

$$\frac{4\kappa_r^2}{\kappa_{r,c}} n_r = |\langle \hat{a}_{\mathrm{in}} \rangle|^2 = \frac{P_{\mathrm{RT}}}{\hbar\omega_r} 10^A \tag{4.3}$$

with the attenuation A. At the buffer mode, we obtain the total attenuation of $A = -81.9\,\mathrm{dB}$.

4.3 Demonstration of irreversible frequency conversion process

In our experiments, we use a horseshoe-shaped aluminum 3D cavity, which contains a transmon qubit chip (as schematically shown in Fig. 4.6(b)). We utilize two of the cavity modes: the waste mode at $\omega_w/2\pi = 7.609\,\mathrm{GHz}$ with a decay rate of $\kappa_w/2\pi = 16.7\,\mathrm{MHz}$ and the buffer mode at $\omega_b/2\pi = 7.955\,\mathrm{GHz}$ with a decay rate of $\kappa_b/2\pi = 3.7\,\mathrm{MHz}$. The qubit frequency is $\omega_q/2\pi = 5.664\,\mathrm{GHz}$, with $T_1 = 28\ \mu\mathrm{s}$ and $T_2 = 16\ \mu\mathrm{s}$, limited by the Purcell effect. The qubit is coupled to the waste and buffer modes with coupling strengths of $g_w/2\pi = 30\,\mathrm{MHz}$ and $g_b/2\pi = 18\,\mathrm{MHz}$, respectively. In a driven system, the ac-Stark effect induces shifts in all three eigenfrequencies as a function of the pump power. These shifted frequencies are denoted by ω_j' for the j-th mode, where $j = \{q, b, w\}$. Its Hamiltonian in the rotating frame of $\hat{\mathcal{H}}_0/\hbar = \omega_q'\hat{a}_q^\dagger\hat{a}_q + \omega_w'\hat{a}_w^\dagger\hat{a}_w + \omega_b'\hat{a}_b^\dagger\hat{a}_b$ is formulated as

$$\begin{aligned}
\hat{\mathcal{H}}_4/\hbar \approx & \\
& \sum_{k=2}^{N_t-1} \frac{\chi^{(k)}}{k!} \left(\hat{a}_q^\dagger\right)^k \hat{a}_q^k + \chi_{qw}\hat{a}_q^\dagger\hat{a}_q\hat{a}_w^\dagger\hat{a}_w + \chi_{qb}\hat{a}_q^\dagger\hat{a}_q\hat{a}_b^\dagger\hat{a}_b \\
& + g_4 \left(\xi_p \hat{a}_q^\dagger\hat{a}_w^\dagger\hat{a}_b e^{i\Delta_{qwbp}t} + \xi_p^* \hat{a}_q\hat{a}_w\hat{a}_b^\dagger e^{-i\Delta_{qwbp}t}\right) \\
& + 2i\varepsilon_q \cos\left(\left(\omega_q' - \omega_p\right)t\right)\left(\hat{a}_q^\dagger - \hat{a}_q\right) + i\varepsilon_b\left(\hat{a}_b^\dagger - \hat{a}_b\right),
\end{aligned} \tag{4.4}$$

where $\hat{a}_q$, $\hat{a}_w$, and $\hat{a}_b$ are the annihilation operators of the qubit, waste, and buffer modes, respectively, and N_t is the dimension of the transmon Hilbert space. The detuning involving all four frequencies is defined as $\Delta_{qwbp} = \omega_q' + \omega_w' - \omega_b' - \omega_p$ and the driving strength of the transmon and buffer mode as $\varepsilon_{q,b}$, respectively. The term $\chi^{(k)}$ corrects for the k-th eigenfrequency of the transmon, with $\chi^{(2)}$ being its anharmonicity. In addition, χ_{qw} and χ_{qb} are the cross-Kerr interaction strengths of the waste and buffer modes, respectively. Lastly, g_4 is the strength of the four-wave mixing interaction, and ξ_p is the pump amplitude at the pump frequency, ω_p. Below the regime, where all relevant excitation and dissipation rates are much less than the anharmonicity $\chi^{(2)}$, the bosonic annihilation operator $\hat{a}_q$ can be replaced by the Pauli operator $\hat{\sigma}$. The irreversible frequency conversion process is based on the dissipation-engineered four-wave mixing process of a nonlinear Josephson junction element [41]. When an incoming photon arrives at the buffer mode frequency, the buffer photon is converted to the excited state of the qubit and waste photon by a strong pump pulse, corresponding to the parametrically activated conversion process ($\hat{a}_b\hat{\sigma}^\dagger\hat{a}_w^\dagger$). However, under the conditions, $\kappa_w \gg |g_4\xi_p|$, the waste resonator state rapidly decays to the vacuum state, making the process irreversible and prohibiting the inverse process ($\hat{a}_b^\dagger\hat{\sigma}\hat{a}_w$). As a result, information of the incoming photon is stored in the qubit state, as shown in Fig. 4.6 (a).

By performing a triple-tone spectroscopy composed of the pump and buffer pulses with identical duration of $t_b = 20\,\mu\mathrm{s}$, followed by a readout pulse at the waste mode frequency with a duration of

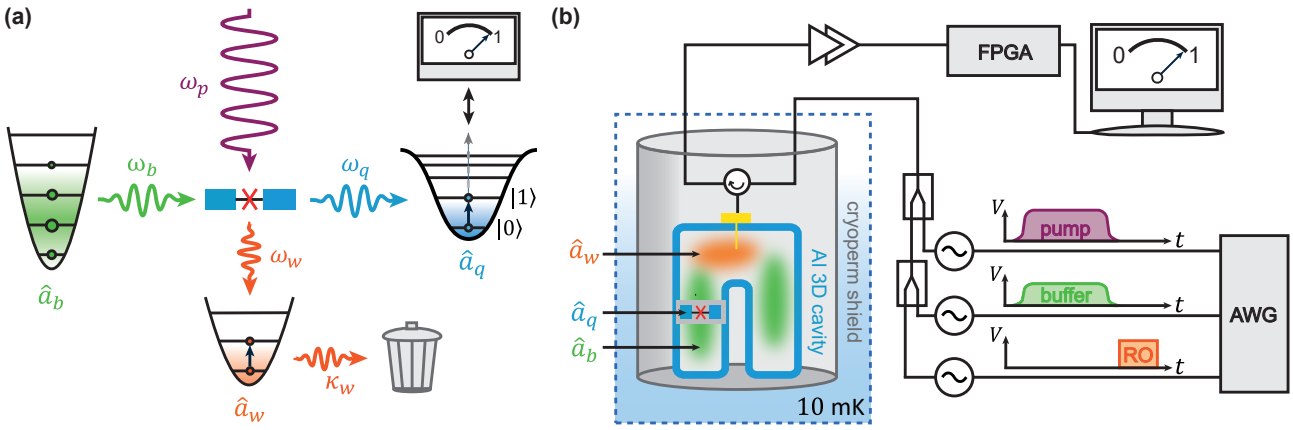

Figure 4.6. (a) Principle of the microwave single-photon detection. A coherent incoming photon (green wave) is absorbed by a buffer mode, $\hat{a}_b$, and is converted to a pair of qubit-waste excitations described with operators $\hat{\sigma}$ ($\hat{a}_q$) and $\hat{a}_w$, respectively, with the interaction strength $g_4\xi_p$. Due to the engineered fast dissipation of the waste mode, $\kappa_w \gg |g_4\xi_p|$, the inverse process ($\hat{a}_b^\dagger\hat{\sigma}\hat{a}_w$) is effectively suppressed. (b) Schematic of the experimental setup. The transmon is mounted in the 3D superconducting cavity coupled to the cavity waste/buffer modes, represented by orange/green shaded areas depicting corresponding electric field distributions, respectively. The buffer (green), readout (orange), and strong pump pulses (purple) are shaped using an the arbitrary wave generator (AWG) for the time-domain experiments. The buffer, ω_b, readout tone, ω_w, and pump, ω_p, carrier frequencies are set by external microwave generators.

$t_r = 2.5\,\mu$s (see Fig. 4.6), we observe the process of the buffer photons to the qubit excited state. As shown in Fig. 4.7 (a), if the buffer pulse is switched on, we find the phase response of the transmon in the pump frequency range of $\omega_p/2\pi = 5.15 - 5.18\,$GHz. This response disappears in the absence of the buffer pulse (see Fig. 4.7 (b)).

4.4 Onset of transmon ionization

In this section, we present a systematic study of the buffer photon conversion to the transmon-waste excitations as a function of the pump power. Our measurements reveal a sudden increase in the transmon population above a certain critical pump power (CPP) of $P_c = -67\,$dBm, as illustrated in Fig. 4.7 (c,d). To maximize the qubit population for each pump power, we tune our pump frequencies accordingly.

For the pump powers below the CPP, we observe a monotonic increase in the transmon population as the steady-state buffer photon number increases. This result is in agreement with theoretical predictions, which will be discussed in the next section. Conversely, for pump powers above the CPP, we again observe the monotonic increase in transmon population, but with a sudden jump (discontinuity) in the transmon response to the buffer power (see Fig. 4.7 (c)). In an independent measurement using a two-tone spectroscopy approach, we also find a disruption of the buffer and waste resonance frequencies at a similar pump power, where the pump power is varied at the fixed pump frequency (see Fig. 4.7 (e)). This observation is consistent with previous studies [71, 83] and numerical simulations [72, 73, 190], and suggests that here the transmon is entering the ionization process, where it eventually "escapes" the confines of the Josephson potential.

We explore the system dynamics numerically by utilizing the Hamiltonian presented in Eq. (4.4). By relying on experimentally determined parameters, we solve the Lindblad-Master equation given

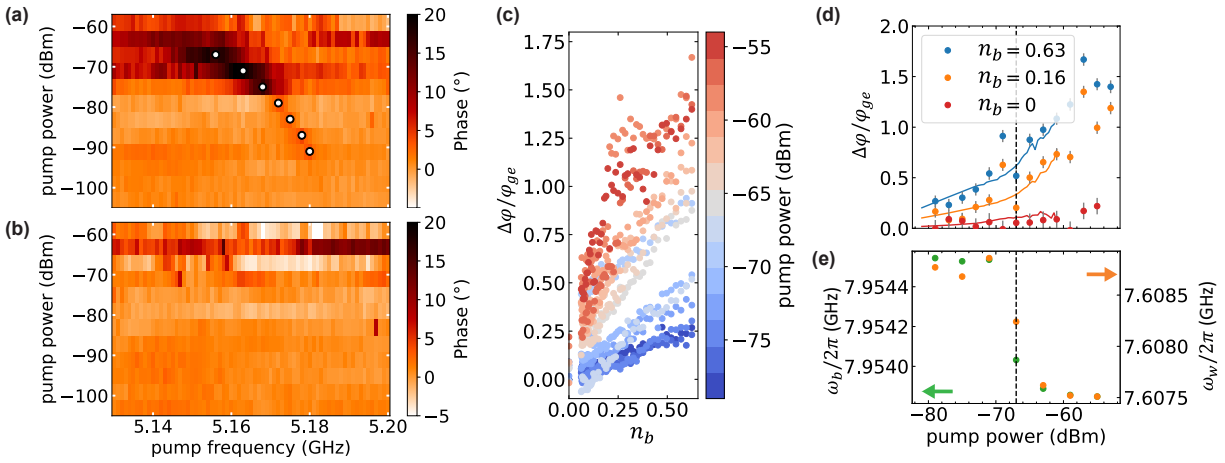

Figure 4.7. (a) Triple-tone pulsed spectroscopy of the coupled transmon-resonator system as explained in the main text. An inclined feature (cyan dots) indicates the four-wave mixing process. (b) Reference two-tone pulsed spectroscopy of the coupled transmon-resonator system without the buffer signal. (c) Phase shift of the transmon response $\Delta\varphi$ normalized to the phase shift between the ground and first excited states φ_{ge} as a function of the steady state photon number n_b. Different colors correspond to specific pump power values as indicated by the color code. (d) Transmon phase response for three selected buffer photon numbers $n_b = 0.00, 0.16, 0.63$ (red, orange, blue) as a function of the pump power. The vertical black dashed line indicates the CPP, at which the abrupt change of the qubit population can be observed. Solid lines are the simulation results using Eq. (4.4) with $n_b = 0.00, 0.16, 0.63$ (red, orange, blue). (e) The buffer and waste resonance frequencies as a function of the pump power at $\omega_p/2\pi = 5.1595\,\mathrm{GHz}$. A distinct jump of the resonance frequencies can be observed in both resonators at the CPP of $-67\,\mathrm{dBm}$.

in Eq. (2.97) and subsequently validate the proposed Hamiltonian by juxtaposing our results with measurements shown in Fig. 4.7 (d). During the simulation, the Hilbert space dimensions of the transmon, waste, and buffer modes are chosen to be 9, 3, and 3, respectively. The eigenenergy calculation of the transmon with the experimental parameters show that the first eight transmon states are confined states, while the last one lies already above the Josephson junction potential corresponding to the first ionized state.

To interpret the dynamics of our system, we utilize the Rényi entropy, Floquet theory, and Husimi Q function, as shown in Figs. 4.8 and 4.9. We begin by considering the Rényi entropy. This entropy quantitiy can offer valuable insights into the phase transition of our tripartite system around the critical point [79, 192, 193, 241]. Mathematically, the Rényi entropy is defined as

$$S_2 = -\log_2 \mathrm{Tr}\left(\hat{\rho}_t^2\right), \tag{4.5}$$

where the reduced density matrix of the transmon, $\hat{\rho}_t$, is achieved by tracing out both the waste and buffer modes, i.e., $\hat{\rho}_t = \mathrm{Tr}_{w,b}\left(\hat{\rho}\right)$. This entropy serves as a key metric for quantifying the purity, and thereby, the "classicality" of the associated density matrix. Intuitively, a system with higher entropy is more mixed or less pure, and consequently, is more classical in nature. This entropy allows us to observe the quantum-to-classical phase transition. As illustrated in Fig. 4.8 (a), a distinct jump in entropy is evident at the CPP, a feature that is absent without the buffer drive. This marked change provides clear evidence for the transition of the system from a predominantly quantum state to a more classical one, thus, supporting the observed quantum-to-classical phase transition [71–74, 80].

Furthermore, we apply the Floquet theory, which is particularly suited for examining strongly-

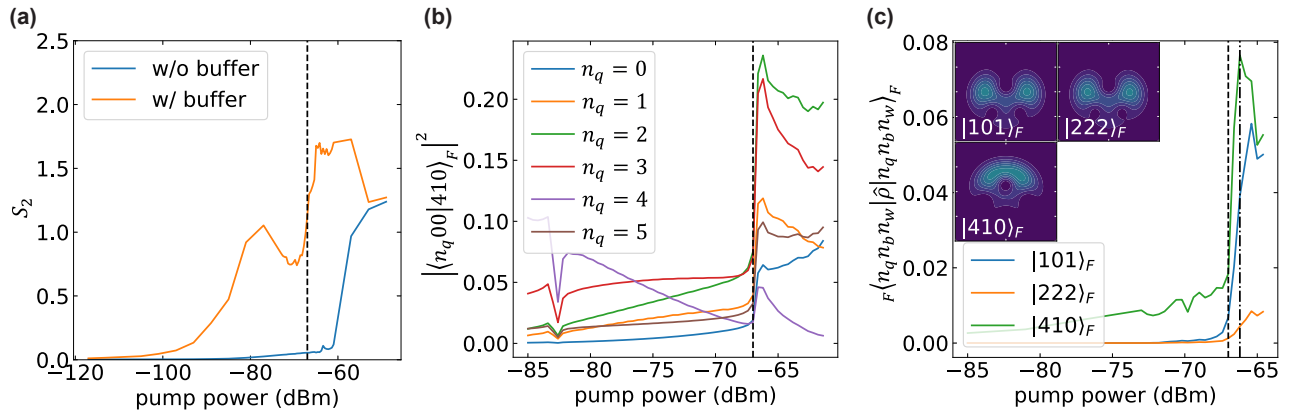

Figure 4.8. Rényi entropy, Floquet simulation, and Husimi Q distribution using the Hamiltonian in Eq. (4.4) with the parameters extracted from the measurements. We choose $\varepsilon_b = 0$ for the case "without buffer drive". The vertical black dashed line marks the CPP at $P_c = -67\,\mathrm{dBm}$. (a) Rényi entropy, S_2, obtained from the simulated reduced transmon density matrix without (blue) and with (orange) the buffer drive as a function of the pump power. At the CPP, $P_c = -67\,\mathrm{dBm}$, the Rényi entropy remains rather smooth in the absence of buffer photons, while its sudden increase is observed for finite buffer signal powers. (b) The overlap between the transmon state $|n_q 00\rangle$ and the Floquet mode $|410\rangle_F$ as a function of pump power. At the CPP, we find a drastic increase of this overlap for transmon states characterized by different n_q. (c) Probability of finding specific Floquet modes in the simulated density matrix as a function of the pump power. A sudden increase of the probabilities can be observed. Insets show Husimi Q distributions of the Floquet states $|101\rangle_F$, $|222\rangle_F$ and $|410\rangle_F$ at $-66.2\,\mathrm{dBm}$ (vertical dash-dotted line).

driven systems, making it suitable for our quantum-to-classical phase transition studies [74, 82]. We analyze the overlap between the transmon qubit and Floquet states as a function of the pump power. The Floquet modes are designated as $|n_q n_b n_w\rangle_F$, aligning with $|n_q n_b n_w\rangle$ at minimal pump levels, which are the eigenstates of $\hat{\mathcal{H}}_0$. As illustrated in Fig. 4.8 (b), a distinct transition in the overlap of the Floquet state, $|410\rangle_F$, is evident at the CPP, $P_c = -67\,\mathrm{dBm}$. Comparable trends are noted for Floquet modes $|101\rangle_F$ and $|222\rangle_F$ (not shown). We further investigate the dynamical properties of probabilities corresponding to these Floquet modes in the resulting density matrix, deduced from the Lindblad-Master simulation. In line with the previous findings, a sharp increase in these probabilities is observed at the CPP, as shown in Fig. 4.8 (c). Henceforth, after the CPP, these Floquet states, $|101\rangle_F$, $|222\rangle_F$, and $|410\rangle_F$, emerge as predominant features of the system for the increased pump powers. The insets of the figure in Fig. 4.8 (c) present the Husimi Q distribution of these Floquet states at $-66.2\,\mathrm{dBm}$, slightly above the CPP. They reveal extensive delocalization, where $|101\rangle_F$ and $|222\rangle_F$ states are further characterized by the double-peak distributions.

Lastly, we aim to affirm that this bimodal nature observed in the Husimi Q function of the Floquet modes distinctly manifests in the phase space of the transmon after the CPP. In Fig. 4.9, we show the Husimi Q representation of the transmon in scenarios with and without the buffer signal. We employ the double peak of the Husimi Q distribution in the phase space as an indicator of coexisting states. This characteristic bimodal structure of the Q function is a recognized feature of dissipative quantum phase transitions observed in quantum Duffing oscillator [78, 79, 81, 190, 242]. Thus, the identification of such a structure within our system suggests the occurrence of the first-order dissipative phase transition in the transmon-resonator system. As shown in the top panel of Fig. 4.9, the Gaussian-like distribution of the Husimi Q function remains largely unchanged until around $P_p = -61\,\mathrm{dBm}$, if the buffer drive is switched off. In other words, the delocalization does not appear even after $P_c = -67\,\mathrm{dBm}$. Conversely,

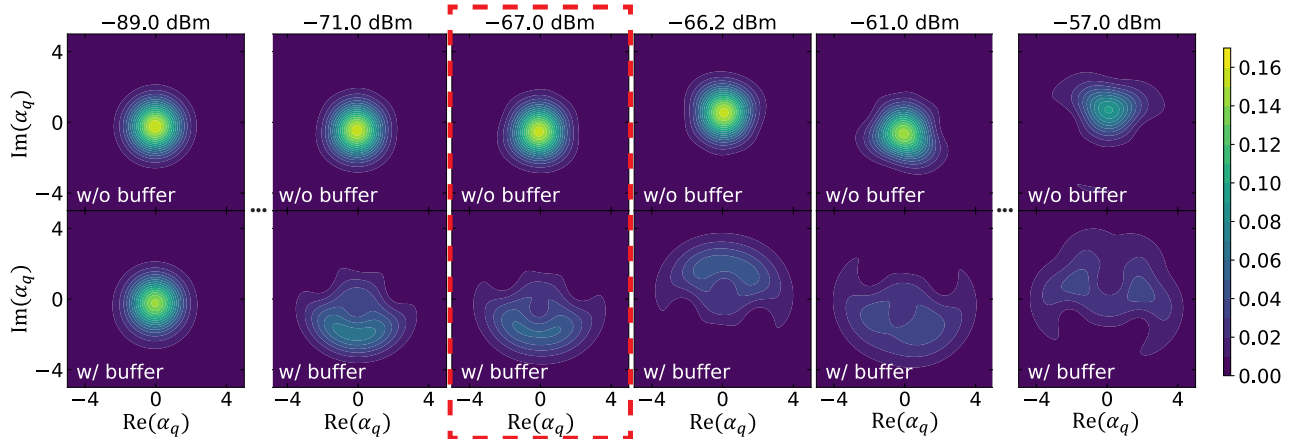

Figure 4.9. Simulation of the transmon Husimi Q function using the Hamiltonian in Eq. (4.4) in the absence (top) and presence (bottom) of the buffer signal for various pump powers. In the absence of the buffer signal, minimal variation is observed around the CPP. Conversely, in the presence of the buffer signal, the Husimi Q function spreads across the phase space, progressively converging to a double-peak distribution for higher pump powers. The red dashed box highlights the transmon Husimi Q function at the CPP. We choose $\varepsilon_b = 0$ for the case "without buffer drive".

with the buffer drive switched on, the system undergoes a delocalization in the phase space around the CPP, progressively converging to a double-peak formation at stronger pump powers, as illustrated in the bottom panel of Fig. 4.9 at $-57\,\mathrm{dBm}$. This observation, along with prior simulation results, reveals that the delocalization in phase space is influenced by the emergence of double-peak distributions. These distributions are characterized by the Floquet modes, $|101\rangle_F$, $|222\rangle_F$, and $|410\rangle_F$. Importantly, the manifestation of this bimodal structure is not a gradual transition but occurs abruptly at the CPP. This phenomenon corresponds to the observed change in the slope of transmon population versus pump power in the transmon system, as depicted in Fig. 4.7 (d).

4.5 Single-photon detection performance

We further investigate our device as a single-photon detector. An important figure of merit of such device is its detection efficiency. We extract corresponding efficiencies for various pump frequencies and powers up to the CPP at various calibrated buffer signal powers (see Fig. 4.10). Performance of the conversion process is characterized by a separate conversion efficiency defined as [41]

$$\eta_c = 4\frac{\kappa_{\mathrm{nl}}\kappa_b}{(\kappa_{\mathrm{nl}}+\kappa_b)^2}, \tag{4.6}$$

with $\kappa_{\mathrm{nl}} = 4\left|g_4\xi_p\right|^2/\kappa_w$. Its relationship with the qubit population $n_q = \langle\hat{\sigma}^\dagger\hat{\sigma}\rangle$ is

$$n_q = n^*\left(1-\exp\left(\eta_c\left|b_{\mathrm{in}}\right|^2 t_b\right)\right), \tag{4.7}$$

where $|b_{\mathrm{in}}|^2$ is buffer photon flux and t_b is the buffer pulse length. Here, $n^* \leq 1$ is the saturated qubit population, whence the detection efficiency is defined as

$$\eta_{\mathrm{det}} := n^*\eta_c. \tag{4.8}$$

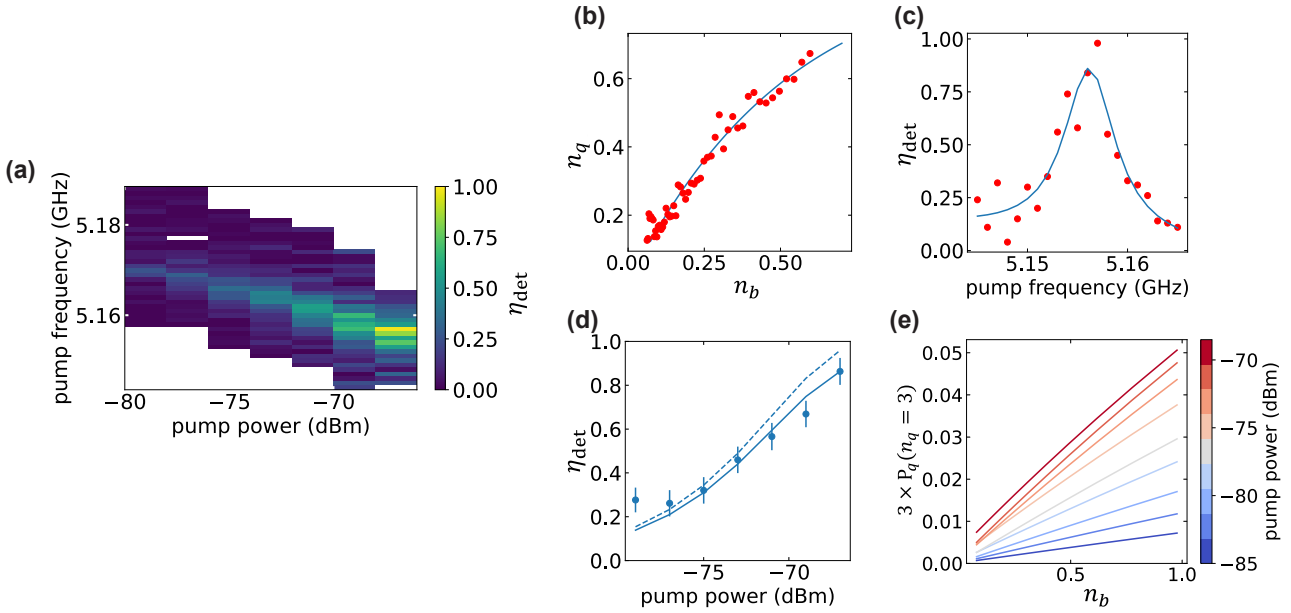

Figure 4.10. (a) Measurement of the detection efficiency as a function of the pump frequency and power. (b) Qubit population as a function of the steady state buffer photon number n_b. The red dots are the measured data points, while the blue line is fitted by numerically solving the quantum Lindblad-Master equation with $t_b = 0.55\,\mu$s (see Eq. (4.4)). (c) Lorentzian fit of η_{det} at $P_p = -67\,$dBm and $f_p = 5.156\,$GHz. (d) Single-photon detection efficiency η_{det} as a function of the pump power. The blue dots are the optimal detection efficiency extracted from the Lorentzian fit described in (c). The solid line is the fit using Eq. (4.6) and Eq. (4.8). The dashed line shows the case for $n^* = 1$. (e) The simulation of the qubit population of the state $|n_q = 3\rangle$ as a function of n_b for various pump powers. The population is calculated as $\langle 3|\,\hat{a}_q^\dagger \hat{a}_q \hat{\rho}_t\,|3\rangle = 3 \times \langle 3|\,\hat{\rho}_t\,|3\rangle = 3 \times \mathrm{P}_q(n_q = 3)$, where the probability being in the state $|n_q = 3\rangle$ is denoted as $\mathrm{P}_q(n_q = 3) = \langle 3|\,\hat{\rho}_t\,|3\rangle$.

In actual experiments, reduced detection efficiencies, $\eta_{\mathrm{det}} < 1$, are attributed to factors such as a finite energy relaxation rate and finite thermal waste photon numbers, which stem from heating due to the elevated pump powers and microwave noise from the input lines [103, 152, 153]. The detection efficiencies η_{det} are extracted using the Lindblad-Master simulations of the Hamiltonian given in Eq. (4.4): We simulate the qubit population n_q for various $g_4\xi_p$, $|b_{\mathrm{in}}|^2$, and thermal bath temperatures at a fixed buffer pulse length t_b. We finally choose η_{det}, such that the simulated $n_q(n_b)$ fits all experimentally measured curves (see Fig. 4.10 (b)). For these simulations, the qubit driving term is neglected, i.e., $\varepsilon_q = 0$. Additionally, the detuning parameter Δ_{qwbp} is set to zero, and the transmon Hilbert space dimension is set to $N_t = 3$, i.e., we take the second excited state into account. These fits are conducted for every pump power and frequency, as shown in Fig. 4.10 (a). Fig. 4.10 (c) shows a Lorentzian fit to obtain the optimal detection efficiencies at each pump power. Finally, we utilize the pump power dependence of η_c, such that n^* and η_c are determined by fitting the optimal detection efficiencies as a function of the pump power using Eq. (4.6) and Eq. (4.8), as demonstrated in Fig. 4.10 (d). In our studies, the maximum conversion and detection efficiencies are $\eta_c = (96 \pm 8)\%$ and $\eta_{\mathrm{det}} = (86 \pm 6)\%$, respectively. In other words, we have a detection infidelity of $1 - \eta_{\mathrm{det}} = (14 \pm 6)\%$. As derived in Subsec. 2.5.4, by taking into account the qubit energy relaxation rate, the saturated qubit population can be determined as

$$n_q^* = \frac{\eta_c\,|b_{\mathrm{in}}|^2}{\eta_c\,|b_{\mathrm{in}}|^2 + \gamma_q}. \tag{4.9}$$

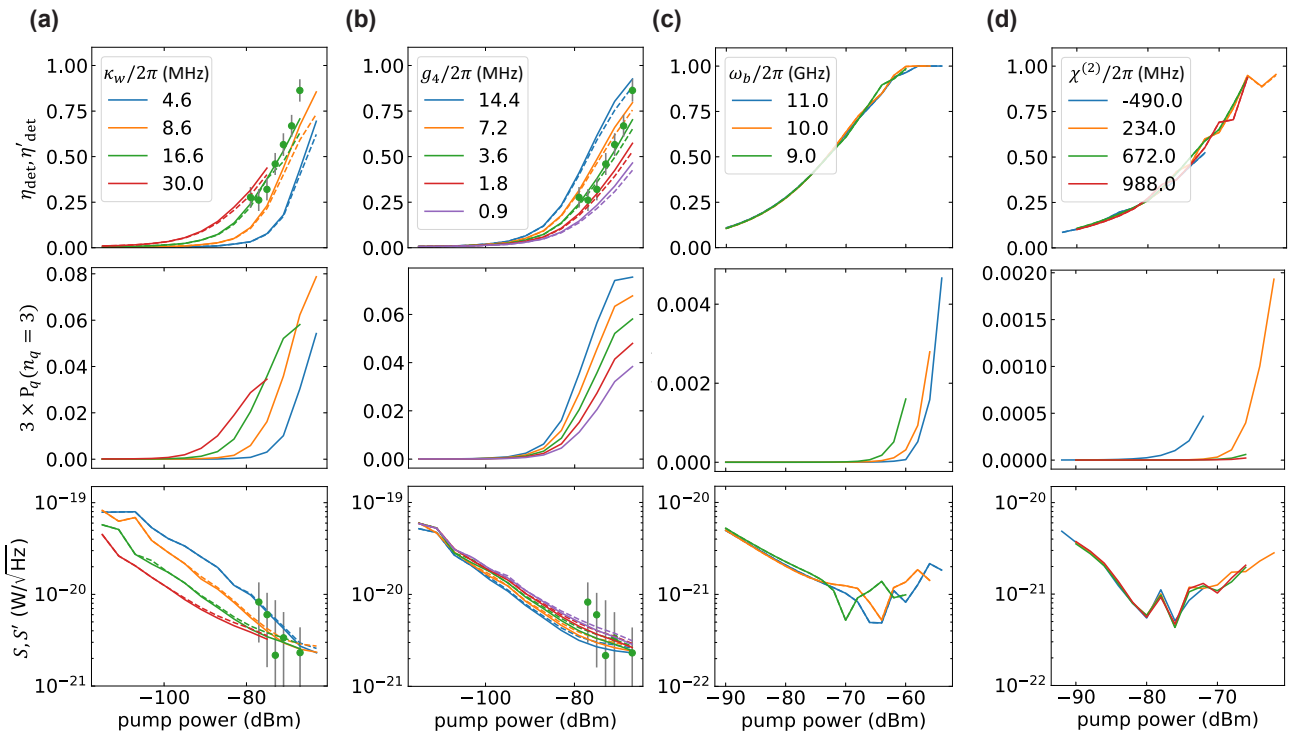

Figure 4.11. Detection efficiency, qubit population contribution of the state $|n_q = 3\rangle$, and sensitivity as a function of the pump power for different system parameters. TI-uncorrected efficiencies $\eta_{\rm det}$ and sensitivities S are represented by solid lines, while TI-corrected efficiencies $\eta'_{\rm det}$ and sensitivities S' are represented by dashed lines. The qubit population of $|n_q = 3\rangle$ is calculated as $\langle 3|\, \hat{a}_q^\dagger \hat{a}_q \hat{\rho}_t\, |3\rangle = 3 \times \mathrm{P}_q(n_q = 3)$, where the probability being in the state $|n_q = 3\rangle$ is denoted as $\mathrm{P}_q(n_q = 3)$. (a) The impact of various dissipation rates of the waste mode $\kappa_w/2\pi = 4.6, 8.6, 16.6, 30\,\mathrm{MHz}$ (blue, orange, green, red line). The green dots are the experimentally extracted values for $\kappa_w/2\pi = 16.6\,\mathrm{MHz}$. (b) The impact of various four-wave interaction strength $g_4/2\pi = 0.9, 1.8, 3.6, 7.2, 14.4\,\mathrm{MHz}$ (purple, red, green, orange, blue line). The green dots represent the experimentally extracted values for $g_4/2\pi = 3.6\,\mathrm{MHz}$. (c) The impact of various buffer frequency $\omega_b/2\pi = 9, 10, 11\,\mathrm{GHz}$ (green, orange, blue line), and (d) anharmonicity $\chi^{(2)}/2\pi = -490, 234, 672, 988\,\mathrm{MHz}$ (blue, orange, green, red line). For the simulation with the positive anharmonicity, we consider typical flux qubit values as a reference. (a) and (b) are simulated at $T_{\rm eff} = 98\,\mathrm{mK}$, while (c) and (d) are obtained in the zero temperature limit, $T = 0\,\mathrm{K}$.

In our case, for a buffer photon flux of $|b_{\rm in}|^2 = 1.22 \times 10^6\,\mathrm{s}^{-1}$ corresponding to the steady state photon number of $n_b = 0.25$ we obtain $n_q^* = 0.97$. Notably, although the buffer photon flux significantly surpasses the decoherence rate observed in our measurements, we can reach the detection infidelity of few percents. Inserting this value into Eq. (4.8), we find the detection infidelity of 7%.

In the case of a non-zero waste photon number, the combined quantum system can partially reverse the four-wave mixing process. Given this scenario, the saturated qubit population is quantified as

$$n_w^* = \frac{1 - 6n_{{\rm th},w}}{1 - 4n_{{\rm th},w}}, \tag{4.10}$$

under the condition $n_{{\rm th},w} \ll 1$ (see Subsec. 2.5.4 for more details). We use a dark count probability of the qubit $(5.4 \pm 8.3)\%$, which we find upon measurements over a short time periods, as compared to T_1, to extract the effective temperature of $T_{\rm eff} = 98\,\mathrm{mK}$. Using the formula $n_{{\rm th},w} = (\exp(\hbar\omega_w/k_{\rm B}T_{\rm eff}) - 1)^{-1}$, we obtain $n_w^* = 0.94$. This result leads to the detection infidelity of 10%. Adding up both infidelities, we obtain a total infidelity of 17%, which aligns well with the measured detection infidelity of 14%.

The discussion so far has omitted effects of the TI process. To address this, we consider the impact of the higher qubit level excitation, $|n_q \geq 3\rangle$, which may additionally lead to an overestimation of the detection efficiency. For that purpose, we extract the occupation probability of $|n_q \geq 3\rangle$ as a function of n_b at the various pump powers, and find that the occupation probabilities of the states $|n_q \geq 4\rangle$ are negligibly small. In Fig. 4.10 (e), the buffer photon number and pump power dependence of the state $|n_q = 3\rangle$ can be clearly observed. Crucially, the dependence on the buffer photon number leads to an overestimation of the detection efficiency. This effect arises because the occupation of this state additionally contributes to the qubit population. In order to estimate the TI influence on the detection efficiency, we remove the contribution of higher excited states, i.e. $\sum_{n_q \leq 2} \langle n_q | \hat{a}_q^\dagger \hat{a}_q \hat{\rho}_t | n_q \rangle$, and extract its efficiency with the same method used in the experiments. Upon this adjustment, we observe a reduction in the detection efficiency by 10% with the optimal parameters. We assume that the correction applied to the simulated data is also applicable to the experimental results. Under this assumption, the original detection efficiency of $\eta_{\mathrm{det}} = 86\%$ reduces to the TI-corrected detection efficiency of $\eta'_{\mathrm{det}} = 78\%$.

Next, we conduct an extensive analysis to enhance the detection efficiency and sensitivity of our SPD. Furthermore, we also discuss how to suppress the influence of the TI process. Referring to Fig. 4.11, we present the TI-uncorrected and TI-corrected detection efficiencies and sensitivities across various parameters. The sensitivities are defined as [243]

$$S = \frac{\hbar\omega_b\sqrt{r_{\mathrm{dc}}}}{\eta_{\mathrm{det}}}, \qquad S' = \frac{\hbar\omega_b\sqrt{r_{\mathrm{dc}}}}{\eta'_{\mathrm{det}}}, \tag{4.11}$$

with the dark count rate r_{dc}. We denote S as the TI-uncorrected sensitivity, and S' as the TI-corrected one. We observe an early rise of the detection efficiency η_{det} (η'_{det}) for the higher dissipation rate of the waste mode κ_w, as demonstrated in Fig. 4.11 (a). However, the increase of κ_w also leads to an enhancement of the Purcell decay rate of the qubit. Thus, ε_q increases for the same pump power accelerating the onset of the TI, which sets the upper bound of the conversion process. Consequently, despite the early rise in detection efficiency, η_{det} (η'_{det}) fails to achieve higher values for larger κ_w. The early increase of the probability $\mathrm{P}_q(n_q = 3)$ supports the argument of this early onset of the TI. Therefore, the optimal detection efficiency, η_{det} (η'_{det}), along with the sensitivity S (S'), is more favorably achieved at lower κ_w. As shown in Fig. 4.11 (b), an enhancement in the coupling strength g_4 improves both η_{det} (η'_{det}) and S (S'). Since the CPP does not change under g_4 variation, we can reach higher η_{det} (η'_{det}) before reaching the CPP. Additionally, when we tune the buffer frequency ω_b to higher frequencies, Fig. 4.11 (c) predicts that $\mathrm{P}_q(n_q = 3)$ decreases. This is attributed to a large detuning between pump and qubit frequencies, which reduces the impact of TI. In other words, η_{det} converges to η'_{det}. Finally, we investigate the influence of the TI for different anharmonicities $\chi^{(2)}$. We observe that large $\left|\chi^{(2)}\right|$ suppresses the TI process, as expected from the previous studies [244–246]. Accordingly, η_{det} asymptotically approaches η'_{det}. Notably, the configuration of the buffer and waste frequencies should be chosen considering a particular value of $\chi^{(2)}$. In general, the pump frequency can match a frequency of a certain multi-photon process at a certain pump power due to the power-dependent frequency shift of the qubit frequency. In the regime of negative anharmonicity, this situation can occur if $\omega_w < \omega_b$, such that $\omega_p, \omega_{0k}/k < \omega'_q$, where ω_{0k}/k is the multi-photon transition frequency. If the pump frequency is close to such a transition frequency, the dark count rate increases, which eventually degrades the single-photon detector performance. For example, for $\chi^{(2)}/2\pi = -490\,\mathrm{MHz}$, the SPD can reach $\eta_{\mathrm{det}} \approx 0.5$, until the pump collides with the two-photon process in the spectral

domain. In simulations considering positive anharmonicity values, we use a flux qubit parameters [246], and predict that it is possible to reach high detection efficiencies up to 95%. Importantly, for the flux qubit, multi-photon processes become relevant at frequencies exceeding the qubit frequency, and given that $\omega_p < \omega_q'$ for $\omega_w < \omega_b$, such processes are effectively far-detuned, resulting in reduction of dark counts (Fig. 4.11 (d)).

Lastly, we compare the sensitivity of our detector for the cases with $T_{\text{eff}} = 98\,\text{mK}$ (Fig. 4.11 (a,b)) and $T = 0\,\text{K}$ (Fig. 4.11 (c,d)). Although the sensitivity for an ideal environment ($T = 0\,\text{K}$) generally improves, it does not reach the state of the art value of $S = 10^{-22}\ \text{W}/\sqrt{\text{Hz}}$ [243]. This is attributed to the filtering effect of our cavity, which requires a stronger pump power to reach the same detection efficiency, and hence, results into a higher dark count probability due to the pump heating. In our case, the dark count rate gives $26 \pm 4\,\text{kHz}$ at the pump power of $P_p = -67\,\text{dBm}$, at which we measure the maximum η_{det} (η_{det}'). Despite of the cavity filtering effect, the dark count rate reported here is comparable to the values reported in the previous studies [56–58].

Chapter 5

TOWARDS MULTI-PHOTON FOCK-STATE GENERATOR BASED ON IRREVERSIBLE COUPLING

In the novel single-photon detection scheme developed by the Flurin group [41], the concept of irreversible qubit-photon coupling plays a pivotal role. This technique, originally conceptualized for single-photon detection, can be appropriately modified to facilitate multi-photon Fock-state generation, as explored in recent studies [93, 247]. Central to this adaptation is the exploitation of three distinct cavity modes: namely, the buffer, waste, and memory modes. Our own horseshoe cavity, characterized by several eigenmodes, is well suitable for this application. Specifically, the first three modes of this cavity are optimally designated as waste, memory, and buffer modes, respectively, as depicted in Fig. 5.1.

An important observation in the horseshoe cavity setup is the fact that there are different coupling rates of these modes to the antenna coupling the feed line to the cavity. The waste and buffer modes exhibit strong coupling, whereas the memory mode is characterized by a markedly weaker interaction. For an antenna length of 2.3 mm, in the absence of qubit chips, the external quality factors for these modes are quantified as 7.61×10^{6}, 4.22×10^{14}, and 6.12×10^{6}, respectively. This configuration results in comparable coupling strengths for the waste and buffer modes. The feasibility of employing the same horseshoe cavity design as a quantum memory has been previously demonstrated in [97, 106, 239], where the introduction of a dummy chip, alongside the transmon chip, ensures the symmetry of the electric field distributions. Thus, the memory mode still couples very weakly to the environment.

Building on the insights from this quantum memory research, we extend our investigation to the potential application of this system in Fock-state generation. This process is facilitated by two distinct pumping mechanisms: (1) a pump to induce parametric interactions between the buffer, qubit, and waste, and (2) a subsequent parametric interactions between the qubit, waste, and memory. The latter pump is activated following the transfer from the buffer to the qubit, thereby transferring the excited qubit state to the memory state.

This chapter commences with an exposition of the fundamental working principles of the Fock-state generator. Following this introduction, we will delve into the detailed theoretical underpinnings that support this application, providing a comprehensive framework for understanding the intricacies of this advanced quantum system.

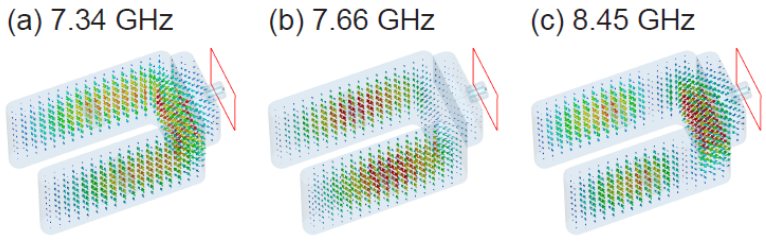

Figure 5.1. The first three eigenmodes of the horseshoe cavity obtained by the CST simulation. (a) waste mode, (b) memory mode, and (c) buffer mode. The waste mode and the buffer mode is strongly coupled to the antenna, whereas the memory mode is very weakly coupled to the antenna.

5.1 Working principle of multi-photon Fock-state generation

The key mechanism of Fock-state generation in our system is based on a sequential, two-pump process. Initially, a photon captured by the buffer mode is transferred to the qubit and waste mode via the first pump. The waste photon rapidly dissipates into the environment. Subsequently, the first pump is deactivated, and the second pump is switched on. This second phase involves the relocation of the qubit excited state to the memory mode, with the waste mode once again playing the role of dissipating photons into the environment[1].

Thus, the whole process can be described by two effective Hamiltonians: The first buffer-to-qubit process is formulated as[2]

$$\hat{\mathcal{H}}_{\text{eff},bqw}/\hbar = g_{bqw}\hat{a}_b\hat{\sigma}\hat{a}_w^\dagger + \text{h.c.}, \tag{5.1}$$

while the second qubit-to-memory process is given by

$$\hat{\mathcal{H}}_{\text{eff},qwm}/\hbar = g_{qwm}\hat{\sigma}\hat{a}_w^\dagger\hat{a}_m^\dagger + \text{h.c.}, \tag{5.2}$$

where the pump is driving at the frequency

$$\omega_{p,qwm} = \omega_w^g + \omega_m^g - \omega_q.$$

After the adiabatic elimination of the waste, the nonlinear single loss operators for both processes are calculated as

$$\hat{L}_{bq} = \sqrt{\kappa_{bq}}\hat{a}_b\hat{\sigma}^\dagger, \qquad \hat{L}_{qm} = \sqrt{\kappa_{qm}}\hat{\sigma}\hat{a}_m^\dagger, \tag{5.3}$$

with the engineered dissipation rate $\kappa_{bq} = 4\left|g_{bqw}\right|^2/\kappa_w$ and

$$\kappa_{qm} = \frac{\left|g_{qwm}\right|^2}{\left(\frac{\kappa_w}{2}\right)^2 + \Delta_{bwq}^2}\kappa_w$$

for an arbitrary detuning Δ_{bwq} (see Sec. 5.3 below for more details.). Hence, both conversion processes are irreversible. Subsequently, the overall process can be summarized as below

$$\begin{aligned}
|1_b0_q0_w0_m\rangle &\xrightarrow{g_{bqw}\hat{a}_b\hat{\sigma}^\dagger\hat{a}_w^\dagger} |0_b1_q1_w0_m\rangle \\
&\xrightarrow{\kappa_w} |0_b1_q0_w0_m\rangle \\
&\xrightarrow{g_{qwm}\hat{\sigma}\hat{a}_w^\dagger\hat{a}_m^\dagger} |0_b0_q1_w1_m\rangle \\
&\xrightarrow{\kappa_w} |0_b0_q0_w1_m\rangle\,.
\end{aligned}$$

[1] An alternative scenario where both pumps are continuously active until the readout process has also been examined. However, this configuration has led to a persistent transfer of photons to an increasingly larger memory photon state due to the parametric qubit-memory interaction, thereby not taking into account the system's functionality as a Fock-state generator (refer to Sec. 5.4 for brief analysis).

[2] We refer to Sec. 2.5 and Ref. [41] for more details.

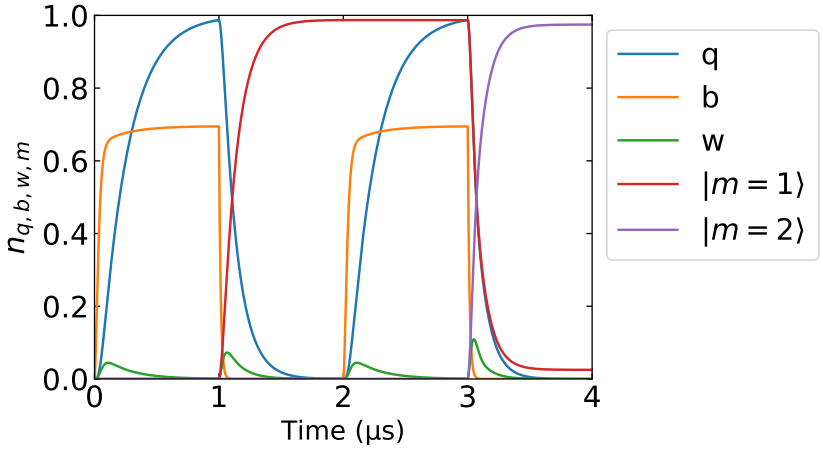

Figure 5.2. Calculated population of the qubit (blue solid line), buffer (orange solid line), and waste mode (green solid line), as well as the probability for the presence of a memory photon in state $|1\rangle$ and $|2\rangle$ (red, purple solid line) with two consecutive pulses. The buffer-qubit interaction is switched on for $0 \leq t < t_{bq} = 1\,\mu$s and $2t_{bq} \leq t < 3t_{bq} = 1\,\mu$s, while the qubit-memory interaction is switched on for $t_{bq} \leq t < 2t_{bq}$ and $3t_{bq} \leq t < 4t_{bq}$. The final qubit population at $1\,\mu$s and $3\,\mu$s is $n_q = 0.987$, while the probability of memory mode occupying $|m = 1\rangle$ at $2\,\mu$s is $\mathrm{P}(m = 1) = 0.987$ and at $4\,\mu$s $\mathrm{P}(m = 2) = 0.975$ for $|m = 2\rangle$. For the simulation, we used a qubit frequency of $\omega_q/2\pi = 5.29\,\mathrm{GHz}$ and qubit anharmonicity of $\alpha/2\pi = 200\,\mathrm{MHz}$, an eigenfrequency of the buffer mode of $\omega_b/2\pi = 8.25\,\mathrm{GHz}$ with the coupling rate of qubit mode of $g_b/2\pi = 54\,\mathrm{MHz}$ and the external decay rate $\kappa_b/2\pi = 12\,\mathrm{MHz}$, an eigenfrequency of the waste mode of $\omega_w/2\pi = 7.45\,\mathrm{GHz}$ with the coupling strength $g_w/2\pi = 44\,\mathrm{MHz}$ and the external decay rate $\kappa_w/2\pi = 12\,\mathrm{MHz}$, and a memory mode frequency of $\omega_m/2\pi = 7.87\,\mathrm{GHz}$ with the coupling strength $g_m/2\pi = 64\,\mathrm{MHz}$.

For the second incoming photon, we obtain

$$\begin{aligned}|1_b0_q0_w1_m\rangle &\xrightarrow{g_{bqw}\hat{a}_b\hat{\sigma}^\dagger\hat{a}_w^\dagger} |0_b1_q1_w1_m\rangle \\ &\xrightarrow{\kappa_w} |0_b1_q0_w1_m\rangle \\ &\xrightarrow{g_{qwm}\hat{\sigma}\hat{a}_w^\dagger\hat{a}_m^\dagger} |0_b0_q1_w2_m\rangle \\ &\xrightarrow{\kappa_w} |0_b0_q0_w2_m\rangle\,.\end{aligned}$$

The principle of irreversibility in the Fock-state generation process, a key aspect of our system, is demonstrated through simulations employing Eq. (5.5). These simulations are shown in Fig. 5.2, where the populations of the qubit, buffer, waste, and the occupation probability of the Fock states of the memory mode are plotted. In this scenario, a pulsed drive mechanism is utilized to initiate the population dynamics.

In our simulation, the temporal dynamics of the interactions between the buffer, qubit, and memory modes are meticulously orchestrated. The buffer-qubit transfer is activated during two distinct intervals: from 0 to $t_{bq} = 1\,\mu$s and subsequently from $2t_{bq}$ to $3t_{bq} = 3\,\mu$s. Conversely, the qubit-memory transfer is operational in the intervening periods, specifically from t_{bq} to $2t_{bq} = 2\,\mu$s and from $3t_{bq}$ to $4t_{bq} = 4\,\mu$s. This staggered approach allows for a controlled sequence of population transfer between the modes. Crucially, at the end of the first and second buffer-qubit transfer periods (at $1\,\mu$s and $3\,\mu$s, respectively), the qubit population achieves a high value of $n_q = 0.987$. This high population indicates efficient population transfer from the buffer to the qubit. Subsequently, following each qubit-memory transfer period, the memory mode occupancy demonstrates significant probabilities for specific

Fock states. At $2\,\mu$s, the probability of the memory mode being in the single-photon state $|m=1\rangle$ is $\mathrm{P}(m=1)=0.987$. Furthermore, at $4,\mu$s, the probability of observing the memory mode in the two-photon state $|m=2\rangle$ is $\mathrm{P}(m=2)=0.975$. The primary reason for not achieving a fidelity close to unity is the presence of a nonzero number of waste photons at the beginning of the pulse sequence, which leads to a finite reverse interaction.

We can extend this discussion to estimate the highest achievable Fock state. The typical timescale to write a Fock state into the memory is $t_F = 1/\kappa_{bq} + 1/\kappa_{qm} \approx 270\,\mathrm{ns}$. To achieve a transfer fidelity over 99%, the total writing time should be $t = 5t_F \approx 1.5\,\mu$s, as the fidelity evolves approximately according to $1-\exp(-t/t_F)$ [3]. Additionally, we must consider the fidelity loss due to the initial waste photon population. Based on simulations demonstrated in Fig. 5.2, the estimated total fidelity loss per Fock state generation is 1.3%. Under these conditions, we can achieve an eighth Fock state with a fidelity of around $0.987^8 \approx 0.90$ over a total duration of $t_{\mathrm{tot}} = 8t \approx 12\,\mu$s. The effect of internal qubit and memory loss rates is negligible if we assume a reasonable loss rate of $1/\kappa_q = 1/\kappa_m = 500\,\mu$s for the qubit and memory, respectively, as reported in [105].

These probabilities underscore the potentially high performance of the sequential interaction strategy in generating distinct Fock states within the memory mode. The achievable high values of $\mathrm{P}(m=1)$ and $\mathrm{P}(m=2)$ at these specific times require the precise and controlled nature of the photon state transfer from the qubit to the memory mode. If this can be realized, there is an interesting potential of our system for reliable multi-photon Fock-state generation.

Additionally, we address the critical issue of releasing the generated Fock states, a notable challenge in our current methodology. The primary limitation arises from the inherent characteristics of the qubit used in our system. While the process of generating Fock states is efficient, the release mechanism is constrained by the capacity of the qubit to convert only one photon at a time. This limitation precludes the direct reversal of the state generation process for multi-photon Fock states. Consequently, while sequential single-photon Fock states can be released, the simultaneous release of a multi-photon Fock state remains unfeasible under this setup. To overcome this bottleneck, we propose pivoting from the 3D cavity design to a 2D chip-based approach. Central to this alternative strategy is the modification of the waste mode into a frequency-tunable waste resonator. This resonator frequency can be dynamically aligned with that of the memory mode. Given the high dissipation rate of the waste mode, such an alignment would effectively enhance the coupling of the memory mode to the environment. This enhanced coupling is pivotal for facilitating the release of multi-photon Fock states. The technical realization of this frequency tuning can be achieved using a direct-current superconducting quantum interference device (SQUID), terminating a $\lambda/4$ CPW resonator. Drawing parallels with the Josephson parametric amplifier [248], the application of a magnetic flux through the SQUID alters the inductance of the resonator. This alteration enables us to modulate the effective resonance frequency of the waste resonator, thereby creating a tunable system capable of controlled release of multi-photon Fock states.

Lastly, we want to shortly discuss the limitation of a 2D resonator towards a 3D cavity from the quality factor standpoint. As mentioned in Sec.2.2, due to the weak vacuum field of the 3D cavity, its internal quality factors can reach up to reaching up to $Q_i \sim 10^9$[99, 108], while that of 2D resonators can reach up to $Q_i \sim 10^7$[213].

[3] We refer to Sec. 2.5 and Ref. [41] for the discussion of the temporal evolution of the conversion process.

5.2 System Hamiltonian Derivation

The key idea of the derivation follows the description in the paper [41]. The quantum system consists of a qubit, buffer, waste, and memory mode, and two pump drives for parametric interactions, which Hamiltonian is read as

$$\begin{aligned}\hat{\mathcal{H}}/\hbar = &\sum_{k=b,w,q,m} \omega_k \hat{a}_k^\dagger \hat{a}_k - \frac{E_J}{\hbar}\left(\cos\varphi + \frac{\varphi^2}{2}\right) \\ &+ 2\epsilon_{bwq}\cos\left(\omega_{p,bqw}t\right)\left(\hat{a}_q + \hat{a}_q^\dagger\right) \\ &+ 2\epsilon_{qwm}\cos\left(\omega_{p,qwm}t\right)\left(\hat{a}_q + \hat{a}_q^\dagger\right)\end{aligned} \tag{5.4}$$

with the phase across the junction

$$\hat{\varphi} = \sum_{k=b,w,q,m} \varphi_k \left(\hat{a}_k + \hat{a}_k^\dagger\right),$$

where the indices q, b, w, m refers to the qubit, buffer, waste, and memory modes, respectively, φ_k is the zero-point fluctuations of the phase across mode k, and E_J the Josephson energy. The pump amplitudes are denoted as ϵ_{bwq} and ϵ_{qwm} for the irreversible transfer from buffer to qubit and from qubit to memory, respectively.

We first transform our Hamiltonian into the displaced frame to account for the strong pump with the mean field amplitudes $\xi_{p,bwq} \approx -\epsilon_{bwq}/\left(\omega_q - \omega_{p,bqw}\right)$ and $\xi_{p,qwm} \approx -\epsilon_{qwm}/\left(\omega_q - \omega_{p,qwm}\right)$ [39, 41]. Furthermore, after transforming into the interaction picture

$$\hat{\mathcal{H}}_0/\hbar = \sum_{k=b,w,q,m} \left(\omega_k - \delta_k\right)\hat{a}_t^\dagger \hat{a}_k$$

with the arbitrary detuning $\delta_k = \delta_{k,bqw} + \delta_{k,qwm}$, which will be used by the pump tones to cancel ac-Stark shifts due to the Kerr effect. As a result, we obtain

$$\hat{\mathcal{H}}'/\hbar = \sum_{k=b,w,q,m} \delta_k \hat{a}_k^\dagger \hat{a}_k - \frac{E_J}{\hbar}\left(\cos\varphi' + \frac{\varphi'^2}{2}\right)$$

with

$$\begin{aligned}\hat{\varphi}' = &\sum_{k=b,w,m} \varphi_k \left(\hat{a}_k e^{-i(\omega_k - \delta_k)} + \hat{a}_k^\dagger e^{i(\omega_k - \delta_k)}\right) \\ &+ \varphi_q\left(\xi_{p,bwq}e^{-i\omega_{p,bqw}t} + \xi_{p,bwq}^* e^{i\omega_{p,bqw}t}\right) \\ &+ \varphi_q\left(\xi_{p,qwm}e^{-i\omega_{p,qwm}t} + \xi_{p,qwm}^* e^{i\omega_{p,qwm}t}\right)\end{aligned}$$

and the pump frequencies

$$\begin{aligned}\omega_{p,bqw} &= \left(\omega_q - \delta_{q,bqw}\right) + \left(\omega_w - \delta_{w,bqw}\right) - \left(\omega_b - \delta_{b,bqw}\right) \\ \omega_{p,qwm} &= \left(\omega_m - \delta_{m,qwm}\right) + \left(\omega_w - \delta_{w,qwm}\right) - \left(\omega_q - \delta_{q,qwm}\right)\end{aligned}$$

Due to

$$\begin{aligned}\frac{\hat{\varphi}'^4}{24} =&\xi_{p,bwq}e^{-i\omega_{p,bqw}t}\varphi_q\hat{a}_q^\dagger e^{i\left(\omega_q-\delta_{q,bqw}\right)t}\varphi_w\hat{a}_w^\dagger e^{i\left(\omega_w-\delta_{w,bqw}\right)t}\varphi_b\hat{a}_b e^{-i\left(\omega_b-\delta_{b,bqw}\right)t}\\ &+\xi_{p,qwm}e^{-i\omega_{p,qwm}t}\varphi_w\hat{a}_w^\dagger e^{i(\omega_w-\delta_{w,qwm})t}\varphi_m\hat{a}_m^\dagger e^{-i(\omega_m-\delta_{m,qwm})t}\varphi_q\hat{a}_q e^{-i(\omega_q-\delta_{q,qwm})t}\\ &+\sum_{k,k'}\varphi_k^2\varphi_{k'}^2\hat{a}_k^\dagger\hat{a}_k\hat{a}_{k'}^\dagger\hat{a}_{k'}+\sum_{k\neq q}\varphi_k^2\varphi_q^2\hat{a}_k^\dagger\hat{a}_k\left(\left|\xi_{p,bwq}\right|^2+\left|\xi_{p,qwm}\right|^2\right)\\ &+\varphi_q^4\left(\left|\xi_{p,bwq}\right|^2+\left|\xi_{p,qwm}\right|^2\right)\hat{a}_q^\dagger\hat{a}_q+\frac{1}{2}\sum_k\varphi_k^4\hat{a}_k^\dagger\hat{a}_k^\dagger\hat{a}_k\hat{a}_k\\ &+\text{h.c.}+\text{fast rotating terms}\end{aligned}$$

expanding the cosine term to the forth order leads to

$$\begin{aligned}\hat{\mathcal{H}}' \approx&\hat{\mathcal{H}}_{\text{Stark}}+\hat{\mathcal{H}}_{\text{Kerr}}+\hat{\mathcal{H}}_{\text{4WM}}\\ \hat{\mathcal{H}}_{\text{Stark}}/\hbar =&\sum_{k=b,w,m}\left(\delta_k-\chi_{qk}\left(\left|\xi_{p,bwq}\right|^2+\left|\xi_{p,qwm}\right|^2\right)\right)\hat{a}_k^\dagger\hat{a}_k\\ &+\left(\delta_q-2\chi_{qq}\left(\left|\xi_{p,bwq}\right|^2+\left|\xi_{p,qwm}\right|^2\right)\right)\hat{a}_q^\dagger\hat{a}_q\\ \hat{\mathcal{H}}_{\text{Kerr}}/\hbar =&-\sum_{k=q,b,w,m}\frac{\chi_{kk}}{2}\hat{a}_k^\dagger\hat{a}_k^\dagger\hat{a}_k\hat{a}_k-\sum_{k,k'}\chi_{kk'}\hat{a}_k^\dagger\hat{a}_k\hat{a}_{k'}^\dagger\hat{a}_{k'}\\ \hat{\mathcal{H}}_{\text{4WM}}/\hbar =&g_{bwq}\hat{a}_b\hat{a}_w^\dagger\hat{a}_q^\dagger+g_{bwq}^*\hat{a}_b^\dagger\hat{a}_w\hat{a}_q+g_{qwm}\hat{a}_q^\dagger\hat{a}_w\hat{a}_m+g_{qwm}^*\hat{a}_q\hat{a}_w^\dagger\hat{a}_m^\dagger\end{aligned}$$

with the detunings

$$\begin{aligned}\delta_{q,bqw} =&2\chi_{qq}\left|\xi_{p,bwq}\right|^2, & \delta_{q,qwm} =&2\chi_{qq}\left|\xi_{p,qwm}\right|^2,\\ \delta_{b,bqw} =&\chi_{qb}\left|\xi_{p,bwq}\right|^2, & \delta_{b,qwm} =&\chi_{qb}\left|\xi_{p,qwm}\right|^2,\\ \delta_{m,bqw} =&\chi_{qm}\left|\xi_{p,bwq}\right|^2, & \delta_{m,qwm} =&\chi_{qm}\left|\xi_{p,qwm}\right|^2,\\ \delta_{w,bqw} =&\chi_{qw}\left|\xi_{p,bwq}\right|^2+\Delta_{bwq}, & \delta_{w,qwm} =&\chi_{qw}\left|\xi_{p,qwm}\right|^2,\end{aligned}$$

the Kerr interaction strengths

$$\chi_{kk} =E_J\varphi_k^4/2/\hbar, \qquad \chi_{kk'} =E_J\varphi_k^2\varphi_k'^2/\hbar,$$

and the effective parametric interaction strengths

$$g_{bwq} =-E_J\xi_{p,bwq}\varphi_q^2\varphi_w\varphi_b/\hbar, \qquad g_{qwm} =-E_J\xi_{p,qwm}\varphi_q^2\varphi_w\varphi_m/\hbar.$$

5.3 Derivation of Nonlinear Decay

In this section, we derive the nonlinear decay by tracing out the waste modes with adiabatic elimination. After canceling out the ac-Stark terms and restrict the Hilbert space of the qubit mode to a two level

system ($\hat{a}_q \to \hat{\sigma}$), we arrive at

$$\begin{aligned}
\hat{\mathcal{H}}'' =& \hat{\mathcal{H}}_w + \hat{\mathcal{H}}_{qbm} \\
\hat{\mathcal{H}}_w/\hbar =& g_{bwq}\hat{a}_b\hat{a}_w^\dagger\hat{\sigma}^\dagger + g_{bwq}^*\hat{a}_b^\dagger\hat{a}_w\hat{\sigma} + g_{qwm}\hat{\sigma}^\dagger\hat{a}_w\hat{a}_m + g_{qwm}^*\hat{\sigma}\hat{a}_w^\dagger\hat{a}_m^\dagger \\
&+ \left(\Delta_{bwq} - \chi_{qw}\hat{\sigma}^\dagger\hat{\sigma} - \chi_{bw}\hat{a}_b^\dagger\hat{a}_b\right)\hat{a}_w^\dagger\hat{a}_w - \frac{\chi_{ww}}{2}\hat{a}_w^\dagger\hat{a}_w^\dagger\hat{a}_w\hat{a}_w \\
\hat{\mathcal{H}}_{qbm}/\hbar =& -\sum_{k=b,m}\frac{\chi_{kk}}{2}\hat{a}_k^\dagger\hat{a}_k^\dagger\hat{a}_k\hat{a}_k - \sum_{k\neq k'=q,b,m}\chi_{kk'}\hat{a}_k^\dagger\hat{a}_k\hat{a}_{k'}^\dagger\hat{a}_{k'},
\end{aligned}$$

which dynamics is described by the Lindblad master equation in Eq. (2.105)

$$\begin{aligned}
\frac{\mathrm{d}}{\mathrm{d}t}\hat{\rho} =& -i\left[\hat{\mathcal{H}}'', \hat{\rho}\right] + \kappa_w\mathcal{D}[\hat{a}_w]\hat{\rho} + \kappa_b\mathcal{D}[\hat{a}_b]\hat{\rho} + \gamma_q\mathcal{D}[\hat{\sigma}]\hat{\rho} + \gamma_\phi\mathcal{D}[\hat{\sigma}^\dagger\hat{\sigma}]\hat{\rho} \\
=& -i\left[\hat{\mathcal{H}}_w, \hat{\rho}\right] + \kappa_w\mathcal{D}[\hat{a}_w]\hat{\rho} + \mathcal{L}_{qbm}\left[\hat{\rho}\right]
\end{aligned} \tag{5.5}$$

and

$$\mathcal{L}_{qbm}\left[\hat{\rho}\right] = -i\left[\hat{\mathcal{H}}_{qbm}, \hat{\rho}\right] + \kappa_b\mathcal{D}[\hat{a}_b]\hat{\rho} + \gamma_q\mathcal{D}[\hat{\sigma}]\hat{\rho} + \gamma_\phi\mathcal{D}[\hat{\sigma}^\dagger\hat{\sigma}]\hat{\rho}.$$

For the adiabatic elimination, we assume that

$$\left|\frac{g_{bwq,qwm}}{\kappa_w}\right|, \left|\frac{\chi_{kk'}}{\kappa_w}\right| \sim \delta \ll 1,$$

such that the waste mode is dominantly in the vacuum state due to the fast decay rate κ_w. In particular, for the density matrix $\hat{\rho}$, the reduced density matrices acting on the qubit, buffer, and memory Hilbert space have the following relations:

$$\langle 0|\hat{\rho}|0\rangle = \hat{\rho}_{00}, \qquad \langle 0|\hat{\rho}|1\rangle = \delta\hat{\rho}_{01}, \qquad \langle 1|\hat{\rho}|1\rangle = \delta^2\hat{\rho}_{11}, \qquad \langle 0|\hat{\rho}|2\rangle = \delta^2\hat{\rho}_{02}$$

with $|k\rangle, |k'\rangle$ being the Fock states basis of the waste mode. By projecting Eq. (5.5) with $\langle 0|...|0\rangle, \langle 0|...|1\rangle, \langle 1|...|1\rangle$, respectively, we obtain

$$\begin{aligned}
\frac{\mathrm{d}}{\mathrm{d}t}\hat{\rho}_{00} =& -i\langle 0|\left[g_{bwq}\hat{a}_b\hat{a}_w^\dagger\hat{\sigma}^\dagger + g_{bwq}^*\hat{a}_b^\dagger\hat{a}_w\hat{\sigma} + g_{qwm}\hat{\sigma}^\dagger\hat{a}_w\hat{a}_m + g_{qwm}^*\hat{\sigma}\hat{a}_w^\dagger\hat{a}_m^\dagger, \hat{\rho}\right]|0\rangle \\
&- i\langle 0|\left[\left(\Delta_{bwq} - \chi_{qw}\hat{\sigma}^\dagger\hat{\sigma} - \chi_{bw}\hat{a}_b^\dagger\hat{a}_b - \chi_{mw}\hat{a}_m^\dagger\hat{a}_m\right)\hat{a}_w^\dagger\hat{a}_w, \hat{\rho}\right]|0\rangle \\
&+ \langle 0|\kappa_w\mathcal{D}[\hat{a}_w]\hat{\rho}|0\rangle + \mathcal{L}_{qbm}\left[\hat{\rho}_{00}\right] \\
=& -i\delta\left[g_{bwq}^*\hat{a}_b^\dagger\hat{\sigma}\hat{\rho}_{10} - g_{bwq}\hat{\rho}_{01}\hat{a}_b\hat{\sigma}^\dagger + g_{qwm}^*\hat{\sigma}^\dagger\hat{a}_m\hat{\rho}_{10} - g_{qwm}\hat{\rho}_{01}\hat{\sigma}\hat{a}_m^\dagger\right] \\
&+ \delta^2\kappa_w\hat{\rho}_{11} + \mathcal{L}_{qbm}\left[\hat{\rho}_{00}\right] + \mathcal{O}\left(\delta^3\right)
\end{aligned} \tag{5.6}$$

$$
\begin{aligned}
\delta\frac{\mathrm{d}}{\mathrm{d}t}\hat{\rho}_{01} =& -i\delta^2\left[g^*_{bwq}\hat{a}^\dagger_b\hat{\sigma}\hat{\rho}_{11} - g_{bwq}\hat{\rho}_{02}\hat{a}_b\hat{\sigma}^\dagger + g^*_{qwm}\hat{\sigma}\hat{a}^\dagger_m\hat{\rho}_{11} - g_{qwm}\hat{\rho}_{02}\hat{\sigma}^\dagger\hat{a}_m\right]\\
&+ i\hat{\rho}_{00}\left[g^*_{bwq}\hat{a}^\dagger_b\hat{\sigma} + g^*_{qwm}\hat{\sigma}^\dagger\hat{a}_m\right]\\
&+ i\delta\hat{\rho}_{01}\left[\Delta_{bwq} - \chi_{qw}\hat{\sigma}^\dagger\hat{\sigma} - \chi_{bw}\hat{a}^\dagger_b\hat{a}_b - \chi_{mw}\hat{a}^\dagger_m\hat{a}_m\right]\\
&- \delta\frac{\kappa_w}{2}\hat{\rho}_{01} + \delta\mathcal{L}_{qbm}\left[\hat{\rho}_{01}\right] + \mathcal{O}\left(\delta^3\right)\\
\overset{\delta\sim g/\kappa_w}{=}& i\hat{\rho}_{00}\left[g^*_{bwq}\hat{a}^\dagger_b\hat{\sigma} + g^*_{qwm}\hat{\sigma}^\dagger\hat{a}_m\right]\\
&+ i\delta\hat{\rho}_{01}\left[\Delta_{bwq} - \chi_{qw}\hat{\sigma}^\dagger\hat{\sigma} - \chi_{bw}\hat{a}^\dagger_b\hat{a}_b - \chi_{mw}\hat{a}^\dagger_m\hat{a}_m\right]\\
&- \delta\frac{\kappa_w}{2}\hat{\rho}_{01} + \delta\mathcal{L}_{qbm}\left[\hat{\rho}_{01}\right] + \mathcal{O}\left(\delta^3\right)
\end{aligned}
\tag{5.7}
$$

$$
\begin{aligned}
\delta^2\frac{\mathrm{d}}{\mathrm{d}t}\hat{\rho}_{11} =& -i\delta^3\left[g^*_{bwq}\hat{a}^\dagger_b\hat{\sigma}\hat{\rho}_{21} - g_{bwq}\hat{\rho}_{12}\hat{a}_b\hat{\sigma}^\dagger + g^*_{qwm}\hat{\sigma}\hat{a}^\dagger_m\hat{\rho}_{21} - g_{qwm}\hat{\rho}_{12}\hat{\sigma}^\dagger\hat{a}_m\right]\\
&- i\delta\left[g_{bwq}\hat{a}_b\hat{\sigma}^\dagger\hat{\rho}_{01} - g^*_{bwq}\hat{\rho}_{10}\hat{a}^\dagger_b\hat{\sigma} + g_{qwm}\hat{\sigma}^\dagger\hat{a}_m\hat{\rho}_{01} - g^*_{qwm}\hat{\rho}_{10}\hat{\sigma}\hat{a}^\dagger_m\right]\\
&+ i\delta^2\left[\Delta_{bwq} - \chi_{qw}\hat{\sigma}^\dagger\hat{\sigma} - \chi_{bw}\hat{a}^\dagger_b\hat{a}_b - \chi_{mw}\hat{a}^\dagger_m\hat{a}_m, \hat{\rho}_{11}\right]\\
&+ \delta^2\kappa_w\left(\underbrace{\hat{\rho}_{02}}_{|2\rangle\notin\mathcal{H}_w} - \hat{\rho}_{11}\right) + \delta^2\mathcal{L}_{qbm}\left[\hat{\rho}_{11}\right] + \mathcal{O}\left(\delta^3\right)\\
=& -i\delta\left[g_{bwq}\hat{a}_b\hat{\sigma}^\dagger\hat{\rho}_{01} - g^*_{bwq}\hat{\rho}_{10}\hat{a}^\dagger_b\hat{\sigma} + g_{qwm}\hat{\sigma}^\dagger\hat{a}_m\hat{\rho}_{01} - g^*_{qwm}\hat{\rho}_{10}\hat{\sigma}\hat{a}^\dagger_m\right]\\
&+ i\delta^2\left[\Delta_{bwq} - \chi_{qw}\hat{\sigma}^\dagger\hat{\sigma} - \chi_{bw}\hat{a}^\dagger_b\hat{a}_b - \chi_{mw}\hat{a}^\dagger_m\hat{a}_m, \hat{\rho}_{11}\right]\\
&- \delta^2\kappa_w\hat{\rho}_{11} + \delta^2\mathcal{L}_{qbm}\left[\hat{\rho}_{11}\right] + \mathcal{O}\left(\delta^3\right)
\end{aligned}
\tag{5.8}
$$

Focusing the relevant dynamics, we find that Eqs. (5.7) and (5.8) include a damping term of order δ^0, while all terms in Eq. (5.6) are of order δ^2. Hence, this allows us to treat $\hat{\rho}_{01}$ and $\hat{\rho}_{11}$ as a steady-state (adiabatic approximation), which results to

$$
\begin{aligned}
\hat{\rho}_{01} =& i\hat{\rho}_{00}\left[g^*_{bwq}\hat{a}^\dagger_b\hat{\sigma} + g^*_{qwm}\hat{\sigma}^\dagger\hat{a}_m\right]\left[\frac{\kappa_w}{2} - i\left(\Delta_{bwq} - \chi_{qw}\hat{\sigma}^\dagger\hat{\sigma} - \chi_{bw}\hat{a}^\dagger_b\hat{a}_b - \chi_{mw}\hat{a}^\dagger_m\hat{a}_m\right)\right]^{-1}\\
\approx& \hat{\rho}_{00}\frac{ig^*_{bwq}}{\frac{\kappa_w}{2} - i\left(\Delta_{bwq} - \chi_{qw}\right)}\hat{a}^\dagger_b\hat{\sigma} + \hat{\rho}_{00}\frac{ig^*_{qwm}}{\frac{\kappa_w}{2} - i\Delta_{bwq}}\hat{\sigma}^\dagger\hat{a}_m,
\end{aligned}
\tag{5.9}
$$

where we used $\hat{a}^\dagger_b\hat{\sigma}\hat{\sigma}^\dagger\hat{\sigma} = \hat{a}^\dagger_b\hat{\sigma}$ and $|\chi_{bw}|, |\chi_{mw}| \ll |\chi_{qw}|$, which is justified because the zero-point fluctuations of the resonator modes are very small compared to the qubit mode. As for the steady-state solution for $\hat{\rho}_{11}$, we get

$$
\begin{aligned}
\hat{\rho}_{11} =& \frac{1}{\left(\frac{\kappa_w}{2}\right)^2 + \left(\Delta_{bwq} - \chi_{qw}\right)^2}\frac{|g_{bwq}|^2}{\delta}\hat{a}_b\hat{\sigma}^\dagger\hat{\rho}_{00}\hat{a}^\dagger_b\hat{\sigma}\\
&+ \frac{1}{\left(\frac{\kappa_w}{2}\right)^2 + \Delta^2_{bwq}}\frac{|g_{qwm}|^2}{\delta}\hat{\sigma}\hat{a}^\dagger_m\hat{\rho}_{00}\hat{\sigma}^\dagger\hat{a}_m.
\end{aligned}
\tag{5.10}
$$

Inserting the steady-state solutions into Eq. (5.6), we obtain

$$\begin{aligned}
\frac{\mathrm{d}}{\mathrm{d}t}\hat{\rho}_{00} =& -i\delta\left[\frac{-i\left|g_{bwq}\right|^2}{\frac{\kappa_w}{2}+i\left(\Delta_{bwq}-\chi_{qw}\right)}\hat{a}_b^\dagger\hat{a}_b\hat{\sigma}\hat{\sigma}^\dagger\hat{\rho}_{00}-\frac{i\left|g_{bwq}\right|^2}{\frac{\kappa_w}{2}-i\left(\Delta_{bwq}-\chi_{qw}\right)}\hat{\rho}_{00}\hat{a}_b^\dagger\hat{a}_b\hat{\sigma}\hat{\sigma}^\dagger\right] \\
& -i\delta\left[\frac{-i\left|g_{qwm}\right|^2}{\frac{\kappa_w}{2}+i\Delta_{bwq}}\hat{\sigma}^\dagger\hat{\sigma}\hat{a}_m\hat{a}_m^\dagger\hat{\rho}_{00}-\frac{i\left|g_{qwm}\right|^2}{\frac{\kappa_w}{2}-i\Delta_{bwq}}\hat{\rho}_{00}\hat{\sigma}^\dagger\hat{\sigma}\hat{a}_m\hat{a}_m^\dagger\right] \\
& +\frac{\left|g_{bwq}\right|^2}{\left(\frac{\kappa_w}{2}\right)^2+\left(\Delta_{bwq}-\chi_{qw}\right)^2}\hat{a}_b\hat{\sigma}^\dagger\hat{\rho}_{00}\hat{a}_b^\dagger\hat{\sigma} \\
& +\frac{\left|g_{qwm}\right|^2}{\left(\frac{\kappa_w}{2}\right)^2+\Delta_{bwq}^2}\hat{\sigma}\hat{a}_m^\dagger\hat{\rho}_{00}\hat{\sigma}^\dagger\hat{a}_m \\
& +\mathcal{L}_{qbm}\left[\hat{\rho}_{00}\right] \\
=& i\delta\left[\frac{\left|g_{bwq}\right|^2}{\left(\frac{\kappa_w}{2}\right)^2+\left(\Delta_{bwq}-\chi_{qw}\right)^2}\left(\Delta_{bwq}-\chi_{qw}\right)\hat{a}_b^\dagger\hat{a}_b\hat{\sigma}\hat{\sigma}^\dagger,\hat{\rho}_{00}\right] \\
& +i\delta\left[\frac{\left|g_{qwm}\right|^2}{\left(\frac{\kappa_w}{2}\right)^2+\Delta_{bwq}^2}\Delta_{bwq}\hat{\sigma}^\dagger\hat{\sigma}\hat{a}_m\hat{a}_m^\dagger,\hat{\rho}_{00}\right] \\
& +\kappa_{bq}\mathcal{D}\left[\hat{a}_b\hat{\sigma}^\dagger\right]\hat{\rho}_{00}+\kappa_{qm}\mathcal{D}\left[\hat{\sigma}\hat{a}_m^\dagger\right]\hat{\rho}_{00}+\mathcal{L}_{qbm}\left[\hat{\rho}_{00}\right]
\end{aligned} \tag{5.11}$$

with the nonlinear decay rates

$$\kappa_{bq}=\frac{\left|g_{bwq}\right|^2}{\left(\frac{\kappa_w}{2}\right)^2+\left(\Delta_{bwq}-\chi_{qw}\right)^2}\kappa_w, \qquad \kappa_{qm}=\frac{\left|g_{qwm}\right|^2}{\left(\frac{\kappa_w}{2}\right)^2+\Delta_{bwq}^2}\kappa_w. \tag{5.12}$$

5.4 Memory Transfer Dynamics

The dynamics governing transfer quantum information from the buffer mode to memory mode is derived in the following. We add the driving term $i\sqrt{\kappa_b}b_{\mathrm{in}}\left(\hat{a}_b-\hat{a}_b^\dagger\right)$ into the master equation (Eq. (5.11)), where b_{in} is the amplitude of the coherent drive. For simplicity, we further omit the first two terms in Eq. (5.11) and assume $\hat{\mathcal{H}}_{qbm},\gamma_q,\gamma_\phi\ll\kappa_w$ in the zeroth order approximation. This gives us

$$\frac{\mathrm{d}}{\mathrm{d}t}\hat{\rho}_{00}=\kappa_{bq}\mathcal{D}\left[\hat{a}_b\hat{\sigma}^\dagger\right]\hat{\rho}_{00}+\kappa_{qm}\mathcal{D}\left[\hat{\sigma}\hat{a}_m^\dagger\right]\hat{\rho}_{00}+\kappa_b\mathcal{D}\left[\hat{a}_b\right]\hat{\rho}_{00}+\epsilon\left[\hat{a}_b-\hat{a}_b^\dagger,\hat{\rho}_{00}\right] \tag{5.13}$$

with $\epsilon=\sqrt{\kappa_b}b_{\mathrm{in}}$. Since the time evolution of the memory mode is dependent on the qubit state, we first consider $\hat{\rho}_g:==\langle g|\,\hat{\rho}_{00}\,|g\rangle$ and $\hat{\rho}_e:==\langle e|\,\hat{\rho}_{00}\,|e\rangle$, such that

$$\frac{\mathrm{d}}{\mathrm{d}t}\hat{\rho}_g=\kappa_{qm}\hat{a}_m^\dagger\hat{\rho}_e\hat{a}_m-\frac{1}{2}\kappa_{bq}\left(\hat{\rho}_g\hat{a}_b\hat{a}_b^\dagger+\hat{a}_b\hat{a}_b^\dagger\hat{\rho}_g\right)+\kappa_b\mathcal{D}\left[\hat{a}_b\right]\hat{\rho}_g+\epsilon\left[\hat{a}_b-\hat{a}_b^\dagger,\hat{\rho}_g\right], \tag{5.14}$$

$$\frac{\mathrm{d}}{\mathrm{d}t}\hat{\rho}_e=-\frac{1}{2}\kappa_{qm}\left(\hat{\rho}_e\hat{a}_m\hat{a}_m^\dagger+\hat{a}_m\hat{a}_m^\dagger\hat{\rho}_e\right)+\kappa_{bq}\hat{a}_b\hat{\rho}_g\hat{a}_b^\dagger+\kappa_b\mathcal{D}\left[\hat{a}_b\right]\hat{\rho}_e+\epsilon\left[\hat{a}_b-\hat{a}_b^\dagger,\hat{\rho}_e\right]. \tag{5.15}$$

To be able to study how the memory mode acquires the quantum information, we further distinguish the quantum state $\hat{\rho}_{g/e}$ between the memory states by defining $\hat{\rho}_{g/e,m} := \langle m| \hat{\rho}_{g/e} |m\rangle$

$$\begin{aligned}\frac{\mathrm{d}}{\mathrm{d}t}\hat{\rho}_{g,m} =&\kappa_{qm}\hat{a}_m\hat{\rho}_{e,m-1} - \frac{1}{2}\kappa_{bq}\left(\hat{\rho}_{g,m}\hat{a}_b\hat{a}_b^\dagger + \frac{1}{2}\hat{a}_b\hat{a}_b^\dagger\rho_{g,m}\right)\\ &+ \kappa_b\mathcal{D}\left[\hat{a}_b\right]\hat{\rho}_{g,m} + \epsilon\left[\hat{a}_b - \hat{a}_b^\dagger, \hat{\rho}_{g,m}\right], \end{aligned} \tag{5.16}$$

$$\begin{aligned}\frac{\mathrm{d}}{\mathrm{d}t}\hat{\rho}_{e,m} =& -\kappa_{qm}(m+1)\hat{\rho}_{e,m} + \kappa_{bq}\hat{a}_b\hat{\rho}_{g,m}\hat{a}_b^\dagger\\ &+ \kappa_b\mathcal{D}\left[\hat{a}_b\right]\hat{\rho}_{e,m} + \epsilon\left[\hat{a}_b - \hat{a}_b^\dagger, \hat{\rho}_{e,m}\right]. \end{aligned} \tag{5.17}$$

Hence, $\hat{\rho}_{g,m}, \hat{\rho}_{e,m}$ are now the density matrices acting solely on the buffer Hilbert space. In the same spirit as in Sec. 2.5 and Ref. [41], we use the ansatz $\hat{\rho}_{g/e,m} \propto |\beta\rangle\langle\beta|$, which give us after tracing out the density matrix completely

$$\frac{\mathrm{d}}{\mathrm{d}t}p_{g,m} = \kappa_{qm}mp_{e,m-1} - \kappa_{bq}|\beta|^2 p_{g,m}, \tag{5.18}$$

$$\frac{\mathrm{d}}{\mathrm{d}t}p_{e,m} = -\kappa_{qm}(m+1)p_{e,m} + \kappa_{bq}|\beta|^2 p_{g,m}. \tag{5.19}$$

We remind ourselves that $\kappa_{bq,qm}$ are controlled by the pump. For example, if the pump responsible for the buffer-qubit transfer (qubit-memory transfer) is switched off, we have $\kappa_{bq} = 0$ ($\kappa_{qm} = 0$). For the conversion processes explained in Sec. 5.1, the case study of each process is required for the differential equations shown above, which are

$$\frac{\mathrm{d}}{\mathrm{d}t}p_{g,m} = \begin{cases} -\kappa_{bq}|\beta|^2 p_{g,m}, & \text{buffer-qubit transfer} \\ \kappa_{qm}mp_{e,m-1}, & \text{qubit-memory transfer} \end{cases} \tag{5.20}$$

$$\frac{\mathrm{d}}{\mathrm{d}t}p_{e,m} = \begin{cases} \kappa_{bq}|\beta|^2 p_{g,m}, & \text{buffer-qubit transfer,} \\ -\kappa_{qm}(m+1)p_{e,m}, & \text{qubit-memory transfer.} \end{cases} \tag{5.21}$$

We assume that $p_{g,0}(t=0) = 1$ and that the buffer-qubit transfer process is followed by the qubit-memory transfer. Then, the solution of the differential equation reads

$$p_{g,0}(t) = \begin{cases} e^{-\kappa_{bq}|\beta|^2 t}, & t < t_{bq}, \text{ buffer-qubit transfer,} \\ e^{-\kappa_{bq}|\beta|^2 t_{bq}}, & t > t_{bq}, \text{ qubit-memory transfer,} \end{cases} \tag{5.22}$$

$$p_{e,0}(t) = \begin{cases} 1 - e^{-\kappa_{bq}|\beta|^2 t}, & t < t_{bq}, \text{ buffer-qubit transfer,} \\ \left(1 - e^{-\kappa_{bq}|\beta|^2 t_{bq}}\right) e^{-\kappa_{qm}t}, & t > t_{bq}, \text{ qubit-memory transfer,} \end{cases} \tag{5.23}$$

$$p_{g,1}(t) = \begin{cases} 0, & t < t_{bq}, \text{ buffer-qubit transfer,} \\ \left(1 - e^{-\kappa_{bq}|\beta|^2 t_{bq}}\right)\left(1 - e^{-\kappa_{qm}(t-t_{bq})}\right), & t > t_{bq}, \text{ qubit-memory transfer,} \end{cases} \tag{5.24}$$

where t_{bq} is the cut-off time of the buffer-qubit transfer process and the beginning of the qubit-memory process.

The theoretical framework outlined above finds a compelling alignment with the previously presented simulation results (see Fig. 5.2). These theoretical insights delve into the intricate dynamics of state probabilities within our system under specific interaction conditions. In the initial phase of the pulse-driven interaction, for durations $t < t_{bq}$, we observe significant developments in the state

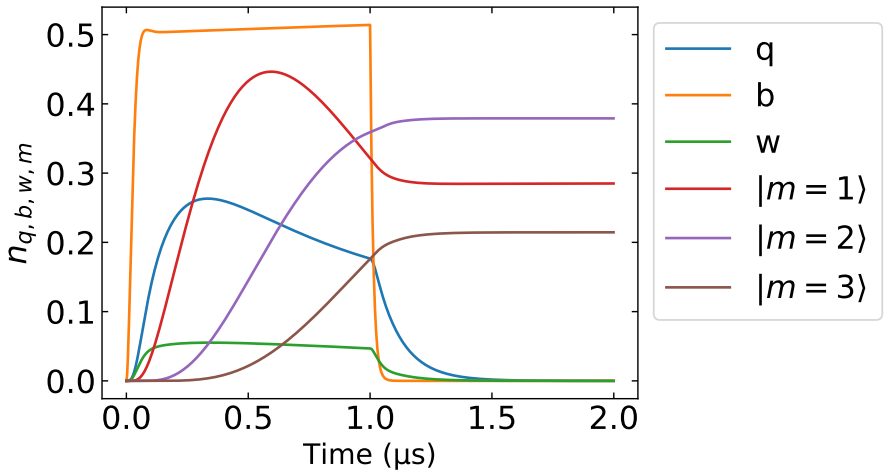

Figure 5.3. Calculated population of qubit (blue solid line), buffer (orange solid line), and waste mode (green solid line), as well as the probability of memory photon in states $|m = 1, 2, 3\rangle$ (red, purple, brown solid lines).

probabilities. The probability of the system residing in the qubit ground state and in a zero-photon memory Fock state, $p_{g,0}$, demonstrates an exponential decrease with increasing pulse length. This trend indicates the effective excitation of the qubit away from its ground state due to the buffer-qubit transfer. Indeed, the probability of encountering the system in the excited state of the qubit with no photons in the memory mode, $p_{e,0}$, exhibits an increasing trend, converging towards $1 - e^{-\kappa_{bq}|\beta|^2 t_{bq}}$. Notably, throughout this phase, the probability $p_{g,1}$, corresponding to the qubit being in the ground state with a single-photon in the memory mode, remains consistently at zero. This observation is in line with the theoretical expectation that the memory mode does not yet acquire any photons during this initial interaction period. As the interaction transitions to the qubit-memory phase (for $t > t_{bq}$), the theoretical model predicts a notable shift in these probabilities. The $p_{e,0}$ value, which was previously increasing, now begins to decrease exponentially, reflecting the transfer of excitation from the qubit to the memory mode. Concurrently, $p_{g,1}$ starts to increase, ultimately saturating at $1 - e^{-\kappa_{bq}|\beta|^2 t_{bq}}$.

Memory transfer dynamics with continuous operation of both pumps

In scenarios where both parametric interactions are perpetually active, the dynamics of memory transfer exhibit distinctive characteristics. The theoretical formulations for the time-dependent probabilities of various states are as follows

$$p_{g,0}(t) = e^{-\kappa_{bq}|\beta|^2 t}, \tag{5.25}$$

$$p_{e,0}(t) = \frac{\kappa_{bq}|\beta|^2}{\kappa_{qm} - \kappa_{bq}|\beta|^2}\left(e^{-\kappa_{bq}|\beta|^2 t} - e^{-\kappa_{qm} t}\right), \tag{5.26}$$

$$p_{g,1}(t) = \frac{\kappa_{qm}\kappa_{bq}|\beta|^2 t}{\kappa_{qm} - \kappa_{bq}|\beta|^2} e^{-\kappa_{bq}|\beta|^2 t} + \frac{\kappa_{qm}\kappa_{bq}|\beta|^2}{\left(\kappa_{qm} - \kappa_{bq}|\beta|^2\right)^2}\left(e^{-\kappa_{qm} t} - e^{-\kappa_{bq}|\beta|^2 t}\right). \tag{5.27}$$

An important observation from these expressions is the behavior of the occupation probability $p_{g,1}$, and by extension $p_{g,m}$, for higher Fock states. Contrary to approaching a saturation near unity, these probabilities demonstrate an exponential decay towards zero. This decay emphasizes the fact that the generation of a controlled multi-photon Fock state is unfeasible under the conditions of simultaneous

and continuous application of both pumps.

This theoretical prediction is visually corroborated in Fig. 5.3, which illustrates the occupation probabilities for each memory Fock state. The plot reveals a concurrent rise in the probabilities of multiple Fock states. Consequently, this pump configuration does not favor the selective generation of a specific multi-photon Fock state. Rather, it leads to a non-discriminatory increase in the probabilities of various states, thus hindering the precise control necessary for effective Fock state generation in this quantum system.

Chapter 6

CONCLUSION AND OUTLOOK

In this thesis, we have addressed two aspects with significant relevance for the improvement of the performance of superconducting quantum technology. First, we have performed a systematic study aiming at the reduction of internal losses in our samples, achieving an improvement by two orders of magnitude through the implementation of novel fabrication techniques. Second, we have conducted a thorough experimental and numerical analysis of the onset of transmon ionization (TI) and the performance of single-photon detectors (SPDs) in a transmon qubit system integrated with a multi-mode 3D cavity.

Regarding the improvement of superconducting quantum circuits, our study has underscored the crucial role of surface treatment and material selection, particularly focusing on the superconductors niobium (Nb) and aluminum (Al), in conjunction with the design of sample boxes. The internal quality factor of coplanar resonators, fabricated using an Al-based lift-off technique developed at the WMI, has been measured. We have observed that in the single-photon limit the internal loss rate of our reference sample was $\delta_i = 3.38 \times 10^{-5}$, comprising both power-dependent two-level-system (TLS) losses ($\delta^0_{\mathrm{TLS}} = 2.49 \times 10^{-5}$) and power-independent losses ($\delta_0 = 0.89 \times 10^{-5}$).

A pivotal reduction of loss channels was realized through the implementation of buffered-oxide etching (BOE) for surface treatment, which substantially mitigates surface oxides and contaminants that lead to TLSs. This treatment significantly reduced the internal losse rate of the Al resonators by approximately an order of magnitude, with $\delta_i \sim 10^{-6}$ being achieved for both lift-off and etching processes. A further enhancement has been observed upon replacing Al by Nb as the superconducting material, leading to an around 50% reduction in internal loss and our best measured internal loss value o $\delta_i = 0.66 \times 10^{-6}$ in the single-photon limit.

The influence of the sample box environment on both the internal and external loss rate has also been investigated. Particularly, the presence of parasitic chip and box modes can introduce additional loss channels in quantum devices under test. Employing the SLH framework, we analyzed the impact of these parasitic modes. We found that the interference effects between the resonator and parasitic modes alter the external loss of the resonator. Additionally, direct interactions between the resonator and parasitic modes create additional decay channels, affecting the internal losses. Experiments with three different sample boxes revealed that changing from an eight-port box without a hole to a two-port box with a hole improved the internal loss rate by 70%.

A second main focus of this thesis was the experimental and numerical study of the transmon-ionization (TI) onset and the single-photon detector (SPD) performance of a transmon qubit coupled to a multi-mode 3D cavity. We have investigated a dependence of the transmon population on the buffer photon number n_b and pump powers, and observed that the transmon is highly-sensitive to n_b at the region close to critical pump powers (CPP). Through a comprehensive analysis employing the Rényi entropy, Floquet theory, and Husimi Q function, we found clear evidence for the presence of a quantum-to-classical phase transition around the CPP. Our numerical simulations are in very

good agreement with the experimental observations, demonstrating the appropriateness of the chosen methodologies for simulating the experimental system.

We have also investigated the device as a single-photon detector, and extracted its detection efficiencies for various pump frequencies and powers up to the CPP. Our measurements show that a maximum TI-uncorrected detection efficiency reaches 86%, while we estimate the TI-corrected detection efficiency to only 78%. The conversion efficiency η_c between the buffer and the qubit-waste mode was found to be limited by the TI, while the reduction of the saturated qubit population n^* can be attributed to a thermal waste photon number and the qubit energy relaxation rate. Finally, increasing the frequency detuning between the pump and qubit frequencies and the qubit anharmonicity was found to strongly suppress the influence of the TI process and leads to a distinct improvement of the TI-corrected detection efficiency and sensitivity. The spectral positioning of the buffer and waste mode frequencies ought to be determined based on the sign of the qubit anharmonicity to ensure that the pump and multi-photon processes do not overlap.

In conclusion, our systematic investigations offer potential advantages inherent to the onset of TI, suggesting its prospective extension to high-efficiency microwave SPDs compatible with 3D cavity architectures. Moreover, this study demonstrates the necessity for a careful analysis of the efficiency extraction, particularly given the impact of the TI process. These insights bear significant implications for the development of parametric device applications, which are essential in advancing quantum information processing and communication based on superconducting circuits.

In the final segment of this thesis, we have explored the prospective application of our advanced SPD system as a multi-photon Fock-state generator, utilizing the concept of irreversible coupling. By incorporating an additional memory mode into the existing SPD configuration, our system is suitable for at converting an excited state of the qubit into a memory photon. This conversion is facilitated through a sequential application of two distinct pump processes. Our simulation results have particularly demonstrated the capabilities of our system for the generation of multi-photon Fock states. Using parameters of present day superconducting circuit technology, our simulation results yield a high probability for successfully transferring the qubit excited state into the memory photon states. Notably, high probabilities of finding the memory mode in Fock states 1 and 2 of $\mathrm{P}(m = 1) = 0.987$ and $\mathrm{P}(m = 2) = 0.975$, respectively, have been found. These probabilities underscore the potential of our system in reliably generating multi-photon Fock states, marking a significant step forward in the field of quantum state manipulation and generation.

Appendix A

DERIVATION OF THREE-LEVEL TRANSMON EIGENENERGIES

Let us derive the transmon energies for a three-level system, which we mostly follow the approach provided by [113]. We expand the Josephson term to the fourth order and calculate the eigenenergies of this system after rewriting $(\hat{n}, \hat{\varphi})$ into the annihilation/creation operators. What does this mean from the two-level system point of view compared to the harmonic oscillator result?

The essential point of the transmon qubit from the two-level quantum system point of view is the non-linearity of the potential of the Josephson junction, namely,

$$\hat{V} = -E_J \cos\hat{\varphi}.$$

Evidently, then the level spacing is not equal as for an harmonic potential of a quantum harmonic oscillator.
In order to discuss the impact of the nonlinearity, we perform a power series expansion of the cosine potential up to fourth order. We find [1]

$$\begin{aligned}\hat{\mathcal{H}} =& 4E_C\hat{n}^2 - E_J\cos\hat{\varphi} \\ =& 4E_C\hat{n}^2 - E_J\left(1 - \frac{1}{2!}\hat{\varphi}^2 + \frac{1}{4!}\hat{\varphi}^4 + \mathcal{O}\left(\hat{\varphi}^6\right)\right) \\ =& 4E_C\hat{n}^2 + \frac{1}{2!}E_J\hat{\varphi}^2 - \frac{1}{4!}E_J\hat{\varphi}^4 - E_J + \mathcal{O}\left(\hat{\varphi}^6\right)\end{aligned}$$

considering only small values of φ, this is a good approximation. Note that the power expansion contains only even terms in $\hat{\varphi}$ and therefore there will be no three-wave mixing. An asymmetry can be easily introduced by applying a finite current or a flux bias.

First, let us focus on the Hamiltonian up to the second order for obtaining the eigenenergy of the simple quantum harmonic oscillator E_0. We can obtain the above eigenequation (neglecting the offset energy and correcting terms) by using the algebraic derivation of the quantum harmonic oscillator, however, this form reminds us of the equation of the ellipse given by

$$\frac{x^2}{a^2} + \frac{y^2}{b^2} = 1,$$

for our case in particular,

$$\frac{\hat{\mathcal{H}}}{2E_CE_J} = \frac{\hat{n}^2}{E_J/2} + \frac{\hat{\varphi}^2}{4E_C}.$$

But the elliptic method can be more simplified, if we can transform it to a circle. So, for that purpose let us rescale them by introducing the energy E_0 and define

$$\hat{n} = \sqrt{\frac{E_J/2}{E_0}}\hat{p}, \qquad \hat{\varphi} = \sqrt{\frac{4E_C}{E_0}}\hat{q}$$

[1] Here, we omit the offset charge n_g w.l.o.g.

with the commutation relation

$$[\hat{n},\hat{\varphi}] = -\frac{i}{2}\left[\hat{a}_q^\dagger - \hat{a}_q, \hat{a}_q^\dagger + \hat{a}_q\right] = \sqrt{\frac{2E_JE_C}{E_0^2}}\,[\hat{p},\hat{q}] = i$$

such that these operators are equally scaled in that sense that the ellipse equation only depends on E_0

$$\frac{\hat{\mathcal{H}}}{2E_CE_J} = \frac{\hat{p}^2}{E_0} + \frac{\hat{q}^2}{E_0}.$$

Here, E_0 is the energy spacing of the quantum harmonic oscillator. That is, $\hat{\mathcal{H}}\,|m\rangle = E_m\,|m\rangle = E_0(m+1/2)\,|m\rangle$. This can be used to obtain

$$\begin{aligned}
\hat{n} =& \sqrt{\frac{E_J/2}{E_0}}\left(\frac{E_0^2}{2E_JE_C}\right)^{1/4} i\frac{\hat{a}_q^\dagger - \hat{a}_q}{\sqrt{2}} = \left(\frac{E_J}{8E_C}\right)^{1/4} i\frac{\hat{a}_q^\dagger - \hat{a}_q}{\sqrt{2}},\\
\hat{\varphi} =& \sqrt{\frac{4E_C}{E_0}}\left(\frac{E_0^2}{2E_JE_C}\right)^{1/4} \frac{\hat{a}_q^\dagger + \hat{a}_q}{\sqrt{2}} = \left(\frac{8E_C}{E_J}\right)^{1/4} \frac{\hat{a}_q^\dagger + \hat{a}_q}{\sqrt{2}}
\end{aligned}$$

such that

$$\begin{aligned}
\frac{\hat{\mathcal{H}}}{2E_CE_J} =& \frac{\hat{n}^2}{E_J/2} + \frac{\hat{\varphi}^2}{4E_C}\\
=& \frac{1}{E_J/2}\left(\left(\frac{E_J}{8E_C}\right)^{1/4} i\frac{\hat{a}_q^\dagger - \hat{a}_q}{\sqrt{2}}\right)^2 + \frac{1}{4E_C}\left(\left(\frac{8E_C}{E_J}\right)^{1/4} \frac{\hat{a}_q^\dagger + \hat{a}_q}{\sqrt{2}}\right)^2\\
=& \frac{1}{\sqrt{2E_JE_C}}\left(i\frac{\hat{a}_q^\dagger - \hat{a}_q}{\sqrt{2}}\right)^2 + \frac{1}{\sqrt{2E_JE_C}}\left(\frac{\hat{a}_q^\dagger + \hat{a}_q}{\sqrt{2}}\right)^2.
\end{aligned}$$

From this calculation we can deduce $E_0 = \sqrt{2E_JE_C}$ and $E_m = 2E_0(m+1/2)$ for the mth energy state. $\omega_{\text{plasma}} = 2E_0/\hbar$ is called as plasma frequency.

Now, let us consider the next leading order of the Hamiltonian, namely the $\hat{\varphi}^4$, leading to the deviation from equaly spaced energy levels

$$\begin{aligned}
\delta E_m =& -\frac{E_J}{4!}\,\langle m|\,\hat{\varphi}^4\,|m\rangle\\
=& -\frac{E_J}{4!}\left(\frac{8E_C}{E_J}\right)\langle m|\left(\hat{a}_q^\dagger + \hat{a}_q\right)^4|m\rangle\\
=& -\frac{E_C}{3}\,\langle m|\left(\hat{a}_q^\dagger\right)^2\hat{a}_q^2 + \left(\hat{a}_q^\dagger\hat{a}_q\right)^2 + \hat{a}_q^\dagger\hat{a}_q\hat{a}_q\hat{a}_q^\dagger\,|m\rangle\\
& -\frac{E_C}{3}\,\langle m|\,\hat{a}_q\hat{a}_q^\dagger\hat{a}_q^\dagger\hat{a}_q + \left(\hat{a}_q\hat{a}_q^\dagger\right)^2 + \hat{a}_q^2\left(\hat{a}_q^\dagger\right)^2|m\rangle\\
=& -\frac{E_C}{3}\,\langle m|\,\hat{a}_q^\dagger\left(\hat{a}_q\hat{a}_q^\dagger - 1\right)\hat{a}_q + \left(\hat{a}_q^\dagger\hat{a}_q\right)^2 + \hat{a}_q^\dagger\hat{a}_q\hat{a}_q\hat{a}_q^\dagger\,|m\rangle\\
& -\frac{E_C}{3}\,\langle m|\,\hat{a}_q\hat{a}_q^\dagger\hat{a}_q^\dagger\hat{a}_q + \left(\hat{a}_q^\dagger\hat{a}_q + 1\right)^2 + \hat{a}_q\left(\hat{a}_q^\dagger\hat{a}_q + 1\right)\hat{a}_q^\dagger\,|m\rangle\\
=& -\frac{E_C}{3}\\
& \times\left(m^2 - m + m^2 + 2m(m+1) + (m+1)^2 + (m+1)^2 + m + 1\right)\\
=& -E_C\left(2m^2 + 2m + 1\right).
\end{aligned}$$

Henceforth, we see that the nonlinearity of the Josephson junction potential induces a non-equal energy spacing such that the energy level difference between the ground state and the first excited state is not equal to that between other energy differences. That is, we can specifically assign the ground state and the first excited state as logical states $|0\rangle$ and $|1\rangle$, respectively, with a (approximate) qubit frequency of $\omega_q = \omega_{01} = (\sqrt{8E_C E_J} - E_C)/\hbar$. The frequency of 1-2 transition is $\omega_{12} \approx \omega_q - E_C/\hbar$.

Appendix B

DERIVATION OF COUPLED SYSTEMS

B.1 Derivation of qubit-resonator system in cQED

Here, we derive the Hamiltonian of a qubit-resonator system, where we mostly follow the approach provided by [113, 249]. We first consider two LC resonators capacitively coupled with each other and show

$$\hat{\mathcal{H}} = \frac{1}{2}\frac{(C_2 + C_c)\,\hat{Q}_1^2 + (C_1 + C_c)\,\hat{Q}_2^2 + 2C_c\hat{Q}_1\hat{Q}_2}{C_1C_2 + C_c(C_1 + C_2)} + \frac{\hat{\Phi}_1^2}{2L_1} + \frac{\hat{\Phi}_2^2}{2L_2}.$$

For that purpose, we consider first the Lagrangian with the node fluxes $\Phi_i, \dot{\Phi}_i$ as a system variable and then transform it to the Hamiltonian by obtaining the node charges Q_i via an Euler-Lagrange transformation. If we define $\mathrm{d}\Phi_i/\mathrm{d}t$ as the general momentum and Φ_i the position of the ith quantum system, then the Lagrangian without interaction is written as

$$\mathcal{L}_0 = \frac{C_1}{2}\left(\frac{\mathrm{d}\Phi_1}{\mathrm{d}t}\right)^2 + \frac{C_2}{2}\left(\frac{\mathrm{d}\Phi_2}{\mathrm{d}t}\right)^2 - \frac{\Phi_1^2}{2L_1} - \frac{\Phi_2^2}{2L_2}.$$

What we are left with, is now the interaction part. The key point of the interaction is that the voltage difference between two quantum systems contributes to the energy such that

$$\frac{C_c}{2}\left(\frac{\mathrm{d}\Phi_1}{\mathrm{d}t} - \frac{\mathrm{d}\Phi_2}{\mathrm{d}t}\right)^2.$$

Henceforth, the total Lagrangian is formulated as

$$\mathcal{L} = \frac{C_1}{2}\left(\frac{d\Phi_1}{dt}\right)^2 + \frac{C_2}{2}\left(\frac{\mathrm{d}\Phi_2}{\mathrm{d}t}\right)^2 + \frac{C_c}{2}\left(\frac{\mathrm{d}\Phi_1}{\mathrm{d}t} - \frac{\mathrm{d}\Phi_2}{\mathrm{d}t}\right)^2 - \frac{\Phi_1^2}{2L_1} - \frac{\Phi_2^2}{2L_2}.$$

We can then use the Euler-Lagrange formulation and obtain the Hamiltonian. However, let us use a more elegant way. We first recognize that the kinetic term is in bilinear form, that is it has terms like

$$\left(\frac{\mathrm{d}\Phi_1}{dt}\right)^2, \left(\frac{\mathrm{d}\Phi_2}{\mathrm{d}t}\right)^2, \frac{\mathrm{d}\Phi_1}{dt}\frac{\mathrm{d}\Phi_2}{dt}.$$

This insight can be used to construct a capacitance matrix, that is,

$$\mathcal{L} = \frac{1}{2}\begin{bmatrix} \frac{\mathrm{d}\Phi_1}{\mathrm{d}t} & \frac{\mathrm{d}\Phi_2}{\mathrm{d}t} \end{bmatrix} \underbrace{\begin{bmatrix} C_1 + C_c & -C_c \\ -C_c & C_2 + C_c \end{bmatrix}}_{\mathbf{C}} \begin{bmatrix} \frac{\mathrm{d}\Phi_1}{\mathrm{d}t} \\ \frac{\mathrm{d}\Phi_2}{\mathrm{d}t} \end{bmatrix} - \frac{\Phi_1^2}{2L_1} - \frac{\Phi_2^2}{2L_2}.$$

This formulation is very helpful because we have the relation between the charge and voltage as

$$\begin{bmatrix} Q_1 \\ Q_2 \end{bmatrix} = \begin{bmatrix} \frac{\partial\mathcal{L}}{\partial\frac{\mathrm{d}\Phi_1}{\mathrm{d}t}} \\ \frac{\partial\mathcal{L}}{\partial\frac{\mathrm{d}\Phi_2}{\mathrm{d}t}} \end{bmatrix} = \mathbf{C}\begin{bmatrix} \frac{\mathrm{d}\Phi_1}{\mathrm{d}t} \\ \frac{\mathrm{d}\Phi_2}{\mathrm{d}t} \end{bmatrix}.$$

Thus, we obtain for the Hamiltonian

$$\begin{aligned}\hat{\mathcal{H}} =& \frac{1}{2}\begin{bmatrix} \hat{Q}_1 & \hat{Q}_2 \end{bmatrix} \mathbf{C}^{-1} \begin{bmatrix} \hat{Q}_1 \\ \hat{Q}_2 \end{bmatrix} + \frac{\hat{\Phi}_1^2}{2L_1} + \frac{\hat{\Phi}_2^2}{2L_2} \\ =& \frac{1}{2}\frac{(C_2+C_c)\,\hat{Q}_1^2 + (C_1+C_c)\,\hat{Q}_2^2 + 2C_c\hat{Q}_1\hat{Q}_2}{C_1C_2 + C_c(C_1+C_2)} + \frac{\hat{\Phi}_1^2}{2L_1} + \frac{\hat{\Phi}_2^2}{2L_2}.\end{aligned}$$

We now rewrite the Hamiltonian into the annihilation/creation operators $\hat{a}_{1,2}^{(\dagger)}$, and regard one of the LC-circuits as qubit, i.e. replace $\hat{a}_1 \to \hat{a}$, $\hat{a}_2 \to \hat{\sigma}$ and the qubit term accordingly. We then derive the resonance frequency of the resonator ω_r, the qubit frequency ω_q and the qubit-resonator coupling strength g_{qr}.

First, let us define the effective self-capacitance and coupling capacitance for charges

$$\begin{aligned}\frac{1}{\tilde{C}_1} :=& \frac{C_2+C_c}{C_1C_2 + C_c(C_1+C_2)}, \\ \frac{1}{\tilde{C}_2} :=& \frac{C_1+C_c}{C_1C_2 + C_c(C_1+C_2)}, \\ \frac{1}{\tilde{C}_c} :=& \frac{C_c}{C_1C_2 + C_c(C_1+C_2)}.\end{aligned}$$

such that

$$\hat{\mathcal{H}} = \frac{\hat{Q}_1^2}{2\tilde{C}_1} + \frac{\hat{Q}_2^2}{2\tilde{C}_2} + \frac{\hat{Q}_1\hat{Q}_2}{\tilde{C}_c} + \frac{\hat{\Phi}_1^2}{2L_1} + \frac{\hat{\Phi}_2^2}{2L_2}.$$

Now, inserting

$$\hat{Q}_i = \sqrt{\frac{\hbar}{2Z_{c,i}}}\left(\hat{a}_i^\dagger + \hat{a}_i\right), \qquad \hat{\Phi}_i = i\sqrt{\frac{\hbar Z_{c,i}}{2}}\left(\hat{a}_i^\dagger - \hat{a}_i\right)$$

with $Z_{c,i} = 1/\omega_i\tilde{C}_i$ we get

$$\hat{\mathcal{H}} = \omega_1\left(\hat{a}_1^\dagger\hat{a}_1 + \frac{1}{2}\right) + \omega_2\left(\hat{a}_2^\dagger\hat{a}_2 + \frac{1}{2}\right) + g\left(\hat{a}_1^\dagger + \hat{a}_1\right)\left(\hat{a}_2^\dagger + \hat{a}_2\right),$$

where

$$\begin{aligned}\omega_i =& \frac{1}{\sqrt{L_iC_i}} \\ g_{qr} =& \frac{1}{2\tilde{C}_c\sqrt{Z_1Z_2}} = \sqrt{\omega_1\omega_2}\frac{C_c}{2\sqrt{(C_1+C_c)\,(C_2+C_c)}}.\end{aligned}$$

Since we actually wanted to calculate the qubit-resonator system, we replace $a_1 \to a$, $a_2 \to \sigma$ such that

$$\hat{\mathcal{H}} = \omega_r\left(\hat{a}^\dagger\hat{a} + \frac{1}{2}\right) + \omega_q\left(\hat{\sigma}^\dagger\hat{\sigma} + \frac{1}{2}\right) + g_{qr}\left(\hat{a}^\dagger + \hat{a}\right)\left(\hat{\sigma}^\dagger + \hat{\sigma}\right).$$

B.2 Fouth order calculation

Here, the fourth order of $\cos(\tilde{Q'}_q)$ is calculated. We use the definition $\varphi_{qp} := (\varphi_{qq}\xi_q + \varphi_{qb}\xi_b + \varphi_{qw}\xi_w)/\xi_p$ for clarity. Neglecting $\mathcal{O}\left(\varphi^3_{qb,qw}\right)$, we obtain[1]

$$
\begin{aligned}
\frac{\tilde{Q'}_q^4}{24} \approx & \varphi_{qb}^2\left(\frac{\varphi_{qq}^2+(\varphi_{qp}X_p)^2}{2}\right)a_b^\dagger a_b + \varphi_{qw}^2\left(\frac{\varphi_{qq}^2+(\varphi_{qp}X_p)^2}{2}\right)a_w^\dagger a_w + \varphi_{qq}^2\left(\frac{\varphi_{qb}^2+\varphi_{qq}^2+\varphi_{qw}^2+(\varphi_{qp}X_p)^2}{2}\right)a_q^\dagger a_q \\
& + \frac{\varphi_{qq}^4}{4}{a_q^\dagger}^2 a_q^2 + \varphi_{qb}^2\varphi_{qq}^2 a_q^\dagger a_q a_b^\dagger a_b + \varphi_{qq}^2\varphi_{qw}^2 a_q^\dagger a_q a_w^\dagger a_w \\
& + \varphi_{qq}\left(\frac{\varphi_{qp}X_p}{2}\left(\varphi_{qb}^2+\varphi_{qw}^2+\varphi_{qq}^2\right)+\frac{(\varphi_{qp}X_p)^3}{6}\right)\left(a_q^\dagger + a_q\right) \\
& + \varphi_{qb}\left(\frac{\varphi_{qp}X_p}{2}\varphi_{qq}^2+\frac{(\varphi_{qp}X_p)^3}{6}\right)\left(a_b^\dagger + a_b\right) + \varphi_{qw}\left(\frac{\varphi_{qp}X_p}{2}\varphi_{qq}^2+\frac{(\varphi_{qp}X_p)^3}{6}\right)\left(a_w^\dagger + a_w\right) \\
& + \varphi_{qq}\varphi_{qw}\left(\frac{\varphi_{qq}^2}{2}+\frac{(\varphi_{qp}X_p)^2}{2}\right)\left(a_q^\dagger + a_q\right)\left(a_w + a_w^\dagger\right) \\
& + \varphi_{qb}\varphi_{qq}\left(\frac{\varphi_{qq}^2}{2}+\frac{(\varphi_{qp}X_p)^2}{2}\right)\left(a_b^\dagger + a_b\right)\left(a_q^\dagger + a_q\right) \\
& + \varphi_{qb}\varphi_{qw}\left(\frac{\varphi_{qq}^2}{2}+\frac{(\varphi_{qp}X_p)^2}{2}\right)\left(a_w^\dagger + a_w\right)\left(a_b^\dagger + a_b\right) \\
& + \varphi_{qb}^2\varphi_{qq}\left(\varphi_{qp}X_p\right)a_b^\dagger a_b\left(a_q + a_q^\dagger\right) + \varphi_{qq}\varphi_{qw}^2\left(\varphi_{qp}X_p\right)a_w^\dagger a_w\left(a_q + a_q^\dagger\right) \\
& + \varphi_{qq}^2\varphi_{qw}\left(\varphi_{qp}X_p\right)a_q^\dagger a_q\left(a_w^\dagger + a_w\right) + \varphi_{qb}\varphi_{qq}^2\left(\varphi_{qp}X_p\right)a_q^\dagger a_q\left(a_b^\dagger + a_b\right) \\
& + \frac{\varphi_{qb}^2\varphi_{qq}^2}{4}\left({a_q^\dagger}^2 a_b^2 + a_q^2{a_b^\dagger}^2\right) + \varphi_{qq}\varphi_{qb}^2\frac{\varphi_{qp}X_p}{2}\left(a_q^\dagger a_b^2 + a_q{a_b^\dagger}^2\right) \\
& + \varphi_{qb}^2\frac{(\varphi_{qp}X_p)^2}{4}\left({a_b^\dagger}^2 + a_b^2\right) + \varphi_{qq}^2\frac{(\varphi_{qp}X_p)^2}{4}\left({a_q^\dagger}^2 + a_q^2\right) + \varphi_{qw}^2\frac{(\varphi_{qp}X_p)^2}{4}\left({a_w^\dagger}^2 + a_w^2\right) \\
& + \left(\varphi_{qb}\varphi_{qq}^2\varphi_{qw}a_q^\dagger a_q\right)\left(a_b^\dagger a_w + a_b a_w^\dagger\right) + \frac{\varphi_{qb}\varphi_{qw}}{2}\varphi_{qq}^2\left({a_q^\dagger}^2 a_b a_w + a_q^2 a_b^\dagger a_w^\dagger\right) \\
& + \varphi_{qb}\varphi_{qq}^2\frac{\varphi_{qp}X_p}{2}\left({a_q^\dagger}^2 a_b + a_q^2 a_b^\dagger\right) + \frac{\varphi_{qb}\varphi_{qq}^3}{2}\left(a_q^\dagger a_q^2 a_b^\dagger + {a_q^\dagger}^2 a_q a_b\right) \\
& + \varphi_{qq}^3\frac{(\varphi_{qp}X_p)}{2}\left(a_q^\dagger a_q^2 + {a_q^\dagger}^2 a_q\right) + \frac{\varphi_{qq}^3\varphi_{qw}}{2}\left(a_q^\dagger a_q^2 a_w^\dagger + {a_q^\dagger}^2 q a_w\right) \\
& + \frac{\varphi_{qq}^2\varphi_{qw}^2}{4}\left({a_q^\dagger}^2 a_w^2 + a_q^2{a_w^\dagger}^2\right) + \varphi_{qq}^2\varphi_{qw}\left(\frac{\varphi_{qp}X_p}{2}\right)\left({a_q^\dagger}^2 a_w + a_q^2 a_w^\dagger\right) \\
& + \varphi_{qq}\varphi_{qw}^2\left(\frac{\varphi_{qp}X_p}{2}\right)\left(a_q^\dagger a_w^2 + a_q{a_w^\dagger}^2\right) \\
& + \varphi_{qb}\varphi_{qq}\varphi_{qw}(\varphi_{qp}X_p)a_q^\dagger a_b^\dagger a_w + \varphi_{qb}\varphi_{qq}\varphi_{qw}(\varphi_{qp}X_p)a_q^\dagger a_b a_w^\dagger \\
& + \varphi_{qb}\varphi_{qq}\varphi_{qw}(\varphi_{qp}X_p)a_q^\dagger a_b a_w + \varphi_{qb}\varphi_{qq}\varphi_{qw}(\varphi_{qp}X_p)a_q a_b^\dagger a_w^\dagger \\
& + \varphi_{qb}\varphi_{qq}\varphi_{qw}(\varphi_{qp}X_p)a_q a_b^\dagger a_w + \varphi_{qb}\varphi_{qq}\varphi_{qw}(\varphi_{qp}X_p)a_q a_b a_w^\dagger \\
& + \varphi_{qb}\varphi_{qw}\varphi_{qq}(\varphi_{qp}X_p)\xi_b^*\xi_w a_q^\dagger + \varphi_{qb}\varphi_{qq}\varphi_{qw}(\varphi_{qp}X_p)\xi_b\xi_w^* a_q^\dagger \\
& + \varphi_{qb}\varphi_{qq}\varphi_{qw}(\varphi_{qp}X_p)\xi_b\xi_w a_q^\dagger + \varphi_{qb}\varphi_{qq}\varphi_{qw}(\varphi_{qp}X_p)\xi_b^*\xi_w^* a_q \\
& + \varphi_{qb}\varphi_{qq}\varphi_{qw}(\varphi_{qp}X_p)\xi_b^*\xi_w a_q + \varphi_{qb}\varphi_{qq}\varphi_{qw}(\varphi_{qp}X_p)\xi_b\xi_w^* a_q
\end{aligned}
$$

[1] In our case, $\varphi^3_{qb,qw} \approx 10^{-5}$. Its frequency regime corresponds to $E_J\varphi^3_{qb,qw} \approx 1$ MHz. Since our interested frequency range is around $100 \sim 1000$ MHz (because the detunings are also around $100 \sim 1000$ MHz), we can safely neglect this term from the rotating wave approximation point of view.

Note that we defined $X_p := \xi_p(t)+\xi_p^*(t) = 2\,|\xi_p|\cos(\omega_d t)$ for better clarity. Further, we use the rotating wave approximation. For that purpose, we transform into the rotating frame of $\mathcal{H}_0 = \omega_{m,q} a_q^\dagger a_q + \omega_{m,b} a_b^\dagger a_b + \omega_{m,w} a_w^\dagger a_w$. Analyzing the terms carefully, we can recognize that we can boil them down into the following categories

$$
\begin{aligned}
X_p\left(a_j(t)+a_j^\dagger(t)\right) \propto & a_j e^{i\omega_d t - i\omega_{m,j}t} + \cancel{a_j e^{-i\omega_d t - i\omega_{m,j}t}} + \text{h.c.}\\
(\varphi_{qp}X_p)^3\left(a_j(t)+a_j^\dagger(t)\right) \propto & \cancel{(\varphi_{qp}\,|\xi_p|)^3\, a_j e^{3i\omega_d t - i\omega_{m,j}t}}\\
& + 3\,(\varphi_{qp}\,|\xi_p|)^3\, a_j e^{i\omega_d t - i\omega_{m,j}t}\\
& + \text{h.c.}\\
(\varphi_{qp}X_p)^2\left(a_j+a_j^\dagger\right)\left(a_{j'}+a_{j'}^\dagger\right) \propto & \cancel{(\varphi_{qp}\,|\xi_p|)^2\, a_j a_{j'} e^{-2i\omega_d t - i\omega_{m,j}t - i\omega_{m,j'}t}}\\
& + \cancel{(\varphi_{qp}\,|\xi_p|)^2\, a_j a_{j'}^\dagger e^{2i\omega_d t - i\omega_{m,j}t + i\omega_{m,j'}t}}\\
& + (\varphi_{qp}\,|\xi_p|)^2\, a_j a_{j'} e^{2i\omega_d t - i\omega_{m,j}t - i\omega_{m,j'}t}\\
& + 2\,(\varphi_{qp}\,|\xi_p|)^2\, a_j a_{j'}^\dagger e^{-i\omega_{m,j}t + i\omega_{m,j'}t}\\
& + \text{h.c.}\\
X_p\left(a_j^\dagger a_{j'}^2 + a_{j'}^\dagger a_j^2\right) \propto & a_j^\dagger a_{j'}^2 e^{i\omega_d t + i\omega_{m,j}t - 2i\omega_{m,j'}t}\\
& + \cancel{a_j^\dagger a_{j'}^2 e^{-i\omega_d t + i\omega_{m,j}t - 2i\omega_{m,j'}t}}\\
& + \text{h.c.}\\
X_p a_j a_{j'} a_{j''}^\dagger \propto & a_j a_{j'} a_{j''}^\dagger e^{i\omega_d t + i\omega_{m,j''}t - i\omega_{m,j}t - i\omega_{m,j'}t}\\
& + \cancel{a_j a_{j'} a_{j''}^\dagger e^{-i\omega_d t + i\omega_{m,j''}t - i\omega_{m,j}t - i\omega_{m,j'}t}}
\end{aligned}
$$

Neglecting fast rotating terms, which interaction strength is much less then the minimal detunings[2]

$$
\begin{aligned}
\frac{\tilde{Q}_q'^4}{24} \approx & \varphi_{qb}^2 \frac{\varphi_{qq}^2}{2} a_b^\dagger a_b + \varphi_{qw}^2 \frac{\varphi_{qq}^2}{2} a_w^\dagger a_w + \varphi_{qq}^2\left(\frac{\varphi_{qq}^2}{2} + \frac{(\varphi_{qp}X_p)^2}{2}\right) a_q^\dagger a_q\\
& + \frac{\varphi_{qq}^4}{4} {a_q^\dagger}^2 a_q^2 + \varphi_{qb}^2\varphi_{qq}^2 a_q^\dagger a_q a_b^\dagger a_b + \varphi_{qq}^2\varphi_{qw}^2 a_q^\dagger a_q a_w^\dagger a_w\\
& + \varphi_{qq}\left(\frac{\varphi_{qp}X_p}{2}\varphi_{qq}^2 + \frac{(\varphi_{qp}X_p)^3}{6} + \varphi_{qb}\varphi_{qq}\varphi_{qw}(\varphi_{qp}X_p)\,(\xi_b+\xi_b^*)\,(\xi_w+\xi_w^*)\right)\left(a_q^\dagger + a_q\right)\\
& + \varphi_{qb}\varphi_{qq}\varphi_{qw}\left(\varphi_{qp}\xi_p^*\right) a_q a_b^\dagger a_w + \varphi_{qb}\varphi_{qq}\varphi_{qw}\left(\varphi_{qp}\xi_p\right) a_q^\dagger a_b a_w^\dagger
\end{aligned}
$$

Here, we have chosen the drive frequency[3] $\omega_d = \omega_p \approx \omega_{m,q} + \omega_{m,w} - \omega_{m,b}$.

[2] In our case, this is for example, $E_J\varphi_{qq}^3\varphi_{qw} \approx 20$ MHz $\ll |\omega_{m,w} - \omega_{m,q}| \approx 2$ GHz. Terms, which we do not omit, are e.g. terms with the detunings less than 1 GHz associated with the driving strength in the order of few 100 MHz.

[3] The approximation here is because of the ac-Stark shift consideration.

Appendix C

UNITARY TRANSFORMATION

C.1 Transformation into the rotating frame

Here, we briefly review the unitary transformation into the rotating frame, which can be found in many textbooks [250–252], and show some working examples.

Generally, the unitary transformation of a Hamiltonian is calculated by

$$\hat{\mathcal{H}}'(t) = \hat{U}(t)\hat{\mathcal{H}}\hat{U}^{\dagger}(t) - i\hat{U}(t)\frac{\partial}{\partial t}\hat{U}^{\dagger}(t), \tag{C.1}$$

where $\hat{U}(t)$ is some time-dependent unitary operator. Note that for the Hamiltonian $\hat{\mathcal{H}} = \hat{\mathcal{H}}_0 + \hat{\mathcal{H}}_{\text{int}}(t)$ with $\hat{U}(t) = e^{-i\hat{\mathcal{H}}_0 t/\hbar}$ we are in the interaction picture with

$$\hat{\mathcal{H}}'(t) = \hat{U}(t)\hat{\mathcal{H}}\hat{U}^{\dagger}(t) - \hat{\mathcal{H}}_0 = \hat{U}(t)\hat{\mathcal{H}}_{\text{int}}(t)\hat{U}^{\dagger}(t). \tag{C.2}$$

Example: qubit drive

Given the Hamiltonian of a qubit driven by a microwave signal with amplitude A and angular frequency ω_d

$$\hat{\mathcal{H}} = \frac{\hbar\omega_q}{2}\hat{\sigma}_z + \hbar A\cos(\omega_d t + \phi)\hat{\sigma}_x,$$

we show that the Hamiltonian can be expressed

$$\hat{\mathcal{H}}' = \frac{\hbar}{2}\left(\Omega_x\hat{\sigma}_x + \Omega_y\hat{\sigma}_y + \Delta_{qd}\hat{\sigma}_z\right)$$

by using the rotating wave approximation. Here, $\Delta_{qd} = \omega_q - \omega_d$ is the detuning between qubit and drive.

We first decompose $\hat{\sigma}_x = \hat{\sigma} + \hat{\sigma}^{\dagger}$ and also note that the operators $\sigma^{(\dagger)}$ in the rotating frame can be written as

$$\hat{\sigma}^{(\dagger)} \to \hat{\sigma}^{(\dagger)}e^{\mp i\omega_d t}.$$

Thus, in the rotating frame of the drive $\hat{\mathcal{H}}_0 = \hbar\omega_d\hat{\sigma}_z/2$

$$\begin{aligned}
\hat{\mathcal{H}}' =& \hat{U}\hat{\mathcal{H}}\hat{U}^\dagger - i\hat{U}\frac{\partial}{\partial t}\hat{U}^\dagger \\
=& \frac{\hbar\omega_q}{2}\hat{\sigma}_z + \hbar A\cos(\omega_d t+\phi)\hat{U}\hat{\sigma}_x\hat{U}^\dagger - \frac{\hbar\omega_d}{2}\hat{\sigma}_z \\
=& \hbar\frac{\omega_q-\omega_d}{2}\hat{\sigma}_z + \hbar A\cos(\omega_d t+\phi)\left(\hat{\sigma}e^{-i\omega_d t} + \hat{\sigma}^\dagger e^{i\omega_d}\right) \\
=& \hbar\frac{\omega_q-\omega_d}{2}\hat{\sigma}_z + \hbar A\cos(\omega_d t)\cos(\phi)\left(\hat{\sigma}e^{-i\omega_d t} + \hat{\sigma}^\dagger e^{i\omega_d}\right) \\
& - \hbar A\sin(\omega_d t)\sin(\phi)\left(\hat{\sigma}e^{-i\omega_d t} + \hat{\sigma}^\dagger e^{i\omega_d}\right) \\
=& \hbar\frac{\omega_q-\omega_d}{2}\hat{\sigma}_z + \frac{\hbar A\cos(\phi)}{2}\left(\hat{\sigma}\left(1+e^{-2i\omega_d t}\right) + \hat{\sigma}^\dagger\left(1+e^{2i\omega_d t}\right)\right) \\
& - \frac{\hbar A\sin(\phi)}{2i}\left(\hat{\sigma}\left(1-e^{-2i\omega_d t}\right) + \hat{\sigma}^\dagger\left(-1+e^{-2i\omega_d t}\right)\right) \\
\overset{RWA}{\to}& \hbar\frac{\omega_q-\omega_d}{2}\hat{\sigma}_z + \frac{\hbar A\cos(\phi)}{2}\hat{\sigma}_x - \frac{\hbar A\sin(\phi)}{2}\hat{\sigma}_y \\
=& \frac{\hbar\Omega_x}{2}\hat{\sigma}_x + \frac{\hbar\Omega_y}{2}\hat{\sigma}_y + \frac{\hbar\Delta_{qd}}{2}\hat{\sigma}_z
\end{aligned}$$

with

$$\Omega_x = A\cos\phi, \qquad \Omega_y = -A\sin\phi, \qquad \Delta_{qd} = \omega_q - \omega_d.$$

We now calculate the time-evolution of the qubit state for the ground state as an initial state by making use of the following definition

$$\hat{\mathcal{H}}' = \frac{\hbar\Omega_{\text{Rabi}}}{2}\begin{bmatrix} \frac{\Delta_{qd}}{\Omega_{\text{Rabi}}} & \frac{iAe^{-i\phi}}{\Omega_{\text{Rabi}}} \\ -\frac{iAe^{i\phi}}{\Omega_{\text{Rabi}}} & -\frac{\Delta_{qd}}{\Omega_{\text{Rabi}}} \end{bmatrix} =: \frac{\hbar\Omega_{\text{Rabi}}}{2}\begin{bmatrix} \cos\theta & ie^{-i\phi}\sin\theta \\ -ie^{i\phi}\sin\theta & -\cos\theta \end{bmatrix}.$$

The Hamiltonian can be rewritten in the matrix form as

$$\hat{\mathcal{H}}' = \frac{\hbar}{2}\begin{bmatrix} \Delta_{qd} & iAe^{-i\phi} \\ -iAe^{i\phi} & -\Delta_{qd} \end{bmatrix}$$

First, let us obtain the eigenfrequencies given by

$$\omega_\pm = \pm\Omega_{\text{Rabi}} = \pm\sqrt{\Delta_{qd}^2 + A^2}.$$

and use this for the normalization of the matrix

$$\hat{\mathcal{H}}' = \frac{\hbar\Omega_{\text{Rabi}}}{2}\begin{bmatrix} \frac{\Delta_{qd}}{\Omega_{\text{Rabi}}} & \frac{iAe^{-i\phi}}{\Omega_{\text{Rabi}}} \\ -\frac{iAe^{i\phi}}{\Omega_{\text{Rabi}}} & -\frac{\Delta_{qd}}{\Omega_{\text{Rabi}}} \end{bmatrix} =: \frac{\hbar\Omega_{\text{Rabi}}}{2}\begin{bmatrix} \cos\theta & ie^{-i\phi}\sin\theta \\ -ie^{i\phi}\sin\theta & -\cos\theta \end{bmatrix}.$$

In this case, it is known that the eigenstates are symmetric and anti-symmetric superpositions of the

qubit states[1]

$$
\begin{aligned}
|\Psi_+\rangle =& ie^{-i\phi/2}\cos\left(\frac{\theta}{2}\right)|0\rangle + e^{i\phi/2}\sin\left(\frac{\theta}{2}\right)|1\rangle\,,\\
|\Psi_-\rangle =& e^{-i\phi/2}\sin\left(\frac{\theta}{2}\right)|0\rangle - ie^{i\phi/2}\cos\left(\frac{\theta}{2}\right)|1\rangle\,.
\end{aligned}
$$

Then, we can decompose an arbitrary stationary state $|\psi(t_0=0)\rangle$ into

$$
|\psi(t)\rangle = \langle\psi(t_0)|\Psi_-\rangle\, e^{-i\Omega_{\text{Rabi}}t/2}\,|\Psi_-\rangle + \langle\psi(t_0)|\Psi_+\rangle\, e^{i\Omega_{\text{Rabi}}t/2}\,|\Psi_+\rangle\,. \tag{C.3}
$$

In particular, for the ground state we get

$$
|\psi(t)\rangle = e^{-i\phi/2}\sin\left(\frac{\theta}{2}\right)e^{-i\Omega_{\text{Rabi}}t/2}\,|\Psi_-\rangle + ie^{-i\phi/2}\cos\left(\frac{\theta}{2}\right)e^{i\Omega_{\text{Rabi}}t/2}\,|\Psi_+\rangle\,.
$$

Physically, the result of the eigenstates tells us that the axis, about which the qubit rotates with $\pm\Omega_{\text{Rabi}}$, goes away from the z-axis and approaches more towards the $x-y$ plane the stronger the Rabi strength gets. For example, let us take a quantum state parallel to z-axis and the system is detuned. While the quantum state feels only rotations about z-axis without driving and does not change its vector in the Bloch sphere, the quantum state starts to *oscillate* about the eigenvector in case of driving such that the z-component of the quantum state now oscillates, as well.

Example: From full Rabi model to Jaynes-Cummings Hamiltonian

We briefly derive the Jaynes-Cummings Hamiltonian from the full Rabi Hamiltonian

$$
\hat{\mathcal{H}}_{\text{Rabi}} = \hbar\omega_r\hat{a}_r^\dagger\hat{a}_r + \frac{\hbar\omega_q}{2}\hat{\sigma}_z + \hbar g_{qr}\left(\hat{\sigma}^\dagger + \hat{\sigma}\right)\left(\hat{a}_r + \hat{a}_r^\dagger\right).
$$

For that purpose, we go into the interaction picture with $|\psi(t)\rangle_{\text{int}} = e^{i\hat{\mathcal{H}}_0 t/\hbar}\,|\psi(t)\rangle$ with

$$
\hat{\mathcal{H}}_0 = \hbar\omega_r\hat{a}_r^\dagger\hat{a}_r + \frac{\hbar\omega_q}{2}\hat{\sigma}_z.
$$

We insert them into Eq. (C.2) such that we get

$$
\begin{aligned}
\hat{\mathcal{H}}'_{\text{Rabi}}(t) =& \hbar g_{qr}e^{i\hat{\mathcal{H}}_0 t/\hbar}\left(\hat{\sigma}^\dagger + \hat{\sigma}\right)\left(\hat{a}_r + \hat{a}_r^\dagger\right)e^{-i\hat{\mathcal{H}}_0 t/\hbar}\\
=& \hbar g_{qr}e^{i\omega_q t\hat{\sigma}_z/2}\left(\hat{\sigma}_+ + \hat{\sigma}_-\right)e^{-i\omega_q t\hat{\sigma}_z/2}e^{i\omega_r t\hat{a}_r^\dagger\hat{a}_r}\left(\hat{a}_r + \hat{a}_r^\dagger\right)e^{-i\omega_r t\hat{a}_r^\dagger\hat{a}_r}\\
=& \hbar g_{qr}\left(\hat{\sigma}_+e^{i\omega_q t} + \hat{\sigma}_-e^{-i\omega_q t}\right)\left(\hat{a}_r e^{-i\omega_r t} + \hat{a}_r^\dagger e^{i\omega_r t}\right),
\end{aligned}
$$

where we know from the Heisenberg equation of motion

$$
\begin{aligned}
\frac{\partial}{\partial t}\hat{\sigma}^\pm =& i\frac{\omega_q}{2}\left[\hat{\sigma}_z, \hat{\sigma}^\pm\right]\\
=& i\omega_q\hat{\sigma}^\pm\\
\frac{\partial}{\partial t}\hat{a}_r^{(\dagger)} =& i\omega_r\left[\hat{a}_r^\dagger\hat{a}_r, \hat{a}_r^{(\dagger)}\right]\\
=& \mp i\omega_r\hat{a}_r^{(\dagger)}.
\end{aligned}
$$

[1] This can be proved by decomposing the trigonometries into exponentials and simplifying them again.

Within the rotating wave approximation, we can neglect the fast rotating terms, i.e. oscillating with the frequency $\omega_q + \omega_r$, and obtain the Jaynes-Cummings Hamiltonian

$$\hat{\mathcal{H}}_{\mathrm{JC}} = \hbar\omega_r \hat{a}_r^\dagger \hat{a}_r + \frac{\hbar\omega_q}{2}\hat{\sigma}_z + \hbar g_{qr}\left(\hat{\sigma}^\dagger \hat{a}_r + \hat{\sigma}\hat{a}_r^\dagger\right)$$

by transforming back into the laboratory frame.

C.2 Schrieffer-Wolff transformation

The Schrieffer-Wolff transformation is a perturbative method to diagonalize the Hamiltonian of an interacting qubit-resonator system. For the Jaynes-Cummings Hamiltonian, this transformation is given by

$$\hat{\mathcal{H}}_{\mathrm{disp}} = \hat{U}\hat{\mathcal{H}}\hat{U}^\dagger$$

with $\hat{U} = e^{\hat{S}}$ and

$$\hat{S} = \frac{g_{qr}}{\Delta_{qr}}\left(\hat{a}_r\hat{\sigma}^\dagger - \hat{a}_r^\dagger\hat{\sigma}\right)$$

with $\Delta_{qr} = \omega_q - \omega_r$. However, for our purpose we only want to obtain terms up to the second order of g_{qr}/Δ_{qr}. Here, we show that this approximation allows us to finally get

$$\hat{\mathcal{H}}_{\mathrm{disp}}/\hbar = \left(\omega_r + \frac{g_{qr}^2}{\Delta_{qr}}\hat{\sigma}_z\right)\hat{a}_r^\dagger\hat{a}_r + \frac{1}{2}\left(\omega_q + \frac{g_{qr}^2}{\Delta_{qr}}\right)\hat{\sigma}_z$$

by using the following instructions[2]:

The problem of diagonalizing the Jaynes-Cummings Hamiltonian is the off-diagonal interaction term, since the qubit and resonator terms are diagonal. The essential point of this Schrieffer-Wolff transformation is to be able to eliminate the off-diagonal interaction term

$$\hat{V} = g_{qr}\left(\hat{a}_r\hat{\sigma}^\dagger + \hat{a}_r^\dagger\hat{\sigma}\right).$$

That is,

$$\left[\hat{S}, \hat{\mathcal{H}}_0\right] = -\hat{V}.$$

Let us first calculate the following commutation relations

$$\left[\hat{a}_r\hat{\sigma}^\dagger, \hat{\sigma}_z\right] = -2\hat{a}_r\hat{\sigma}^\dagger \qquad \left[\hat{a}_r^\dagger\hat{\sigma}, \hat{\sigma}_z\right] = 2\hat{a}_r^\dagger\hat{\sigma}$$

$$\left[\hat{a}_r\hat{\sigma}^\dagger, \hat{a}_r^\dagger\hat{a}_r\right] = \hat{a}_r\hat{\sigma}^\dagger \qquad \left[\hat{a}_r^\dagger\hat{\sigma}, \hat{a}_r^\dagger\hat{a}_r\right] = -\hat{a}_r^\dagger\hat{\sigma}.$$

[2]This result can also be obtained by straight forward calculation. Here, we would like to provide the essence of this transformation.

We then can verify

$$\begin{aligned}\left[\hat{S},\hat{\mathcal{H}}_0\right] &= \left[\frac{g_{qr}}{\Delta_{qr}}\left(\hat{a}_r\hat{\sigma}^\dagger - \hat{a}_r^\dagger\hat{\sigma}\right), \frac{\omega_q}{2}\hat{\sigma}_z + \omega_r\hat{a}_r^\dagger\hat{a}_r\right] \\ &= \left[\frac{g_{qr}}{\Delta_{qr}}\left(\hat{a}_r\hat{\sigma}^\dagger - \hat{a}_r^\dagger\hat{\sigma}\right), \frac{\omega_q}{2}\hat{\sigma}_z\right] + \left[\frac{g_{qr}}{\Delta_{qr}}\left(\hat{a}_r\hat{\sigma}^\dagger - \hat{a}_r^\dagger\hat{\sigma}\right), \omega_r\hat{a}_r^\dagger\hat{a}_r\right] \\ &= -\frac{g_{qr}}{\Delta_{qr}}\omega_q\left(\hat{a}_r\hat{\sigma}^\dagger + \hat{a}_r^\dagger\hat{\sigma}\right) + \frac{g_{qr}}{\Delta_{qr}}\omega_r\left(\hat{a}_r\hat{\sigma}^\dagger + \hat{a}_r^\dagger\hat{\sigma}\right) \\ &= -\hat{V}.\end{aligned}$$

Our next strategy is to make use of the Baker-Campbell-Hausdorff formula

$$e^{\hat{S}}\hat{\mathcal{H}}e^{-\hat{S}} = \hat{\mathcal{H}} + \left[\hat{S},\hat{\mathcal{H}}\right] + \frac{1}{2!}\left[\hat{S},\left[\hat{S},\hat{\mathcal{H}}\right]\right] + \dots .$$

We see that it is composed of repeated commutation relations. Since we have already calculated the commutation relation between the generator $\hat{S}$ and the system Hamiltonian $\hat{\mathcal{H}}_0$, we calculate the remained commutation relation

$$\begin{aligned}\left[\hat{S},\hat{V}\right] =& \left[\frac{g_{qr}}{\Delta_{qr}}\left(\hat{a}_r\hat{\sigma}^\dagger - \hat{a}_r^\dagger\hat{\sigma}\right), g_{qr}\left(\hat{a}_r\hat{\sigma}^\dagger + \hat{a}_r^\dagger\hat{\sigma}\right)\right] \\ =& \frac{g_{qr}^2}{\Delta_{qr}}\left(\left[\hat{a}_r\hat{\sigma}^\dagger, a^\dagger\hat{\sigma}\right] + \left[-\hat{a}_r^\dagger\hat{\sigma}, \hat{a}_r\hat{\sigma}^\dagger\right]\right) \\ =& 2\frac{g_{qr}^2}{\Delta_{qr}}\left(\hat{a}_r\hat{a}_r^\dagger\hat{\sigma}^\dagger\hat{\sigma} - \hat{a}_r^\dagger\hat{a}_r\hat{\sigma}\hat{\sigma}^\dagger\right) \\ =& 2\frac{g_{qr}^2}{\Delta_{qr}}\left(\hat{a}_r^\dagger\hat{a}_r\left(\hat{\sigma}^\dagger\hat{\sigma} - \hat{\sigma}\hat{\sigma}^\dagger\right) + \hat{\sigma}^\dagger\hat{\sigma}\right) \\ =& 2\frac{g_{qr}^2}{\Delta_{qr}}\left(\hat{a}_r^\dagger\hat{a}_r\hat{\sigma}_z + \hat{\sigma}^\dagger\hat{\sigma}\right) \\ \to& 2\frac{g_{qr}^2}{\Delta_{qr}}\left(\hat{a}_r^\dagger\hat{a}_r\hat{\sigma}_z + \frac{1}{2}\hat{\sigma}_z\right),\end{aligned}$$

where in the last "equation" we subtracted by ω_q. This yields us to evaluate

$$\begin{aligned}e^{\hat{S}}\hat{\mathcal{H}}e^{-\hat{S}} =& \hat{\mathcal{H}}_0 + \hat{V} + \left[\hat{S},\hat{\mathcal{H}}_0\right] + \left[\hat{S},\hat{V}\right] + \frac{1}{2!}\left[\hat{S},\left[\hat{S},\hat{\mathcal{H}}\right]\right] + \mathcal{O}\left(g_{qr}^3\right) \\ =& \mathcal{H}_0 + \frac{1}{2}\left[\hat{S},\hat{V}\right] + \mathcal{O}\left(g_{qr}^3\right) \\ =& \left(\omega_r + \frac{g_{qr}^2}{\Delta_{qr}}\hat{\sigma}_z\right)\hat{a}_r^\dagger\hat{a}_r + \frac{1}{2}\left(\omega_q + \frac{g_{qr}^2}{\Delta_{qr}}\right)\hat{\sigma}_z + \mathcal{O}\left(g_{qr}^3\right) \\ =& \left(\omega_r + \frac{\chi_{qr}}{2}\hat{\sigma}_z\right)\hat{a}_r^\dagger\hat{a}_r + \frac{1}{2}\left(\omega_q + \frac{\chi_{qr}}{2}\right)\hat{\sigma}_z + \mathcal{O}\left(g_{qr}^3\right)\end{aligned}$$

with $\chi_{qr} := 2g_{qr}^2/\Delta_{qr}$.

Quantum Non-Demolition Measurement

We show that the Jaynes-Cummings Hamiltonian in the dispersive regime is suited for performing repeated measurements on $\hat{\sigma}_z$ without further changing the state. Furthermore, we ask the question what the condition for the QND measurement of a certain quantum state is in general?

To show that the Jaynes-Cummings Hamiltonian in the dispersive regime does not further change

its state by repeated measurements, we have to think about the meaning of repeated measurements and no-state-change.

To perform repeated measurements means that we perform another measurement after some time after we have measured its quantum state. So, the time evolution is involved. If the state does not change after the first measurement, this is equivalent to say that in the Heisenberg picture the measurement operator is constant in time. In particular, we should obtain

$$\langle\psi|\,\hat{\sigma}_z(t_0)\,|\psi\rangle = \langle\psi|\,\hat{\sigma}_z(t_0+t)\,|\psi\rangle\,, \forall t,$$

since we do repeated measurements on $\hat{\sigma}_z$, where $\hat{\sigma}_z$ is our measurement operator[3]. So, our task is to prove that $\hat{\sigma}_z$ is constant in time. Fortunately, we can use the Heisenberg equation of motion for this purpose, i.e.

$$\frac{d\hat{\sigma}_z(t)}{dt} = \frac{i}{\hbar}\left[\hat{\mathcal{H}}, \hat{\sigma}_z(t)\right] \stackrel{!}{=} 0.$$

Inserting the dispersive Jaynes-Cummings Hamiltonian, we can easily prove that it commutes with $\hat{\sigma}_z$. Hence, $\hat{\sigma}_z$ is constant in time, and equivalently the quantum state is constant in time.

In general, if $\hat{P}$ is the measurement operator, it has to commute with the Hamiltonian, i.e.

$$\frac{\mathrm{d}\hat{P}(t)}{\mathrm{d}t} = \frac{i}{\hbar}\left[\hat{\mathcal{H}}, \hat{P}(t)\right] \stackrel{!}{=} 0.$$

C.3 Displacement transformation

Displacement transformation is a transformation in the context of coherent states. The name displacement transformation originates from the fact that the corresponding operator - the displacement operator $\hat{D}$ - has the ability to displace a localized state in phase space by an amount α. Applying the displacement operator to a vacuum state, it is displaced into a coherent state. The coherent states are eigenstates of the annihilation operator

$$\hat{a}\,|\alpha\rangle = \alpha\,|\alpha\rangle\,. \tag{C.4}$$

If we transform $\hat{a}$ with the displacement operator $\hat{D}(\alpha) = \exp(\alpha\hat{a}^\dagger - \alpha^*\hat{a})$, we find

$$\hat{D}^\dagger(\alpha)\hat{a}\hat{D}(\alpha) = \alpha + \hat{a}, \qquad \hat{D}^\dagger(\alpha)\hat{a}^\dagger\hat{D}(\alpha) = \alpha^* + \hat{a}^\dagger, \tag{C.5}$$

where α is an arbitrary complex number.

[3]Some might get confused of the time evolution of the measurement operator. The essential point is that it is an exchange of the unitary time evolution between the quantum state $|\psi\rangle$ and the state onto that we want to project. In our case, since the measurement process is a projection of the quantum state onto the particular state, if we want to project the quantum state onto the state $|0\rangle$, the transformation between the Schrödinger picture and the Heisenberg picture is

$$\langle 0|\underbrace{|\psi(t)\rangle}_{\text{Schrödinger}} = \langle 0|\,e^{-i\hat{\mathcal{H}}(t-t_0)/\hbar}\,|\psi(t_0)\rangle = \underbrace{\langle 0(t)|}_{\text{Heisenberg}}\,|\psi(t_0)\rangle\,.$$

At the same time we also know that the state onto which we want to project can be described by the projection operator. So, rewriting this for the projection (measurement) operator we arrive at

$$\langle\psi(t)|\,\hat{P}\underbrace{|\psi(t)\rangle}_{\text{Schrödinger}} = \langle\psi(t_0)|\,e^{i\hat{\mathcal{H}}(t-t_0)/\hbar}\hat{P}e^{-i\hat{\mathcal{H}}(t-t_0)/\hbar}\,|\psi(t_0)\rangle = \langle\psi(t_0)|\underbrace{\hat{P}(t)}_{\text{Heisenberg}}\,|\psi(t_0)\rangle$$

with $\hat{P} = |0\rangle\langle 0|$.

Within the mean field theory point of view, we treat the annihilation operator as a classical field amplitude α [85]. For example, if we assume a quantum harmonic oscillator described by Eq. (2.16), α_r is treated as the steady state mean field amplitude of $\hat{a}_r$ and is calculated by the quantum Langevin equation (see Eq. (2.28))

$$\begin{aligned}\dot{\hat{a}}_r =& i\left[\hat{\mathcal{H}}_r, \hat{a}_r\right] - \frac{\kappa_r}{2}\hat{a}_r - \sqrt{\kappa_r}\hat{a}_{\mathrm{in}}(t) \\ =& -i\omega_r\hat{a}_r - \frac{\kappa_r}{2}\hat{a}_r - \sqrt{\kappa_r}\hat{a}_{\mathrm{in}}(t).\end{aligned}$$

Here, $\hat{a}_{\mathrm{in}}(t) = 2\hat{a}_{\mathrm{in}}\cos(\omega_d t)$ is not a vacuum quantum fluctuation, but the amplitude of a driving signal (corresponding to the square root of the photon flux of the driving field) with driving frequency ω_d [89]. After the displacement transformation, the quantum Langevin equation is changed to

$$\dot{\alpha}_r = -i\omega_r\alpha_r + 2\sqrt{\kappa_r}\left\langle\hat{a}_{\mathrm{in}}\right\rangle\cos(\omega_d t) - \frac{\kappa_r}{2}\alpha_r.$$

The steady state solution is

$$\begin{aligned}\alpha_r(t) =& e^{-(i\omega_r+\kappa_r/2)t}\alpha_r(t_0) - 2e^{-(i\omega_r+\kappa_r/2)t}\int_{t_0}^{t}\mathrm{d}\tau\sqrt{\kappa_r}\left\langle\hat{a}_{\mathrm{in}}\right\rangle e^{(i\omega_r+\kappa_r/2)t}\cos(\omega_d\tau) \\ \xrightarrow{t\to\infty}& -e^{-(i\omega_r+\kappa_r/2)t}\left[\sqrt{\kappa_r}\left\langle\hat{a}_{\mathrm{in}}\right\rangle\frac{e^{(i\omega_r+i\omega_d+\kappa_r/2)t}}{i\omega_r+i\omega_d+\kappa_r/2} + \sqrt{\kappa_r}\left\langle\hat{a}_{\mathrm{in}}\right\rangle\frac{e^{(i\omega_r-i\omega_d+\kappa_r/2)t}}{i\omega_r-i\omega_d+\kappa_r/2}\right] \\ \approx& -\frac{\sqrt{\kappa_r}\left\langle\hat{a}_{\mathrm{in}}\right\rangle e^{-i\omega_d t}}{i\omega_r-i\omega_d+\kappa_r/2},\end{aligned} \tag{C.6}$$

where we have neglected the first term in the last approximation. Here, it is important to emphasize that the amplitude of the mode will oscillate solely with the driving frequency ω_d for $t\to\infty$, and the term involving ω_r is only relevant over a timescale of $1/\kappa_r$.

C.4 Relation between linear Hamiltonian and Lagrangian

Here, we formulate the relations between the Hamiltonian and Lagrangian. If we consider a linear system in the Hamiltonian and Lagrangian formalism

$$\begin{aligned}\mathcal{H}/\hbar =& \frac{1}{2}\vec{P}^T\Omega_{PP}\vec{P} + \frac{1}{2}\vec{Q}^T\Omega_{QQ}\vec{Q}, \\ \mathcal{L}/\hbar =& \frac{1}{2}\dot{\vec{Q}}^T C\dot{\vec{Q}} - \frac{1}{2}\vec{Q}^T L^{-1}\vec{Q},\end{aligned}$$

then due to

$$\vec{P} = \frac{\partial\mathcal{L}}{\partial\dot{\vec{Q}}} = C\dot{\vec{Q}},$$

we can calculate

$$\begin{aligned}\mathcal{H}/\hbar =& \frac{1}{2}\vec{P}^T\Omega_{PP}\vec{P} + \frac{1}{2}\vec{Q}^T\Omega_{QQ}\vec{Q} = \frac{1}{2}\dot{\vec{Q}}^T C^T\Omega_{PP}C\dot{\vec{Q}} + \frac{1}{2}\vec{Q}^T\Omega_{QQ}\vec{Q} \\ =& \dot{\vec{Q}}^T\vec{P} - \mathcal{L} \\ =& \frac{1}{2}\dot{\vec{Q}}^T C\dot{\vec{Q}} + \frac{1}{2}\vec{Q}^T L^{-1}\vec{Q}.\end{aligned}$$

Thus, we have

$$\frac{1}{2}\dot{\vec{Q}}^T \left(C^T \Omega_{PP} - \mathbf{1}\right) C\dot{\vec{Q}} + \frac{1}{2}\vec{Q}^T \left(\Omega_{QQ} - L^{-1}\right) \vec{Q} = 0$$

and due to the linear independence

$$\Omega_{PP} = C^{T^{-1}} = C^{-1}, \qquad \Omega_{QQ} = L^{-1}, \tag{C.7}$$

where we have used the fact $\Omega_{PP} = \Omega_{PP}^T$.

Bibliography

[1] D. M. Pozar, *Microwave Engineering*, John Wiley and Sons, Inc., Hoboken, NJ, 4 edition, 2012. [Cited on pages 1, 4, 5, 6, and 23.]

[2] A. S. Sedra and K. C. Smith, *Microelectronic Circuits*, Oxford University Press, New York, 2009. [Cited on pages 1 and 4.]

[3] D. Loss and D. P. DiVincenzo, *Quantum computation with quantum dots*, Physical Review A **57**, 120 (1998). [Cited on page 1.]

[4] B. E. Kane, *A silicon-based nuclear spin quantum computer*, Nature **393**, 133 (1998). [Cited on page 1.]

[5] R. Vrijen, E. Yablonovitch, K. Wang, H. W. Jiang, A. Balandin, V. Roychowdhury, T. Mor, and D. DiVincenzo, *Electron-spin-resonance transistors for quantum computing in silicon-germanium heterostructures*, Physical Review A **62**, 012306 (2000). [Cited on page 1.]

[6] R. de Sousa, J. D. Delgado, and S. Das Sarma, *Silicon quantum computation based on magnetic dipolar coupling*, Physical Review A **70**, 052304 (2004). [Cited on page 1.]

[7] L. C. L. Hollenberg, A. D. Greentree, A. G. Fowler, and C. J. Wellard, *Two-dimensional architectures for donor-based quantum computing*, Physical Review B **74**, 045311 (2006). [Cited on page 1.]

[8] A. Morello, J. J. Pla, F. A. Zwanenburg, K. W. Chan, K. Y. Tan, H. Huebl, M. Möttönen, C. D. Nugroho, C. Yang, J. A. Van Donkelaar, A. D. Alves, D. N. Jamieson, C. C. Escott, L. C. Hollenberg, R. G. Clark, and A. S. Dzurak, *Single-shot readout of an electron spin in silicon*, Nature **467**, 687 (2010). [Cited on page 1.]

[9] A. Imamoglu, D. D. Awschalom, G. Burkard, D. P. DiVincenzo, D. Loss, M. Sherwin, and A. Small, *Quantum Information Processing Using Quantum Dot Spins and Cavity QED*, Physical Review Letters **83**, 4204 (1999). [Cited on page 1.]

[10] J. R. Petta, A. C. Johnson, J. M. Taylor, E. A. Laird, A. Yacoby, M. D. Lukin, C. M. Marcus, M. P. Hanson, and A. C. Gossard, *Coherent Manipulation of Coupled Electron Spins in Semiconductor Quantum Dots*, Science **309**, 2180 (2005). [Cited on page 1.]

[11] D. Englund, D. Fattal, E. Waks, G. Solomon, B. Zhang, T. Nakaoka, Y. Arakawa, Y. Yamamoto, and J. Vučković, *Controlling the Spontaneous Emission Rate of Single Quantum Dots in a Two-Dimensional Photonic Crystal*, Physical Review Letters **95**, 013904 (2005). [Cited on page 1.]

[12] R. Hanson, L. P. Kouwenhoven, J. R. Petta, S. Tarucha, and L. M. K. Vandersypen, *Spins in few-electron quantum dots*, Review of Modern Physics **79**, 1217 (2007). [Cited on page 1.]

[13] J. I. Cirac and P. Zoller, *Quantum computations with cold trapped ions*, Physical Review Letters **74**, 4091 (1995). [Cited on page 1.]

[14] D. Leibfried, R. Blatt, C. Monroe, and D. Wineland, *Quantum dynamics of single trapped ions*, Review of Modern Physics **75**, 281 (2003). [Cited on page 1.]

[15] R. Blatt and D. Wineland, *Entangled states of trapped atomic ions*, Nature **453**, 1008 (2008). [Cited on page 1.]

[16] R. Blatt and C. F. Roos, *Quantum simulations with trapped ions*, Nature Physics **8**, 277 (2012). [Cited on page 1.]

[17] I. Bloch, J. Dalibard, and W. Zwerger, *Many-body physics with ultracold gases*, Review of Modern Physics **80**, 885 (2008). [Cited on page 1.]

[18] C. Gross and I. Bloch, *Quantum simulations with ultracold atoms in optical lattices*, Science **357**, 995 (2017). [Cited on page 1.]

[19] R. Hanson, O. Gywat, and D. D. Awschalom, *Room-temperature manipulation and decoherence of a single spin in diamond*, Physical Review B **74**, 161203 (2006). [Cited on page 1.]

[20] M. V. Dutt, L. Childress, L. Jiang, E. Togan, J. Maze, F. Jelezko, A. S. Zibrov, P. R. Hemmer, and M. D. Lukin, *Quantum Register Based on Individual Electronic and Nuclear Spin Qubits in Diamond*, Science **316**, 1312 (2007). [Cited on page 1.]

[21] E. Knill, R. Laflamme, and G. J. Milburn, *A scheme for efficient quantum computation with linear optics*, Nature **409**, 46 (2001). [Cited on page 1.]

[22] J. D. Franson, M. M. Donegan, M. J. Fitch, B. C. Jacobs, and T. B. Pittman, *High-Fidelity Quantum Logic Operations Using Linear Optical Elements*, Physical Review Letters **89**, 137901 (2002). [Cited on page 1.]

[23] P. Krantz, M. Kjaergaard, F. Yan, T. P. Orlando, S. Gustavsson, and W. D. Oliver, *A quantum engineer's guide to superconducting qubits*, Applied Physics Reviews **6**, 1 (2019). [Cited on pages 1, 12, 31, 34, 80, and 89.]

[24] A. Blais, A. L. Grimsmo, S. M. Girvin, and A. Wallraff, *Circuit quantum electrodynamics*, Reviews of Modern Physics **93**, 25005 (2021). [Cited on pages 1, 12, 31, 32, 34, 36, and 38.]

[25] F. Deppe, M. Mariantoni, E. P. Menzel, A. Marx, S. Saito, K. Kakuyanagi, H. Tanaka, T. Meno, K. Semba, H. Takayanagi, E. Solano, and R. Gross, *Two-photon probe of the Jaynes-Cummings model and symmetry breaking in circuit QED*, Nature Physics **4**, 686 (2008). [Cited on pages 1 and 8.]

[26] T. Niemczyk, F. Deppe, H. Huebl, E. P. Menzel, F. Hocke, M. J. Schwarz, J. J. Garcia-Ripoll, D. Zueco, T. Hümmer, E. Solano, A. Marx, and R. Gross, *Circuit quantum electrodynamics in the ultrastrong-coupling regime*, Nature Physics **6**, 772 (2010). [Cited on pages 1 and 8.]

[27] B. Yurke, L. R. Corruccini, P. G. Kaminsky, L. W. Rupp, A. D. Smith, A. H. Silver, R. W. Simon, and E. A. Whittaker, *Observation of parametric amplification and deamplification in a Josephson parametric amplifier*, Physical Review A **39**, 2519 (1989). [Cited on pages 1, 3, and 35.]

[28] M. A. Castellanos-Beltran, K. D. Irwin, G. C. Hilton, L. R. Vale, and K. W. Lehnert, *Amplification and squeezing of quantum noise with a tunable Josephson metamaterial*, Nature Physics **4**, 928 (2008). [Cited on pages 1, 3, and 35.]

[29] N. Bergeal, F. Schackert, M. Metcalfe, R. Vijay, V. E. Manucharyan, L. Frunzio, D. E. Prober, R. J. Schoelkopf, S. M. Girvin, and M. H. Devoret, *Phase-preserving amplification near the quantum limit with a Josephson ring modulator*, Nature **465**, 64 (2010). [Cited on pages 1, 3, and 35.]

[30] B. Abdo, K. Sliwa, L. Frunzio, and M. Devoret, *Directional amplification with a Josephson circuit*, Physical Review X **3**, 3 (2014). [Cited on pages 1, 3, and 35.]

[31] M. Malnou, M. R. Vissers, J. D. Wheeler, J. Aumentado, J. Hubmayr, J. N. Ullom, and J. Gao, *Three-Wave Mixing Kinetic Inductance Traveling-Wave Amplifier with Near-Quantum-Limited Noise Performance*, PRX Quantum **2**, 1 (2021). [Cited on pages 1, 3, and 35.]

[32] J. Y. Qiu, A. Grimsmo, K. Peng, B. Kannan, B. Lienhard, Y. Sung, P. Krantz, V. Bolkhovsky, G. Calusine, D. Kim, A. Melville, B. M. Niedzielski, J. Yoder, M. E. Schwartz, T. P. Orlando, I. Siddiqi, S. Gustavsson, K. P. O. Brien, and W. D. Oliver, *Broadband squeezed microwaves and amplification with a Josephson travelling-wave parametric amplifier*, Nature Physics **19**, 706 (2023). [Cited on pages 1, 3, and 35.]

[33] B. Abdo, F. Schackert, M. Hatridge, C. Rigetti, and M. Devoret, *Josephson amplifier for qubit readout*, Applied Physics Letters **99**, 16 (2011). [Cited on pages 1, 3, and 35.]

[34] A. Kamal, A. Roy, J. Clarke, and M. H. Devoret, *Asymmetric frequency conversion in nonlinear systems driven by a biharmonic pump*, Physical Review Letters **113**, 247003 (2014). [Cited on pages 1, 3, and 35.]

[35] Y. Jiang, E. P. Ruddy, K. O. Quinlan, M. Malnou, N. E. Frattini, and K. W. Lehnert, *Accelerated Weak Signal Search Using Mode Entanglement and State Swapping*, Physical Review Applied **10**, 1 (2023). [Cited on pages 1, 3, and 35.]

[36] M. Pechal, L. Huthmacher, C. Eichler, S. Zeytino, A. A. Abdumalikov, S. Berger, A. Wallraff, and S. Filipp, *Microwave-Controlled Generation of Shaped Single Photons in Circuit Quantum Electrodynamics*, Physical Review X **4**, 041010 (2014). [Cited on pages 1, 3, and 35.]

[37] E. Flurin, N. Roch, F. Mallet, M. H. Devoret, and B. Huard, *Generating entangled microwave radiation over two transmission lines*, Physical Review Letters **109**, 183901 (2012). [Cited on pages 1, 2, 3, and 35.]

[38] K. W. Murch, U. Vool, D. Zhou, S. J. Weber, S. M. Girvin, and I. Siddiqi, *Cavity-assisted quantum bath engineering*, Physical Review Letters **109**, 183602 (2012). [Cited on pages 1, 3, and 35.]

[39] Z. Leghtas, S. Touzard, I. M. Pop, A. Kou, B. Vlastakis, A. Petrenko, K. M. Sliwa, A. Narla, S. Shankar, M. J. Hatridge, M. Reagor, L. Frunzio, R. J. Schoelkopf, M. Mirrahimi, and M. H. Devoret, *Confining the state of light to a quantum manifold by engineered two- photon*, Science **347**, 853 (2015). [Cited on pages 1, 3, 8, 10, 35, and 103.]

[40] R. Dassonneville, R. Assouly, T. Peronnin, P. Rouchon, and B. Huard, *Number-Resolved Photocounter for Propagating Microwave Mode*, Physical Review Applied **14** (2020). [Cited on pages 1, 2, 3, and 35.]

[41] R. Lescanne, S. Deléglise, E. Albertinale, U. Réglade, T. Capelle, E. Ivanov, T. Jacqmin, Z. Leghtas, and E. Flurin, *Irreversible Qubit-Photon Coupling for the Detection of Itinerant Microwave Photons*, Physical Review X **10**, 021038 (2020). [Cited on pages 1, 2, 3, 8, 35, 41, 42, 90, 94, 99, 100, 102, 103, and 108.]

[42] X. S. Ma, T. Herbst, T. Scheidl, D. Wang, S. Kropatschek, W. Naylor, B. Wittmann, A. Mech, J. Kofler, E. Anisimova, V. Makarov, T. Jennewein, R. Ursin, and A. Zeilinger, *Quantum teleportation over 143 kilometres using active feed-forward*, Nature **489**, 269 (2012). [Cited on page 1.]

[43] D. Abdelkhalek, M. Syllwasschy, N. J. Cerf, J. Fiurášek, and R. Schnabel, *Efficient entanglement distillation without quantum memory*, Nature Communications **7**, 11720 (2016). [Cited on page 1.]

[44] X. S. Ma, S. Zotter, J. Kofler, R. Ursin, T. Jennewein, Č. Brukner, and A. Zeilinger, *Experimental delayed-choice entanglement swapping*, Nature Physics **8**, 479 (2012). [Cited on page 1.]

[45] M. O. Scully and K. Drühl, *Quantum eraser: A proposed photon correlation experiment concerning observation and "delayed choice" in quantum mechanics*, Physical Review A **25**, 2208 (1982). [Cited on page 1.]

[46] Z. S. Yuan, Y. A. Chen, B. Zhao, S. Chen, J. Schmiedmayer, and J. W. Pan, *Experimental demonstration of a BDCZ quantum repeater node*, Nature **454**, 1098 (2008). [Cited on page 1.]

[47] Y. H. Deng, S. Q. Gong, Y. C. Gu, Z. J. Zhang, H. L. Liu, H. Su, H. Y. Tang, J. M. Xu, M. H. Jia, M. C. Chen, H. S. Zhong, H. Wang, J. Yan, Y. Hu, J. Huang, W. J. Zhang, H. Li, X. Jiang, L. You, Z. Wang, L. Li, N. L. Liu, C. Y. Lu, and J. W. Pan, *Solving Graph Problems Using Gaussian Boson Sampling*, Physical Review Letters **130**, 190601 (2023). [Cited on page 1.]

[48] X. M. Jin, Z. H. Yi, B. Yang, F. Zhou, T. Yang, and C. Z. Peng, *Experimental quantum error detection*, Scientific Reports **2**, 626 (2012). [Cited on page 1.]

[49] S. Komiyama, O. Asta, V. Antonov, T. Kutsuwa, and H. Hirai, *A single-photon detector in the far-infrared range*, Nature **403**, 405 (2000). [Cited on page 1.]

[50] J. C. Blakesley, P. See, A. J. Shields, B. E. Kardynałł, P. Atkinson, I. Farrer, and D. A. Ritchie, *Efficient single photon detection by quantum dot resonant tunneling diodes*, Physical Review Letters **94**, 067401 (2005). [Cited on page 1.]

[51] E. J. Gansen, M. A. Rowe, M. B. Greene, D. Rosenberg, T. E. Harvey, M. Y. Su, R. H. Hadfield, S. W. Nam, and R. P. Mirin, *Photon-number-discriminating detection using a quantum-dot, optically gated, field-effect transistor*, Nature Photonics **1**, 585 (2007). [Cited on page 1.]

[52] A. Divochiy, F. Marsili, D. Bitauld, A. Gaggero, R. Leoni, F. Mattioli, A. Korneev, V. Seleznev, N. Kaurova, O. Minaeva, G. Gol'Tsman, K. G. Lagoudakis, M. Benkhaoul, F. Lévy, and A. Fiore, *Superconducting nanowire photon-number-resolving detector at telecommunication wavelengths*, Nature Photonics **2**, 302 (2008). [Cited on page 1.]

[53] B. E. Kardynał, Z. L. Yuan, and A. J. Shields, *An avalanchephotodiode-based photon-number-resolving detector*, Nature Photonics **2**, 425 (2008). [Cited on page 1.]

[54] M. A. Albota and F. N. C. Wong, *Efficient single-photon counting at 155 μm by means of frequency upconversion*, Optics Letters **29**, 1449 (2004). [Cited on page 1.]

[55] Y. F. Chen, D. Hover, S. Sendelbach, L. Maurer, S. T. Merkel, E. J. Pritchett, F. K. Wilhelm, and R. McDermott, *Microwave photon counter based on josephson junctions*, Physical Review Letters **107**, 217401 (2011). [Cited on page 1.]

[56] K. Inomata, Z. Lin, K. Koshino, W. D. Oliver, J.-S. Tsai, T. Yamamoto, and Y. Nakamura, *Single microwave-photon detector using an artificial Λ-type three-level system*, Nature Communications **7**, 12303 (2016). [Cited on pages 1 and 98.]

[57] S. Kono, K. Koshino, Y. Tabuchi, A. Noguchi, and Y. Nakamura, *Quantum non-demolition detection of an itinerant microwave photon*, Nature Physics **14**, 546 (2018). [Cited on pages 1, 2, 10, and 98.]

[58] J. C. Besse, S. Gasparinetti, M. C. Collodo, T. Walter, P. Kurpiers, M. Pechal, C. Eichler, and A. Wallraff, *Single-Shot Quantum Nondemolition Detection of Individual Itinerant Microwave Photons*, Physical Review X **8**, 021003 (2018). [Cited on pages 1, 2, and 98.]

[59] M. Varnava, D. E. Browne, and T. Rudolph, *How good must single photon sources and detectors be for efficient linear optical quantum computation?*, Physical Review Letters **100**, 060502 (2008). [Cited on page 1.]

[60] R. H. Hadfield, *Single-photon detectors for optical quantum information applications*, Nature Photonics **3**, 696 (2009). [Cited on page 1.]

[61] S. K. Lamoreaux, K. A. Van Bibber, K. W. Lehnert, and G. Carosi, *Analysis of single-photon and linear amplifier detectors for microwave cavity dark matter axion searches*, Physical Review D **88**, 035020 (2013). [Cited on page 1.]

[62] C. J. Chunnilall, I. P. Degiovanni, S. Kück, I. Müller, and A. G. Sinclair, *Metrology of single-photon sources and detectors: a review*, Optical Engineering **53**, 081910 (2014). [Cited on page 1.]

[63] S. Barzanjeh, S. Guha, C. Weedbrook, D. Vitali, J. H. Shapiro, and S. Pirandola, *Microwave quantum illumination*, Physical Review Letters **114**, 080503 (2015). [Cited on page 1.]

[64] R. Assouly, R. Dassonneville, T. Peronnin, A. Bienfait, and B. Huard, *Quantum advantage in microwave quantum radar*, Nature Physics **19**, 1418 (2023). [Cited on pages 1 and 2.]

[65] F. Kronowetter, F. Fesquet, M. Renger, K. Honasoge, Y. Nojiri, K. Inomata, Y. Nakamura, A. Marx, R. Gross, and K. G. Fedorov, *Quantum Microwave Parametric Interferometer*, Physical Review Applied **20**, 024049 (2023). [Cited on pages 1 and 2.]

[66] Z. Wang, L. Balembois, M. Rančić, E. Billaud, M. Le Dantec, A. Ferrier, P. Goldner, S. Bertaina, T. Chanelière, D. Esteve, D. Vion, P. Bertet, and E. Flurin, *Single-electron spin resonance detection by microwave photon counting*, Nature **619**, 276 (2023). [Cited on pages 1 and 2.]

[67] E. Billaud, L. Balembois, M. Le Dantec, M. Rančić, E. Albertinale, S. Bertaina, T. Chanelière, P. Goldner, D. Estève, D. Vion, P. Bertet, and E. Flurin, *Microwave Fluorescence Detection of Spin Echoes*, Physical Review Letters **131**, 100804 (2023). [Cited on pages 1 and 2.]

[68] U. Las Heras, R. Di Candia, K. G. Fedorov, F. Deppe, M. Sanz, and E. Solano, *Quantum illumination reveals phase-shift inducing cloaking*, Scientific Reports **7**, 9333 (2017). [Cited on page 1.]

[69] K. G. Fedorov, M. Renger, S. Pogorzalek, R. Di Candia, Q. Chen, Y. Nojiri, K. Inomata, Y. Nakamura, M. Partanen, A. Marx, R. Gross, and F. Deppe, *Experimental quantum teleportation of propagating microwaves*, Science Advances **7**, eabk0891 (2021). [Cited on page 2.]

[70] M. Renger, S. Pogorzalek, Q. Chen, Y. Nojiri, K. Inomata, Y. Nakamura, M. Partanen, A. Marx, R. Gross, F. Deppe, and K. G. Fedorov, *Beyond the standard quantum limit for parametric amplification of broadband signals*, npj Quantum Information **7**, 160 (2021). [Cited on page 2.]

[71] R. Lescanne, L. Verney, Q. Ficheux, M. H. Devoret, B. Huard, M. Mirrahimi, and Z. Leghtas, *Escape of a Driven Quantum Josephson Circuit into Unconfined States*, Physical Review Applied **11**, 014030 (2019). [Cited on pages 2, 10, 54, 77, 86, 91, and 92.]

[72] L. Verney, R. Lescanne, M. H. Devoret, and Z. Leghtas, *Structural Instability of Driven Josephson Circuits Prevented by an Inductive Shunt*, Physical Review Applied **10**, 024003 (2019). [Cited on pages 2, 41, 54, 77, 86, 91, and 92.]

[73] R. Shillito, A. Petrescu, J. Cohen, J. Beall, M. Hauru, M. Ganahl, A. G. Lewis, G. Vidal, and A. Blais, *Dynamics of Transmon Ionization*, Physical Review Applied **18**, 034031 (2022). [Cited on pages 2, 3, 47, 48, 54, 78, 86, 91, and 92.]

[74] J. Cohen, A. Petrescu, R. Shillito, and A. Blais, *Reminiscence of classical chaos in driven transmons*, PRX Quantum **4**, 020312 (2023). [Cited on pages 2, 3, 4, 47, 49, 50, 55, 56, 78, 92, and 93.]

[75] M. Boissonneault, J. M. Gambetta, and A. Blais, *Improved superconducting qubit readout by qubit-induced nonlinearities*, Physical Review Letters **105**, 100504 (2010). [Cited on pages 2, 3, and 47.]

[76] L. S. Bishop, E. Ginossar, and S. M. Girvin, *Response of the Strongly Driven Jaynes-Cummings Oscillator*, Physical Review Letters **105**, 100505 (2010). [Cited on pages 2, 3, and 47.]

[77] I. Pietikäinen, J. Tuorila, D. S. Golubev, and G. S. Paraoanu, *Photon blockade and the quantum-to-classical transition in the driven-dissipative Josephson pendulum coupled to a resonator*, Physical Review A **99**, 063828 (2019). [Cited on pages 2, 3, 4, 14, 47, 53, and 78.]

[78] H. J. Carmichael, *Breakdown of photon blockade: A dissipative quantum phase transition in zero dimensions*, Physical Review X **5**, 031028 (2015). [Cited on pages 2, 4, 47, 49, 53, and 93.]

[79] T. K. Mavrogordatos, *Quantum phase transitions in the driven dissipative Jaynes-Cummings oscillator: From the dispersive regime to resonance*, EPL **116**, 54001 (2016). [Cited on pages 2, 47, 49, 51, 92, and 93.]

[80] T. Fink, A. Schade, S. Höfling, C. Schneider, and A. Imamoglu, *Signatures of a dissipative phase transition in photon correlation measurements*, Nature Physics **14**, 365 (2018). [Cited on pages 2, 3, 47, 78, and 92.]

[81] Q.-M. Chen, M. Fischer, Y. Nojiri, M. Renger, E. Xie, M. Partanen, S. Pogorzalek, K. G. Fedorov, A. Marx, F. Deppe, and R. Gross, *Quantum behavior of a superconducting Duffing oscillator at the dissipative phase transition*, Nature Communications **14**, 2896 (2023). [Cited on pages 2, 3, 14, 47, 49, 52, 78, and 93.]

[82] R. Utermann, T. Dittrich, and P. Hänggi, *Tunneling and the onset of chaos in a driven bistable system*, Physical Review E **49**, 273 (1994). [Cited on pages 2, 4, 47, 49, 50, and 93.]

[83] M. D. Reed, L. Dicarlo, B. R. Johnson, L. Sun, D. I. Schuster, L. Frunzio, and R. J. Schoelkopf, *High-fidelity readout in circuit quantum electrodynamics using the jaynes-cummings nonlinearity*, Physical Review Letters **105**, 173601 (2010). [Cited on pages 2, 77, and 91.]

[84] S. A. Maas, *Nonlinear Micorwave and RF Circuits*, Artech House, Inc., Norwood, MA 02062, 2003. [Cited on page 3.]

[85] D. F. Walls and G. J. Milburn, *Quantum Optics*, Springer-Verlag, Berlin Heidelberg, 2008. [Cited on pages 3, 9, 14, 17, 23, 36, 48, 49, 51, and 127.]

[86] P. D. Drummond and D. F. Walls, *Quantum theory of optical bistability. I. Nonlinear polarisability model*, Journal of Physics A: Mathematical and General **13**, 725 (1980). [Cited on pages 3, 14, 49, 51, and 78.]

[87] U. Vool and M. H. Devoret, *Introduction to Quantum Electromagnetic Circuits*, International Journal of Circuit Theory and Applications **45**, 897 (2017). [Cited on pages 4, 6, 11, and 12.]

[88] R. C. Jaeger and T. N. Blalock, *Microelectronic Circuit Design*, McGraw-Hill, New York, 2011. [Cited on page 4.]

[89] A. A. Clerk, M. H. Devoret, S. M. Girvin, F. Marquardt, and R. J. Schoelkopf, *Introduction to quantum noise, measurement, and amplification*, Reviews of Modern Physics **82**, 2 (2010). [Cited on pages 5, 6, 7, 14, and 127.]

[90] J. Koch, T. M. Yu, J. Gambetta, A. A. Houck, D. I. Schuster, J. Majer, A. Blais, M. H. Devoret, S. M. Girvin, and R. J. Schoelkopf, *Charge-insensitive qubit design derived from the Cooper pair box*, Physical Review A **76**, 042319 (2007). [Cited on pages 8, 11, 12, 31, 32, 34, 36, 38, and 47.]

[91] Y. Kubo, C. Grezes, A. Dewes, T. Umeda, J. Isoya, H. Sumiya, N. Morishita, H. Abe, S. Onoda, T. Ohshima, V. Jacques, A. Dréau, J. F. Roch, I. Diniz, A. Auffeves, D. Vion, D. Esteve, and P. Bertet, *Hybrid quantum circuit with a superconducting qubit coupled to a spin ensemble*, Physical Review Letters **107**, 220501 (2011). [Cited on page 8.]

[92] E. A. Sete, J. M. Gambetta, and A. N. Korotkov, *Purcell effect with microwave drive: Suppression of qubit relaxation rate*, Physical Review B **89**, 1 (2014). [Cited on pages 8 and 35.]

[93] M. Hofheinz, E. M. Weig, M. Ansmann, R. C. Bialczak, E. Lucero, M. Neeley, A. D. O'Connell, H. Wang, J. M. Martinis, and A. N. Cleland, *Generation of Fock states in a superconducting quantum circuit*, Nature **454**, 310 (2008). [Cited on pages 8 and 99.]

[94] R. Lescanne, M. Villiers, T. Peronnin, A. Sarlette, M. Delbecq, B. Huard, T. Kontos, M. Mirrahimi, and Z. Leghtas, *Exponential suppression of bit-flips in a qubit encoded in an oscillator*, Nature Physics **16**, 509 (2020). [Cited on page 8.]

[95] W. P. Schleich, *Quantum Optics in Phase Space*, Wiley-VCH, Berlin, 2001. [Cited on pages 9 and 36.]

[96] M. J. Reagor, *Superconducting Cavities for Circuit Quantum Electrodynamics*, Ph. D. Thesis, Yale University, 2015. [Cited on pages 9 and 36.]

[97] E. Xie, *A Scalable Quantum Memory*, Ph. D. Thesis, Technical University of Munich, 2018. [Cited on pages 9, 36, and 99.]

[98] A. Blais, R. S. Huang, A. Wallraff, S. M. Girvin, and R. J. Schoelkopf, *Cavity quantum electrodynamics for superconducting electrical circuits: An architecture for quantum computation*, Physical Review A **69**, 062320 (2004). [Cited on pages 9, 10, and 31.]

[99] H. Paik, D. I. Schuster, L. S. Bishop, G. Kirchmair, G. Catelani, A. P. Sears, B. R. Johnson, M. J. Reagor, L. Frunzio, L. I. Glazman, S. M. Girvin, M. H. Devoret, and R. J. Schoelkopf, *Observation of High Coherence in Josephson Junction Qubits Measured in a Three-Dimensional Circuit QED Architecture*, Physical Review Letters **107**, 240501 (2011). [Cited on pages 10, 12, and 102.]

[100] C. Rigetti, J. M. Gambetta, S. Poletto, B. L. Plourde, J. M. Chow, A. D. Córcoles, J. A. Smolin, S. T. Merkel, J. R. Rozen, G. A. Keefe, M. B. Rothwell, M. B. Ketchen, and M. Steffen, *Superconducting qubit in a waveguide cavity with a coherence time approaching 0.1 ms*, Physical Review B **86**, 100506 (2012). [Cited on pages 10 and 35.]

[101] G. Kirchmair, B. Vlastakis, Z. Leghtas, S. E. Nigg, H. Paik, E. Ginossar, M. Mirrahimi, L. Frunzio, S. M. Girvin, and R. J. Schoelkopf, *Observation of quantum state collapse and revival due to the single-photon Kerr effect*, Nature **495**, 205 (2013). [Cited on page 10.]

[102] L. Bretheau, P. Campagne-Ibarcq, E. Flurin, F. Mallet, and B. Huard, *Quantum dynamics of an electromagnetic mode that cannot contain N photons*, Science **348**, 776 (2015). [Cited on page 10.]

[103] X. Y. Jin, A. Kamal, A. P. Sears, T. Gudmundsen, D. Hover, J. Miloshi, R. Slattery, F. Yan, J. Yoder, T. P. Orlando, S. Gustavsson, and W. D. Oliver, *Thermal and Residual Excited-State Population in a 3D Transmon Qubit*, Physical Review Letters **114**, 240501 (2015). [Cited on pages 10, 26, 45, and 95.]

[104] M. Reagor, W. Pfaff, C. Axline, R. W. Heeres, N. Ofek, K. Sliwa, E. Holland, C. Wang, J. Blumoff, K. Chou, M. J. Hatridge, L. Frunzio, M. H. Devoret, L. Jiang, and R. J. Schoelkopf, *Quantum memory with millisecond coherence in circuit QED*, Physical Review B **94**, 014506 (2016). [Cited on pages 10, 32, and 36.]

[105] W. Pfaff, C. J. Axline, L. D. Burkhart, U. Vool, P. Reinhold, L. Frunzio, L. Jiang, M. H. Devoret, and R. J. Schoelkopf, *Controlled release of multiphoton quantum states from a microwave cavity memory*, Nature Physics **13**, 882 (2017). [Cited on pages 10 and 102.]

[106] E. Xie, F. Deppe, M. Renger, D. Repp, P. Eder, M. Fischer, J. Goetz, S. Pogorzalek, K. G. Fedorov, A. Marx, and R. Gross, *Compact 3D quantum memory*, Applied Physics Letters **112** (2018). [Cited on pages 10, 32, 35, and 99.]

[107] M. Kudra, J. Biznárová, A. Fadavi Roudsari, J. J. Burnett, D. Niepce, S. Gasparinetti, B. Wickman, and P. Delsing, *High quality three-dimensional aluminum microwave cavities*, Applied Physics Letters **117**, 070601 (2020). [Cited on page 10.]

[108] O. Milul, B. Guttel, U. Goldblatt, S. Hazanov, L. M. Joshi, D. Chausovsky, N. Kahn, E. Çiftyürek, F. Lafont, and S. Rosenblum, *A superconducting quantum memory with tens of milliseconds coherence time*, (2023). [Cited on pages 10 and 102.]

[109] V. V. Sivak, A. Eickbusch, B. Royer, S. Singh, I. Tsioutsios, S. Ganjam, A. Miano, B. L. Brock, A. Z. Ding, L. Frunzio, S. M. Girvin, R. J. Schoelkopf, and M. H. Devoret, *Real-time quantum error correction beyond break-even*, (2022). [Cited on page 10.]

[110] D. I. Schuster, A. A. Houck, J. A. Schreier, A. Wallraff, J. M. Gambetta, A. Blais, L. Frunzio, J. Majer, B. Johnson, M. H. Devoret, S. M. Girvin, and R. J. Schoelkopf, *Resolving photon number states in a superconducting circuit*, Nature **445**, 515 (2007). [Cited on page 10.]

[111] G. Rempe, R. J. Thompson, H. J. Kimble, and R. Lalezari, *Measurement of ultralow losses in an optical interferometer*, Optical Letters **17**, 363 (1992). [Cited on page 10.]

[112] CST STUDIO SUITE www.cst.com. [Cited on page 11.]

[113] Z. Chen, *Metrology of Quantum Control and Measurement in Superconducting Qubits*, Ph.D. Thesis, University of California Santa Barbara, 2018. [Cited on pages 11, 12, 113, and 117.]

[114] A. Cottet, *Implementation of a quantum bit in a superconducting circuit*, Ph.D. Thesis, l'Universite Paris VI, 2002. [Cited on pages 12, 36, and 38.]

[115] D. I. Schuster, *Circuit Quantum Electrodynamics*, Ph.D. Thesis, Yale University, 2007. [Cited on page 12.]

[116] N. S. Maslova, E. V. Anikin, N. A. Gippius, and I. M. Sokolov, *Effects of tunneling and multiphoton transitions on squeezed-state generation in bistable driven systems*, Physical Review A **99**, 043802 (2019). [Cited on pages 14 and 51.]

[117] J. Raftery, D. Sadri, S. Schmidt, H. E. Türeci, and A. A. Houck, *Observation of a Dissipation-Induced Classical to Quantum Transition*, Physical Review X **4**, 031043 (2014). [Cited on page 14.]

[118] M. Fitzpatrick, N. M. Sundaresan, A. C. Y. Li, J. Koch, and A. A. Houck, *Observation of a Dissipative Phase Transition in a One-Dimensional Circuit QED Lattice*, Physical Review X **7**, 011016 (2017). [Cited on page 14.]

[119] R. Ma, B. Saxberg, C. Owens, N. Leung, Y. Lu, J. Simon, and D. I. Schuster, *A dissipatively stabilized Mott insulator of photons*, Nature **566**, 51 (2019). [Cited on page 14.]

[120] J. Combes, J. Kerckhoff, and M. Sarovar, *The SLH framework for modeling quantum input-output networks*, Advances in Physics: X **2:3**, 784 (2016). [Cited on pages 14, 16, and 17.]

[121] C. W. Gardiner and P. Zoller, *Quantum Noise*, Springer-Verlag, Berlin Heidelberg, 2004. [Cited on page 16.]

[122] H. J. Carmichael, *Statistical Methods in Quantum Optics 1*, Springer-Verlag, Berlin Heidelberg, 2002. [Cited on page 16.]

[123] N. Yamamoto, *Quantum feedback amplification*, Physical Review Applied **5**, 044012 (2016). [Cited on page 18.]

[124] R. Shimazu and N. Yamamoto, *Quantum Functionalities Via Feedback Amplification*, Physical Review Applied **15**, 044006 (2021). [Cited on page 18.]

[125] R. Hamerly and H. Mabuchi, *Advantages of coherent feedback for cooling quantum oscillators*, Physical Review Letters **109**, 173602 (2012). [Cited on page 18.]

[126] Y. Kashiwamura and N. Yamamoto, *Dispersive-dissipative control strategy for quantum coherent feedback*, IFAC-PapersOnLine **50**, 1 (2017). [Cited on page 18.]

[127] Y. Kashiwamura and N. Yamamoto, *Replacing measurement feedback with coherent feedback for quantum state preparation*, Physical Review A **97**, 062341 (2018). [Cited on page 18.]

[128] Y. Yokotera and N. Yamamoto, *Geometric control theory for quantum back-action evasion*, EPJ Quantum Technology **3**, 15 (2016). [Cited on page 18.]

[129] N. Yamamoto, *Coherent versus measurement feedback: Linear systems theory for quantum information*, Physical Review X **4**, 10 (2014). [Cited on page 18.]

[130] P.-O. Guimond, B. Vermersch, M. L. Juan, A. Sharafiev, G. Kirchmair, and P. Zoller, *A unidirectional on-chip photonic interface for superconducting circuits*, npj Quantum Information **6**, 32 (2020). [Cited on page 18.]

[131] S. Kono, K. Koshino, D. Lachance-Quirion, A. F. van Loo, Y. Tabuchi, A. Noguchi, and Y. Nakamura, *Breaking the trade-off between fast control and long lifetime of a superconducting qubit*, Nature Communications **11**, 3683 (2020). [Cited on page 18.]

[132] J. Gough and M. R. James, *The series product and its application to quantum feedforward and feedback networks*, IEEE Transactions on Automatic Control **54**, 2530 (2009). [Cited on page 19.]

[133] J. Gough and M. R. James, *Quantum feedback networks: Hamiltonian formulation*, Communications in Mathematical Physics **287**, 1109 (2009). [Cited on page 19.]

[134] S. Probst, F. B. Song, P. A. Bushev, A. V. Ustinov, and M. Weides, *Efficient and robust analysis of complex scattering data under noise in microwave resonators*, Review of Scientific Instruments **86**, 024706 (2015). [Cited on pages 23 and 24.]

[135] Q.-M. Chen, M. Pfeiffer, M. Partanen, F. Fesquet, K. E. Honasoge, F. Kronowetter, Y. Nojiri, M. Renger, K. G. Fedorov, A. Marx, F. Deppe, and R. Gross, *Scattering coefficients of superconducting microwave resonators. I. Transfer matrix approach*, Physical Review B **106**, 214505 (2022). [Cited on pages 23 and 24.]

[136] Q.-M. Chen, M. Partanen, F. Fesquet, K. E. Honasoge, F. Kronowetter, Y. Nojiri, M. Renger, K. G. Fedorov, A. Marx, F. Deppe, and R. Gross, *The scattering coefficients of superconducting microwave resonators: II. System-bath approach*, Physical Review B **106**, 214506 (2022). [Cited on pages 23 and 24.]

[137] C. Müller, J. H. Cole, and J. Lisenfeld, *Towards understanding two-level-systems in amorphous solids: insights from quantum circuits*, Reports on progress in physics **82**, 124501 (2019). [Cited on pages 23, 26, and 27.]

[138] J. Lisenfeld, A. Bilmes, A. Megrant, R. Barends, J. Kelly, P. Klimov, G. Weiss, J. M. Martinis, and A. V. Ustinov, *Electric field spectroscopy of material defects in transmon qubits*, npj Quantum Information **5**, 105 (2019). [Cited on pages 23, 26, and 27.]

[139] C. Chernov, N. and Lesort, *Least Squares Fitting of Circles*, Journal of Mathematical Imaging and Vision **23**, 239 (2005). [Cited on page 24.]

[140] M. S. Khalil, M. J. Stoutimore, F. C. Wellstood, and K. D. Osborn, *An analysis method for asymmetric resonator transmission applied to superconducting devices*, Journal of Applied Physics **111**, 054510 (2012). [Cited on page 26.]

[141] C. R. McRae, H. Wang, J. Gao, M. R. Vissers, T. Brecht, A. Dunsworth, D. P. Pappas, and J. Mutus, *Materials loss measurements using superconducting microwave resonators*, Review of Scientific Instruments **91**, 091101 (2020). [Cited on pages 26, 27, and 29.]

[142] B. Lienhard, J. Braumüller, W. Woods, D. Rosenberg, G. Calusine, S. Weber, A. Vepsälä, K. O'Brien, T. P. Orlando, S. Gustavsson, and W. D. Oliver, *Microwave Packaging for Superconducting Qubits*, in *2019 IEEE MTT-S International Microwave Symposium (IMS)*, pages 275–278, 2019. [Cited on pages 26 and 29.]

[143] S. Huang, B. Lienhard, G. Calusine, A. Vepsäläinen, J. Braumüller, D. K. Kim, A. J. Melville, B. M. Niedzielski, J. L. Yoder, B. Kannan, T. P. Orlando, S. Gustavsson, and W. D. Oliver, *Microwave Package Design for Superconducting Quantum Processors*, PRX Quantum **2**, 020306 (2021). [Cited on pages 26, 29, and 30.]

[144] J. M. Martinis, K. B. Cooper, R. McDermott, M. Steffen, M. Ansmann, K. D. Osborn, K. Cicak, S. Oh, D. P. Pappas, R. W. Simmonds, and C. C. Yu, *Decoherence in Josephson qubits from dielectric Loss*, Physical Review Letters **95**, 210503 (2005). [Cited on page 26.]

[145] Y. Shalibo, Y. Rofe, D. Shwa, F. Zeides, M. Neeley, J. M. Martinis, and N. Katz, *Lifetime and Coherence of Two-Level Defects in a Josephson Junction*, **105**, 177001 (2010). [Cited on page 26.]

[146] A. M. Holder, K. D. Osborn, C. J. Lobb, and C. B. Musgrave, *Bulk and surface tunneling hydrogen defects in alumina*, Physical Review Letters **111**, 065901 (2013). [Cited on page 26.]

[147] L. Gordon, H. Abu-farsakh, A. Janotti, and C. G. V. D. Walle, *Hydrogen bonds in Al 2 O 3 as dissipative two-level systems in superconducting qubits*, Scientific Reports **4**, 7590 (2014). [Cited on page 26.]

[148] K. Agarwal, I. Martin, M. D. Lukin, and E. Demler, *Polaronic model of two-level systems in amorphous solids*, Physical Review B **87**, 144201 (2013). [Cited on page 26.]

[149] L. Faoro and L. B. Ioffe, *Interacting tunneling model for two-level systems in amorphous materials and its predictions for their dephasing and noise in superconducting microresonators*, Physical Review B **91**, 014201 (2015). [Cited on pages 26 and 81.]

[150] P. Kumar, S. Sendelbach, M. A. Beck, J. W. Freeland, Z. Wang, H. Wang, C. C. Yu, R. Q. Wu, D. P. Pappas, and R. McDermott, *Origin and Reduction of 1 /f Magnetic Flux Noise in Superconducting Devices*, Physical Review Applied **6**, 041001 (2016). [Cited on pages 26 and 27.]

[151] J. Lisenfeld, G. J. Grabovskij, C. Müller, J. H. Cole, G. Weiss, and A. V. Ustinov, *Observation of directly interacting coherent two-level systems in an amorphous material*, Nature Communications **6**, 7182 (2015). [Cited on pages 26 and 27.]

[152] A. D. Córcoles, J. M. Chow, J. M. Gambetta, C. Rigetti, J. R. Rozen, G. A. Keefe, M. Beth Rothwell, M. B. Ketchen, and M. Steffen, *Protecting superconducting qubits from radiation*, Applied Physics Letters **99** (2011). [Cited on pages 26, 29, 45, and 95.]

[153] K. Geerlings, Z. Leghtas, I. M. Pop, S. Shankar, L. Frunzio, R. J. Schoelkopf, M. Mirrahimi, and M. H. Devoret, *Demonstrating a driven reset protocol for a superconducting qubit*, Physical Review Letters **110**, 120501 (2013). [Cited on pages 26, 45, and 95.]

[154] A. A. Houck, J. A. Schreier, B. R. Johnson, J. M. Chow, J. Koch, J. M. Gambetta, D. I. Schuster, L. Frunzio, M. H. Devoret, S. M. Girvin, and R. J. Schoelkopf, *Controlling the spontaneous emission of a superconducting transmon qubit*, Physical Review Letters **101**, 1 (2008). [Cited on pages 26, 29, and 31.]

[155] J. Wenner, M. Neeley, R. C. Bialczak, M. Lenander, E. Lucero, A. D. O'Connell, D. Sank, H. Wang, M. Weides, A. N. Cleland, and J. M. Martinis, *Wirebond crosstalk and cavity modes in large chip mounts for superconducting qubits*, Superconductor Science and Technology **24** (2011). [Cited on pages 26 and 29.]

[156] J. Goetz, F. Deppe, M. Haeberlein, F. Wulschner, C. W. Zollitsch, S. Meier, M. Fischer, P. Eder, E. Xie, K. G. Fedorov, E. P. Menzel, A. Marx, and R. Gross, *Loss mechanisms in superconducting thin film microwave resonators*, Journal of Applied Physics **119**, 015304 (2016). [Cited on pages 26, 27, 29, 68, and 69.]

[157] A. Bilmes and J. D. Brehm, *Quantum sensors for microscopic tunneling systems*, npj Quantum Information **7**, 27 (2021). [Cited on page 27.]

[158] P. Dutta and P. M. Horn, *Low-frequency fluctuations in solids: 1/f noise*, Reviews of Modern Physics **53**, 497 (1981). [Cited on page 27.]

[159] E. Paladino, Y. Galperin, G. Falci, and B. L. Altshuler, *1/f noise: Implications for solid-state quantum information*, Reviews of Modern Physics **86**, 361 (2014). [Cited on page 27.]

[160] M. V. P. Altoé, A. Banerjee, C. Berk, A. Hajr, A. Schwartzberg, C. Song, M. Alghadeer, S. Aloni, M. J. Elowson, J. M. Kreikebaum, E. K. Wong, S. M. Griffin, S. Rao, A. Weber-Bargioni, A. M. Minor, D. I. Santiago, S. Cabrini, I. Siddiqi, and D. F. Ogletree, *Localization and Mitigation of Loss in Niobium Superconducting Circuits*, PRX Quantum **3**, 020312 (2022). [Cited on pages 27 and 58.]

[161] S. K. Lee, S. B. Lee, S. Y. Park, Y. S. Yi, and C. W. Ahn, *Structure of amorphous aluminum oxide*, Physical Review Letters **103**, 095501 (2009). [Cited on page 27.]

[162] W. A. Phillips, *Tunneling states in amorphous solids*, Journal of Low Temperature Physics **7**, 351 (1972). [Cited on pages 27 and 68.]

[163] M. V. Schickfus and S. Hunklinger, *Saturation of the dielectric absorption of vitreous silica at low temperatures*, Physics Letters A **64**, 144 (1977). [Cited on pages 27 and 68.]

[164] A. J. Leggett, S. Chakravarty, A. T. Dorsey, M. P. A. Fisher, A. Garg, and W. Zwerger, *Dynamics of the disspative two-state system*, Reviews of Modern Physics **59**, 1 (1987). [Cited on pages 27 and 68.]

[165] H. Wang, M. Hofheinz, J. Wenner, M. Ansmann, R. C. Bialczak, M. Lenander, E. Lucero, M. Neeley, A. D. O'Connell, D. Sank, M. Weides, A. N. Cleland, and J. M. Martinis, *Improving the coherence time of superconducting coplanar resonators*, Applied Physics Letters **95**, 233508 (2009). [Cited on page 27.]

[166] J. M. Sage, V. Bolkhovsky, W. D. Oliver, B. Turek, and P. B. Welander, *Study of loss in superconducting coplanar waveguide resonators*, Journal of Applied Physics **109**, 063915 (2011). [Cited on page 27.]

[167] B. El-Kareh, *Fundamentals of Semiconductor Processing Technologies*, Springer New York, New York, 1994. [Cited on pages 28 and 58.]

[168] D. C. Mattis and J. Bardeen, *Theory of the anomalous skin effect in normal and superconducting metals*, Physical Review **111**, 412 (1958). [Cited on page 28.]

[169] R. Barends, J. Wenner, M. Lenander, Y. Chen, R. C. Bialczak, J. Kelly, E. Lucero, P. O'Malley, M. Mariantoni, D. Sank, H. Wang, T. C. White, Y. Yin, J. Zhao, A. N. Cleland, J. M. Martinis, and J. J. Baselmans, *Minimizing quasiparticle generation from stray infrared light in superconducting quantum circuits*, Applied Physics Letters **99**, 113507 (2011). [Cited on page 29.]

[170] J. M. Kreikebaum, A. Dove, W. Livingston, E. Kim, and I. Siddiqi, *Optimization of infrared and magnetic shielding of superconducting TiN and Al coplanar microwave resonators*, Superconductor Science and Technology **29**, 104002 (2016). [Cited on page 29.]

[171] K. Karatsu, A. Endo, J. Bueno, P. J. De Visser, R. Barends, D. J. Thoen, V. Murugesan, N. Tomita, and J. J. Baselmans, *Mitigation of cosmic ray effect on microwave kinetic inductance detector arrays*, Applied Physics Letters **114**, 032601 (2019). [Cited on page 29.]

[172] M. McEwen, L. Faoro, K. Arya, A. Dunsworth, T. Huang, S. Kim, B. Burkett, A. Fowler, F. Arute, J. C. Bardin, A. Bengtsson, A. Bilmes, B. B. Buckley, N. Bushnell, Z. Chen, R. Collins, S. Demura, A. R. Derk, C. Erickson, M. Giustina, S. D. Harrington, S. Hong, E. Jeffrey, J. Kelly, P. V. Klimov, F. Kostritsa, P. Laptev, A. Locharla, X. Mi, K. C. Miao, S. Montazeri, J. Mutus, O. Naaman, M. Neeley, C. Neill, A. Opremcak, C. Quintana, N. Redd, P. Roushan, D. Sank, K. J. Satzinger, V. Shvarts, T. White, Z. J. Yao, P. Yeh, J. Yoo, Y. Chen, V. Smelyanskiy, J. M. Martinis, H. Neven, A. Megrant, L. Ioffe, and R. Barends, *Resolving catastrophic error bursts from cosmic rays in large arrays of superconducting qubits*, Nature Physics **18**, 107 (2022). [Cited on page 29.]

[173] H. Johnson and M. Graham, *High-Speed Signal Propagation*, Prentice Hall, New Jersey, 2003. [Cited on page 29.]

[174] J. Schirk, *Controlling the Environment of Superconducting Qubits*, Master Thesis, Technical University of Munich, 2022. [Cited on pages 30 and 74.]

[175] I. Khukhareva, *The superconducting properties of thin aluminum films*, Sov. Phys. JETP **16**, 828 (1963). [Cited on page 31.]

[176] B. L. Brandt, R. D. Parks, and R. D. Chaudhari, *Intermediate state of thin superconductors*, Journal of Low Temperature Physics **4**, 41 (1971). [Cited on page 31.]

[177] D. Kleppner, *Inhibited spontaneous emission*, Physical Review Letters **47**, 233 (1981). [Cited on page 31.]

[178] R. J. Bartlett and M. Musiał, *Coupled-cluster theory in quantum chemistry*, Reviews of Modern Physics **79**, 291 (2007). [Cited on page 31.]

[179] A. Blais, J. Gambetta, A. Wallraff, D. I. Schuster, S. M. Girvin, M. H. Devoret, and R. J. Schoelkopf, *Quantum-information processing with circuit quantum electrodynamics*, Physical Review A **75**, 032329 (2007). [Cited on pages 31 and 33.]

[180] J. Gambetta, A. Blais, M. Boissonneault, A. A. Houck, D. I. Schuster, and S. M. Girvin, *Quantum trajectory approach to circuit QED: Quantum jumps and the Zeno effect*, Physical Review A **77**, 012112 (2008). [Cited on page 34.]

[181] E. M. Purcell, H. C. Torrey, and R. V. Pound, *Resonance Absorption by Nuclear Magnetic Moments in a Solid*, Physical Review **69**, 37 (1946). [Cited on page 35.]

[182] M. Fox, *Quantum Optics*, Oxford University Press, New York, 2006. [Cited on pages 35 and 48.]

[183] E. A. Sete, J. M. Martinis, and A. N. Korotkov, *Quantum theory of a bandpass Purcell filter for qubit readout*, Physical Review A **92**, 012325 (2015). [Cited on page 35.]

[184] A. E. Krasnok, A. P. Slobozhanyuk, C. R. Simovski, S. A. Tretyakov, A. N. Poddubny, A. E. Miroshnichenko, Y. S. Kivshar, and P. A. Belov, *An antenna model for the Purcell effect*, Scientific Reports **5**, 12956 (2015). [Cited on page 35.]

[185] A. Kamal, J. Clarke, and M. H. Devoret, *Gain, directionality, and noise in microwave SQUID amplifiers: Input-output approach*, Physical Review B **86**, 144510 (2012). [Cited on page 35.]

[186] H. Goldstein, C. Poole, and J. Safko, *Classical Mechanics*, Addison Wesley, Boston, 2000. [Cited on page 36.]

[187] Z. K. Minev, Z. Leghtas, S. O. Mundhada, L. Christakis, I. M. Pop, and M. H. Devoret, *Energy-participation quantization of Josephson circuits*, npj Quantum Information **11** (2021). [Cited on page 38.]

[188] J. Ikonen, J. Goetz, J. Ilves, A. Keränen, A. M. Gunyho, M. Partanen, K. Y. Tan, D. Hazra, L. Grönberg, V. Vesterinen, S. Simbierowicz, J. Hassel, and M. Möttönen, *Qubit Measurement by Multichannel Driving*, Physical Review Letters **122**, 080503 (2019). [Cited on page 41.]

[189] R. Gross and A. Marx, *Festkörperphysik*, De Gruyter Oldenbourg, Berlin, Boston, 2022. [Cited on pages 47 and 50.]

[190] M. Elliott and E. Ginossar, *Applications of the Fokker-Planck equation in circuit quantum electrodynamics*, **94**, 043840 (2016). [Cited on pages 47, 49, 91, and 93.]

[191] P. Brookes, G. Tancredi, A. D. Patterson, J. Rahamim, M. Esposito, T. K. Mavrogordatos,

P. J. Leek, E. Ginossar, and M. H. Szymanska, *Critical slowing down in circuit quantum electrodynamics*, Science Advances **7**, eabe9492 (2021). [Cited on pages 47 and 49.]

[192] A. Rényi, *On measures of information and entropy*, Proceedings of the fourth Berkeley Symposium on Mathematics, Statistics and Probability **1**, 547 (1960). [Cited on pages 48 and 92.]

[193] S. Qolibikloo and A. Ghodsi, *More on phase transition and Rényi entropy*, European Physical Journal C **79**, 406 (2019). [Cited on pages 48 and 92.]

[194] S. Abramsky and B. Coecke, *Physical Traces: Quantum vs. Classical Information Processing*, Electronic Notes in Theoretical Computer Science **69**, 1 (2003). [Cited on page 48.]

[195] M. Renger, *Inter-lab Quantum Microwave Teleportation*, Ph. D. Thesis, Technical University of Munich, 2023. [Cited on page 48.]

[196] A. Kitaev and J. Preskill, *Topological Entanglement Entropy*, Physical Review Letters **96**, 110404 (2006). [Cited on page 48.]

[197] S. Ryu and T. Takayanagi, *Holographic Derivation of Entanglement Entropy from the anti–de Sitter Space/Conformal Field Theory Correspondence*, Physical Review Letters **96**, 181602 (2006). [Cited on page 48.]

[198] A. Bäcker, R. Ketzmerick, S. Löck, and L. Schilling, *Regular-to-chaotic tunneling rates using a fictitious integrable system*, Physical Review Letters **100**, 104101 (2008). [Cited on pages 49 and 50.]

[199] R. Ketzmerick and W. Wustmann, *Statistical mechanics of Floquet systems with regular and chaotic states*, Physical Review E **82**, 021114 (2010). [Cited on pages 49 and 50.]

[200] M. Grifoni and P. Hänggi, *Driven quantum tunneling*, Physics Reports **304**, 229 (1998). [Cited on pages 49 and 55.]

[201] M. Holthaus, *Floquet engineering with quasienergy bands oferiodically driven optical lattices*, Journal of Physics B: Atomic, Molecular and Optical Physics **49**, 013001 (2015). [Cited on page 49.]

[202] G. E. Santoro, *Introduction to Floquet - Lecture notes -*, Galileo Galilei Institute, 2019. [Cited on page 49.]

[203] K. Viebahn, *Introduction to Floquet theory*, Institute for Quantum Electronics, ETH Zürich, 8093 Zürich, Switzerland, 2020. [Cited on page 49.]

[204] J. Chávez-Carlos, R. G. Cortiñas, M. A. P. Reynoso, I. García-Mata, V. S. Batista, F. Pérez-Bernal, D. A. Wisniacki, and L. F. Santos, *Driving superconducting qubits into chaos*, (2023). [Cited on page 50.]

[205] A. J. Lichtenberg and M. A. Lieberman, *Regular and Stochastic Motion*, Springer-Verlag, New York, 1983. [Cited on page 50.]

[206] K. Macieszczak, M. Guţă, I. Lesanovsky, and J. P. Garrahan, *Towards a Theory of Metastability in Open Quantum Dynamics*, Physical Review Letters **116**, 240404 (2016). [Cited on page 52.]

[207] M. Greiner, O. Mandel, T. Esslinger, T. W. Haensch, and I. Bloch, *Quantum Phase Transition from a Superfluid to a Mott Insulator in a Gas of Ultracold Atoms.*, Nature **415**, 39 (2002). [Cited on page 53.]

[208] W. S. Bakr, A. Peng, M. E. Tai, R. Ma, J. Simon, J. I. Gillen, S. Fölling, L. Pollet, and

M. Greiner, *Probing the superfluid-to-Mott insulator transition at the single-atom level*, Science **329**, 547 (2010). [Cited on page 53.]

[209] M. P. A. Fisher, P. B. Weichman, G. Grinstein, and D. S. Fisher, *Boson localization and the superfluid-insulator transition*, Physical Review B **40**, 546 (1989). [Cited on page 53.]

[210] I. Carusotto and C. Ciuti, *Quantum fluids of light*, Reviews of Modern Physics **85**, 299 (2013). [Cited on page 53.]

[211] D. Jaksch, C. Bruder, J. I. Cirac, C. W. Gardiner, and P. Zoller, *Cold Bosonic Atoms in Optical Lattices*, Physical Review Letters **81**, 3108 (1998). [Cited on page 53.]

[212] M. V. Berry, *Regular and irregular semiclassical wavefunctions*, Journal of Physics A: Mathematical and General **10**, 2083 (2010). [Cited on page 55.]

[213] https://twitter.com/jaygambetta/status/1395347923123245056 Accessed: 2023/08/01. [Cited on pages 57 and 102.]

[214] J. Goetz, *The Interplay of Superconducting Quantum Circuits and Propagating Microwave States*, Ph.D. Thesis, Technical University of Munich, 2017. [Cited on pages 57, 59, 66, 69, 80, and 81.]

[215] P. Missale, *Fabrication of Low-Loss Josephson Junctions for Quantum Devices*, Bachelor Thesis, Technical University of Munich, 2021. [Cited on pages 57 and 63.]

[216] C. Scheuer, *Fabrication of Superconducting Thin-Film Resonators and Josephson Junctions*, Master Thesis, Technical University of Munich, 2021. [Cited on pages 57 and 63.]

[217] N. Bruckmoser, *Development of a Fabrication Process for High-Coherence Niobium Qubits*, Master Thesis, Technical University of Munich, 2021. [Cited on pages 57, 63, and 70.]

[218] L. Hölscher, *Optimization of Aluminum Thin Films and Fabrication of Superconducting Qubit Systems*, Master Thesis, Technical University of Munich, 2021. [Cited on pages 57, 63, and 74.]

[219] D. C. Bunch, *Minimizing Losses in Superconducting Coplanar Waveguide Resonators*, Master Thesis, Technical University of Munich, 2022. [Cited on pages 57 and 70.]

[220] K.-S. Koh, J. Chin, J. Chia, and C.-L. Chiang, *Quantitative Studies on PDMS-PDMS Interface Bonding with Piranha Solution and its Swelling Effect*, Micromachines **3**, 427 (2012). [Cited on page 58.]

[221] N. Ikarashi, K. Watanabe, and Y. Miyamoto, *High-resolution transmission electron microscopy of an atomic structure at a Si(001) oxidation front*, Physical Review B **62**, 15989 (2000). [Cited on page 58.]

[222] D. S. Wisbey, J. Gao, M. R. Vissers, F. C. S. da Silva, J. S. Kline, L. Vale, and D. P. Pappas, *Effect of metal/substrate interfaces on radio-frequency loss in superconducting coplanar waveguides*, Journal of Applied Physics **108**, 093918 (2010). [Cited on page 58.]

[223] D. M. Knotter, *Etching Mechanism of Vitreous Silicon Dioxide in HF-Based Solutions*, Journal of the American Chemical Society **122**, 4345 (2000). [Cited on page 58.]

[224] G. J. Dolan, *Offset masks for lift-off photoprocessing*, Applied Physics Letters **31**, 337 (1977). [Cited on page 61.]

[225] M. Wang, *Lithography*, IntechOpen, Rijeka, 2010. [Cited on page 62.]

[226] T. Brenninger, *A new thin film deposition system for the preparation of persistent current qubits*, Master Thesis, Technical University of Munich, 2007. [Cited on page 63.]

[227] M. V. Costache, G. Bridoux, I. Neumann, and S. O. Valenzuela, *Lateral metallic devices made by a multiangle shadow evaporation technique*, Journal of Vacuum Science and Technology B **30**, 04E105 (2012). [Cited on page 64.]

[228] A. Dunsworth, A. Megrant, C. Quintana, Z. Chen, R. Barends, B. Burkett, B. Foxen, Y. Chen, B. Chiaro, A. Fowler, R. Graff, E. Jeffrey, J. Kelly, E. Lucero, J. Y. Mutus, M. Neeley, C. Neill, P. Roushan, D. Sank, A. Vainsencher, J. Wenner, T. C. White, and J. M. Martinis, *Characterization and reduction of capacitive loss induced by sub-micron Josephson junction fabrication in superconducting qubits*, Applied Physics Letters **111**, 022601 (2017). [Cited on page 65.]

[229] R.-Y. Yang, C.-Y. Hung, Y.-K. Su, M.-H. Weng, and H.-W. Wu, *Loss characteristics of silicon substrate with different resistivities*, Microwave and Optical Technology Letters **48**, 1773 (2006). [Cited on page 70.]

[230] J. Verjauw, A. Potočnik, M. Mongillo, R. Acharya, F. Mohiyaddin, G. Simion, A. Pacco, T. Ivanov, D. Wan, A. Vanleenhove, L. Souriau, J. Jussot, A. Thiam, J. Swerts, X. Piao, S. Couet, M. Heyns, B. Govoreanu, and I. Radu, *Investigation of Microwave Loss Induced by Oxide Regrowth in High-Q Niobium Resonators*, Physical Review Applied **16**, 014018 (2021). [Cited on page 70.]

[231] D. I. Schuster, A. Wallraff, A. Blais, L. Frunzio, R.-S. Huang, J. Majer, S. M. Girvin, and R. J. Schoelkopf, *ac Stark Shift and Dephasing of a Superconducting Qubit Strongly Coupled to a Cavity Field*, Physical Review Letters **94**, 123602 (2005). [Cited on pages 78 and 88.]

[232] C. M. Caves, *Quantum limits on noise in linear amplifiers*, Physical Review D **26**, 1817 (1982). [Cited on page 80.]

[233] H. Friis, *Noise Figures of Radio Receivers*, Proceedings of the IRE **32**, 419 (1944). [Cited on page 80.]

[234] C. Müller, J. Lisenfeld, A. Shnirman, and S. Poletto, *Interacting two-level defects as sources of fluctuating high-frequency noise in superconducting circuits*, Physical Review B **92**, 035442 (2015). [Cited on page 81.]

[235] P. V. Klimov, J. Kelly, Z. Chen, M. Neeley, A. Megrant, B. Burkett, R. Barends, K. Arya, B. Chiaro, Y. Chen, A. Dunsworth, A. Fowler, B. Foxen, C. Gidney, M. Giustina, R. Graff, T. Huang, E. Jeffrey, E. Lucero, J. Y. Mutus, O. Naaman, C. Neill, C. Quintana, P. Roushan, D. Sank, A. Vainsencher, J. Wenner, T. C. White, S. Boixo, R. Babbush, V. N. Smelyanskiy, H. Neven, and J. M. Martinis, *Fluctuations of Energy-Relaxation Times in Superconducting Qubits*, Physical Review Letters **121**, 090502 (2018). [Cited on page 81.]

[236] S. M. Meißner, A. Seiler, J. Lisenfeld, A. V. Ustinov, and G. Weiss, *Probing individual tunneling fluctuators with coherently controlled tunneling systems*, Physical Review B **97**, 180505 (2018). [Cited on page 81.]

[237] S. Schlör, J. Lisenfeld, C. Müller, A. Bilmes, A. Schneider, D. P. Pappas, A. V. Ustinov, and M. Weides, *Correlating Decoherence in Transmon Qubits: Low Frequency Noise by Single Fluctuators*, Physical Review Letters **123**, 190502 (2019). [Cited on page 81.]

[238] Y. Nojiri, K. E. Honasoge, A. Marx, K. G. Fedorov, and R. Gross, *Onset of transmon ionization in microwave single-photon detection*, Phys. Rev. B **109**, 174312 (2024). [Cited on page 83.]

[239] J. Lamprich, *Optimized Geometry for a Compact 3D Quantum Memory*, Master Thesis, Technical University of Munich, 2020. [Cited on pages 84 and 99.]

[240] M. Naghiloo and M. Lab, *Introduction to experimental quantum measurement with superconducting qubits*, 2019. [Cited on pages 88 and 89.]

[241] B. Q. Jin and V. E. Korepin, *Quantum spin chain, Toeplitz determinants and the Fisher-Hartwig conjecture*, Journal of Statistical Physics **116**, 79 (2004). [Cited on page 92.]

[242] A. P. Hines, R. H. McKenzie, and G. J. Milburn, *Quantum entanglement and fixed-point bifurcations*, Physical Review A **71**, 042303 (2005). [Cited on page 93.]

[243] L. Balembois, J. Travesedo, L. Pallegoix, A. May, E. Billaud, M. Villiers, D. Estève, D. Vion, P. Bertet, and E. Flurin, *Practical Single Microwave Photon Counter with* 10^{-22} $\mathrm{W}/\sqrt{\mathrm{Hz}}$ *sensitivity*, (2023). [Cited on pages 97 and 98.]

[244] J. M. Gambetta, F. Motzoi, S. T. Merkel, and F. K. Wilhelm, *Analytic control methods for high-fidelity unitary operations in a weakly nonlinear oscillator*, Physical Review A **83**, 012308 (2011). [Cited on page 97.]

[245] Z. Chen, J. Kelly, C. Quintana, R. Barends, B. Campbell, Y. Chen, B. Chiaro, A. Dunsworth, A. G. Fowler, E. Lucero, E. Jeffrey, A. Megrant, J. Mutus, M. Neeley, C. Neill, P. J. O'Malley, P. Roushan, D. Sank, A. Vainsencher, J. Wenner, T. C. White, A. N. Korotkov, and J. M. Martinis, *Measuring and Suppressing Quantum State Leakage in a Superconducting Qubit*, Physical Review Letters **116**, 020501 (2016). [Cited on page 97.]

[246] F. Yan, S. Gustavsson, A. Kamal, J. Birenbaum, A. P. Sears, D. Hover, T. J. Gudmundsen, D. Rosenberg, G. Samach, S. Weber, J. L. Yoder, T. P. Orlando, J. Clarke, A. J. Kerman, and W. D. Oliver, *The flux qubit revisited to enhance coherence and reproducibility*, Nature Communications **7**, 12964 (2016). [Cited on pages 97 and 98.]

[247] S. Li, Z. Ni, L. Zhang, Y. Cai, J. Mai, S. Wen, P. Zheng, X. Deng, S. Liu, Y. Xu, and D. Yu, *Autonomous stabilization of Fock states in an oscillator against multi-photon losses*, (2023). [Cited on page 99.]

[248] T. Yamamoto, K. Inomata, M. Watanabe, K. Matsuba, T. Miyazaki, W. D. Oliver, Y. Nakamura, and J. S. Tsai, *Flux-driven Josephson parametric amplifier*, Applied Physics Letters **93**, 042510 (2008). [Cited on page 102.]

[249] S. E. Rasmussen, K. S. Christensen, S. P. Pedersen, L. B. Kristensen, T. Bækkegaard, N. J. S. Loft, and N. T. Zinner, *Superconducting Circuit Companion - an Introduction with Worked Examples*, Physical Review Applied **2**, 040204 (2021). [Cited on page 117.]

[250] W. Greiner, *Quantum Mechanics*, Springer-Verlag, Berlin Heidelberg, 2001. [Cited on page 121.]

[251] D. J. Griffiths, *Introduction to Quantum Mechanics*, Prentice Hall, Upper Saddle River, New Jersey, 1995. [Cited on page 121.]

[252] J. J. Sakurai and S. F. Tuan, *Modern Quantum Mechanics*, Addison-Wesley Publishing Company, Inc., Massachusetts, 1994. [Cited on page 121.]

List of publications (2019.09-2024.05)

Yuki Nojiri, Kedar E. Honasoge, Achim Marx, Kirill G. Fedorov, and Rudolf Gross, *Onset of transmon ionization in microwave single-photon detection*, Physical Review B, **109**, 174312 (2024)

Michael Renger, Simon Gandorfer, Wun Yam, Florian Fesquet, Maria-Teresa Handschuh, Kedar E. Honasoge, Fabian Kronowetter, Yuki Nojiri, Matti Partanen, Meike Pfeiffer, Harriet van der Vliet, Anthony J. Matthews, Joonas Govenius, Robab N. Jabdaraghi, Mika Prunnila, Achim Marx, Frank Deppe, Rudolf Gross, Kirill G. Fedorov, *Cryogenic microwave link for quantum local area networks*, arXiv:2308.12398 (2023)

Fabian Kronowetter, Florian Fesquet, Michael Renger, Kedar Honasoge, Yuki Nojiri, Kunihiro Inomata, Yasunobu Nakamura, Achim Marx, Rudolf Gross, Kirill G. Fedorov, *Quantum Microwave Parametric Interferometer*, Physical Review Applied, **20**, 024049 (2023)

Qi-Ming Chen, Michael Fischer, Yuki Nojiri, Michael Renger, Edwar Xie, Matti Partanen, Stefan Pogorzalek, Kirill G. Fedorov, Achim Marx, Frank Deppe, and Rudolf Gross, *Quantum behavior of the Duffing oscillator at the dissipative phase transition*, Nature Communications **14**, 2896 (2023)

Florian Fesquet, Fabian Kronowetter, Michael Renger, Qi-Ming Chen, Kedar Honasoge, Oscar Gargiulo, Yuki Nojiri, Achim Marx, Frank Deppe, Rudolf Gross, and Kirill G. Fedorov, *Perspectives of microwave quantum key distribution in open-air*, Physical Review A **108**, 032607 (2023)

Michael Renger, Stefan Pogorzalek, Florian Fesquet, Kedar Honasoge, Fabian Kronowetter, Qi-Ming Chen, Yuki Nojiri, Kunihiro Inomata, Yasunobu Nakamura, Achim Marx, Frank Deppe, Rudolf Gross, Kirill G. Fedorov, *Flow of quantum correlations in noisy two-mode squeezed microwave states*, Physical Review A **106**, 052415 (2022)

Qi-Ming Chen, Fabian Kronowetter, Florian Fesquet, Kedar E. Honasoge, Yuki Nojiri, Michael Renger, Kirill G. Fedorov, Achim Marx, Frank Deppe, and Rudolf Gross, *Tuning and amplifying the interactions in superconducting quantum circuits with subradiant qubits*, Physical Review A **105**, 012405 (2022)

Qi-Ming Chen, Matti Partanen, Florian Fesquet, Kedar E. Honasoge, Fabian Kronowetter, Yuki Nojiri, Michael Renger, Kirill G. Fedorov, Achim Marx, Frank Deppe, and Rudolf Gross, *The scattering coefficients of superconducting microwave resonators: II. System-bath approach*, Physical Review B **106**, 214506 (2022)

Qi-Ming Chen, Meike Pfeiffer, Matti Partanen, Florian Fesquet, Kedar E. Honasoge, Fabian Kronowetter, Yuki Nojiri, Michael Renger, Kirill G. Fedorov, Achim Marx, Frank Deppe, and Rudolf Gross, *The scattering coefficients of superconducting microwave resonators: I. Transfer-matrix approach*, Physical Review B **106**, 214505 (2022)

Kirill G. Fedorov, Michael Renger, Stefan Pogorzalek, Roberto Di Candia, Qi-Ming Chen, Yuki Nojiri, Kunihiro Inomata, Yasunobu Nakamura, Matti Partanen, Achim Marx, Rudolf Gross, and Frank Deppe, *Experimental quantum teleportation of propagating microwaves*, Science Advances 7 (52), eabk0891 (2021)

Michael Renger, Stefan Pogorzalek, Qi-Ming Chen, Yuki Nojiri, Kunihiro Inomata, Yasunobu Nakamura, Matti Partanen, Achim Marx, Rudolf Gross, Frank Deppe, and Kirill G. Fedorov, *Beyond the standard quantum limit for parametric amplification of broadband signals*, njp Quantum Information **7**, 160 (2021)

Qi-Ming Chen, Frank Deppe, Re-Bing Wu, Luyan Sun, Yu-xi Liu, Yuki Nojiri, Stefan Pogorzalek,

Michael Renger, Matti Partanen, Kirill G. Fedorov, Achim Marx, and Rudolf Gross, *Quantum Fourier transform in oscillating modes*, arXiv:1912.09861 (2019)

Acknowledgement

In these past four years, it was a remarkably exciting, inspiring, and challenging experience ranging from the science, engineering to private life. Especially, I enjoyed analytically deriving the formulas, numerically simulating complex quantum systems, setting up the labs, conducting experiments, and analyzing the measurement data. But these enjoyments could not be achieved without my colleagues, with whom I discussed the underlying physics, fabricated the chips, set up the new labs, opened and closed the fridge, stilled our dehydration (with beer, sake, and Glühwein), ate in Honghong, played games, enjoyed Munich city life, and took trips. Each single experience shaped my life. Thus, hereby, I would like to take this as an opportunity to thank all of the people, who supported me during my Ph.D.:

First, I would like to deeply thank **Prof. Dr. Rudolf Gross** for making it possible to pursuing the Ph.D. here in Walther-Meißner-Institute. I always admire your broad and deep knowledge about physics. Especially, your textbook of solid state physics helped me a lot during my bachelor, master, and Ph.D. times. Furthermore, your positive comments, how important our single-photon detection research is, motivated me a lot.

Next, I really would like to thank **Dr. Kirill G. Fedorov**. The achievements in this work are thanks to your constant support, your patience and your clear guidance. You were always available for me, if I needed any help and always had time for discussions. Our weekly discussions about the measurement, simulation and theoretical results and your clear suggestions to the next step helped me a lot to progress and delve further into the field of quantum physics and engineering. I learned a lot from you ranging from quantum physics, step-by-step simulations, proper lab work, experiments, to professional work. In my heart, I was always so happy, when you gave me positive feedbacks. Spaciba!

Special thanks also go to **Dr. Frank Deppe** for inviting me to pursue my Ph.D. in WMI. Everything has started, when I have asked you to supervise my master thesis during my stay in Japan. After my master thesis and my one-year stay in Dresden, you have invited me to pursue my Ph.D. here in WMI. I obtained the opportunity to learn about the depth of fabrication and qubit experiments. I enjoyed discussing with you along with the Coke in your hand. The deep discussions about the experimental results and also physics lead me to understand the key aspects.

Furthermore, I would like to express my thanks to **Dr. Achim Marx** for your active support in cryogenic engineering. Without your help, our CIRQUS fridge and our LD400 fridge in the MCQST lab could not be operated so smoothly. The conversations with you, flavored with your good humor, were always encouraging.

I further would like to thank **Prof. Dr. Stefan Filipp**. Since you have joined the WMI as a director, various things changed in WMI. Especially, the fabrication processes had improved enormously thanks to all new equipment and regulations, which lead to a fabrication of high-performing quantum chips. Also drinking beer in the backyard and in the Oktoberfest together was a good time.

Next, many special thanks go to our father of fabrication, **Dr. Johneph Sukham**. In the fab, you helped us a lot in improving the fabrication process. Especially, pushing the HF-dip resulted to a breakthrough in the high quality factors in WMI. Moreover, you were always taking time to discuss about the fabrication results, and keeping asking questions. Your passion to fabrication inspired me a lot. Beside of the work in WMI, you always invited us to meet in the weekends by saying "We should not work, but rest!". Cooking, eating curry and drinking were our routines. I still cannot understand how much beer you could drink. I really wish you were still here to celebrate our remarkable fabrication results achieved by our fab team and to enjoy our weekends.

In addition, I would like to thank **Dr. Hans Hübl** for helping me, when I was searching for specific things required for my research and lab. Besides, your cheerful character was amusing, especially in the Oktoberfest. Thank you for inviting us for a mass!

Special thanks go to **Dr. Jürgen Lisenfeld** and **Dr. Alexander Bilmes** for inviting me to Karlsruhe, but also helping me to figure out the problems occurred in the fabrication, even after I left Karlsruhe. I cannot forget your openness to sharing any knowledge you gained. You explained me

everything in details, which was so astonishing to me. This open spirit is also now part of me. Thanks to your support, I learned a lot about the fabrication. Your hospitality in Karlsruhe was perfect. Especially, I did not expect at all that I would play Mahjong with you and with your great friends in a bar, Alex! I also would like to thank **Dr. Akira Mochihashi** for your hospitality during the stay in Karlsruhe. I did not expect that we would meet each other again so early, when we met in the conference in Dresden. Thank you very much for letting me stay at your home and showing your large accelerator facility, KARA.

Thanks to all my colleagues in WMI during my time as a Ph.D. student. First, I would like to thank our fab specialist and the member of our Honghong group **Kedar E. Honasoge**. You are the most humorous person I have ever met in my entire life. I'm pretty sure that your existence changed uncountable things in WMI. Ranging from work to private, from hard times to joyful moments, from discussions to jokes, from cooking to drinking, from watching movies at home to traveling to Amsterdam and Las Vegas, from hiking to skiing, we experienced everything together. I still can remember, when Frank introduced us each other, saying that "we should work coherently". Yes, you were the best partner ever. I enjoyed a lot fabricating new chips with you, analyzing the measurement data, staying late for closing the fridge, and having our cooldown beer in the backyard. By the way, 361.

Next, I would like to express my dearest thanks to my soul, tea and office mate and the member of our Honghong group **Daniil Bazulin**. You are the most entertaining person I have ever met in my entire life. Together with Kedar, we experienced so much in the work and life. Thanks to you, our office was always filled with laugh. Especially, the interplay with Dave and Maria was always so much fun. Of course, not to be forgotten, your fashion, your unique policy and your dedication to cocktails, tea and coffee definitely contributed to this. It was so nice drinking with you in a cozy bar, going snowboarding in Kufstein, visiting Amsterdam, chilling at someone's home, and, of course, going to Honghong. I'm convinced that your special JTWPA operation will be more than successful! Spaciba!!

Moreover, I would like to thank our fab queen and my office mate **Maria-Teresa Handschuh**. You realized me how much potential a mere power point has: it is not a software, but an art. Your kindness was always heartwarming. It was so warm that our other office mates started to complain that our office is too hot - which I do not agree. Your character as a perfectionist is definitely needed for improving the fabrication processes. Also in private, we had together so many nice times in the WMI backyard, Amsterdam, Sonthofen, Dresden, Munich and of course in the Isar in the summer days.

I furthermore would like to thank our fab Yankee and my office mate **David Cole Bunch**. You are the beloved Capitalist who forms the yin and yang with our beloved Communist. You were also the last missing piece in our office. We know each other, since you joined us as a master student. The fact that Daniil and Kedar convinced Hans to place you in our office already tells how incredible person you are. Indeed, I was really happy, when you invited me for your Christmas party and sauna. Nice memories also include the bike trip to the neighborhood aiming to reach the Biergarten, along with the hike trip in Tegernsee. Naturally not to be forgotten, you are the most integrated person in the Bavarian culture. We need to play more Schafkopfen!

Many thanks also go to our former office mate, our toughest drinker, and the member of our Honghong group **Janine Gückelhorn**. It is incredible that we shared our office for more than three years together. You were the holy mother in our office, who warmly observed over us, whatever ridiculous things we did. Although you usually left WMI in the evening, I really appreciated, when you were with us in our (really late) Honghong dinner. Beside of playing board games, I had great times skiing with you in Kufstein. My still unsolved mystery is how much you can drink and outperform others by far - I still cannot understand. I hope you have an enjoyable life in Barcelona!

I would like to express my thanks to our former office mate **Dr. Daniel Schwienbacher**. Besides being really funny, you always helped me with the fab and answered my questions, whenever I had questions. You continued helping our fab team as a postdoc, which was a great help. I hope you have a great time in Australia!

I would like to express my thanks to our former office mates **Dr. Daniel Schwienbacher**, **Dr. Leander Peis** and **Dr. Lukas Liensberger**.

Dr. Edwar Xie is the first person, who introduced me to the superconducting quantum circuit fabrication in WMI. Thank you very much for your time!

Of course, I have to further express my dearest thanks to all the members of qubit team! I would like to start with my good Bavarian sir, **Dr. Michael Renger**. Your deep understanding in physics surprised me always. The occasional sight of you smoking a pipe I think well represents your personality. This is also the reason why you were always welcome in our Honghong table.

Je tiens à toi remercier, **Florian Fesquet**. Bien que tu és vraiment occupé par ton propre travail, tu as toujours été là pour m'aider et également pour discuter de la physique. En dehors de notre temps à Hongkong, j'ai aussi apprécié les moments passés dans le métro à parler de nombreuses choses, y compris des anime et des manga ! Plus tard, nous avons aussi été de bons partenaires sur Duolingo. Flan is (not) a cheese cake.

I further would like to thank to another good colleague, **Fabian Kronowetter**. I always admired your working discipline. Not always working too much, but still achieving all the results are truly astonishing. Aside from work, I can still remember, when you, Kedar, and I were trying hard to eat the entire Chicago pizza with the IPA in Las Vegas.

Also, thank you very much, **Dr. Stefan Pogorzalek** and **Dr. Matti Pattanen**, for discussing about the physics and also helping me out resolving the technical issues in WMI! I always liked your chilled character.

In addition, I would like to thank **Dr. Qiming Chen** for your constant support, especially regarding the circle fit and phase transition. You always amazed me with your experimental and theoretical expertise!

Then, we have our colleagues, **Simon Gandorfer** and **Wun Kwan Yam**, who were always an important part of the physics discussion starting from your masters in WMI.

Of course, this work is supported by my students, **Christoph Scheuer**, **Patrick Missale**, **Aristo P**, **Valentin Weidemann**, and **Marius Strassner**. Although I might not have been a good supervisor, I'm really thankful for everything which you have achieved during the studies in WMI.

I furthermore owe thanks to our beer protector and supplier, **Thomas Luschmann**. Thank you for keeping us, Ph.D. and master students, always hydrated. Together with Kedar, Daniil, Maria, Dave, and Leon, we shared a lot of joyful times! I especially enjoyed the trip in Las Vegas with you! But please do not use your right hand ... it can be dangerous.

Next, my dearest thanks goes to our fab god **Leon Koch**. Without you, our fab did not reach the highest standard as we have now today. You are always one of our hanging out people not only in the WMI backyard or in Munich, but also in the Las Vegas trip!

Another unforgettable member of our Honghong group is, of course, our professor in Lehrstuhl für Alles, **Dr. Manuel Müller**, who achieved his title "Professor" before "Dr.". This is only possible because of your incomparable ingenuity, which amazed us all. All the time with you, in the backyard, game night, Isar, Munich, or in Amsterdam was truly amazing! Together with Kedar and Daniil, all the pranks we did against each other lie as a good memory. Yep ... locking your computer is important.

Speaking of Honghong group, there is another member **Matthias Grammer**. I'm glad that you came back to WMI after your master thesis and stay in Chile. Your always-positive mood and smile are truly encouraging and definitely motivated us all. I appreciated that you tried to separate me from my desk and join to the hydration event or Honghong.

Further, I would like to thank our "controversial" Honghong member, **Malay Singh**. The comments you sometimes randomly give are always one of the highlights in the backyard or in Honghong. Together with Kedar and Johneph, we definitely had a great time. I deeply appreciate your kindness, and also your present from India!

Moreover, we have our handsome looking postdoc, **Dr. Gleb Kyrlov**. I always enjoyed the times with you drinking beer in the backyard, but also eating in Honghong or chilling in Munich area. Spaciba!

Another spaciba goes to **Shamil Erkenov**. Although a silent person, the occasional conversations

in the morning and Honghong were always enjoyable. Please do not bully the police officers too much.

I further would like to express my gratitude to **Ana Strinic**, **Patricia Oehrl**, and **Korbinian Rubenbauer**. Among all the events we shared together, I definitely enjoyed the lunch time and the occasional hiking in Sonthofen with Fabian.

Thank you, **Dr. Max Werninghaus**, for sharing our dream to become the pirate king. Kaizoku-ou ni, ore wa naru!

Lea Richard, thank you for sharing many information to make the life in Paris easier! Merci beaucoup!

I would like to thank **Frederico Roy**, **Niklas Glaser**, **Frederik Pfeiffer**, **Maximilian Nägele** for organizing the volleyball events! These were one of the summer events I was looking forward to.

If the volleyball were the much-anticipated summer events, the Glühwein events were the winter events which I were really enjoying. Thank you very much **Niklas Bruckmoser**, **Monika Scheufele**, **Johannes Schirk**, and all others for organizing this amazing fun after work!

I am grateful to my Japanese colleagues, **Shugo Yoshii** and **Keita Takahashi**. It has been always nice to talk with you!

Additionally, I would like to express my gratitude to **Sebastian Kammerer** and **Astrid Habel** for their invaluable assistance with the provision and oversight of the clean room equipment and chemicals.

I am thankful to **Georg Nitschke**, **Mario Nodes**, **Christian Reichlmeier**, and **Alexander Röß** from the technical workshop for their support in bringing to life the various technical designs for the sample holders and resonator enclosures.

I owe thanks to the Helium liquefaction team, including **Peter Binkert**, **Harald Schwaiger**, and **Jan Naundorf**, for supplying the cryogenic liquids necessary for my experiments in CIRQUS.

My gratitude also extends to **Andreas Russo** for his support in electrical engineering.

I am also thankful to **Thomas Brenninger** for maintaining all the fab equipments in tact. Without your support, our fabrication process has never been finished.

I appreciate our administrative people, **Emel Dönertas**, **Andrea Person**, **Martina Meven**, and **Carola Siegmayer**, for their consistent help with the orders and administrative matters.

I am grateful to the cleaning personnel, **Maria Botta** and **Sybilla Plöderl**, for maintaining the cleanliness of the institute. Additionally, our chats were always a delightful bonus.

Dr. Juncheng E for the short vacation trips every year. I enjoyed the time outside of the institute, once in a while.

Patrick, **Markus**, and **Alexander** for the numerous board game nights w've shared, as well as all the trips we've embarked on together, I must confess, stepping out of the Institute occasionally was a welcome change.

In enclosing, I am deeply grateful to my parents, **Hiromi Nojiri** and **Naoki Nojiri**, for your constant support throughout my entire life.